East European Journal of Physics

East European Journal of Physics

East European Journal of Physics

ORIGINAL PAPERS

East European Journal of Physics

No 2.   2020

WEAKLY NONLINEAR MAGNETIC CONVECTION IN A NONUNIFORMLY ROTATING ELECTRICALLY CONDUCTIVE MEDIUM UNDER THE ACTION OF MODULATION OF EXTERNAL FIELDS

🆔**Michael I. Kopp[a]***, 🆔**Anatoly V. Tur[c]**, 🆔**Volodymyr V. Yanovsky[a,b]**

[a]Institute for Single Cristals, Nat. Academy of Science Ukraine,
Nauky Ave. 60, Kharkov 31001,Ukraine
[b]V.N. Karazin Kharkiv National University
Sq. Svobody 4, Kharkiv, 61022 Ukraine
[c]Universite Toulouse [UPS], CNRS, Institute of Research for Astrophysics and Planetology
9 avenue du Colonel Roche, BP 44346, 31028 Toulouse Cedex 4, France
*Corresponding Author: michaelkopp0165@gmail.com
Received March 18, 2020; revised March 25, 2020; accepted March 27, 2020

In this paper we studied the weakly nonlinear stage of stationary convective instability in a nonuniformly rotating layer of an electrically conductive fluid in an axial uniform magnetic field under the influence of: a) temperature modulation of the layer boundaries; b) gravitational modulation; c) modulation of the magnetic field; d) modulation of the angular velocity of rotation. To describe the nonlinear convective phenomena the local Cartesian coordinate system was used, where the inhomogeneous rotation of the fluid layer was represented as the rotation with a constant angular velocity $\vec{\Omega}_0$ and azimuthal shear $\vec{U}_0(X)$ with linear dependence on the coordinate X. As a result of applying the method of perturbation theory for the small parameter $\varepsilon = \sqrt{(Ra - Ra_c)/Ra_c}$ of supercriticality of the stationary Rayleigh number nonlinear non-autonomous Ginzburg-Landau equations for the above types of modulation were obtaned. The amplitudes of the modulated fields were considered small, which having a second order ε^2, and the parametric effects influence to the development of stationary convection in the third order ε^3. Numerical solutions of the Ginzburg-Landau equations for various types of modulation of the external parametric influence had showed that: 1) by the nonuniform rotation with a positive Rossby number $Ro > 0$ the heat transfer in the fluid increases; 2) the increasing of modulation frequency ω_{mod} leads to suppression of heat transfer as with positive $(Ro > 0)$, so with negative $(Ro < 0)$ rotation profiles; 3) the effect of increasing the modulation amplitude of δ_{mod} is to increase the heat transfer anyway of the rotation profile. It is shown that the rotational modulation has the greatest influence on the change in heat flow in the system. At the same time, gravity modulation slightly exceeds magnetic modulation, and thermal phase modulation has a lesser effect on heat transfer in comparison with other types of modulations.
KEY WORDS: magnetorotational instability, Rayleigh-Benard convection, critical Rayleigh numbers, weakly nonlinear theory, non-autonomous Ginzburg-Landau equation

As known, the instability of a horizontal fluid layer heated from below in the field of gravity (the Rayleigh-Benard convection) is a classic problem of fluid dynamics [1-3]. The problems related to the effect of rotation and magnetic field on the Rayleigh-Benard convection cause particular interest. These problems are of applied nature for astrophysical, geophysical and for engineering-technological research [4]. The problem of rotating Rayleigh-Benard convection was studied sufficiently detailed in [5-6], where it was found that the Coriolis force with the rotation vector $\vec{\Omega}$ parallel to the gravity vector $\vec{g}$ inhibits the onset of convection and thus induces a stabilizing effect. Rayleigh-Benard convection, in which the axis of rotation of the medium and the uniform magnetic field coincide with the direction of the gravity vector, was well studied in [1-2]. The case is also interesting for astrophysical problems when the directions of the axes of rotation and the magnetic field are perpendicular to each other, and the direction of the magnetic field is perpendicular to the direction of the gravity vector. Such problem statement corresponds to convection in fluid layers located in the equatorial region of a rotating object, where the azimuthal magnetic field plays a significant role. The linear theory of such convection was first constructed in [7-8]. The linear theory of rotating magnetic convection for a random deviation of the axes of rotation and the magnetic field from the vertical axis (gravity field) was developed in [9]. A weakly nonlinear theory and stability analysis of azimuthal magnetic convection with $B_{0\varphi}(R) = const$ was performed in [10]. It proposes a model in which the centrifugal acceleration $g_c = \Omega^2(R_1 + R_2)$ can play the role of gravitational acceleration $\vec{g}$ for free convection in the local Cartesian approximation. The weakly nonlinear theory of centrifugal magnetoconvection considered in [10] was applied to the problem of a hydromagnetic dynamo. In all works on rotating magnetic convection [1-10], the rotation of a horizontal fluid layer with a constant angular velocity $\Omega = const$ was considered.

However, it is known that the majority of various space objects consisting of dense gases or liquid (Jupiter, Saturn, Sun, etc.) rotate non-uniformly, i.e. different parts of the object rotate around a common axis of rotation with different

angular velocities. Differential (non-uniform) rotation is also observed in galaxies, accretion disks, and extended rings of planets. Besides, such large-scale vortex structures as typhoons, cyclones and anticyclones, etc. also rotate non-uniformly. This circumstance served as the motivation for a theoretical study of Rayleigh-Benard convection in a non-uniformly rotating electrically conductive fluid in the axial uniform magnetic field [11-13], as well as in an external spiral magnetic field [14] with the nontrivial topology $B_0 rot B_0 \neq 0$.

The problem of the stability of an electrically conducting fluid between two rotating cylinders (Couette flow) and the Rayleigh-Benard problem in an external constant magnetic field were both considered in [11-12]. There was also carried out a study of the chaotic regime based on the equations of nonlinear dynamics of a six-dimensional $(6D)$ phase space. The analysis of these equations has shown the existence of a complex chaotic structure - a strange attractor. A convection mode in which a chaotic change in direction (inversion) and amplitude of the perturbed magnetic field, taking into account the inhomogeneous rotation of the medium, occurs was found as well. A study of the chaotic regime of magnetic convection of a nonuniformly rotating electrically conductive fluid in a spiral magnetic field based on the equations of nonlinear dynamics of an eight-dimensional $(8D)$ phase space was carried out in [14]. There was also found a convection regime in which a chaotic change in direction (inversion) and amplitude of the perturbed magnetic field occurs, taking into account the nonuniform rotation of the medium and the nonuniform external azimuthal magnetic field. Earlier, a weakly nonlinear stage for rotating magnetoconvection (for $\Omega = const$), in which a chaotic regime occurs, was studied in rotating fluid layers [15-16], in conducting media with a uniform magnetic field [17-20], and in conducting mediums rotating with a magnetic field [21]. However, the dynamics of the magnetic field itself was not considered in these works, which corresponds to the non-inductive approximation. Such tasks have great importance for technological applications: crystal growth, chemical processes of solidification and centrifugal casting of metals, etc.

The study of the dynamics of a magnetic field generated by convective motions of a fluid is important for the theory of magnetic dynamo [22]. A special role in this is played by issues related to the physical nature of inversions and variations in the magnetic field of the Earth, the Sun, and other space objects. In [23] Rikitaki proposed an electromechanical model of terrestrial magnetism. The study of the dynamic system of Rikitaki equations was also used to explain the chaotic inversion of the geomagnetic field [24-27]. In recent works [28-29] was investigated a modified system of Rikitaki equations taking into account friction and not reducing it to a three-dimensional form as for example in [24]. This made it possible to more clearly show that at first the oscillations of the current (or magnetic) variable near a certain stationary state with an increase in amplitude go into oscillations around an another stationary state, which simulated inversions [29]. In [28] it is established that after chaotic behavior the system goes into stable mode. According to the authors of [28], such a regime can describe superchrons in the inversion of the geomagnetic field. In contrast to the works [23-29], in [11-12], [14] it is proposed to model the magnetic field inversion by a dynamic system of equations of Lorentz type, respectively, for $(6D)$ and $(8D)$ - dimensional phase space.

In [13], the weakly nonlinear stage of stationary convective instability in a nonuniformly rotating layer of an electrically conductive fluid in an axial uniform magnetic field was studied. As a result of applying the perturbation theory method for a small parameter of supercriticality of the stationary Rayleigh number [30], the nonlinear autonomous Ginzburg-Landau equation was obtained. This equation describes the evolution of the finite amplitude of perturbations. A numerical analysis of this equation showed that the heat flux increases with rotation of the medium with positive Rossby numbers $Ro > 0$. In [13] it is shown that the weakly nonlinear convection based on the equations of the six-mode $(6D)$ Lorentz model transforms into the identical Ginzburg-Landau equation. The weakly nonlinear theory of convection was especially developed with regard to modulation of the parameters that control the convection process, what is very important for solving many technological problems. Different types of modulation, such as rotation [31-34], gravity [35-37], temperature [38-40] and magnetic field [41-42], were studied for stationary weakly nonlinear convection in various media: porous media, nanofluids, and so on. In these papers [31-42] the effect of modulation of the parameters (rotation, gravity, temperature, magnetic field) on the heat and mass transfer in convective media was determined. A parametric effect on convection can lead to either an increase or a decrease in heat transfer. In addition to technological problems, considering of the modulation of external fields plays an important role in modeling convective processes on the Earth, the Sun, and other space objects [43-44].

The aim of this work is to study a linear and weakly nonlinear theory of the stationary convection in a non-uniformly rotating layer of the electrically conductive fluid in the axial uniform magnetic field under the influence of: a) temperature modulation of the layer boundaries; b) gravitational modulation; c) modulation of the magnetic field; d) modulation of the angular velocity of rotation. The content of the work is outlined in the following sections. The basic equations for the evolution of small perturbations in the Boussinesq approximation, that describe non-uniformly rotating convection in external periodic fields: a) temperature modulation of the layer boundaries, b) gravitational modulation, c) modulation of the magnetic field, d) modulation of the angular velocity of rotation, are obtained in Section **PROBLEM STATEMENT AND BASIC EVOLUTION EQUATIONS**. In Section **EQUATIONS OF EVOLUTION OF FINITE AMPLITUDE FOR DIFFERENT TYPES OF MODULATION** we study the weakly nonlinear stage of stationary convection in a nonuniformly rotating layer of an electrically conductive fluid under the action of modulation of external fields. Using the method of perturbation theory with respect to the small parameter of

supercriticality of the Rayleigh number $\varepsilon = \sqrt{(Ra - Ra_c)/Ra_c}$) we obtained the nonlinear Ginzburg-Landau equation with a periodic coefficient for each type of modulation. The results of numerical solutions of the non-autonomous Ginzburg-Landau equation for each type of modulation show the dependence of the heat transfer (Nusselt number Nu) on the amplitude δ_{mod}, the frequency ω_{mod} of the modulation and the profile of the nonuniformly rotation (number Rossby Ro) are also presented in Section **EQUATIONS OF EVOLUTION OF FINITE AMPLITUDE FOR DIFFERENT TYPES OF MODULATION**.

The results developed in this work can be applied to various astrophysical and geophysical problems that consider magnetic convection in the rotating layers of the Sun, hot galactic clusters, accretion disks and other objects.

PROBLEM STATEMENT AND BASIC EVOLUTION EQUATIONS

Let us consider a nonuniformly rotating flow of an electrically conductive fluid located between two impermeable horizontal planes $z = 0$ and $z = h$, which are heated from below and cooled from above according to the periodic law. The temperature of the lower and upper horizontal boundaries is modulated in accordance with a time-harmonic law:

$$T_1 = T_0 + \frac{\Delta T}{2}[1 + \varepsilon^2 \delta_1 \cos(\tilde{\omega}_T t)] \quad at \quad z = 0 \tag{1}$$

$$T_2 = T_0 - \frac{\Delta T}{2}[1 - \varepsilon^2 \delta_1 \cos(\tilde{\omega}_T t + \phi)] \quad at \quad z = h,$$

where $T_0 = const$ is the temperature relative to which oscillations occur with a frequency of $\tilde{\omega}_T$ and a phase shift of φ, ΔT is the temperature difference between the lower and upper planes in the absence of modulation, δ_1 is the amplitude of thermal modulation, ε is a small parameter. In a cylindrical coordinate system an electrically conductive medium (plasma) rotates in the azimuthal direction with the speed $v_\phi = R\Omega(R, t)$. Here $\Omega(R, t)$ is the angular velocity of rotation, which makes small oscillations in time according to the periodic law:

$$\Omega(R, t) = \Omega(R)(1 + \varepsilon^2 \delta_2 \cos(\tilde{\omega}_R t)), \tag{2}$$

where $\tilde{\omega}_R$ is the frequency of rotation modulation, δ_2 is the amplitude of rotational modulation.

It is convenient to switch from a cylindrical coordinate system (R, φ, z) to a local Cartesian system (X, Y, Z) in order to describe nonlinear convective phenomena in a nonuniformly rotating layer of an electrically conducting fluid. If we consider a fixed region of a fluid layer with a radius R_0 and an angular velocity of rotation

$$\Omega_0(t) = \Omega(R_0, t) = \Omega_{00}(1 + \varepsilon^2 \delta_2 \cos(\tilde{\omega}_R t)), \quad \Omega_{00} = const,$$

then the coordinates $X = R - R_0$ correspond to the radial direction, $Y = R_0(\varphi - \varphi_0)$ to the azimuth and $Z = z$ - to the vertical direction (see Fig.1).
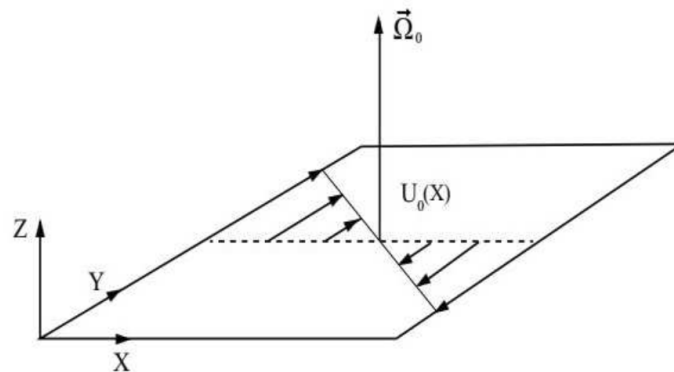
Fig. 1. Scheme of the shear flow in rotating flows, the flow being approximated in the local Cartesian coordinate system as a linear shift with velocity $U_0(X)$.

Then, nonuniform rotation of the fluid layer can be represented locally as a rotation with a constant angular velocity $\Omega_0(t)$ and azimuthal width [46], which velocity profile is locally linear: $U_0 = -q\Omega_0(t)Xe_y$, where $q \equiv -d\ln\Omega/d\ln R$ is the dimensionless shear flow parameter defined using the profile of angular velocity of rotation

$\Omega(R) = \Omega_0 (R/R_0)^{-q}$. The parameter q is related to the hydrodynamic Rossby number $Ro = \dfrac{R}{2\Omega}\dfrac{\partial \Omega}{\partial R}$ by the relation: $q = -2Ro$. Note that the accretion disks with the shear flow parameter $q = 3/2$ ($Ro = -3/4$) correspond to the Keplerian disk, $q = 2$ ($Ro = -1$) corresponds to the disk with a constant angular momentum or Rayleigh rotation profile. The case $q = 1$ ($Ro = -1/2$) corresponds to a system with a flat rotation curve, while $q = 0$ ($Ro = 0$) corresponds to a uniform (or solid-body) rotation with a constant angular velocity.

We assume that the direction of the external magnetic field B_0 coincides with the axis of rotation of the fluid $\Omega \parallel OZ$. In addition, the external magnetic field B_0 and the gravitational acceleration vector $g = (0, 0, -g)$ change with time according to the harmonic law

$$B_0 = B_{00}(1 + \varepsilon^2 \delta_3 \cos(\tilde{\omega}_B t)) e_Z, \tag{3}$$

$$g = -g_0 (1 + \varepsilon^2 \delta_4 \cos(\omega_g t)) e_Z, \tag{}$$

where δ_3, δ_4 are small amplitudes of magnetic and gravitational modulation, $B_{00} = const$, $\tilde{\omega}_B, \tilde{\omega}_g$ are frequencies modulation of magnetic and gravitational fields.

The influence of modulation of external fields will consider on the basis of the equations of magnetohydrodynamics in the Boussinesq approximation [1-2]:

$$\frac{\partial \vec{v}}{\partial t} + (\vec{v}\nabla)\vec{v} = -\frac{1}{\rho_0}\nabla(P + \frac{B^2}{8\pi}) + \frac{1}{4\pi\rho_0}(\vec{B}\nabla)\vec{B} + g\beta T \vec{e}_z + \nu\nabla^2 \vec{v} \tag{4}$$

$$\frac{\partial \vec{B}}{\partial t} + (\vec{v}\nabla)\vec{B} - (\vec{B}\nabla)\vec{v} = \eta\nabla^2 \vec{B} \tag{5}$$

$$\frac{\partial T}{\partial t} + (\vec{v}\nabla)T = \chi\nabla^2 T \tag{6}$$

$$div\vec{B} = 0, \quad div\vec{v} = 0, \tag{7}$$

where $\vec{e}_z$ is the unit vector directed vertically up the OZ axis, β is the coefficient of thermal expansion, $\rho_0 = const$ is the density of the medium, ν is the kinematic viscosity coefficient, $\eta = c^2/4\pi\sigma$ is the magnetic viscosity coefficient, σ is the conductivity coefficient, χ is the coefficient thermal conductivity of the medium. Let us represent all quantities in Eqs. (4)-(7) as the sum of the stationary and perturbed components $\vec{v} = \vec{U}_0 + \vec{u}$, $\vec{B} = \vec{B}_0 + \vec{b}$, $P = p_0 + p$, $T = T_b + \theta$. The equations for the stationary state are:

$$\frac{dp_0}{dZ} = \rho_0 g\beta T_b \tag{8}$$

$$-2q\Omega_0^2 X = \frac{1}{\rho_0}\frac{dp_0}{dX} \tag{9}$$

$$\frac{\partial T_b}{\partial t} = \frac{d^2 T_b}{dZ^2} \tag{10}$$

The expressions (8)-(9) show that centrifugal equilibrium is established in the radial direction and hydrostatic in the vertical direction. The solution of the equation (10) with boundary conditions (1) has the form [45]:

$$T_b(z, t) = T_S(z) + \varepsilon^2 \delta_1 \cdot f_1(z, t)\Delta T, \tag{11}$$

where

$$T_S(z) = T_0 + \frac{\Delta T}{2}\left(1 - \frac{2z}{h}\right),$$

$$f_1(z,t) = Re\left\{\left(a(\lambda)e^{\frac{\lambda z}{h}} + a(-\lambda)e^{-\frac{\lambda z}{h}}\right)e^{-i\tilde{\omega}_T t}\right\}, \; \lambda^2 = -\frac{i\tilde{\omega}_T h^2}{\chi}, \; a(\lambda) = \frac{1}{2}\cdot\frac{e^{-i\phi} - e^{-\lambda}}{e^{\lambda} - e^{-\lambda}},$$

where $T_S(z)$ is the stationary temperature, $f_1(z,t)$ is the oscillating part of T_b, the symbol Re denotes the real part. Subtracting the equations for the stationary state (8)-(10) from (4)-(7) we can find the evolution equations for small perturbations:

$$\frac{\partial \vec{u}}{\partial t} - q\Omega_0 X \frac{\partial \vec{u}}{\partial Y} + (\vec{u}\nabla)\vec{U}_0 + 2\vec{\Omega}_0 \times \vec{u} + (\vec{u}\nabla)\vec{u} = -\frac{1}{\rho_0}\nabla\tilde{p} + \frac{1}{4\pi\rho_0}\left((B_0\nabla)b + (b\nabla)b\right) + g\beta\theta\vec{e}_Z + \nu\nabla^2\vec{u}$$

$$\frac{\partial \vec{b}}{\partial t} - q\Omega_0 X \frac{\partial \vec{b}}{\partial Y} - (\vec{B}_0\nabla)\vec{u} - (\vec{b}\nabla)\vec{U}_0 + (\vec{u}\nabla)\vec{b} - (\vec{b}\nabla)\vec{u} = \eta\nabla^2\vec{b} \tag{12}$$

$$\frac{\partial \theta}{\partial t} - q\Omega_0 X \frac{\partial \theta}{\partial y} + (\vec{u}\nabla)T_b + (\vec{u}\nabla)\theta = \chi\nabla^2\theta$$

$$divb = 0, \quad divu = 0$$

Here the pressure $\tilde{p}$ includes the disturbed magnetic pressure $p_m = \frac{\vec{b}^2}{8\pi} + \frac{\vec{b}\vec{B}_0}{4\pi}$: $\tilde{p} = p + p_m$.

Let us consider the dynamics of axisymmetric perturbations, then all the perturbed quantities in the equations (11) will depend only on two variables (X, Z):

$$\vec{u} = (u(X,Z), v(X,Z), w(X,Z)), \vec{b} = (\tilde{u}(X,Z), \tilde{v}(X,Z), \tilde{w}(X,Z)), \tilde{p} = \tilde{p}(X,Z), \theta = \theta(X,Z)$$

The solenoidal equations for axisymmetric velocity and magnetic field perturbations will take the form

$$\frac{\partial u}{\partial X} + \frac{\partial w}{\partial Z} = 0, \quad \frac{\partial \tilde{u}}{\partial X} + \frac{\partial \tilde{w}}{\partial Z} = 0 \tag{13}$$

The remaining equations in the coordinate representation will take the following form:

$$\left(\frac{\partial}{\partial t} - \nu\nabla^2\right)u + (\vec{u}\nabla)u = -\frac{1}{\rho_0}\frac{\partial\tilde{p}}{\partial X} + 2\Omega_{00}f_R v + \frac{1}{4\pi\rho_0}(\vec{b}\nabla)\tilde{u} + \frac{B_{00}f_m}{4\pi\rho_0}\frac{\partial\tilde{u}}{\partial Z} \tag{14}$$

$$\left(\frac{\partial}{\partial t} - \nu\nabla^2\right)v + (\vec{u}\nabla)v = -2\Omega_{00}f_R u\left(1 - \frac{q}{2}\right) + \frac{1}{4\pi\rho_0}(\vec{b}\nabla)\tilde{v} + \frac{B_{00}f_m}{4\pi\rho_0}\frac{\partial\tilde{v}}{\partial Z} \tag{15}$$

$$\left(\frac{\partial}{\partial t} - \nu\nabla^2\right)w + (\vec{u}\nabla)w = -\frac{1}{\rho_0}\frac{\partial\tilde{p}}{\partial Z} + g_0 f_g \beta\theta + \frac{1}{4\pi\rho_0}(\vec{b}\nabla)\tilde{w} + \frac{B_{00}f_m}{4\pi\rho_0}\frac{\partial\tilde{w}}{\partial Z} \tag{16}$$

$$\left(\frac{\partial}{\partial t} - \eta\nabla^2\right)\tilde{u} - B_{00}f_m\frac{\partial u}{\partial Z} + (\vec{u}\nabla)\tilde{u} - (\vec{b}\nabla)u = 0 \tag{17}$$

$$\left(\frac{\partial}{\partial t} - \eta\nabla^2\right)\tilde{v} - B_{00}f_m\frac{\partial v}{\partial Z} + q\Omega_{00}f_R\tilde{u} + (\vec{u}\nabla)\tilde{v} - (\vec{b}\nabla)v = 0 \tag{18}$$

$$\left(\frac{\partial}{\partial t} - \eta\nabla^2\right)\tilde{w} - B_{00}f_m\frac{\partial w}{\partial Z} + (\vec{u}\nabla)\tilde{w} - (\vec{b}\nabla)w = 0 \tag{19}$$

$$\left(\frac{\partial}{\partial t} - \chi\nabla^2\right)\theta - Cw + \varepsilon^2\delta_1\cdot\frac{\partial f_1}{\partial Z}\Delta Tw + (\vec{u}\nabla)\theta = 0, \; C = \frac{\Delta T}{h}, \tag{20}$$

where $f_R = 1 + \varepsilon^2\delta_2\cos\tilde{\omega}_R t$, $f_m = 1 + \varepsilon^2\delta_3\cos\tilde{\omega}_B t$, $f_g = 1 + \varepsilon^2\delta_4\cos\tilde{\omega}_g t$.

In the equations (14)-(20) the nabla operators can be described as:

$$(\vec{a}\nabla) = a_x \frac{\partial}{\partial X} + a_z \frac{\partial}{\partial Z}, \quad \nabla^2 = \frac{\partial^2}{\partial X^2} + \frac{\partial^2}{\partial Z^2}.$$

To eliminate the pressure $\tilde{p}$ in the equations (14) and (16), we need to differentiate the equation (14) with respect to Z. The equation (16) is required to be differentiated with respect to X and then by subtracting them from each other, we can obtain the equation for Y - the components of the vortex $rot\vec{u} = \vec{e}_Y \omega$:

$$\left(\frac{\partial}{\partial t} - \nu\nabla^2 \right)\omega + \frac{\partial}{\partial Z}\left(u\frac{\partial u}{\partial X} + w\frac{\partial u}{\partial Z} \right) - \frac{\partial}{\partial X}\left(u\frac{\partial w}{\partial X} + w\frac{\partial w}{\partial Z} \right) = \frac{B_{00}f_m}{4\pi\rho_0}\frac{\partial I}{\partial Z} + \tag{21}$$

$$+ \frac{1}{4\pi\rho_0}\left(\frac{\partial}{\partial Z}\left(\tilde{u}\frac{\partial \tilde{u}}{\partial X} + \tilde{w}\frac{\partial \tilde{u}}{\partial Z} \right) - \frac{\partial}{\partial X}\left(\tilde{u}\frac{\partial \tilde{w}}{\partial X} + \tilde{w}\frac{\partial \tilde{w}}{\partial Z} \right) \right) + 2\Omega_{00}f_R\frac{\partial v}{\partial Z} - g_0 f_g\beta\frac{\partial \theta}{\partial X}$$

where $\omega = \frac{\partial u}{\partial Z} - \frac{\partial w}{\partial X}$ is the Y - component of the vortex, $I = \frac{\partial \tilde{u}}{\partial Z} - \frac{\partial \tilde{w}}{\partial X}$ - Y -current component $\vec{I} = rot\vec{b} = I\vec{e}_Y$.

According to the equations (13) it is convenient to introduce the stream function ψ through which the components of the perturbed velocity are expressed:

$$u = -\frac{\partial \psi}{\partial Z}, \quad w = \frac{\partial \psi}{\partial X}$$

Similarly, we can introduce the stream function ϕ for perturbations of the magnetic field:

$$\tilde{u} = -\frac{\partial \varphi}{\partial Z}, \quad \tilde{w} = \frac{\partial \varphi}{\partial X}$$

As a result, the equations (2) and (15) become more compact

$$\left(\frac{\partial}{\partial t} - \nu\nabla^2 \right)\nabla^2\psi + 2\Omega_{00}f_R\frac{\partial v}{\partial Z} - \frac{B_{00}f_m}{4\pi\rho_0}\frac{\partial}{\partial Z}\nabla^2\varphi - g_0 f_g\beta\frac{\partial \theta}{\partial X} = \frac{1}{4\pi\rho_0}J(\varphi,\nabla^2\varphi) - J(\psi,\nabla^2\psi) \tag{22}$$

$$\left(\frac{\partial}{\partial t} - \nu\nabla^2 \right)v - 2\Omega_{00}f_R(1+Ro)\frac{\partial \psi}{\partial Z} - \frac{B_{00}f_m}{4\pi\rho_0}\frac{\partial \tilde{v}}{\partial Z} = \frac{1}{4\pi\rho_0}J(\varphi,\tilde{v}) - J(\psi,v) \tag{23}$$

The notation $J(a,b) = \frac{\partial a}{\partial X}\frac{\partial b}{\partial Z} - \frac{\partial a}{\partial Z}\frac{\partial b}{\partial X}$ - the Jacobian operator or the Poisson bracket $J(a,b) \equiv \{a,b\}$.

Further, by differentiating the equation (17) with respect to Z and by differentiation the equation (19) with respect to X, and then by subtracting them from each other, we can find the equation for the current I:

$$\left(\frac{\partial}{\partial t} - \eta\nabla^2 \right)I + \frac{\partial}{\partial Z}\left(u\frac{\partial \tilde{u}}{\partial X} + w\frac{\partial \tilde{u}}{\partial Z} - \tilde{u}\frac{\partial u}{\partial X} - \tilde{w}\frac{\partial u}{\partial Z} \right) - \tag{24}$$

$$- \frac{\partial}{\partial X}\left(u\frac{\partial \tilde{w}}{\partial X} + w\frac{\partial \tilde{w}}{\partial Z} - \tilde{u}\frac{\partial w}{\partial X} - \tilde{w}\frac{\partial w}{\partial Z} \right) = B_{00}f_m\frac{\partial \omega}{\partial Z}$$

Equations (20) and (14) can also be written in a compact form using the definitions of the stream functions ψ and ϕ:

$$\left(\frac{\partial}{\partial t} - \eta\nabla^2 \right)\varphi - B_{00}f_m\frac{\partial \psi}{\partial Z} = -J(\psi,\varphi) \tag{25}$$

$$\left(\frac{\partial}{\partial t} - \eta\nabla^2 \right)\tilde{v} - B_{00}f_m\frac{\partial v}{\partial Z} + 2\Omega_{00}f_R Ro\frac{\partial \varphi}{\partial Z} = J(\varphi,v) - J(\psi,\tilde{v}) \tag{26}$$

The form of the equation (16) for temperature disturbances is simplified in a similar way:

$$\left(\frac{\partial}{\partial t} - \chi\nabla^2 \right)\theta - C\frac{\partial \psi}{\partial X} + \varepsilon^2\delta_1 \cdot \frac{\partial f_1}{\partial Z}\frac{\partial \psi}{\partial X}\Delta T = -J(\psi,\theta) \tag{27}$$

Equations (18), (19), (21), (22) and (23) together with the boundary conditions

$$\psi = \nabla^2\psi = 0, \quad \frac{dv}{dZ} = 0, \quad \tilde{v} = 0, \quad \frac{d\varphi}{dZ} = 0, \quad \theta = 0 \quad at \quad Z = 0, h \tag{28}$$

describe nonuniformly rotating convection under the action of modulation of external fields. For convenience, in equations (22)-(27) we turn to the dimensionless variables, which we mark with an asterisk:

$$(X, Z) = h(x^*, z^*), t = \frac{h^2}{\nu}t^*, \psi = \chi\psi^*, \varphi = hB_{00}\varphi^*, v = \frac{\chi}{h}v^*, \tilde{v} = B_{00}\tilde{v}^*, \theta = Ch\theta^*.$$

Omitting the asterisk symbol, we will rewrite equations (22)-(27) in dimensionless variables:

$$\left(\frac{\partial}{\partial t} - \nabla^2\right)\nabla^2\psi + \sqrt{Ta}\cdot f_R\frac{\partial v}{\partial z} - \Pr Pm^{-1}Qf_m\frac{\partial}{\partial z}\nabla^2\varphi - Ra\cdot f_g\frac{\partial\theta}{\partial x} =$$

$$= \Pr Pm^{-1}Q\cdot J(\varphi, \nabla^2\varphi) - \Pr^{-1}\cdot J(\psi, \nabla^2\psi)$$

$$\left(\frac{\partial}{\partial t} - \nabla^2\right)v - \sqrt{Ta}\cdot f_R(1 + Ro)\frac{\partial\psi}{\partial z} - \Pr Pm^{-1}Qf_m\frac{\partial\tilde{v}}{\partial z} =$$

$$= \Pr Pm^{-1}Q\cdot J(\varphi, \tilde{v}) - \Pr^{-1}\cdot J(\psi, v)$$

$$\left(\frac{\partial}{\partial t} - Pm^{-1}\nabla^2\right)\varphi - \Pr^{-1}f_m\frac{\partial\psi}{\partial z} = -\Pr^{-1}J(\psi, \varphi)) \tag{29}$$

$$\left(\frac{\partial}{\partial t} - Pm^{-1}\nabla^2\right)\tilde{v} - \Pr^{-1}f_m\frac{\partial v}{\partial z} + Ro\sqrt{Ta}\cdot f_R\frac{\partial\varphi}{\partial z} = \Pr^{-1}(J(\varphi, v) - J(\psi, \tilde{v}))$$

$$\left(\Pr\frac{\partial}{\partial t} - \nabla^2\right)\theta - \frac{\partial\psi}{\partial x}\left(1 - \varepsilon^2\delta_1\frac{\partial f_1}{\partial z}\right) = -J(\psi, \theta),$$

where the dimensionless parameters are: $Pr = \nu/\chi$ (Prandtl number), $Pm = \nu/\eta$ (magnetic Prandtl number), $Ta = \frac{4\Omega_{00}^2 h^4}{\nu^2}$ (Taylor number), $Q = \frac{B_{00}^2 h^2}{4\pi\rho_0\nu\eta}$ (Chandrasekhar number), $Ra = \frac{g_0\beta Ch^4}{\nu\chi}$ (Rayleigh number on scale h).

In the absence of the thermal phenomena $Ra = 0$ and $f_R = f_m = f_g = 1$, the system of equations (29) was used to study the nonlinear saturation mechanism of the standard MRI [47]. In the case when the external field modulation is absent $\delta_{1,2,3,4} = 0$ and $Ra \neq 0$, the system of equations (29) was used to study the weakly nonlinear and chaotic modes of stationary convection in a nonuniformly rotating magnetoactive electrically conductive medium [11-13].

EQUATIONS OF EVOLUTION OF FINITE AMPLITUDE FOR DIFFERENT TYPES OF MODULATION

In this section, we analyze the nonlinear stage of stationary convection in a nonuniformly rotating electrically conductive medium in a constant magnetic field under the influence of small oscillations: a) the temperature field at the layer boundaries; b) gravitational field; c) external magnetic field; g) the angular velocity of rotation. We will consider all these effects separately (see Fig. 2). Then we will compare the value of the heat transfer (Nusselt number) for each type of modulation, i.e. quantify heat transfer in terms of finite amplitudes. These amplitudes arise when an interaction occurs between several modes of perturbations. Such an interaction can be described only in the framework of a nonlinear or weakly nonlinear theory based on the perturbation theory method. Here we will perform our research in the framework of a weakly nonlinear theory. The small expansion parameter in this theory is the relative deviation of the Rayleigh number Ra from the critical value Ra_c:

$$\varepsilon^2 = \frac{Ra - Ra_c}{Ra_c} \ll 1$$

Then all the perturbed quantities U in equations of the type $\mathcal{L}U = -N(U|U)$ ($N(\ldots)$ are nonlinear terms) are represented as a series in the perturbation theory

$$U \to \varepsilon U^{(1)} + \varepsilon^2 U^{(2)} + \varepsilon^3 U^{(3)} + \ldots$$

The equations for the perturbations in various orders of ε take the following form:

$$\varepsilon^1 : \mathcal{L}^{(0)} U^{(1)} = 0,$$

$$\varepsilon^2 : \mathcal{L}^{(0)} U^{(2)} = -N(U^{(1)} \mid U^{(1)})$$

$$\varepsilon^3 : \mathcal{L}^{(0)} U^{(3)} = -\mathcal{L}^{(2)} U^{(0)} - N(U^{(1)} \mid U^{(2)}) - N(U^{(2)} \mid U^{(1)})$$

The condition for solving this chain of nonlinear equations is known as Fredholm's alternative (see, for example [48])
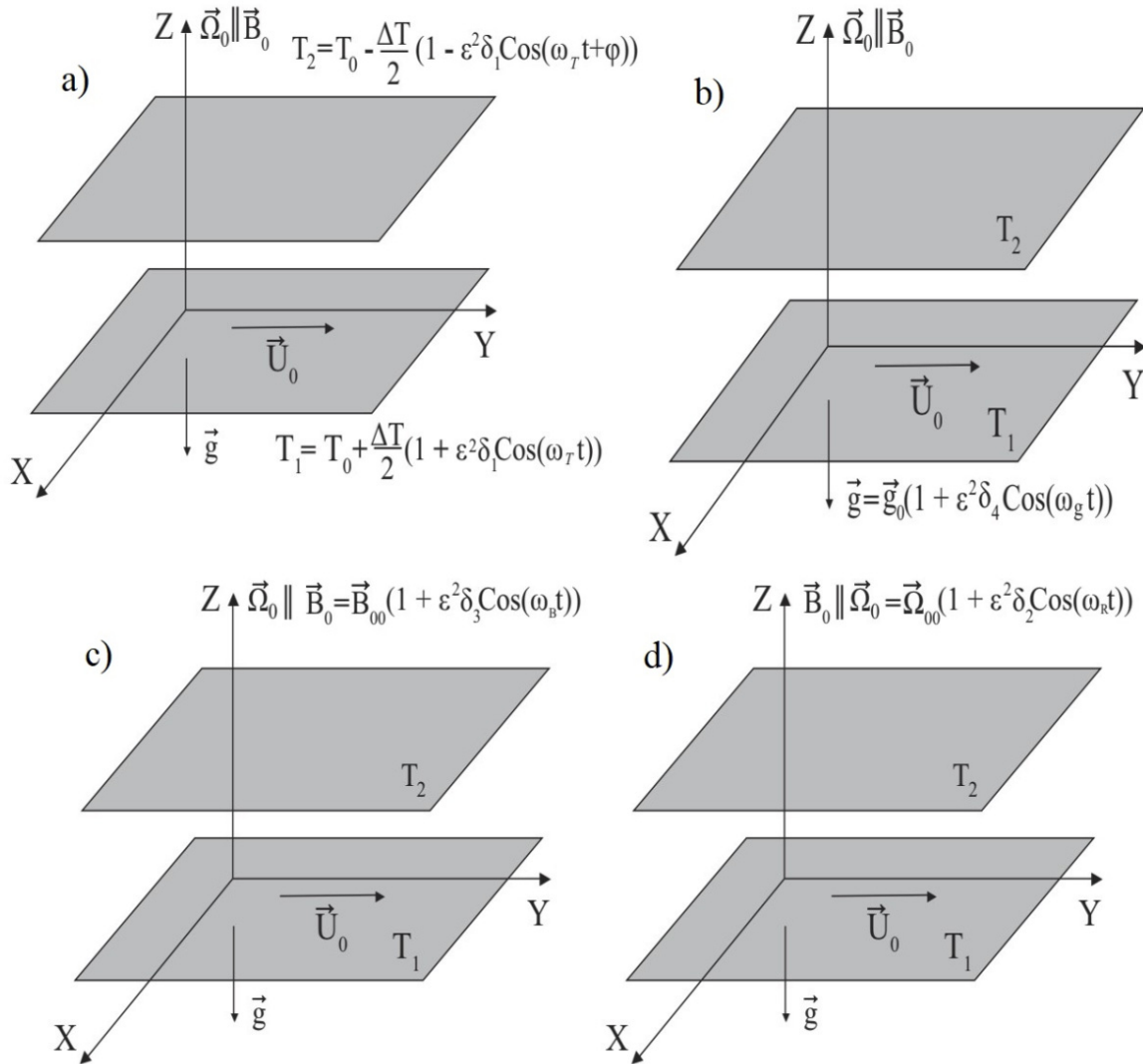
Fig. 2. Cartesian approximation for a nonuniformly rotating magnetoconvection under parametric influence: a) temperature modulation of the boundaries of the liquid layer; b) modulation of the gravity field; c) modulation of the external magnetic field; d) modulation of the angular velocity of rotation. A nonuniformly rotation in the local Cartesian coordinate system consists of rotation with a constant angular velocity Ω_0 and shear velocity $U_0 \parallel OY$.

$$\langle U^\dagger, R.H. \rangle = 0. \tag{30}$$

Here $U^\dagger$ is a non-trivial solution of the linear self-adjoint problem $\mathcal{L}^\dagger U^\dagger = 0$, where $\mathcal{L}^\dagger$ is a self-adjoint operator, which is determined from the following relation:

$$\langle U^\dagger, \mathcal{L}U \rangle \equiv \langle \mathcal{L}^\dagger U^\dagger, U \rangle, \tag{31}$$

where $\langle , \rangle$ is the inner product, which here has the following definition:

$$\langle f,g\rangle = \int\limits_{z=0}^{1}\int\limits_{x=0}^{2\pi/k_c} f\cdot g\,dxdz,$$

where $R.H.$ are right sides of the perturbed equations with nonlinear terms. We represent all the variables in equations (29) as an asymptotic expansion:

$$Ra = Ra_c + \varepsilon^2 R_2 + \varepsilon^4 R_4 + \dots$$
$$\psi = \varepsilon\psi_1 + \varepsilon^2\psi_2 + \varepsilon^3\psi_3 + \dots$$
$$v = \varepsilon v_1 + \varepsilon^2 v_2 + \varepsilon^3 v_3 + \dots \tag{32}$$
$$\varphi = \varepsilon\varphi_1 + \varepsilon^2\varphi_2 + \varepsilon^3\varphi_3 + \dots$$
$$\tilde{v} = \varepsilon\tilde{v}_1 + \varepsilon^2\tilde{v}_2 + \varepsilon^3\tilde{v}_3 + \dots$$
$$\theta = \varepsilon\theta_1 + \varepsilon^2\theta_2 + \varepsilon^3\theta_3 + \dots$$

Here Ra_c is the critical value of the Rayleigh number for convection without modulation. The amplitudes of the perturbed quantities depend only on the slow time $\tau = \varepsilon^2 t$. For simplicity we will take into account the nonlinear terms in (29) only in the heat balance equation. As it is shown in [23], this approximation is equivalent to applying the Galerkin approximation of the minimum order to the equations (29). In the lowest order, we get the equation:

$$\hat{L}M_1 = 0, \tag{33}$$

where $M_1 = \begin{bmatrix} \psi_1 \\ v_1 \\ \varphi_1 \\ \tilde{v}_1 \\ \theta_1 \end{bmatrix}$, $\hat{L}$ is the matrix operator of the form:

$$\hat{L} = \begin{bmatrix} -\nabla^4 & \sqrt{Ta}\dfrac{\partial}{\partial z} & -Pm^{-1}\Pr Q\dfrac{\partial}{\partial z}\nabla^2 & 0 & -Ra_c\dfrac{\partial}{\partial x} \\[2mm] -\sqrt{Ta}(1+Ro)\dfrac{\partial}{\partial z} & -\nabla^2 & 0 & -Pm^{-1}\Pr Q\dfrac{\partial}{\partial z} & 0 \\[2mm] -\Pr^{-1}\dfrac{\partial}{\partial z} & 0 & -Pm^{-1}\nabla^2 & 0 & 0 \\[2mm] 0 & -\Pr^{-1}\dfrac{\partial}{\partial z} & Ro\sqrt{Ta}\dfrac{\partial}{\partial z} & -Pm^{-1}\nabla^2 & 0 \\[2mm] -\Pr^{-1}\dfrac{\partial}{\partial x} & 0 & 0 & 0 & -\Pr^{-1}\nabla^2 \end{bmatrix}.$$

The solutions of the system of equations (33) with the boundary conditions of (28) have, respectively, the following form:

$$\psi_1 = A(\tau)\sin k_c x\sin\pi z, \quad \theta_1 = \frac{A(\tau)k_c}{a^2}\cos k_c x\sin\pi z, \quad \phi_1 = \frac{A(\tau)\pi Pm}{a^2\Pr}\sin k_c x\cos\pi z,$$

$$\tilde{v}_1 = -\frac{A(\tau)\pi^2\sqrt{Ta}(1+Ro(1-Pm))Pm}{\Pr(a^4+\pi^2 Q)}\sin k_c x\sin\pi z, \tag{34}$$

$$v_1 = \frac{A(\tau)\pi\sqrt{Ta}}{a^2}\cdot\frac{(1+Ro)a^4+\pi^2 QPmRo}{a^4+\pi^2 Q}\sin k_c x\cos\pi z, \quad a^2 = k_c^2 + \pi^2.$$

The amplitude $A(\tau)$ is still unknown. The critical value of the Rayleigh number Ra_c for the stationary magnetoconvection in a nonuniformly rotating electrically conducting medium is found from the first equation of the system (34) and has the form of the formula obtained in the linear theory [11-12]:

$$Ra_c = \frac{(\pi^2 + k_c^2)^3}{k_c^2} + \frac{\pi^2(\pi^2 + k_c^2)^2 Q}{k_c^2} + \frac{\pi^2(\pi^2 + k_c^2)^2 Ta}{k_c^2((\pi^2 + k_c^2)^2 + \pi^2 Q)} + \frac{\pi^2 Ta Ro((\pi^2 + k_c^2)^2 + \pi^2 QPm)}{k_c^2((\pi^2 + k_c^2)^2 + \pi^2 Q)}. \tag{35}$$

It should be noted that for the absence of heating $Ra = 0$, the threshold value of the hydrodynamic Rossby number Ro has the form:

$$Ro_{cr} = -\frac{a^2(a^4 + \pi^2 Q)^2 + \pi^2 a^4 Ta}{\pi^2 Ta(a^4 + \pi^2 QPm)}.$$

Passing to dimensional variables

$$\frac{\pi^2 Q}{a^4} \to \frac{\omega_A^2}{\omega_\nu \omega_\eta}, \frac{\pi^2 QPm}{a^4} \to \frac{\omega_A^2}{\omega_\eta^2}, \frac{Ta}{a^4} \to \frac{4\Omega^2}{\omega_\nu^2}, \frac{\pi^2}{a^2} \to \xi^2$$

we obtain the expression for Ro_{cr} [41]:

$$Ro_{cr} = -\frac{(\omega_A^2 + \omega_\nu \omega_\eta)^2 + 4\xi^2 \Omega^2 \omega_\eta^2}{4\Omega^2 \xi^2(\omega_A^2 + \omega_\eta^2)},$$

where the following notation has been introduced: $\omega_\nu = \nu k^2$ and $\omega_\eta = \eta k^2$ are the viscous and Ohmic frequencies, respectively, and ω_A is the Alfven frequency, $\omega_A^2 = k_z^2 c_A^2 = \frac{k_z^2 B_0^2}{4\pi\rho_0}$. Therefore, in the limiting case of $Ra = 0$, magnetorotational instability appears in a nonuniformly rotating electroconducting fluid in a constant magnetic field. The criterion for its appearance is the condition imposed on the angular velocity profile $\Omega(R)$ of the rotating liquid, i.e., Rossby number $Ro > Ro_{cr}$. Figure 3 shows diagrams of the dependency of the critical Rayleigh number Ra_c on the wavenumbers for various angular velocity profiles (Rossby numbers Ro). It can be seen that for negative Rossby numbers $Ro < 0$ the critical Rayleigh number Ra_c^{min} becomes smaller than in the case of uniform rotation $Ro = 0$ and rotation with positive numbers $Ro > 0$.
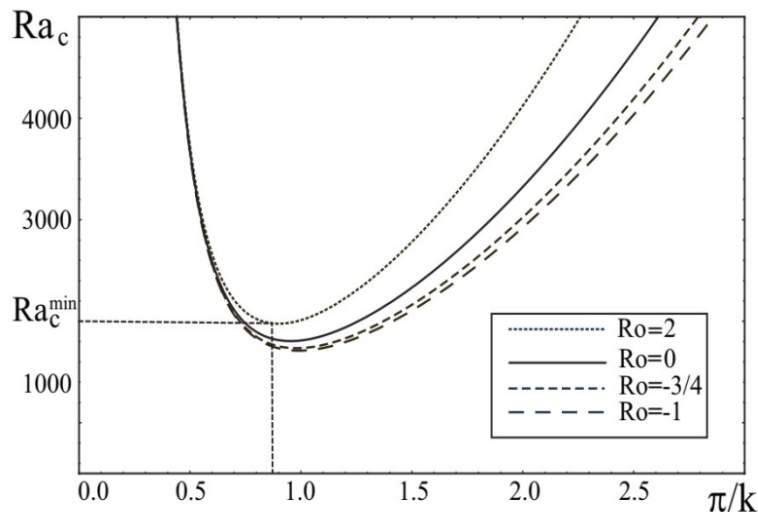
Fig. 3. Dependences of critical Rayleigh number Ra_c on wavenumbers π/k for different Rossby numbers Ro for constant parameters $Q = 50$, $Ta = 100$ and $Pm = 1$.

According to the formula (31), it is necessary to find solutions of the linear self-adjoint problem $\hat{L}^\dagger M_1^\dagger = 0$, where the matrix $M_1^\dagger$ has the form: $M_1^\dagger = (\psi_1^\dagger, \theta_1^\dagger, \varphi_1^\dagger, v_1^\dagger)^{Tr}$ and $\hat{L}^\dagger$ is a self-adjoint matrix operator:

$$\hat{L}^{\dagger} = \begin{bmatrix} -\nabla^4 & Ra_c\hat{P}\dfrac{\partial}{\partial x} & Pm^{-1}\Pr Q\hat{P}\dfrac{\partial}{\partial z}\nabla^2 & -\sqrt{Ta}\hat{P}\dfrac{\partial}{\partial z} \\[2mm] Ra_c\hat{P}\dfrac{\partial}{\partial x} & -Ra_c\hat{P}\nabla^2 & 0 & 0 \\[2mm] Pm^{-1}\Pr Q\hat{P}\dfrac{\partial}{\partial z}\nabla^2 & 0 & -Q\Pr^2 Pm^{-2}\hat{P}\nabla^4 & 0 \\[2mm] -\sqrt{Ta}\hat{P}\dfrac{\partial}{\partial z} & 0 & 0 & \left(\nabla^4 - Q\dfrac{\partial^2}{\partial z^2}\right)\nabla^2 \end{bmatrix} \qquad (36)$$

The solutions of the system of equations (36) have the form:

$$\psi_1^{\dagger} = A(\tau)\sin k_c x \sin \pi z,$$

$$\theta_1^{\dagger} = -\frac{A(\tau)k_c}{a^2}\cos k_c x \sin \pi z, \qquad (37)$$

$$\varphi_1^{\dagger} = -\frac{A(\tau)\pi Pm}{a^2 \Pr}\sin k_c x \cos \pi z,$$

$$v_1^{\dagger} = -\frac{A(\tau)\pi\sqrt{Ta}}{a^2}\cdot\frac{(1+Ro)a^4 + \pi^2 QPmRo}{a^4 + \pi^2 Q}\sin k_c x \cos \pi z.$$

For the second order of ε, we have the following equation:

$$\hat{L}M_2 = N_2, \qquad (38)$$

where

$$M_2 = \begin{bmatrix} \psi_2 \\ v_2 \\ \varphi_2 \\ \tilde{v}_2 \\ \theta_2 \end{bmatrix}, \quad N_2 = \begin{bmatrix} N_{21} \\ N_{22} \\ N_{23} \\ N_{24} \\ N_{25} \end{bmatrix},$$

$$N_{21} = N_{22} = N_{23} = N_{24} = 0,$$

$$N_{25} = -\Pr^{-1}\left[\frac{\partial \psi_1}{\partial x}\frac{\partial \theta_1}{\partial z} - \frac{\partial \theta_1}{\partial x}\frac{\partial \psi_1}{\partial z}\right].$$

Using solutions of (34) and boundary conditions of (28), we can find solutions of equations (38):

$$\psi_2 = 0, \quad \theta_2 = -\frac{A^2(\tau)k_c^2}{8\pi a^2}\sin(2\pi z), \quad \varphi_2 = 0, \qquad (39)$$

$$v_2 = 0, \quad \tilde{v}_2 = 0.$$

To analyze the intensity of the heat transfer, a horizontally-averaged heat flux is introduced at the boundary of the layer of electrically conducting fluid (Nusselt number):

$$Nu(\tau) = 1 + \frac{\left[\dfrac{k_c}{2\pi}\displaystyle\int_0^{2\pi/k_c}\left(\dfrac{\partial \theta_2}{\partial z}\right)dx\right]_{z=0}}{\left[\dfrac{k_c}{2\pi}\displaystyle\int_0^{2\pi/k_c}\left(\dfrac{\partial T_0}{\partial z}\right)dx\right]_{z=0}} = 1 + \frac{k_c^2}{4a^2}A^2(\tau) \qquad (40)$$

The heat flow intensity (of Nusselt number Nu) will be analyzed after the expression for the amplitude $A(\tau)$ is obtained. As can be seen from the an asymptotic expansion (32), modulation effects contribute only in the third order in ε, so we will consider these effects separately from each other in the third order in ε.

Temperature modulation of fluid layer boundaries

Let us consider only the temperature modulation of the layer boundaries, then in the equations (29) it is necessary to put $f_R = f_m = f_g = 1$. At the third order, we have

$$\hat{L}M_3 = N_3, \tag{41}$$

Where
$$M_3 = \begin{bmatrix} \psi_3 \\ v_3 \\ \varphi_3 \\ \tilde{v}_3 \\ \theta_3 \end{bmatrix}, \quad N_3 = \begin{bmatrix} N_{31} \\ N_{32} \\ N_{33} \\ N_{34} \\ N_{35} \end{bmatrix};$$

$$N_{31} = -\frac{\partial}{\partial \tau} \nabla^2 \psi_1 + Ra_2 \frac{\partial \theta_1}{\partial x} = \left(a^2 \frac{\partial A(\tau)}{\partial \tau} - Ra_2 \frac{k_c^2 A(\tau)}{a^2} \right) \sin k_c x \sin \pi z,$$

$$N_{32} = -\frac{\partial v_1}{\partial \tau} = -\frac{\pi \sqrt{Ta}}{a^2} \cdot \frac{(1+Ro)a^4 + \pi^2 QPmRo}{a^4 + \pi^2 Q} \cdot \frac{\partial A(\tau)}{\partial \tau} \sin k_c x \cos \pi z,$$

$$N_{33} = -\frac{\partial \phi_1}{\partial \tau} = -\frac{\pi Pm}{a^2 \Pr} \cdot \frac{\partial A(\tau)}{\partial \tau} \sin k_c x \cos \pi z$$

$$N_{34} = -\frac{\partial \tilde{v}_1}{\partial \tau} = \frac{\pi^2 \sqrt{Ta}(1+Ro(1-Pm))Pm}{\Pr(a^4 + \pi^2 Q)} \cdot \frac{\partial A(\tau)}{\partial \tau} \sin k_c x \sin \pi z,$$

$$N_{35} = -\frac{\partial \theta_1}{\partial \tau} - \Pr^{-1} \delta_1 \frac{\partial f_1}{\partial z} \frac{\partial \psi_1}{\partial x} - \Pr^{-1} \left[\frac{\partial \psi_1}{\partial x} \frac{\partial \theta_2}{\partial z} - \frac{\partial \theta_2}{\partial x} \frac{\partial \psi_1}{\partial z} + \frac{\partial \psi_2}{\partial x} \frac{\partial \theta_1}{\partial z} - \frac{\partial \theta_1}{\partial x} \frac{\partial \psi_2}{\partial z} \right] =$$

$$= -\frac{k_c}{a^2} \frac{\partial A(\tau)}{\partial \tau} \cos k_c x \sin \pi z - \Pr^{-1} \delta_1 \frac{\partial f_1}{\partial z} k_c A(\tau) \cos k_c x \sin \pi z + \frac{\Pr^{-1} k_c^3}{4a^2} A^3(\tau) \cos k_c x \sin \pi z \cos 2\pi z.$$

The solvability condition (Fredholm alternative) for the third-order equations $O(\varepsilon^3)$ is found from the formula (30):

$$\int_{z=0}^{1} \int_{x=0}^{2\pi/k_c} \left[\hat{P}\psi_1^\dagger \cdot R_{31} + Ra_c \hat{P}\theta_1^\dagger \cdot R_{32} + QPr^2 Pm^{-1} \hat{P}\nabla^2 \varphi_1^\dagger \cdot R_{33} + v_1^\dagger \cdot R_{34} \right] dxdz = 0 \tag{42}$$

where the notations are introduced

$$\hat{P} = (1+Ro)\nabla^4 - QPmRo\frac{\partial^2}{\partial z^2}, R_{31} = N_{31}, R_{32} = N_{35}, R_{33} = N_{33},$$

$$R_{34} = -\nabla^4 N_{32} + QPr\frac{\partial}{\partial z}\nabla^2 N_{34} + \sqrt{Ta}QPmPrRo\frac{\partial^2 N_{33}}{\partial z^2}.$$

By integrating into (42), we obtained a nonlinear equation for the amplitude $A(\tau)$, which refers to the non-autonomous Ginzburg-Landau (GL) equation for stationary convective instability, with a time-periodic coefficient in the following form:

$$A_{1T}\frac{\partial A}{\partial \tau} - A_{2T}(\tau)A + A_{3T}A^3 = 0 \tag{43}$$

Here the coefficients $A_{1T,2T,3T}$ have the following form:

$$A_{1T} = a^2 + \frac{k_c^2}{a^4}\Pr Ra_c - \frac{\pi^2}{a^2}QPm - \frac{\pi^2 Ta\left((1+Ro)a^4 + \pi^2 QPm(RoPm-1)\right)}{(a^4 + \pi^2 Q)^2} - \frac{\pi^4 TaRoQPm^2}{a^4(a^4 + \pi^2 Q)}, \tag{44}$$

$$A_{2T}(\tau) = \frac{k_c^2}{a^2}Ra_2 - \frac{k_c^2 Ra_c}{2a^2}\delta_1 \cdot I(\tau), \quad A_{3T} = \frac{k_c^4 Ra_c}{8a^4},$$

where the integral $I(\tau)$ is equal to:

$$I(\tau) = \int_0^1 \frac{\partial f_1(\tau,z)}{\partial z}\sin^2\pi z dz = Re\left\{\frac{\pi^2 e^{-i\omega_T\tau}(e^{-i\phi}-1)}{\lambda^2+4\pi^2}\right\}, \quad \omega_T = \frac{\tilde{\omega}_T}{\varepsilon^2}.$$

In the limiting case, when there is no temperature modulation $\delta_1 = 0$, the equation (43) was obtained in [13]. In the absence of modulation, the equation (43) has an analytical solution with the known initial condition $A_0 = A(0)$:

$$A(\tau) = \frac{A_0}{\sqrt{\frac{A_3}{A_2}A_0^2 + \left(1 - A_0^2\frac{A_3}{A_2}\right)\exp\left(-\frac{2\tau A_2}{A_1}\right)}} \tag{45}$$

In [23], the effect of different rotation profiles (Rossby numbers Ro) on the heat transfer value (Nusselt number Nu) using (45) was studied. The equation (43) will be solved numerically for different rotation profiles and modulation types:

   • In-phase modulation (IPM) $\varphi = 0$,

   • Out-phase modulation (OPM) $\varphi = \pi$,

   • Only Lower boundary modulated $(LBMO)$ $\phi = -i\infty$, which means that the modulation effect will not be considered in the upper boundary but only in the lower boundary.

Further, we will consider $Ra_2 \approx Ra_c$, since the nonlinearity is considered near the critical state of convection.

The results of numerical solutions of the equation (43) for the case of in-phase modulation $\varphi = 0$ for Rossby numbers $Ro = (2,0,-3/4,-1)$ are shown in Fig. 4.
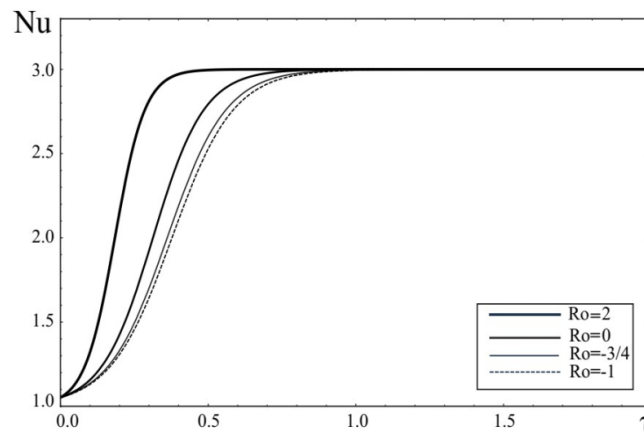
Fig. 4. Dependence of the Nusselt number Nu on time τ for Rossby numbers $Ro = (2,0,-3/4,-1)$ in the case of in-phase $(IPM, \phi = 0)$ of temperature modulation for a frequency $\omega_T = 2$ and an amplitude $\delta_1 = 0.5$.

The fixed parameters of convection and temperature modulation are respectively equal to:

$$Q/\pi^2 = Q_1 = 80, Ta/\pi^4 = T_1 = 10^5, Ra_c/\pi^4 = R_1 = 9500, Pm = 1,$$
$$Pr = 10, A_0 = 0.5, \omega_T = 2, \delta_1 = 0.5.$$

As can be seen from Fig. 4 the heat flow increases towards positive Rossby numbers $(Ro > 0)$ in the time interval $\tau \in [0,1]$. The heat flow reaches the final value for all rotation profiles.

Fig. 5 and Fig. 6 show the numerical solutions of the equation (43) respectively for the case of (OPM) and $(LBMO)$. Here we also see an increase in heat flux towards positive Rossby numbers $(Ro > 0)$, then there is a periodic change in heat transfer for all rotation profiles. The comparison of results of in-phase modulation (IPM), out of phase modulation (OPM) and when only lower boundary temperature is modulated $(LBMO)$ for fixed parameters $Ro = 2$, $\omega_T = 2$, $\delta_1 = 0.5$ is presented in Fig.7.

Comparing these graphs, we can conclude that the variations in the Nusselt number ΔNu are greater for the case of out-phase modulation ((OPM)): $\Delta Nu\big|_{\varphi=\pi} > \Delta Nu\big|_{\varphi=-i\infty} > \Delta Nu\big|_{\varphi=0}$.
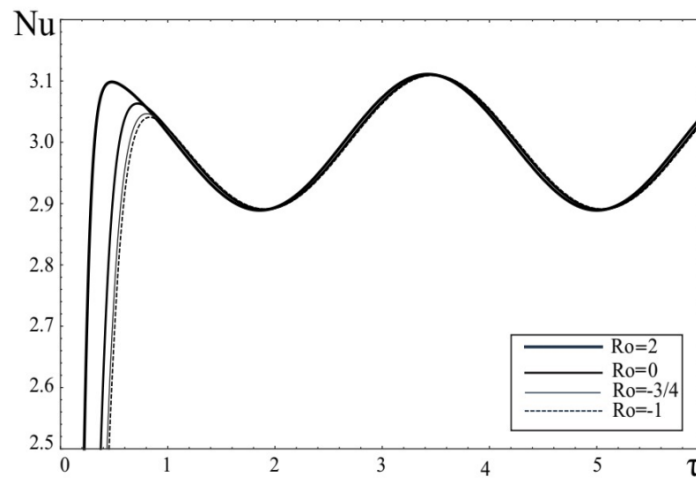
Fig. 5. Dependence of the Nusselt number Nu on the time τ for Rossby numbers $Ro = (2,0,-3/4,-1)$ for the case of phase $(OPM, \phi=\pi)$ of temperature modulation for frequency of $\omega_T = 2$ and amplitude of $\delta_1 = 0.5$.
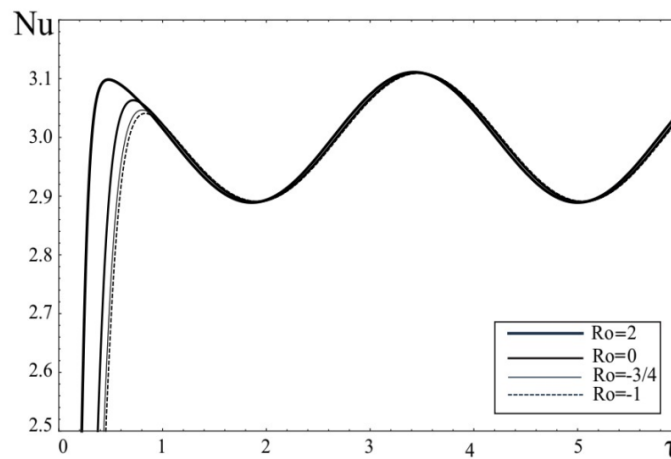
Fig. 6. Dependence of the Nusselt number Nu on the time τ for Rossby numbers $Ro = (2,0,-3/4,-1)$ for the case of temperature modulation of only the lower boundary of the layer $(LBMO, \phi=-i\infty)$ for frequency $\omega_T = 2$ and amplitude $\delta_1 = 0.5$.
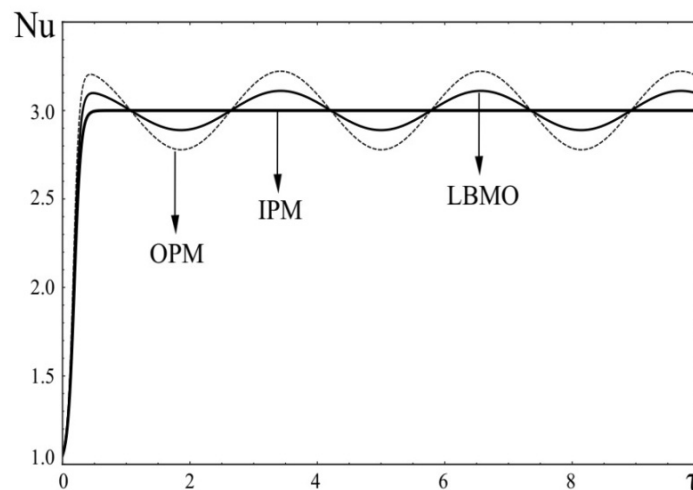
Fig. 7. Three types of temperature modulation: $IPM, OPM, LBMO$ for fixed parameters $Ro = 2$, $\omega_T = 2$, $\delta_1 = 0.5$.

In Fig. 8, we have depicted the variation of $Nu(\tau)$ with time τ for different frequencies of the out-phase ($\varphi = \pi$) modulation of $\omega_T = 2, 5, 10, 30$ and for a fixed Rossby number $Ro = 2$ and amplitude $\delta_1 = 0.5$. Here it can be seen
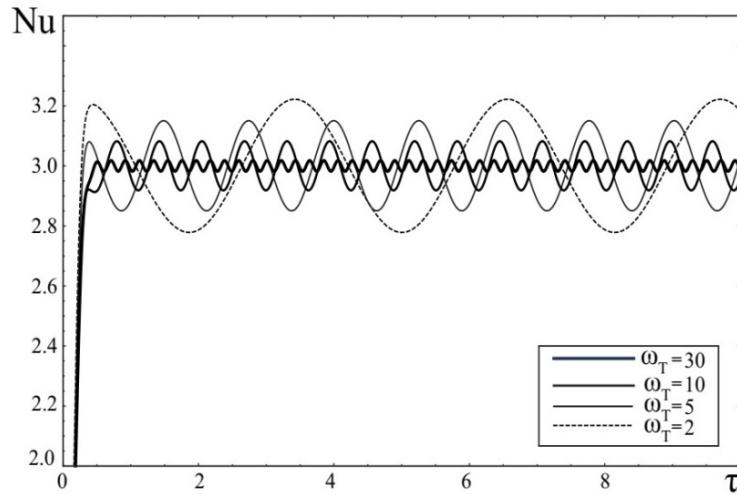
Fig. 8. Dependence of the Nusselt number Nu on the time τ for the case of phase ($\phi = \pi$) temperature modulation for frequency $\omega_T = (2, 5, 10, 30)$, amplitude $\delta_1 = 0.5$ and Rossby number $Ro = 2$.
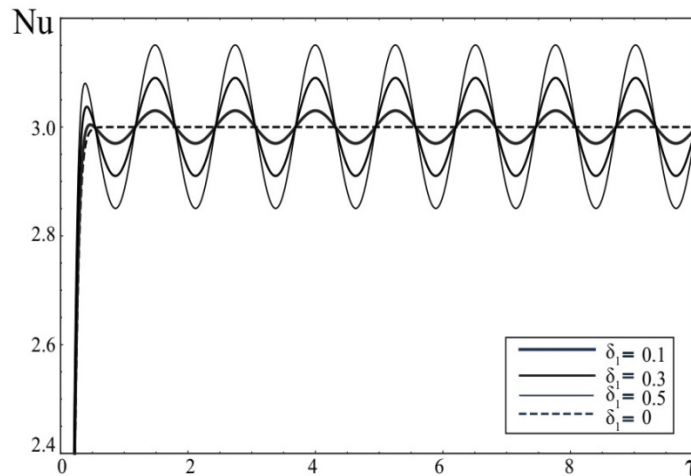
Fig. 9. Variations of the Nusselt number Nu depending on the amplitude of the phase temperature modulation $\delta_1 = (0, 0.1, 0.3, 0.5)$ for the Rossby number $Ro = 2$ and the frequency $\omega_T = 5$.

that an increase in the modulation frequency ω_T leads to suppression of heat transfer, i.e. variations in the number Nu are reduced:

$$\Delta Nu\big|_{\omega_T=2} > \Delta Nu\big|_{\omega_T=5} > \Delta Nu\big|_{\omega_T=10} > \Delta Nu\big|_{\omega_T=30}$$

A similar phenomenon is observed for nonuniformly rotation with other profiles. In Fig. 9, we have presented the unmodulated ($\delta_1 = 0$) result of Eq. (43) and compared it with the present results of modulated case for different amplitudes $\delta_1 = 0.5, 0.3, 0.1$. It can be seen from these graphs that modulation of the temperature boundaries of the layer leads to a periodic change in heat flow, i.e. the value of the number Nu changes periodically in time τ and increases with increasing amplitude δ_1.

Gravity field modulation

We now turn to the next method of parametric action on stationary magnetoconvection in a nonuniformly rotating electrically conductive medium. Let a fluid layer carries out vertical harmonic oscillations with a frequency $\tilde{\omega}_g$ and a small amplitude $\varepsilon^2 \xi$. Then, in the equations of motion written in the reference frame associated with the fluid layer,

the acceleration of gravity g should be replaced by $g_0(1+\varepsilon^2\delta_4\cos(\tilde{\omega}_g t))$ (see formula (3)). In the equations (29) we set $\delta_1 = 0$ and $f_R = f_m = 1$. As a result, the equations of the asymptotic expansion in the third order take the following form:

$$\hat{L}M_3 = N_3,$$

(46)

where $M_3 = \begin{bmatrix} \psi_3 \\ v_3 \\ \varphi_3 \\ \tilde{v}_3 \\ \theta_3 \end{bmatrix}$, $N_3 = \begin{bmatrix} N_{31} \\ N_{32} \\ N_{33} \\ N_{34} \\ N_{35} \end{bmatrix}$,

$$N_{31} = -\frac{\partial}{\partial\tau}\nabla^2\psi_1 + Ra_2\frac{\partial\theta_1}{\partial x} + Ra_c\delta_4\cos(\omega_g\tau)\frac{\partial\theta_1}{\partial x} =$$

$$= \left(a^2\frac{\partial A(\tau)}{\partial\tau} - Ra_2\frac{k_c^2 A(\tau)}{a^2} - Ra_c\delta_4\cos(\omega_g\tau)\frac{k_c^2 A(\tau)}{a^2}\right)\sin k_c x\sin\pi z,$$

$$N_{32} = -\frac{\partial v_1}{\partial\tau} = -\frac{\pi\sqrt{Ta}}{a^2}\cdot\frac{(1+Ro)a^4 + \pi^2 QPmRo}{a^4 + \pi^2 Q}\cdot\frac{\partial A(\tau)}{\partial\tau}\sin k_c x\cos\pi z,$$

$$N_{33} = -\frac{\partial\varphi_1}{\partial\tau} = -\frac{\pi Pm}{a^2\Pr}\cdot\frac{\partial A(\tau)}{\partial\tau}\sin k_c x\cos\pi z$$

$$N_{34} = -\frac{\partial\tilde{v}_1}{\partial\tau} = \frac{\pi^2\sqrt{Ta}(1+Ro(1-Pm))Pm}{\Pr(a^4 + \pi^2 Q)}\cdot\frac{\partial A(\tau)}{\partial\tau}\sin k_c x\sin\pi z,$$

$$N_{35} = -\frac{\partial\theta_1}{\partial\tau} - \Pr^{-1}\left[\frac{\partial\psi_1}{\partial x}\frac{\partial\theta_2}{\partial z} - \frac{\partial\theta_2}{\partial x}\frac{\partial\psi_1}{\partial z} + \frac{\partial\psi_2}{\partial x}\frac{\partial\theta_1}{\partial z} - \frac{\partial\theta_1}{\partial x}\frac{\partial\psi_2}{\partial z}\right] =$$

$$= -\frac{k_c}{a^2}\frac{\partial A(\tau)}{\partial\tau}\cos k_c x\sin\pi z + \frac{\Pr^{-1}k_c^3}{4a^2}A^3(\tau)\cos k_c x\sin\pi z\cos 2\pi z.$$

We substituted the values of the elements of the matrix N_3 into the solvability condition (42) for the third-order equations $O(\varepsilon^3)$. After completing the integration in (42), we have obtained the equation for the evolution of the finite amplitude $A(\tau)$ in the form of a non-autonomous GL equation:

$$A_{1G}\frac{\partial A}{\partial\tau} - A_{2G}(\tau)A + A_{3G}A^3 = 0,$$

(47)

where the coefficients $A_{1G,2G,3G}$ have the form

$$A_{1G} = a^2 + \frac{k_c^2}{a^4}\Pr Ra_c - \frac{\pi^2}{a^2}QPm - \frac{\pi^2 Ta\left((1+Ro)a^4 + \pi^2 QPm(RoPm-1)\right)}{(a^4 + \pi^2 Q)^2} - \frac{\pi^4 TaRoQPm^2}{a^4(a^4 + \pi^2 Q)},$$

(48)

$$A_{2G}(\tau) = \frac{k_c^2}{a^2}Ra_c\left(\frac{Ra_2}{Ra_c} + \delta_4\cos(\omega_g\tau)\right), \quad A_{3G} = \frac{k_c^4 Ra_c}{8a^4}, \quad \omega_g = \frac{\tilde{\omega}_g}{\varepsilon^2}.$$

Using the numerical solution of the equation (47) and the formula (40), we have determined the change in the heat transfer (Nusselt number Nu) from time τ. We chose the parameters of the convective medium and the initial amplitude as in the previous section:

$$Q/\pi^2 = Q_1 = 80, Ta/\pi^4 = T_1 = 10^5, Ra_c/\pi^4 = R_1 = 9500, Pm = 1, Pr = 10, A_0 = 0.5.$$

Fig. 10 shows the time dependence of the Nusselt number Nu τ for different rotation profiles of

$Ro = (2,0,-3/4,-1)$ of the electrically conductive medium (plasma) in an oscillating gravitational field with a frequency of $\omega_g = 10$ and an amplitude of $\delta_4 = 0.3$. From Fig. 10 it is clear that the heat transfer in the plasma increases for a nonuniformly rotation with a positive Rossby number $(Ro > 0)$. This process is well depicted in Fig.10.

Fig. 10. Dependency of the Nusselt number Nu on the time τ for Rossby numbers $Ro = (2,0,-3/4,-1)$ in an oscillating gravitational field with a frequency $\omega_g = 10$ and an amplitude $\delta_4 = 0.3$.

Fig. 11. Dependency of the Nusselt number Nu on the time τ for positive Rossby numbers $Ro = (2,0)$ in an oscillating gravitational field with a frequency $\omega_g = (10,25,50,100)$ and an amplitude $\delta_4 = 0.3$.

Fig. 12. Dependency of the Nusselt number Nu on time τ for negative Rossby numbers $Ro = (-3/4, -1)$ in an oscillating gravitational field with a frequency $\omega_g = (10, 25, 50, 100)$ and an amplitude $\delta_4 = 0.3$.

From Fig. 11 and Fig. 12, we can see the effect the variation of $Nu(\tau)$ with time τ for different frequencies modulation frequencies $\omega_g = 10, 25, 50, 100$ and for different rotation profiles $Ro = (2, 0, -3/4, -1)$ of the electrically conductive medium (plasma).

Fig. 13. Variations of the Nusselt number Nu depending on the amplitude of the oscillating gravitational field $\delta_4 = (0, 0.1, 0.3, 0.5)$ for the Rossby number $Ro = 2$ and the frequency $\omega_g = 10$.

As the frequency increases from 10 to 100, the magnitude of $Nu(\tau)$ decreases, and the effect of modulation on heat transport diminishes. Therefore, the effect of ω_g stabilizes the system:

$$\Delta Nu \big|_{\omega_g=10} > \Delta Nu \big|_{\omega_g=25} > \Delta Nu \big|_{\omega_g=50} > \Delta Nu \big|_{\omega_g=100}$$

Now let us compare the heat transfer in the absence of $\delta_4 = 0$ and in the presence of modulation $(\omega_g = 10)$ for different amplitudes $\delta_4 = 0.5, 0.3, 0.1$ of the gravitational field. This process is shown in Fig. 13.
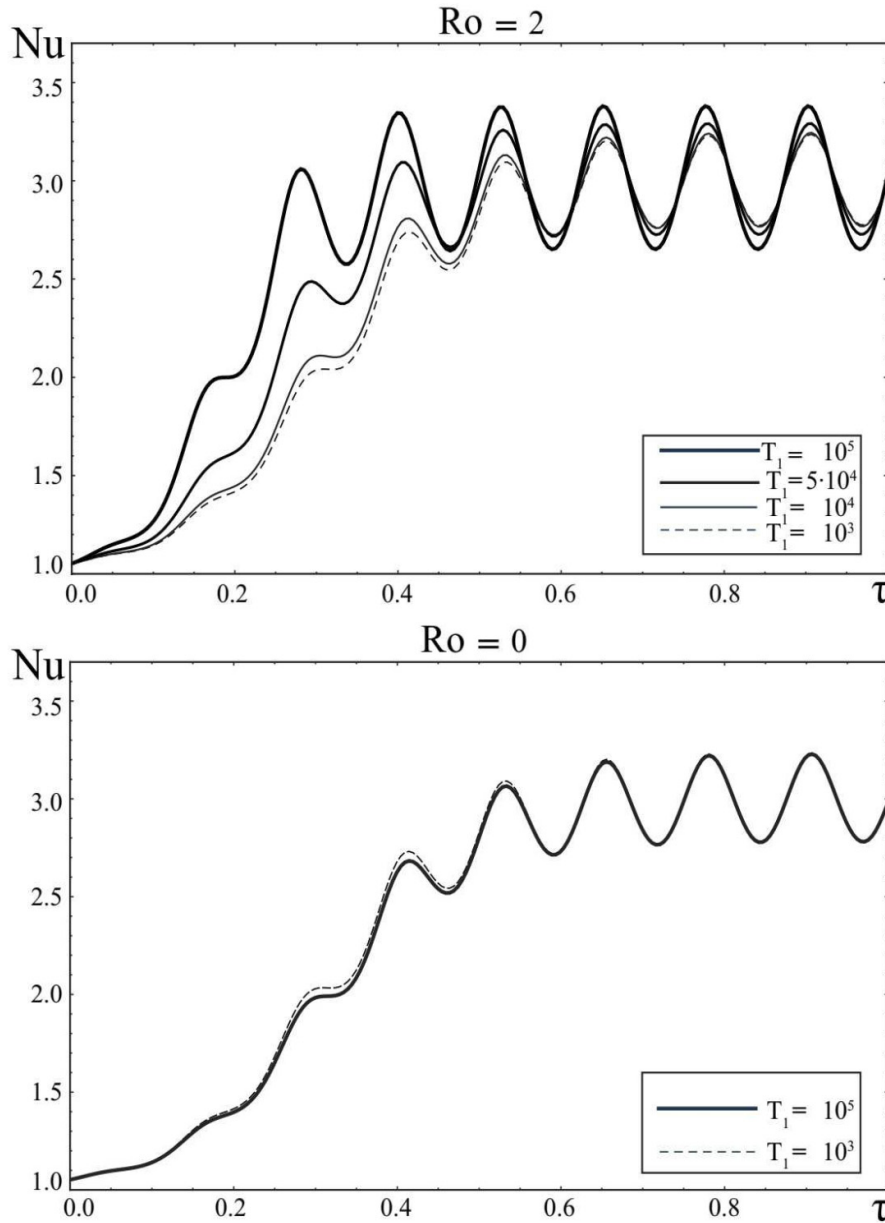
Fig. 14. Variations of the Nusselt number Nu depending on the Taylor number $T_1 = (10^3, 10^4, 5 \cdot 10^4, 10^5)$ for the amplitude parameters of the oscillating gravitational field $\delta_4 = 0.5$, frequencies $\omega_g = 50$ for positive Rossby numbers $Ro = (2, 0)$.

Here, the dashed line shows the mode of establishing the final value of $Nu(\tau)$ for the case $\delta_4 = 0$. Here, the dashed line demonstrates the regime of establishing the final value of $Nu(\tau)$ for the case $\delta_4 = 0$. Obviously, the excess of number $Nu(\tau)$ over the unit is caused by the convection occurrence. From Fig. 13 we can see that modulation of the gravitational field leads to a periodic change in heat flow, i.e. the value of the number Nu changes periodically in time τ and increases with increasing amplitude δ_4.
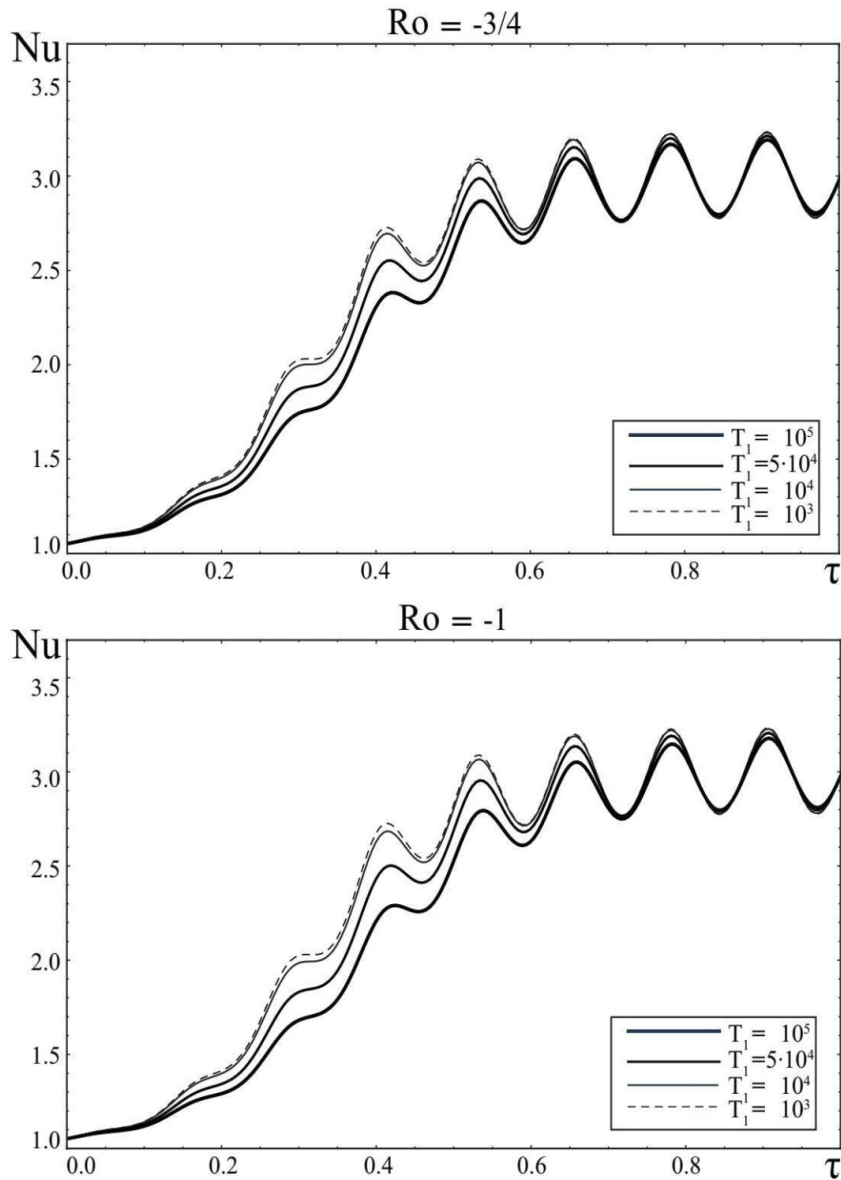
Fig. 15. Variations of the Nusselt number Nu depending on the Taylor number $T_1 = (10^3, 10^4, 5\cdot10^4, 10^5)$ for the amplitude parameters of the oscillating gravitational field $\delta_4 = 0.5$, frequencies $\omega_g = 50$ for negative Rossby numbers $Ro = (-3/4, -1)$.

In Fig. 14 and Fig. 15 we have depicted the effect of Taylor numbers $T_1 = Ta/\pi^4 = (10^3, 10^4, 5\cdot10^4, 10^5)$ on Nusselt number Nu for fixed values of the modulation frequency of the gravitational field $\omega_B = 50$, amplitude $\delta_4 = 0.5$ and Rossby numbers $Ro = (2, 0, -3/4, -1)$. From Fig. 14 it can be seen that for the Rossby number $Ro = 2$, with an increase in the Taylor number T_1 the heat transfer (the Nusselt number Nu) in the system also increases:

$$\Delta Nu\,|_{T_1=10^3} < \Delta Nu\,|_{T_1=10^4} < \Delta Nu\,|_{T_1=5\cdot10^4} < \Delta Nu\,|_{T_1=10^5}$$

Increasing of the Taylor number for solid-state rotation $Ro = 0$ has almost no effect on heat transfer. However, for negative rotation profiles $Ro = -3/4$ and $Ro = -1$ (see Fig. 15) with increasing Taylor number T_1 heat transfer in the system decreases:

$$\Delta Nu\,|_{T_1=10^3} > \Delta Nu\,|_{T_1=10^4} > \Delta Nu\,|_{T_1=5\cdot10^4} > \Delta Nu\,|_{T_1=10^5}$$

Modulation of an external magnetic field

In this section, we will study the stationary regime of nonlinear magnetoconvection under the influence of a time-dependent magnetic field. We represent the magnetic field as the sum of the constant (stationary) and oscillating parts. The oscillating part has the second order $\varepsilon^2 \cdot \delta_3$ with respect to the expansion parameter (the supercriticality parameter of the Rayleigh number ε) (see formula (3)). Assuming in the equations (29) $\delta_1 = 0$ and $f_R = f_g = 1$, the equations of the asymptotic expansion in the third order in ε will take the following form:

$$\hat{L}M_3 = N_3, \tag{49}$$

where

$$M_3 = \begin{bmatrix} \psi_3 \\ v_3 \\ \varphi_3 \\ \tilde{v}_3 \\ \theta_3 \end{bmatrix}, \quad N_3 = \begin{bmatrix} N_{31} \\ N_{32} \\ N_{33} \\ N_{34} \\ N_{35} \end{bmatrix},$$

$$N_{31} = -\frac{\partial}{\partial \tau}\nabla^2 \psi_1 + Ra_2 \frac{\partial \theta_1}{\partial x} + \delta_3 \cos(\omega_B \tau)\tilde{Q}\frac{\partial}{\partial z}\nabla^2 \varphi_1 =$$

$$= \left(a^2 \frac{\partial A(\tau)}{\partial \tau} - Ra_2 \frac{k_c^2 A(\tau)}{a^2} + \pi^2 Q\delta_3 \cos(\omega_B \tau) \right) \sin k_c x \sin \pi z, \quad \tilde{Q} = \Pr Pm^{-1} Q,$$

$$N_{32} = -\frac{\partial v_1}{\partial \tau} + \delta_3 \cos(\omega_B \tau)\tilde{Q}\frac{\partial \tilde{v}_1}{\partial z} =$$

$$= -\frac{\pi\sqrt{Ta}}{a^2(a^4 + \pi^2 Q)}\left[((1+Ro)a^4 + \pi^2 QPmRo)\frac{\partial A(\tau)}{\partial \tau} + \right.$$

$$\left. + \pi^2 a^2 Q(1 + Ro(1 - Pm))\delta_3 \cos(\omega_B \tau)A(\tau) \right]\sin k_c x \cos \pi z,$$

$$N_{33} = -\frac{\partial \varphi_1}{\partial \tau} + \Pr^{-1}\delta_3 \cos(\omega_B \tau)\frac{\partial \psi_1}{\partial z} =$$

$$= \left[-\frac{\pi Pm}{a^2 \Pr}\frac{\partial A(\tau)}{\partial \tau} + \delta_3 \cos(\omega_B \tau)\frac{\pi A(\tau)}{\Pr} \right]\sin k_c x \cos \pi z,$$

$$N_{34} = -\frac{\partial \tilde{v}_1}{\partial \tau} + \Pr^{-1}\delta_3 \cos(\omega_B \tau)\frac{\partial v_1}{\partial z} =$$

$$= \frac{\pi^2 \sqrt{Ta}}{a^2 \Pr(a^4 + \pi^2 Q)}\left[a^2 Pm(1 + Ro(1 - Pm))\frac{\partial A(\tau)}{\partial \tau} - \right.$$

$$\left. - \delta_3 \cos(\omega_B \tau)((1+Ro)a^4 + \pi^2 QPmRo)A(\tau) \right]\sin k_c x \sin \pi z,$$

$$N_{35} = -\frac{\partial \theta_1}{\partial \tau} - \Pr^{-1}\left[\frac{\partial \psi_1}{\partial x}\frac{\partial \theta_2}{\partial z} - \frac{\partial \theta_2}{\partial x}\frac{\partial \psi_1}{\partial z} + \frac{\partial \psi_2}{\partial x}\frac{\partial \theta_1}{\partial z} - \frac{\partial \theta_1}{\partial x}\frac{\partial \psi_2}{\partial z} \right] =$$

$$= -\frac{k_c}{a^2}\frac{\partial A(\tau)}{\partial \tau}\cos k_c x \sin \pi z + \frac{\Pr^{-1} k_c^3}{4a^2}A^3(\tau)\cos k_c x \sin \pi z \cos 2\pi z.$$

Using the solvability condition (42) and the values of the elements of the matrix N_3, we can obtain the equation for the evolution of the finite amplitude $A(\tau)$ in the form of a non-autonomous GL equation:

$$A_{1M} \frac{\partial A}{\partial \tau} - A_{2M}(\tau)A + A_{3M}A^3 = 0, \tag{50}$$

where the coefficients $A_{1M,2M,3M}$ have the form

$$A_{1M} = a^2 + \frac{k_c^2}{a^4}\Pr Ra_c - \frac{\pi^2}{a^2}QPm - \frac{\pi^2 Ta\left((1+Ro)a^4 + \pi^2 QPm(RoPm-1)\right)}{(a^4 + \pi^2 Q)^2} - \frac{\pi^4 TaRoQPm^2}{a^4(a^4 + \pi^2 Q)}, \tag{51}$$

$$A_{2M}(\tau) = \frac{k_c^2}{a^2}Ra_2 - 2Q\pi^2\delta_3\cos(\omega_B\tau) +$$

$$+ \frac{\pi^4 QTa}{a^2(a^4 + \pi^2 Q)}\left[\frac{1}{a^4 + \pi^2 Q}\left(2(1+Ro)a^4 + RoPm(\pi^2 Q - a^4)\right) - PmRo\right]\delta_3\cos(\omega_B\tau),$$

$$\omega_B = \frac{\tilde{\omega}_B}{\varepsilon^2}, \quad A_{3M} = \frac{k_c^4 Ra_c}{8a^4}.$$

In the limiting case, when there is no rotation ($Ta = 0, Ro = 0$), the equation (50) coincides with the result of [41]. Then, let us perform a numerical analysis of the equation (50) for different rotation profiles $Ro = (2, 0, -3/4, -1)$ for fixed convection parameters $Q/\pi^2 = Q_1 = 80$, $Ta/\pi^4 = T_1 = 10^5$, $Ra_c/\pi^4 = R_1 = 9500$, $Pm = 1$, $Pr = 10$, $A_0 = 0.5$ and magnetic field modulation $\omega_B = 10$, $\delta_3 = 0.3$.
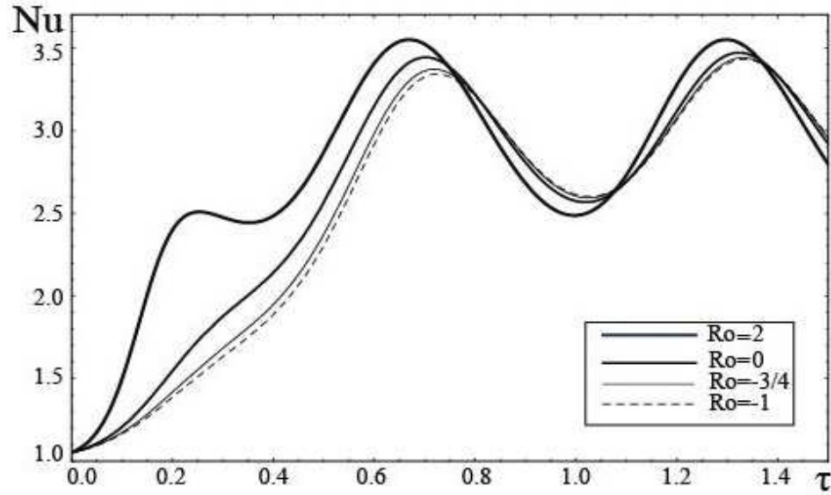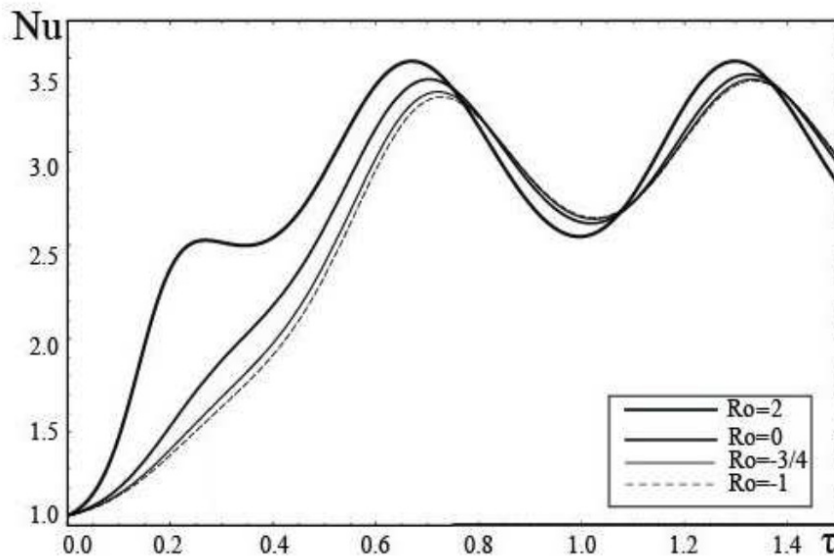

Fig. 16. Dependency of the Nusselt number *Nu* on the time τ for Rossby numbers $Ro = (2, 0, -3/4, -1)$ in an oscillating magnetic field with a frequency of $\omega_B = 10$ and with an amplitude of $\delta_3 = 0.3$.

From Fig. 16 it can be seen that for nonuniformly rotation with a positive Rossby number $(Ro > 0)$, the variations of the heat flux in the plasma increase: $\Delta Nu|_{Ro=-1} \leq \Delta Nu|_{Ro=-3/4} < \Delta Nu|_{Ro=0} < \Delta Nu|_{Ro=2}$.

In Fig. (17) and Fig.(18), the Nusselt number $Nu(\tau)$ with respect to time τ has been plotted for different modulation frequencies $\omega_B = 10, 25, 50, 100$ and for different rotation profiles $Ro = (2, 0, -3/4, -1)$ of the electrically conductive medium (plasma). Here we see that an increase of the modulation frequency ω_B leads to suppression of heat transfer for the different Rossby numbers Ro, i.e. variations in the number Nu are reduced:

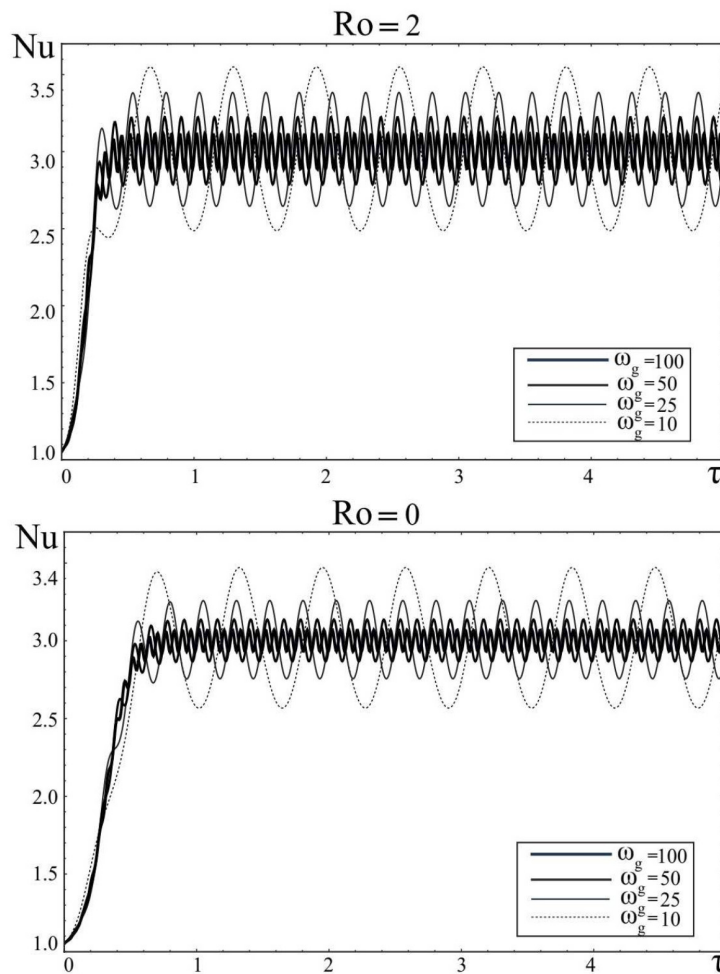$$\Delta Nu|_{\omega_g=10} > \Delta Nu|_{\omega_g=25} > \Delta Nu|_{\omega_g=50} > \Delta Nu|_{\omega_g=100}$$
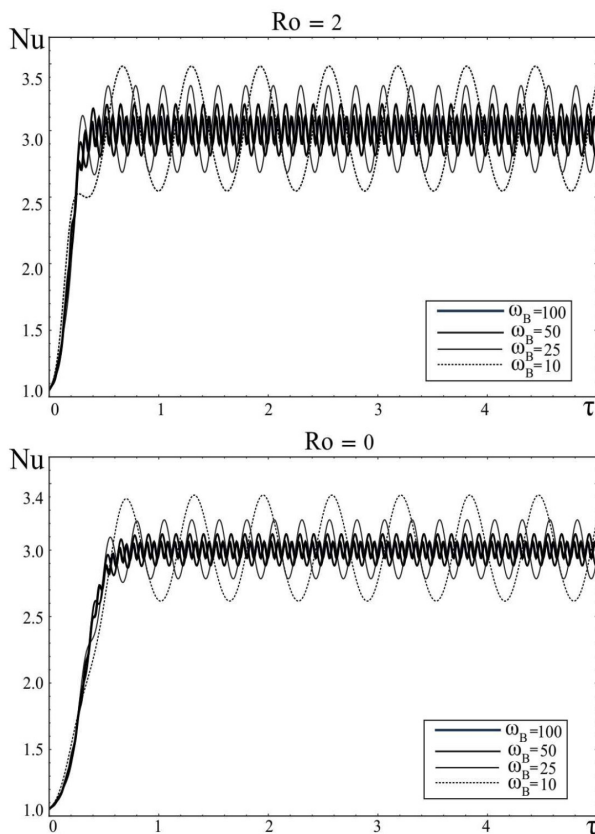
Fig. 17. Dependency of the Nusselt number Nu on the time τ for positive Rossby numbers $Ro = (2,0)$ in an oscillating magnetic field with a frequency of $\omega_B = (10,25,50,100)$ and with an amplitude of $\delta_3 = 0.3$.
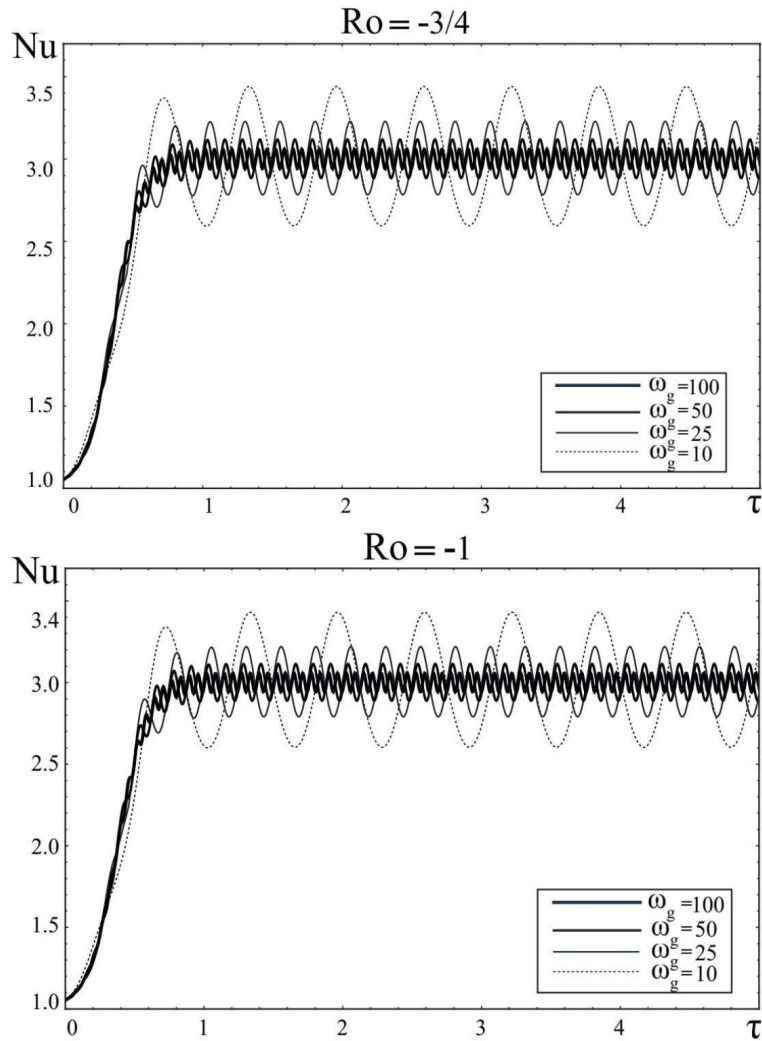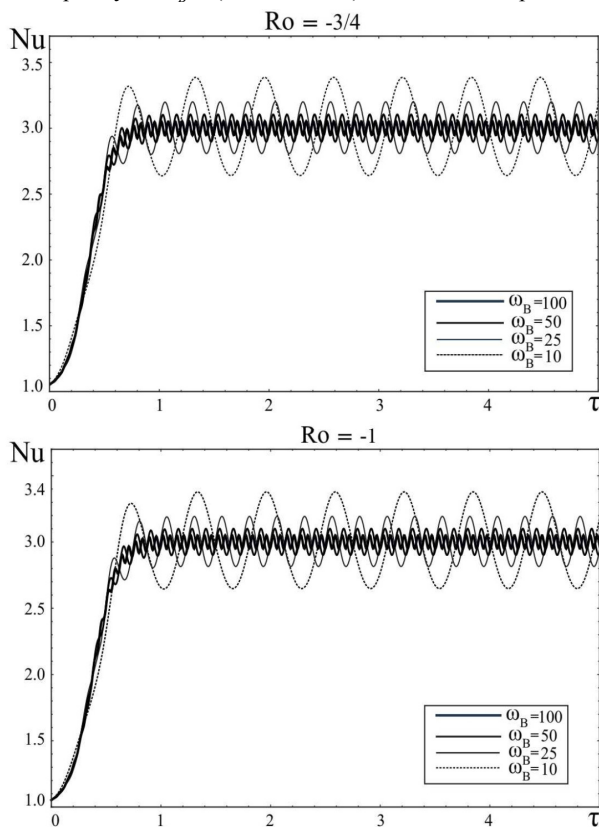

Fig. 18. Dependency of the Nusselt number Nu on the time τ for negative Rossby numbers $Ro = (-3/4,-1)$ in an oscillating magnetic field with a frequency $\omega_B = (10,25,50,100)$ and with an amplitude of $\delta_3 = 0.3$.
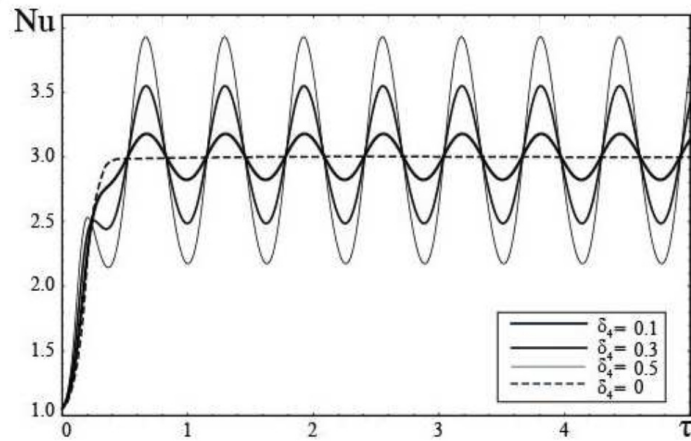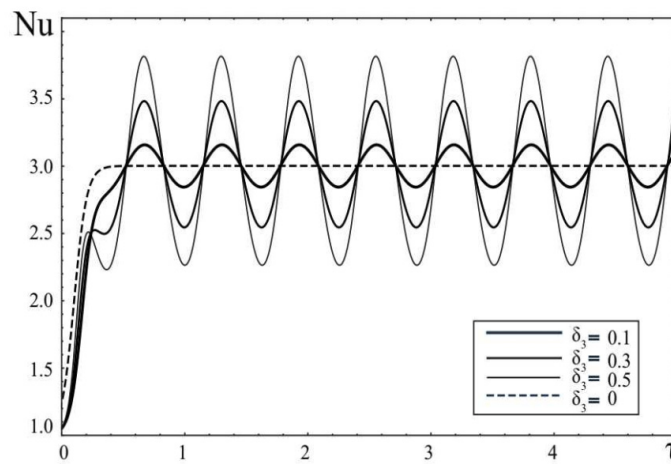
Fig. 19. Variations of the Nusselt number Nu depending on the amplitude of the oscillating magnetic field $\delta_3 = (0, 0.1, 0.3, 0.5)$ for the Rossby number $Ro = 2$ and frequency $\omega_B = 10$.

Fig. (19) shows the dependency of the heat transfer value Nu on τ in the absence of $\delta_3 = 0$ and in the presence of modulation of the magnetic field $(\omega_B = 10)$ for different amplitudes $\delta_3 = 0.5, 0.3, 0.1$. The dashed line shows the regime of establishing the final value of $Nu(\tau)$ for the case $\delta_3 = 0$. In Fig. (19) we can see that the modulation of the magnetic field leads to a periodic change of the heat flux, which increases with increasing amplitude δ_3.
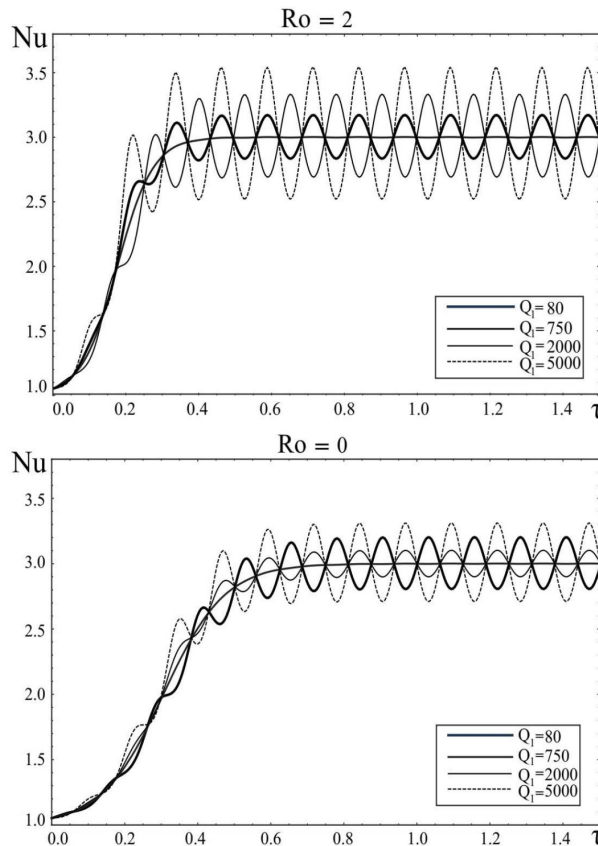
Fig. 20. Variations of the Nusselt number Nu depending on the Chandrasekhar number $Q_1 = (80, 750, 2000, 5000)$ for the amplitude parameters of the oscillating magnetic field $\delta_3 = 0.5$, frequency $\omega_B = 50$ with positive Rossby numbers $Ro = (2, 0)$.

In Fig. (20)-Fig. (21) we have depicted the effect of the external magnetic field (Chandrasekhar number Q_1) on the heat transfer with an oscillating magnetic field of frequency $\omega_B = 10$ and amplitude $\delta_3 = 0.3$ for different profiles of nonuniform rotation of $(Ro = 2, 0, -3/4, -1)$. Increasing the external magnetic field, i.e. Chandrasekhar

numbers from $Q_1 = 80$ to $Q_1 = 750$ for $Ro = 2$ leads to a decrease of the heat flow, which is almost stabilized at a certain level.

The Nusselt number Nu increases with the increasing the value of the magnetic field

$$\Delta Nu\,|_{Q_1=80} < \Delta Nu\,|_{Q_1=2000} < \Delta Nu\,|_{Q_1=5000}$$

Similar picture can be obtained for other rotation profiles $(Ro = 0, -3/4, -1)$:

$$\Delta Nu\,|_{Q_1=80} < \Delta Nu\,|_{Q_1=5000}\,.$$
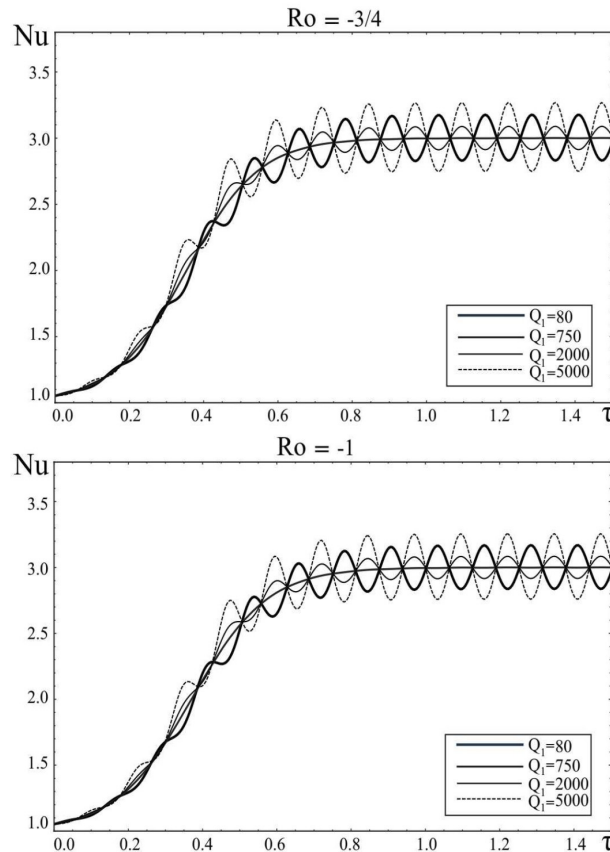
Fig. 21. Variations of the Nusselt number Nu depending on the Chandrasekhar number $Q_1 = (80, 750, 2000, 5000)$ for the amplitude parameters of the oscillating magnetic field $\delta_3 = 0.5$, frequency $\omega_B = 50$ with negative Rossby numbers $Ro = (-3/4, -1)$.

Rotational speed modulation

One of the important ways of parametric influence on convective instability is the modulation of the angular velocity of rotation. The first experiments on rotation modulation were carried out in [50]. It was also found there the onset of instability in Couette flow can be inhibited by modulating the rate of rotation of the inner cylinder. Later, numerical [43] and laboratory experiments [51] were carried out for the effect of rotation modulation on Rayleigh-Benard convection. In [43] it is shown that the modulation of the rotation of $\Omega(t) = \Omega_0 + \Delta\Omega\sin(\omega t)$ causes a periodic change in the Coriolis force, and therefore has an effect on the onset of convection. In [51], the experiments were carried out with a periodic dependency of the angular velocity $\Omega(t) = \Omega_0(1 + \beta\cos(\omega t))$ ($\Omega_0 = 0.104$ rad/s, $\beta = 0.212$) for modeling large-scale atmospheric flow dynamics in order to create a longer-term weather forecast.

Here we also assume that the oscillating part is of the second order of smallness $\varepsilon^2 \cdot \delta_3$ in the expansion parameter (the supercriticality of the Rayleigh number ε) (see the formula (2)). Assuming in the equations (29) $\delta_1 = 0$ and $f_m = f_g = 1$, the equations of the asymptotic expansion in the third order (ε^3) take the form

$$\hat{L}M_3 = N_3, \tag{52}$$

where $M_3 = \begin{bmatrix} \psi_3 \\ v_3 \\ \varphi_3 \\ \tilde{v}_3 \\ \theta_3 \end{bmatrix}$, $N_3 = \begin{bmatrix} N_{31} \\ N_{32} \\ N_{33} \\ N_{34} \\ N_{35} \end{bmatrix}$,

$$N_{31} = -\frac{\partial}{\partial \tau}\nabla^2\psi_1 + Ra_2\frac{\partial\theta_1}{\partial x} - \delta_2\cos(\omega_R\tau)\sqrt{Ta}\frac{\partial v_1}{\partial z} =$$

$$= \left(a^2\frac{\partial A(\tau)}{\partial \tau} - Ra_2\frac{k_c^2 A(\tau)}{a^2} + \delta_2\cos(\omega_R\tau)\cdot\frac{\pi^2 Ta((1+Ro)a^4 + \pi^2 QPmRo)A(\tau)}{a^2(a^4 + \pi^2 Q)}\right)\sin k_c x\sin\pi z,$$

$$N_{32} = -\frac{\partial v_1}{\partial \tau} + \delta_2\cos(\omega_R\tau)\sqrt{Ta}(1+Ro)\frac{\partial\psi_1}{\partial z} =$$

$$= \left[-\frac{\pi\sqrt{Ta}}{a^2(a^4 + \pi^2 Q)}\left((1+Ro)a^4 + \pi^2 QPmRo\right)\frac{\partial A(\tau)}{\partial \tau} + \pi\sqrt{Ta}(1+Ro)\delta_2\cos(\omega_R\tau)A(\tau)\right]\sin k_c x\cos\pi z,$$

$$N_{33} = -\frac{\partial\phi_1}{\partial \tau} = -\frac{\pi Pm}{a^2 \Pr}\cdot\frac{\partial A(\tau)}{\partial \tau}\sin k_c x\cos\pi z,$$

$$N_{34} = -\frac{\partial\tilde{v}_1}{\partial \tau} - \delta_2\cos(\omega_R\tau)Ro\sqrt{Ta}\frac{\partial\varphi_1}{\partial z} =$$
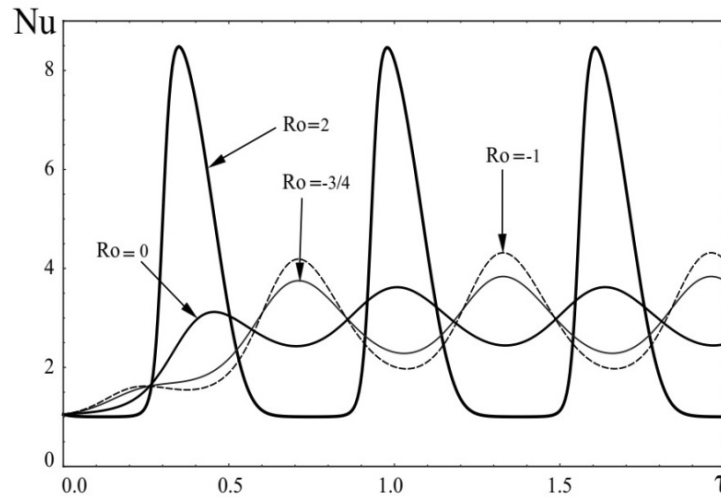
Fig. 22. Dependency of the Nusselt number Nu on the time τ for Rossby numbers $Ro = (2, 0, -3/4, -1)$ when modulating rotation with a frequency of $\omega_R = 10$ and amplitude $\delta = 0.3$.

$$= \left[\frac{\pi^2\sqrt{Ta}(1+Ro(1-Pm))Pm}{\Pr(a^4 + \pi^2 Q)}\frac{\partial A(\tau)}{\partial \tau} + \delta_2\cos(\omega_R\tau)Ro\sqrt{Ta}\frac{\pi^2 Pm}{a^2 \Pr}A(\tau)\right]\sin k_c x\sin\pi z,$$

$$N_{35} = -\frac{\partial\theta_1}{\partial \tau} - \Pr^{-1}\left[\frac{\partial\psi_1}{\partial x}\frac{\partial\theta_2}{\partial z} - \frac{\partial\theta_2}{\partial x}\frac{\partial\psi_1}{\partial z} + \frac{\partial\psi_2}{\partial x}\frac{\partial\theta_1}{\partial z} - \frac{\partial\theta_1}{\partial x}\frac{\partial\psi_2}{\partial z}\right] =$$

$$= -\frac{k_c}{a^2}\frac{\partial A(\tau)}{\partial \tau}\cos k_c x\sin \pi z + \frac{\mathrm{Pr}^{-1}k_c^3}{4a^2}A^3(\tau)\cos k_c x\sin \pi z\cos 2\pi z.$$

By substituting the values of the elements of the matrix N_3 into the solvability condition (42) for the third-order equations $O(\varepsilon^3)$, we can obtain the equation for the evolution of the finite amplitude $A(\tau)$ in the form of a non-autonomous GL equation:

$$A_{1R}\frac{\partial A}{\partial \tau} - A_{2R}(\tau)A + A_{3R}A^3 = 0, \tag{53}$$

where the coefficients $A_{1R,2R,3R}$ have the following form

$$A_{1R} = a^2 + \frac{k_c^2}{a^4}\mathrm{Pr}\,Ra_c - \frac{\pi^2}{a^2}QPm - \frac{\pi^2 Ta\big((1+Ro)a^4 + \pi^2 QPm(RoPm-1)\big)}{(a^4+\pi^2 Q)^2} - \frac{\pi^4 TaRoQPm^2}{a^4(a^4+\pi^2 Q)}, \tag{54}$$

$$A_{2R}(\tau) = \frac{k_c^2}{a^2}Ra_2 - \delta_2\cos(\omega_R\tau)\cdot\frac{2\pi^2 Ta((1+Ro)a^4 + \pi^2 QRoPm)}{a^2(a^4+\pi^2 Q)},\ \omega_R = \frac{\tilde{\omega}_R}{\varepsilon^2},\ A_{3R} = \frac{k_c^4 Ra_c}{8a^4}.$$

Here we carry out a numerical analysis of the equation (50) for different rotation profiles $(Ro = 2,0,-3/4,-1)$ and we also present the results of the dependence of the heat transfer (Nusselt number Nu) from the time τ (see Fig. 22). We consider the convection parameters to be fixed $Q/\pi^2 = Q_1 = 80$, $Ta/\pi^4 = T_1 = 10^5$, $Ra_c/\pi^4 = R_1 = 9500$, $Pm = 1$, $Pr = 10$, $A_0 = 0.5$ and rotation speed modulation has a frequency and an amplitude: $\omega_R = 10$ and $\delta_3 = 0.3$. From Fig. 22, we can observe that for nonuniform rotation with a positive Rossby number $(Ro = 2)$ the variations of heat flow are greater than for nonuniform rotation with negative Rossby numbers $(Ro = -3/4,-1)$ and $(Ro = 0)$:

$$\Delta Nu\,|_{Ro=0} < \Delta Nu\,|_{Ro=-3/4} < \Delta Nu\,|_{Ro=-1} < \Delta Nu\,|_{Ro=2}$$
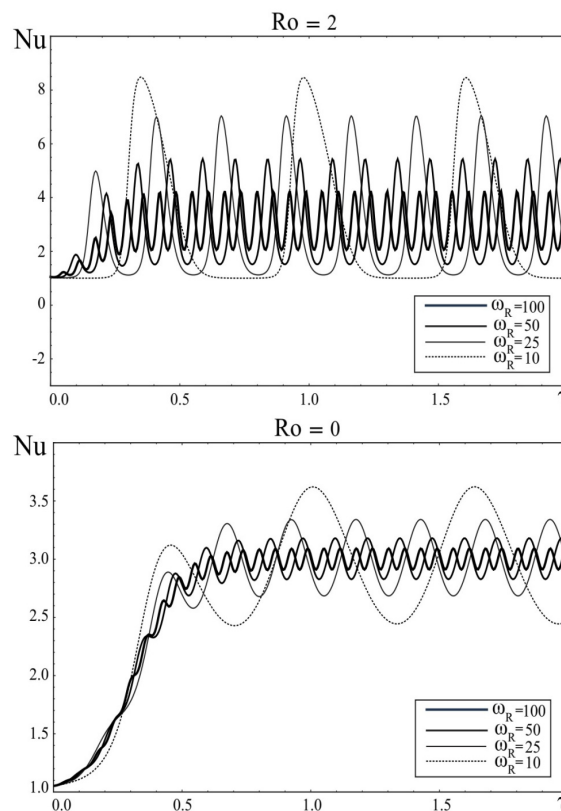
Fig. 23. Dependency of the Nusselt number Nu on time τ for positive Rossby numbers $Ro = (2,0)$ for modulation of rotation with a frequency $\omega_R = (10,25,50,100)$ and the amplitude $\delta = 0.3$.
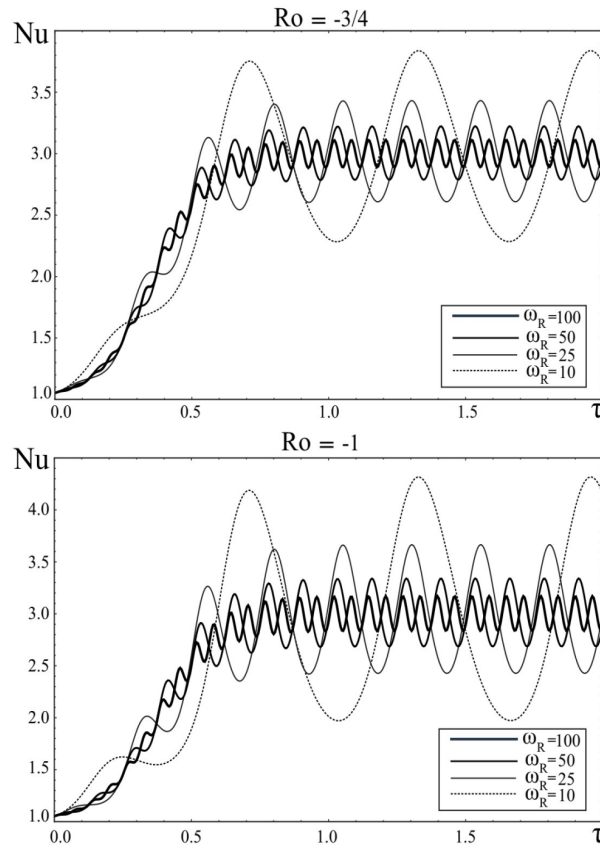
Fig. 24. Dependency of the Nusselt number Nu on time τ for negative Rossby numbers $Ro = (-3/4, -1)$ when modulating rotation with a frequency of $\omega_R = (10, 25, 50, 100)$ and the amplitude $\delta = 0.3$.

In Fig. 23-Fig. 24, we have depicted that for higher value of the modulation frequency ω_R for different Rossby numbers $Ro = (2, 0, -3/4, -1)$ leads to suppression of heat transfer, i.e. the magnitude of Nu decreases:

$$\Delta Nu\big|_{\omega_R = 10} > \Delta Nu\big|_{\omega_R = 25} > \Delta Nu\big|_{\omega_R = 50} > \Delta Nu\big|_{\omega_R = 100}$$
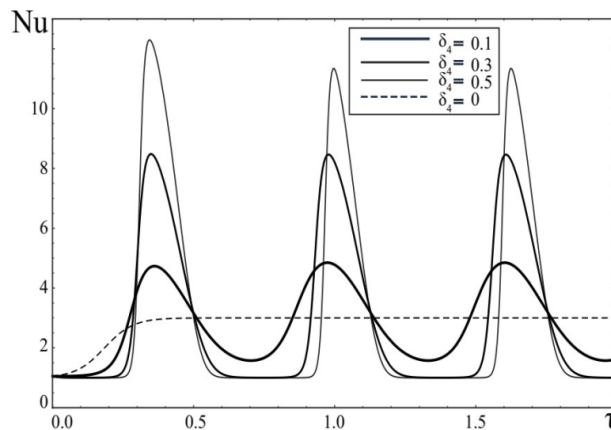
Fig. 25. Variations of the Nusselt number Nu depending on the amplitude of the modulation of rotation $\delta_4 = (0, 0.1, 0.3, 0.5)$ for the Rossby number $Ro = 2$ and the frequency $\omega_R = 10$.

In Fig. 25, we have defined the dependency of the heat transfer Nu on τ in the absence of $\delta_2 = 0$ and in the presence of rotational speed modulation $(\omega_R = 10)$ for different amplitudes $\delta_2 = 0.5, 0.3, 0.1$.

Here, the dashed line depicts the regime of establishing the final value of $Nu(\tau)$ for the case $\delta_2 = 0$. In Fig. 25, we can see that modulation of rotation leads to a periodic change of the heat flow, which increases with increasing amplitude δ_2.
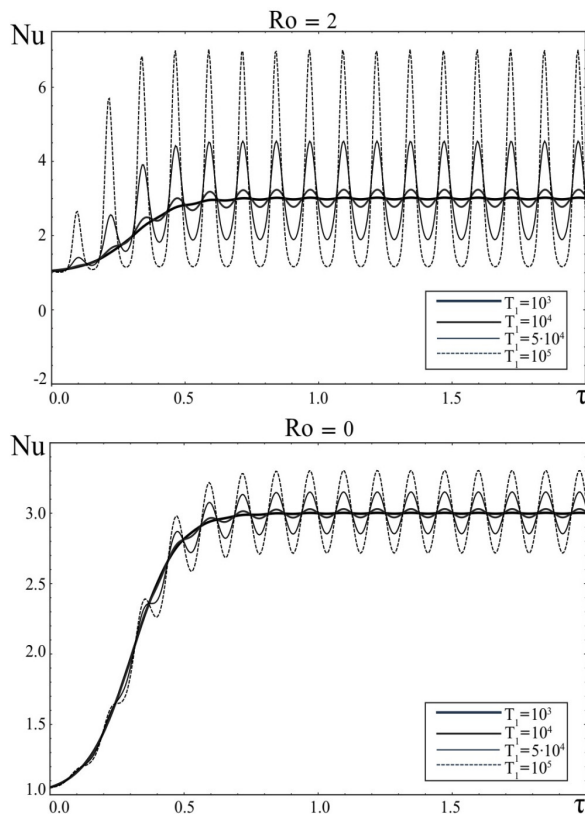
Fig. 26. Variations of the Nusselt number Nu depending on the Taylor number $T_1 = (10^3, 10^4, 5 \cdot 10^4, 10^5)$ for rotation modulation parameters ($\delta_2 = 0.5$, $\omega_R = 50$) with positive Rossby numbers $Ro = (2, 0)$.
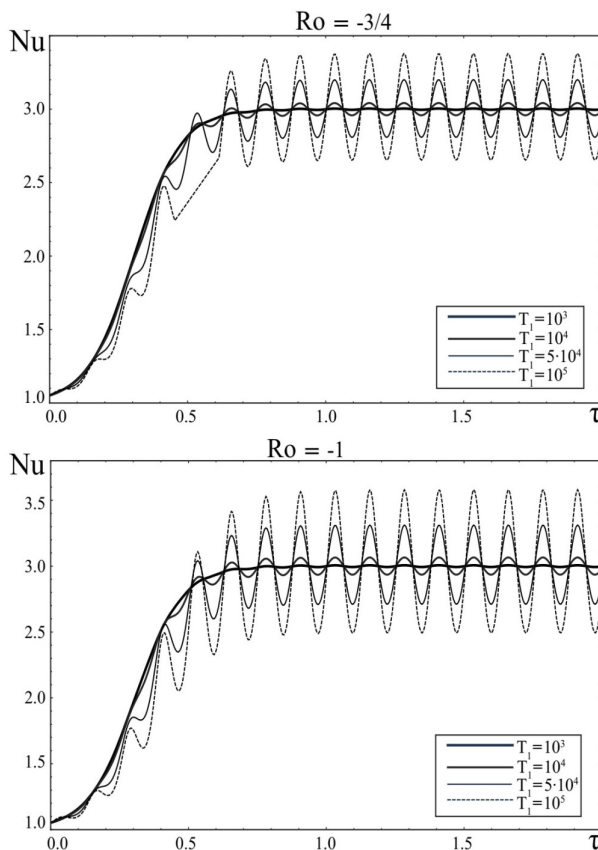
Fig. 27. Variations of the Nusselt number Nu depending on the Taylor number $T_1 = (10^3, 10^4, 5 \cdot 10^4, 10^5)$ for rotation modulation parameters ($\delta_2 = 0.5$, $\omega_R = 50$) for negative Rossby numbers $Ro = (-3/4, -1)$.

From Fig. 26 and Fig. 27, we can determine the change of heat transfer Nu for different Taylor numbers $T_1 = Ta / \pi^4 = (10^3, 10^4, 5 \cdot 10^4, 10^5)$ for a fixed value of the rotation modulation frequency $\omega_R = 50$, amplitude $\delta_2 = 0.5$ and Rossby numbers $Ro = (2, 0, -3/4, -1)$. It can be seen from these graphs that for different Rossby numbers $Ro = (2, 0, -3/4, -1)$, with an increase in the Taylor number T_1 heat transfer (Nusselt number Nu) in the system also increases:

$$\Delta Nu \big|_{T_1 = 10^3} < \Delta Nu \big|_{T_1 = 10^4} < \Delta Nu \big|_{T_1 = 5 \cdot 10^4} < \Delta Nu \big|_{T_1 = 10^5} .$$

CONCLUSION

A weakly nonlinear theory of stationary convection in a nonuniformly rotating electrically conductive fluid with a vertical constant magnetic field under the parametric action of: a) temperature modulation of the layer boundaries, b) modulation of gravity, c) modulation of an external magnetic field, d) modulation of the angular velocity of rotation is developed. We studied the influence of time-periodic modulation on stationary Rayleigh-Benard convection using the perturbation theory method for the small parameter of supercriticality of the Rayleigh number $\varepsilon = \sqrt{(Ra - Ra_c)/Ra_c}$. Furthermore, we considered the amplitudes of the modulated fields to be small, which having a second order $O(\varepsilon^2)$. In the first order ε, the parametric effect does not influence to the development of convection and we obtained the result of the linear theory [11]. In the third order ε^3, the nonlinear Ginzburg-Landau equation with time-periodic coefficients for four types of modulation are obtained. A numerical analysis of these equations have shown a number of general laws:

• The heat transfer increases for nonuniform rotation with a positive Rossby number $(Ro > 0)$.

• With increasing the modulation frequency of ω_{mod} the Nusselt number ΔNu decreases, which leads to suppression of heat transfer as with positive $(Ro > 0)$, so with negative $(Ro < 0)$ rotation profiles.
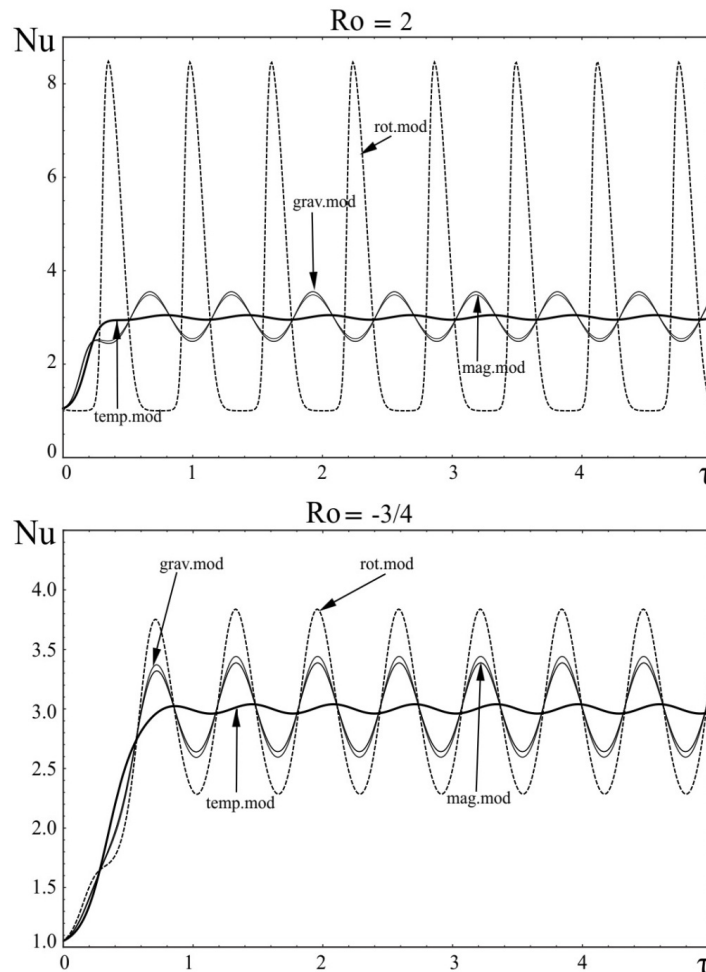
Fig. 28. Dependency of the Nusselt number Nu on τ for various types of modulation for positive $Ro = 2$
and negative $Ro = -3/4$ Rossby numbers

• The effect of increasing the modulation amplitude of δ_{mod} is to increase the heat transfer anyway of the rotation profile.

For the case of gravitational modulation, an increase the Taylor number T_1 leads to a decrease in the variations of the Nusselt number ΔNu (Fig. 14-Fig. 15). However, the heat flux increases (Fig. 26-Fig. 27) for large numbers T_1 in the case of rotation modulation. With increasing the Chandrasekhar number Q_1, heat transfer is at first suppresses and then increases (Fig. 20- Fig. 21) for the case of modulation of the magnetic field.

Finally let us compare the different types of parametric effects on a stationary nonuniformly rotating magnetoconvection among themselves. In Fig. 28 we have depicted the results of numerical solutions of the equations (43), (47), (50), (54) for fixed convection parameters: $Q/\pi^2 = Q_1 = 80$, $Ta/\pi^4 = T_1 = 10^5$, $Ra_c/\pi^4 = R_1 = 9500$, $Pm = 1$, $Pr = 10$, $A_0 = 0.5$. The frequencies and amplitudes of four types of modulation were considered equal: $\omega_T = \omega_g = \omega_B = \omega_R = 10$ and $\delta_1 = \delta_2 = \delta_3 = \delta_4 = 0.3$, phase $\varphi = \pi$. In Fig. 28 we can observe that the rotational modulation has the greatest influence on the change in heat flow in the system for positive $(Ro = 2)$ and negative $(Ro = -3/4)$ rotation profiles. Gravity modulation slightly exceeds magnetic modulation: $\Delta Nu \mid_{grav.mod} \geq \Delta Nu \mid_{mag.mod}$. Thermal phase modulation has a lesser effect on heat transfer in comparison with other types of modulations: $\Delta Nu \mid_{temp.mod} < \Delta Nu \mid_{mag.mod} \leq \Delta Nu \mid_{grav.mod} < \Delta Nu \mid_{rot.mod}$.

ORCID IDs

 Michael I. Kopp https://orcid.org/0000-0001-7457-3272, **Anatoly V. Tur** https://orcid.org/0000-0002-3889-8130,
 Volodymyr V. Yanovsky https://orcid.org/0000-0003-0461-749X

REFERENCES
[1]   S. Chandrasekhar, *Hydrodynamics and Hydromagnetic Stability* (Oxford Uni. Press, London, 1961), p. 652.
[2]   G.Z. Gershuni, and E.M. Zhukhovitckii, *Convective Stability of Incompressible Fluids* (Nauka, Moscow, 1972), pp. 392 (in Russian)
[3]   A.V. Getling, *Rayleigh-Benard Convection: Structures and Dynamics* (URSS, Moscow, 1999), p. 235. (in Russian)
[4]   M. Lappa, *Rotating thermal flows in natural and industrial processes.* (A John Wiley & Sons, Ltd., Publication, 2012), pp. 544.
[5]   S. Chandrasekhar, Proc. R. Soc. Lond. **A217**, 306-327 (1953), https://doi.org/10.1098/rspa.1953.0065.
[6]   S. Chandrasekhar, and D.D. Elbert, Proc. R. Soc. Lond. **A231**, 198-210 (1955), https://doi.org/10.1098/rspa.1955.0166.
[7]   I.A. Eltayeb, Proc. R. Soc. Lond. **A326**, 229-254 (1972), https://doi.org/10.1098/rspa.1972.0007.
[8]   I.A. Eltayeb, J. Fluid Mech. **71**(1), 161–179 (1975), https://doi.org/10.1017/S0022112075002480.
[9]   R. Avila and A. Cabello, Mathematical Problems in Engineering, **2013,** 1-15 (2013), https://doi.org/10.1155/2013/236901.
[10] E. Kurt, F.H. Busse and W. Pesch, Theoret. Comput. Fluid Dynamics, **18**, 251-263 (2004), https://doi.org/10.1007/s00162-004-0132-6.
[11] M.I. Kopp, A.V. Tour, and V.V. Yanovsky, JETP **127**, 1173-1196 (2018), https://doi.org/10.1134/S106377611812018X.
[12] M.I. Kopp, A.V. Tur, and V.V. Yanovsky, Problems of Atomic Science and Technology, **4**(116), 230-234 (2018), https://arxiv.org/abs/1805.11894.
[13] M. Kopp, A. Tur, and V. Yanovsky, East Eur. J. Phys**. 1**, 4-33 (2019), https://doi.org/10.26565/2312-4334-2020-1-01.
[14] M.I. Kopp, A.V. Tur, and V.V. Yanovsky, https://arxiv.org/abs/1905.05472.
[15] P. Vadasz, and S. Olek, Int. J. Heat Mass Transfer **41,** 1417-1435 (1999), https://doi.org/10.1016/S0017-9310(97)00265-2.
[16] V.K. Gupta, B.S. Bhadauria, I. Hasim, J. Jawdat, and A.K. Singh, Alexandria Engineering Journal, **54**, 981-992 (2015), https://doi.org/10.1016/j.aej.2015.09.002.
[17] V.K. Gupta, R. Prasad, and A.K. Singh, International Journal of Energy and Technology, **5**(28), 1-9 (2013).
[18] V.K. Gupta, and A.K. Singh, A Study of Chaos in an Anisotropic Porous Cavity, International Journal of Energy and Technology, **5** (27), 1-27 (2013).
[19] R. Prasad, and A.K. Singh, International Journal of Applied Mathematics and Informatics, **7**(3), 87-96 (2013).
[20] J.M. Jawdat, and I. Hashim, International Journal on Advanced Science, Engineering and Technology, **2**(5), 346-349 (2012), https://doi.org/10.18517/ijaseit.2.5.220.
[21] R. Prasad, and A.K. Singh, Journal of Applied Fluid Mechanics, **9**(6), 2887-2897 (2016). https://doi.org/10.29252/jafm.09.06.24811.
[22] G. Moffat, *Возбуждение магнитного поля в проводящей среде [Magnetic Field Generation in Electrically Conducting Fluids]*, (Mir, Moscow, 1980), pp. 343. (in Russian)
[23] T. Rikitake, Proc. Cambridge Philos. Soc. **54,** 89 (1958).
[24] A.E. Cook, and P.H. Roberts, Proc. Cambridge Philos. Soc. **68**, 547-569 (1970).
[25] Y. Gholipour, A. Ramezani, and M. Mola, Bulletin of Electrical Engineering and Informatics, **3**(4), 273-276 (2014).
[26] Xuedi Wang, Tianyu Yang, Wei Xu, International Journal of Nonlinear Science, **14**(2), 211-215 (2012).
[27] By F. Plunian, Ph. Marty, and A. Alemany, Proc. R. Soc. Lond. A. **454,** 1835-1842 (1998).
[28] I.A. Ilyin, D.S. Noshchenko, and A.S. Perezhogin, Vestnik KRAUNC. Fiz.-Mat. Nauki **2**(7), 43-45 (2013).
[29] V.I. Potapov, Rus. J. Nonlin. Dyn. **6,** 255-265 (2010).
[30] W.V.R. Malkus, and G. Veronis, J. Fluid Mech. **4**(3), 225-260 (1958), https://doi.org/10.1017/S0022112058000410.
[31] J.K. Bhattacharjee, J. Phy. A: Math. Gen. **22**(24), L1135-L1189 (1989), https://doi.org/10.1088/0305-4470/22/24/001.

[32] J.K. Bhattacharjee, Phy. Rev. A. **41**, 5491-5494 (1990), https://doi.org/10.1103/PhysRevA.41.5491.

[33] B.S. Bhadauria, and P. Kiran, Ain Shams Eng. J. **5**(4), 1287-1297 (2015), https://doi.org/10.1016/j.asej.2014.05.005.

[34] R. Ramya, E.J. Shelin, and G.K. Sangeetha, International Journal of Mathematics Trends and Technology, **54**(6), 477-484 (2018), https://doi.org/10.14445/22315373/IJMTT-V54P558

[35] P. Kiran, Ain Shams Eng. J. **7**(2), 639-651 (2016), https://doi.org/10.1016/j.asej.2015.06.005

[36] P.G. Siddheshwar, B.S. Bhadauria, and A. Srivastava, Transp. Porous Media, **91**(2), 585- 604 (2012), https://doi.org/10.1007/s11242-011-9861-3

[37] B.S. Bhadauria, P.G. Siddheshwar, J. Kumar, and O.P. Suthar, Trans. Porous Med. **73**(3), 633-647 (2012), https://doi.org/10.1007/s11242-011-9925-4

[38] P.G. Siddheshwar, B.S. Bhadauria, Pankaj Mishra, and A.K. Srivastava, Int. J. Non Linear Mech. **47**, 418-425 (2012), https://doi.org/10.1016/j.ijnonlinmec.2011.06.006.

[39] B.S. Bhadauria, and P. Kiran, Int. J. Eng. Math. **1,** 2014 (2014), https://doi.org/10.1155/2014/296216.

[40] B.S. Bhadauria, and P. Kiran, Transp. Porous Media. **100**, 279-295 (2013), https://doi.org/10.1007/s11242-013-0216-0.

[41] B.S. Bhadauria, and P. Kiran, Phys. Scr. **89**(9), 095209 (2014), https://doi.org/10.1088/0031-8949/89/9/095209.

[42] S. Aniss, M. Belhaq, and M. Souhar, J. Heat Transfer, **123**(3), 428-433 (2001), https://doi.org/10.1115/1.1370501.

[43] B.J. Geurts, and R. Kunnen, International Journal of Heat and Fluid Flow, **49**, 62-68 (2014).

[44] S.D. Alessio, and K. Ogden, WIT Transactions on Engineering Sciences, **74**, 453-463 (2012).

[45] G. Venezian, J. Fluid Mech. **35**, 243-254 (1969).

[46] P. Goldreich, and D. Lynden-Bell, Mon. Not. R. Astron. Soc. **130** (2), 125-158 (1965), https://doi.org/10.1093/mnras/130.2.125.

[47] E. Knobloch, and K. Jullien, Physics of Fluids, **17**(9), 094106 (2005), https://doi.org/10.1063/1.2047592.

[48] R. Haberman, *Elementary Applied Partial Differential Equations with Fourier Series and Boundary Value Problems*, 4th ed. (Pearson/Prentice Hall, N.J., 2004), p. 769.

[49] O.N. Kirillov, F. Stefani, and Y. Fukumoto, J. Fluid Mech. **760**, 591- 633 (2014), https://doi.org/10.1017/jfm.2014.614.

[50] R.J. Donnelly. Proc. R. Soc. Lond. Ser. **A281**, 130139 (1964).

[51] Jin-Qiang Zhong, Sebastian Sterl, and Hui-Min Li, J. Fluid Mech. **778,** R4 (2015).

СЛАБОНЕЛІНІЙНА МАГНІТНА КОНВЕКЦІЯ В ЕЛЕКТРОПРОВІДНОМУ СЕРЕДОВИЩІ, ЩО НЕОДНОРІДНО ОБЕРТАЄТЬСЯ, ПІД ДІЄЮ МОДУЛЯЦІЇ ЗОВНІШНІХ ПОЛІВ

Михайло Й. Копп[a], Анатолій В. Тур[c], Володимир В. Яновський[a,b]
[a]Інститут монокристалів, Національна Академія Наук України
пр. Науки 60, 61001 Харків, Україна
[b]Харківський національний університет імені В.Н. Каразина
майдан Свободи, 4, 61022, Харків, Україна
Університет Тулузи [UPS], CNRS, Інститут досліджень астрофізики та планетології
9 проспект полковника Роше, BP 44346, 31028 Тулуза Седекс 4, Франція

Досліджується слабонелінійна стадія стаціонарної конвективної нестійкості в шарі електропровідної рідини, що неоднорідно обертається в аксіальному однорідному магнітному полі під дією: а) температурної модуляції меж шару; б) гравітаційної модуляції; в) модуляції магнітного поля; г) модуляції кутової швидкості обертання. Для опису нелінійних конвективних явищ використовувалася локальна декартова система координат, в якій неоднорідне обертання шару рідини представляється у вигляді обертання з постійною кутовою швидкістю $\vec{\Omega}_0$ і азимутальним широм $\vec{U}_0(x)$, профіль швидкості якого є локально лінійним. В результаті застосування методу теорії збурень за малим параметром надкритичності стаціонарного числа Релея отримані неавтономні нелінійні рівняння типу Гінзбурга-Ландау для перелічених вище випадків. Амплітуди модульованих полів вважалися малими, які мають другий порядок ε^2, а параметричний вплив діє на стаціонарну конвекцію в третьому порядку ε^3. Чисельні рішення рівнянь Гінзбурга-Ландау для різних типів модуляції зовнішнього параметричного впливу показали, що: 1) при неоднорідному обертанні з позитивним числом Росбі $Ro > 0$ теплоперенос в рідині збільшується; 2) збільшення частоти модуляції ω_{mod} призводить до подавлення теплоперенесу як при позитивних $Ro > 0$, так і при негативних профілях обертання; 3) збільшення амплітуди модуляції δ_{mod} призводить до підвищення теплообміну для довільного профілю обертання. Показано, що найбільший вплив на зміну теплопотоку в системі оказує обертальна модуляція. При цьому гравітаційна модуляція трохи перевищує магнітну модуляцію, а теплова фазова модуляція, в порівнянні з іншими типами модуляцій, оказує менший вплив на теплоперенос.

КЛЮЧОВІ СЛОВА: конвекція Релея-Бенара, магнітообертальна нестійкість, критичні числа Релея, слабонелінійна теорія, неавтономне рівняння Гінзбурга-Ландау

СЛАБОНЕЛИНЕЙНАЯ МАГНИТНАЯ КОНВЕКЦИЯ В НЕОДНОРОДНО ВРАЩАЮЩЕЙСЯ ЭЛЕКТРОПРОВОДЯЩЕЙ СРЕДЕ ПОД ДЕЙСТВИЕМ МОДУЛЯЦИИ ВНЕШНИХ ПОЛЕЙ

Михаил И. Копп[a], Анатолий В. Тур[c], Владимир В. Яновский[a,b]
[a]Институт монокристаллов, Национальная Академия Наук Украины
пр. Науки 60, 61001 Харьков, Украина
[b]Харьковский национальный университет имени В.Н. Каразина
пл. Свободы, 4, 61022, Харьков, Украина
[c]Университет Тулузы [UPS], CNRS, Институт исследований астрофизики и планетологии
9 Авеню Полковника Роше, BP 44346, 31028 Тулуза Cedex 4, Франция

Исследуется слабонелинейная стадия стационарной конвективной неустойчивости в неоднородно вращающемся слое электропроводящей жидкости в аксиальном однородном магнитном поле под действием: а) температурной модуляции границ слоя; б) гравитационной модуляции; в) модуляции магнитного поля; г) модуляции угловой скорости вращения. Для описания нелинейных конвективных явлений использовалась локальная декартовая система координат, в которой

неоднородное вращение слоя жидкости представляется в виде вращения с постоянной угловой скоростью $\vec{\Omega}_0$ и азимутальным широм $\vec{U}_0(x)$, профиль скорости которого локально линеен. В результате применения метода теории возмущений по малому параметру надкритичности стационарного числа Рэлея $\varepsilon = \sqrt{(Ra - Ra_c)/Ra_c}$ получены неавтономные нелинейные уравнения типа Гинзбурга-Ландау для перечисленных выше случаев. Амплитуды модулируемых полей считались малыми, имеющих второй порядок ε^2, а параметрическое воздействие оказывает влияние на стационарную конвекцию в третьем порядке ε^3. Численные решения уравнений Гинзбурга-Ландау для различных типов модуляции внешнего параметрического воздействия показали, что: 1) при неоднородном вращении с положительным числом Россби $Ro > 0$ теплоперенос в жидкости увеличивается; 2) увеличение частоты модуляции ω_{mod} приводит к подавлению теплопереноса как при положительных $Ro > 0$, так и при отрицательных $Ro < 0$ профилях вращения; 3) увеличение амплитуды модуляции δ_{mod} приводит к повышению теплообмена для произвольного профиля вращения. Показано, что наибольшее влияние на изменение теплопотока в системе оказывает вращательная модуляция. При этом гравитационная модуляция немного превышает магнитную модуляцию, а тепловая фазовая модуляция, по сравнению с другими типами модуляций, оказывает меньшее влияние на теплоперенос.

КЛЮЧЕВЫЕ СЛОВА: конвекция Рэлея-Бенара, магнитовращательная неустойчивость, критические числа Рэлея, слабонелинейная теория, неавтономное уравнение Гинзбурга-Ландау.

RAYLEIGH-PLATEAU DISSIPATIVE INSTABILITY

Oksana L. Andrieieva[a,b], Leonid A. Bulavin[c]**, Viktor I. Tkachenko[a,b]*

[a]NSC "Kharkiv Institute of Physics and Technology"
Academichna Str. 1, 61108, Kharkiv, Ukraine
[b]V.N. Karazin Kharkiv National University, Kharkiv, Ukraine
4 Svobody Sq., 61022, Kharkiv, Ukraine
*Corresponding Author: andreevaoksana@kipt.kharkov.ua
[c]Taras Shevchenko National University of Kyiv
64/13, Volodymyrska Str., 01601, Kyiv, Ukraine
**Corresponding Author: bulavin221@gmail.com
Received November 22, 2020; accepted March 30, 2020

The instability of a freely falling jet of liquid in air taking into account the viscosity of the contacting media is considered. In neglecting the viscosities of both media, instability was studied by Rayleigh and Plateau. They showed that instability develops as a result of the action of surface forces, and is expressed in a change in the cylindrical shape of the boundary of a freely falling jet of liquid with air into a sequence of spherical drops. In subsequent works, by phenomenological consideration of viscosity by means of the Ohnesorge number, it is shown that the viscosity of each of the contacting media affects the nature of the instability. However, this method of taking viscosity into account is not entirely correct, because does not take into account the specificity of the boundary conditions existing at the interface. It is proposed to use percolation boundary conditions, the validity of which is proved by the example of the exact determination of the threshold velocity of occurrence of Kelvin-Helmholtz instability. A dispersion equation of the Rayleigh-Plateau problem with percolation boundary conditions that describes the instability taking into account the viscosity of both media is obtained. The dissipative nature of the development of such instabilities is substantiated. The growth rates of instabilities are determined in cases when: the jet and medium have a low viscosity (ideal fluids); the jet is characterized by high viscosity, and the environment is small; the jet and the environment are highly viscous. It is shown that the theoretical model of droplet decay of the jet in the absence of viscosity of both media is quite good, in quantitative terms, consistent with experimental results. The maximum increment is equal $\gamma_{KG}^{\max} \approx 0.32$, against the Rayleigh-Plateau increment $\gamma_{RP}^{\max} \approx 0.34$, for disturbances with the same wave number $X_{\max} \approx 0.7$. It was also shown that for viscous jets and a weakly viscous environment, the instability increment describes the experimental results with a rather high degree of accuracy. Numerical calculations show that for jets of comparable viscosity, the instability increment decreases with increasing viscosity of the environment. If the viscosity of the environment is constant, then the increment of instability will be greater where the viscosity of the stream is higher. It is shown that the results of theoretical calculations are in good agreement with the available experimental data.
KEYWORDS: Rayleigh-Plateau instability, surface tension, viscosity, percolation boundary conditions, dissipative instability, instability increment, wave number, instability range.

In the classical formulation the Rayleigh-Plateau problem is associated with a study of the hydrodynamic instability of the cylindrical boundary of a freely falling jet of liquid with respect to its decomposition into separate droplets.

Joseph Plateau first observed and characterized this instability in 1873 [1]. He noted that the instability occurred when the liquid column length λ exceeded the column diameter $D = 2R_0$ by a factor of about 3.13, i.e. when the condition $\lambda \geq 3.13 \cdot 2R_0$ was satisfied. Later lord Rayleigh corroborated the Plateau's work results by theory giving an analytical description of this physical phenomenon [2, 3]. He showed that such an unstable behavior of a jet was due to the availability of small perturbations on its surface, which could increase at certain wavelengths. Rayleigh showed that sinusoidal perturbations of the surface were unstable due to effect of surface forces. However, the criterion for instability development defined by him differs from Plato's criterion and takes the following form $\lambda \geq 4.51 \cdot 2R_0$. Taking account of the formation of small intermediate droplets between the main droplets leads to a slight decrease in the unstable wavelength to the value of $\lambda \geq 4.42 \cdot 2R_0$ [4]. However, such a decrease does not violate the general conclusions regarding the criterion for the development of instability, which has been confirmed with a sufficient degree of reliability by a significant number of experiments [5].

The physical phenomenon under consideration has a simple physical substantiation. The process of decomposition the ow into droplets is due to the need of the system to occupy a position with the minimum potential energy. And since in a free state a fixed cylindrical volume of a liquid is subject to surface tension forces, it will tend to take a spherical shape that has a minimal surface and, therefore, the minimum potential energy of capillary forces [6]. The above mentioned refers to a cylindrical liquid jet that is unstable with respect to its decomposition into droplets. However, the list of such processes in the ambient environment is much longer [5]. Study of such processes is motivated not only by their practical application, but also by a scientific content. The latter should include the definition of physical mechanisms leading to decomposition of jets under various conditions, as well as the description of the effect of surface

tension and viscosity on the dynamics of processes. And if the surface tension is the basis of instability, then viscous forces can lead to a change in the characteristic decomposition times without changing the limits in which the stability of the system is observed [5].

As a rule, the viscosity in problems of jet stability is taken into account phenomenologically by introducing, along with the jet radius R_0, a new characteristic length, called the "penetration depth". This length is determined by the Ohnesorge number $Oh = \nu\sqrt{\rho/\sigma R_0}$ [7] and has the form: $l_{Oh} = \sqrt{\nu/\omega}$ where ν - the coefficient of kinematic viscosity, ρ - the liquid density, σ - the coefficient of surface tension.

Comparison of the Rayleigh theory for jets with no viscosity, as well as the Rayleigh-Chandrasekhar theory in viscous media with experimental data [5] indicates a certain agreement. In some cases, the issue of agreement remains open due to the lack of measurement error data in [5]. Therefore, the method of taking account of the viscosity of media by means of the Ohnesorge number is not entirely correct, since it does not take into account the specifics of the boundary conditions at the media interface.

If we consider the liquid jet and the surrounding air as two contacting media with their characteristic parameters, then the Rayleigh problem [2, 3] transforms into the Kelvin-Helmholtz problem [8, 9]. In this case, as shown in [10], the jet instability increment can be obtained from the Kelvin-Helmholtz instability increment, assuming the gravity force equal to zero. At the same time, as shown in [11], only the use of percolation boundary conditions makes it possible to take into account the viscosity of both media, to determine the threshold number and the increment of instability development. Under this approach the threshold velocity of instability development coincides with the experimentally measured. Therefore, on the basis of the foregoing in the present work we consider the Rayleigh-Plateau problem within the framework of the Kelvin-Helmholtz model of instability development, taking into account the viscosity of both media and using percolation boundary conditions.

For further research of the Rayleigh-Plateau problem we will turn our attention to the obtained experimental results. So, in the experimental implementation of the Rayleigh-Plateau problem a liquid jet from a pipe of a certain radius is falling vertically under gravity. Initially, at the exit of the pipe, the jet has a constant radius equal to the radius of the pipe. The length of the falling liquid jet increases and reaches such a critical value, when the jet loses its cylindrical shape as a result of decomposition into a sequence of droplets of almost the same size. Capillary instability of a liquid jet owing under pressure from a pipe of diameter $D = 4$ mm is presented in Fig 1. The initial sonic perturbations superimposed on the jet had a wavelength of λ = 168 mm, 50 mm and 18.4 mm. Their effect on the jet stability during the motion from top to bottom, respectively, is shown in Fig. 1 [12]. The figure shows that the last value of the wavelength is closest to the value of $\lambda/D > 3.13$ found by Joseph Plato.

To understand the physical phenomena underlying the droplet instability of a cylindrical free-falling jet we present below the result of study of the instability of freely falling jet decomposition into droplets obtained by Rayleigh [2, 3].
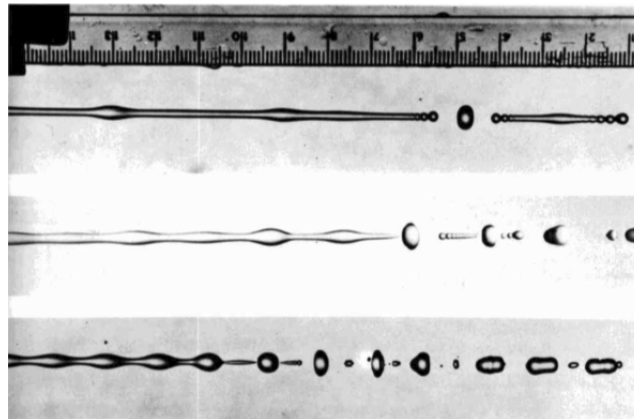
Figure 1. Capillary instability of a liquid jet owing under pressure from a pipe with a diameter of D = 4mm. The initial perturbations of the jet shape are initiated by sound waves of a wavelength equal to 42, 12.5 and 4.6 of the pipe diameter [12].

THE RAYLEIGH'S PROBLEM

Rayleigh investigated the stability of boundary of a cylindrical liquid jet of radius R_0, density ρ and surface tension σ in a cylindrical coordinate system r, ϕ, z, where the axes ϕ, z were parallel to the interface and the axis z was oriented vertically upwards. As the values, describing the stability of the liquid boundary, he chose radial - W_r and vertical - W_z perturbation of liquid velocity, displacement of liquid interface $\varepsilon(r, \phi, z, t)$ from the equilibrium position R_0 $R(r, z, t) = R_0 + \varepsilon(r, z, t)$; $|\varepsilon| << R_0$ and deviation of liquid pressure from equilibrium p_0 $p(r, z, t) = p_0 + \tilde{p}(r, z, t)$, $|\tilde{p}| << p_0$.

For small axially symmetric perturbations of the form

$$W_r = U_r(r)\exp(-i\omega t + ikz); \quad W_z = U_z(r)\exp(-i\omega t + ikz);$$
$$\tilde{p} = P(r)\exp(-i\omega t + ikz); \quad \varepsilon = \varepsilon_0(r)\exp(-i\omega t + ikz). \tag{1}$$

where, ω and $k = \dfrac{2\pi}{\lambda}$ - the frequency and the wavenumber of the interface perturbation, respectively, λ - wavelength of the perturbation, the dispersion equation has the form [2,3]:

$$\omega^2 = -\left(1 - k^2 R_0^2\right)\frac{\sigma k}{\rho R_0^2}\frac{I_1(kR_0)}{I_0(kR_0)}. \tag{2}$$

where, $I_0(x)$, $I_1(x)$ modified Bessel's functions of the first kind of the zero and the first order, respectively [13].

It follows from (2) that the instability arises for negative values of the square of the frequency $\omega^2 < 0$, i.e. when $kR_0 < 1$. In this case the radius perturbation increases with increment:

$$\gamma_{RP}(K) = \Gamma_0\sqrt{\left(1 - K^2\right)K\frac{I_1(K)}{I_0(K)}} \tag{3}$$

where, $\varepsilon \sim \exp(\gamma_{RP} t)$ variation of the liquid boundary displacement in time, $\Gamma_0 = \sqrt{\dfrac{\sigma}{\rho R_0^3}}\,0$, $K = kR_0$ - dimensionless wave number.

From the condition $K > 1$ it follows that the instability is possible when the length of the working circle of the jet is less than the perturbation wave length in vertical direction. Calculations (3) gives the maximum increment is equal to $\gamma_{RP}^{\max} = 0.343\sqrt{\sigma/\rho R_0^3}$ and is reached at $K = 0.7$. For example, for a water jet of 10 cm in diameter at the surface tension coefficient $\sigma = 72.58$ erg/cm^2 (at a temperature of 20°C) and density $\rho = 1$ g/cm^3 [14], the characteristic time of jet decomposition into droplets is about of order:

$$\left(\gamma_{RP}^{\max}\right)^{-1} = 2.91\sqrt{\frac{\rho R_0^3}{\sigma}} = 2.91\sqrt{\frac{5^3}{72.58}} = 3.82 \text{ s}. \tag{4}$$

From (3) follows that if the radius of the jet decreases the characteristic decomposition time decreases. For water jet of 1 mm in diameter this time will be 3.8 ms. Let us compare the obtained expression for the increment (3) with the experimental data given in Fig. 1. It follows from the figure that the last value of the sound wave length does not coincide with, but it is most closely to the Rayleigh value: $K = 0.7 = 2\pi R_0/\lambda \to \lambda = 6.28 \cdot 0.2 / 0.7 = 1.79$ cm, which is about 1.25 cm in the experiment. Comparing theory with experiment there is a slight mismatch of theoretical conclusions with experimental data. Therefore, there is a need to find models that would eliminate this discrepancy. In the next section a model for describing the instability of jet decomposition into droplets based on the Kelvin-Helmholtz theory of instability is proposed, which takes into account surface tension, viscosity of both media and uses percolation boundary conditions.

RAYLEIGH-PLATEAU INSTABILITY IN THE FORMULATION OF THE KELVIN-HELMHOLTZ PROBLEM WITH PERCOLATION BOUNDARY CONDITIONS

Let us consider the problem of stability of a liquid jet owing freely from a pipe in the formulation of the Kelvin-Helmholtz problem. Oscillation of the interface between two media with density ρ_1, ρ_2 and coefficients of dynamic viscosity μ_1, μ_2 in a cylindrical coordinate system ρ, ϕ, z (axes ϕ, z are parallel to the interface, the axis z is oriented vertically upwards) we will describe using three functions: two functions for the velocity potentials $\varphi_{1,2}(r, \phi, z, t)$, the function of the liquid interface displacement from the equilibrium position, where the perturbed radial position of the interface $R(r, \phi, z, t)$ is determined by expression (1). As in the previous section, due to the axial symmetry of the problem we assume the perturbed values independent of the azimuth angle ϕ. With this consideration the velocity of the fluid in media 1, 2 is determined by the expression: $\vec{W}_{1,2} = \vec{\nabla}\varphi_{1,2}(r, z, t) = \vec{\nabla}\left(\varphi_{1,2}^{(0)}(z) + \tilde{\varphi}_{1,2}(r, z, t)\right)$, where $\varphi_{1,2}^{(0)}(z)$ - the potential of liquid velocities in the equilibrium state; $\tilde{\varphi}_{1,2}(r, z, t)$ - the potential of the disturbed velocity of the medium 1, 2; $\tilde{\varphi}_{1,2}(r, z, t)$ - operator of gradient in a cylindrical coordinate system; $\left|\varphi_{1,2}^{(0)}(z)\right| \gg \left|\tilde{\varphi}_{1,2}(r, z, t)\right|$ - the smallness disturbance condition. The location of viscous media and the boundaries

between them are schematically presented in Fig.2. The boundary of viscous media is determined by the expression $R = R_0 + \varepsilon(r,z,t)$ and the media move at different velocities $\vec{V}_{1,2}$ parallel to the axis z.
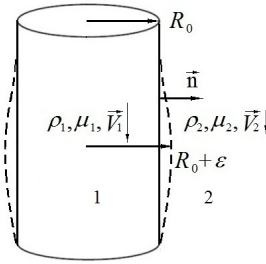
Fig. 2. The layout diagram of the interface of viscous media $R = R_0 + \varepsilon(r,z,t)$ moved

at different velocities $\vec{V}_{1,2}$, parallel to the axis z

For the case shown in Fig. 2 the potential of the equilibrium velocity can be represented as:

$$\varphi_{1,2}^{(0)}(z) = V_{1,2} z + C_{1,2} \tag{5}$$

where, $C_{1,2}$ - constant.

The equations for functions $\varphi_{1,2}(r,z,t)$ and $\varepsilon(r,z,t)$ are well known [15], they consist of the equation for the incompressibility of a liquid and the equation describing the kinematic boundary condition. The equation for the liquid incompressibility is as follows:

$$\Delta \tilde{\varphi}_{1,2} \equiv \Delta_{\perp} \tilde{\varphi}_{1,2} + \frac{\partial^2 \tilde{\varphi}_{1,2}}{\partial z^2} = 0 , \tag{6}$$

where, $\Delta... = \dfrac{1}{r}\dfrac{\partial}{\partial r} r \dfrac{\partial...}{\partial r} + \dfrac{\partial^2 ...}{\partial z^2} = \Delta_{\perp}... + \dfrac{\partial^2 ...}{\partial z^2}$. The potential of the equilibrium velocity of the medium (5) automatically satisfies the equation (6). In further calculations we omit the sign for the convenience of writing. The kinematic boundary condition determines the radial velocity of the liquid at media interface:

$$\frac{dR}{dt} = \left(W_{1,2}\right)_r = \frac{\partial \tilde{\varphi}_{1,2}}{\partial r}; \quad \frac{\partial R}{\partial t} + \left[\left(\vec{W}_{1,2}\vec{\nabla}\right)\vec{R}\right]_r = \frac{\partial \tilde{\varphi}_{1,2}}{\partial r} \tag{7}$$

After linearization (7) we have:

$$\left.\frac{\partial \varepsilon}{\partial t}\right|_{r=R_0+\varepsilon(r,z,t)} + V_{1,2}\left.\frac{\partial \varepsilon}{\partial z}\right|_{r=R_0+\varepsilon(r,z,t)} = \left.\frac{\partial \tilde{\varphi}_{1,2}}{\partial r}\right|_{r=R_0+\varepsilon(r,z,t)} \tag{8}$$

Equations (6), (8) should be supplemented by a dynamic boundary condition. This condition can be obtained by integrating along the coordinate r of the radial component of the linearized Navier-Stokes equation:

$$\vec{T} = \rho\left(\frac{\partial \vec{W}}{\partial t} + \left(\vec{W}\vec{\nabla}\right)\vec{W}\right) + \vec{\nabla} p = 0 \tag{9}$$

over a thin transition boundary layer $-\Delta \le r - R_0 - \varepsilon(R_0,z,t) \le \Delta$, according to the expression:

$$\lim_{\substack{\Delta \to 0 \\ \varepsilon \to 0}}\left(\int_{r=R_0+\varepsilon(R_0,z,t)-\Delta}^{r=R_0+\varepsilon(R_0,z,t)+\Delta} \left(T_r\right) dr\right) = \lim_{\Delta \to 0}\left(\int_{r=R_0-\Delta}^{r=R_0+\Delta} \left(T_r\right) dr\right) \tag{10}$$

Let us obtain this dynamic boundary condition. To simplify the procedure of integration over a thin transition layer we present the coefficient of dynamic viscosity of both media $\mu(r)$ in the following model form:

$$\mu(r) = \mu_1 \theta(-r + R_0 - \Delta) + \mu_2 \theta(r - R_0 - \Delta) + $$
$$+ (\mu_1 + \mu_2)\left(\theta(r - R_0 + \Delta) - \theta(r - R_0 - \Delta)\right), \tag{11}$$

where, $\theta(x)$ - asymmetric unit function $\theta(x) = 1$ at $x \ge 0$ and $\theta(x) = 0$ at $x < 0$. When obtaining a dynamic boundary condition, the model dependence (11) characterizes its percolation boundary conditions [11]. The physical nature of "percolation boundary conditions" is the effect of the mutual periodic penetration of contacting media near the interface in areas not previously occupied by them. Such penetration of media is taken into account by a model representation of the viscosity coefficient at the interface in the form of stepwise functions of the radius. The proposed

model representation is valid, because in the Kelvin-Helmholtz instability problem with a at boundary [15], the use of a viscosity coefficient in the form of superimposed steps of the form (11) leads to the dispersion equation, which gives a threshold ow velocity corresponding to the experimental one. After linearization the Navier-Stokes equation (9) takes the form:

$$\rho\left(\frac{\partial}{\partial t}\frac{\partial\tilde{\varphi}}{\partial x_k}+\frac{1}{2}\frac{\partial}{\partial x_k}\left(\frac{\partial\left(\varphi^{(0)}(z)+\tilde{\varphi}\right)}{\partial x_i}\right)^2\right)-\left(2\frac{\partial\mu(r)}{\partial r}\frac{\partial^2\tilde{\varphi}}{\partial r^2}+2\mu(r)\frac{1}{r^2}\frac{\partial\tilde{\varphi}}{\partial r}\right)+\frac{\partial p}{\partial x_k}=0 \tag{12}$$

where, $k=r$, $i=r,z$, $x_r=r$, $x_z=z$, the corresponding term should be summed on index "i".

For the selected model dependence of the medium viscosity $\mu(r)$ upon the coordinate z the main contribution to the dynamic boundary condition makes a summand proportional to $\partial\mu(z)/\partial z$. Integrating (12) over a thin transition layer $(R_0-\Delta,R_0+\Delta)$ along the radius, taking into account (8), and then tending to zero $\Delta\to0$, we obtain the following dynamic boundary condition:

$$\rho\left(\frac{\partial}{\partial t}\tilde{\varphi}+V_{1,2}\frac{\partial\tilde{\varphi}}{\partial z}\right)\Bigg|_1^2+2\left(\frac{1}{r}\frac{\partial}{\partial r}+\frac{\partial^2}{\partial z^2}\right)\Bigg|_{\mu_2\tilde{\varphi}_1}^{-\mu_1\tilde{\varphi}_2}+p\Big|_1^2+\sigma\frac{\partial^2\varepsilon}{\partial z^2}=const \tag{13}$$

In (13) the pressure difference corresponds to the Bernoulli equation and is determined by the expression: $p\Big|_1^2=p_2-p_1=const$, where, $const=\rho_2\dfrac{V_2^2}{2}-\rho_1\dfrac{V_1^2}{2}$.

Thus, we have a system of equations for perturbed values on the jet boundary:

$$\Delta_\perp\tilde{\varphi}_{1,2}+\frac{\partial^2\tilde{\varphi}_{1,2}}{\partial z^2}=0, \tag{14}$$

$$\frac{\partial\varepsilon}{\partial t}\bigg|_{r=R_0}+V_{1,2}\frac{\partial\varepsilon}{\partial z}\bigg|_{r=R_0}=\frac{\partial\tilde{\varphi}_{1,2}}{\partial r}\bigg|_{r=R_0}, \tag{15}$$

$$\rho\left(\frac{\partial}{\partial t}\tilde{\varphi}+V_{1,2}\frac{\partial\tilde{\varphi}}{\partial z}\right)\Bigg|_1^2+2\left(\frac{1}{r}\frac{\partial}{\partial r}+\frac{\partial^2}{\partial z^2}\right)\Bigg|_{\mu_2\tilde{\varphi}_1}^{-\mu_1\tilde{\varphi}_2}+\sigma\frac{\partial^2\varepsilon}{\partial z^2}=0. \tag{16}$$

We'll submit the velocity potentials $\tilde{\varphi}$ and the interface displacement ε in the form of $\tilde{\varphi}_{1,2}\sim f_{1,2}(r)\exp(ikz-i\omega t)$, $\varepsilon\sim g(r)\exp(ikz-i\omega t)$, where ω and k are the frequency and the wavenumber of the wave, $k=2\pi/d$, d - the perturbation wavelength along the jet axis. Then from equation (14) we obtain a radius-restricted solution for a perturbed velocity potential $f_1(r)$ in medium 1 and an infinity-restricted solution for a perturbed velocity potential in medium 2:

$$\begin{aligned}f_1(r)&=AI_0(kr), \quad 0\le r\le R_0\\ f_2(r)&=BK_0(kr), \quad R_0\le r\le\infty\end{aligned} \tag{17}$$

where, $I_0(x),K_0(x)$ - modified Bessel functions of the second kind of the zero order [13], A,B - constants. From (15), (16) we obtain the system of equations:

$$-i(\omega-kV_1)=AkI_1(kR_0), \tag{18}$$

$$-i(\omega-kV_2)=-BkK_1(kR_0), \tag{19}$$

$$\rho\left(\frac{\partial}{\partial t}\tilde{\varphi}+V_{1,2}\frac{\partial\tilde{\varphi}}{\partial z}\right)\Bigg|_1^2+2\left(\frac{1}{r}\frac{\partial}{\partial r}+\frac{\partial^2}{\partial z^2}\right)\Bigg|_{\mu_2\tilde{\varphi}_1}^{-\mu_1\tilde{\varphi}_2}+\sigma\frac{\partial^2\varepsilon}{\partial z^2}=0. \tag{20}$$

where, $K_1(x)$ - modified Bessel function of the second kind of the first order [13].

Solution of equations (18) - (20) in the Lamb type reference system $\rho_2V_2K_0(kR_0)/K_1(kR_0)+\rho_1V_1I_0(kR_0)/I_1(kR_0)=0$ gives the following dispersion equation:

$$\omega^2 + 2i\omega \frac{\left(\mu_1 k^2 \left(1 + kR_0 \frac{K_0(kR_0)}{K_1(kR_0)} \right) + \mu_2 k^2 \left(1 - kR_0 \frac{I_0(kR_0)}{I_1(kR_0)} \right) \right)}{\left(\rho_2 kR_0 \frac{K_0(kR_0)}{K_1(kR_0)} + \rho_1 kR_0 \frac{I_0(kR_0)}{I_1(kR_0)} \right)} -$$

$$-2ik^3 \frac{\left(\mu_1 V_2 \left(1 + kR_0 \frac{K_0(kR_0)}{K_1(kR_0)} \right) + \mu_2 V_1 \left(1 - kR_0 \frac{I_0(kR_0)}{I_1(kR_0)} \right) \right)}{\left(\rho_2 kR_0 \frac{K_0(kR_0)}{K_1(kR_0)} + \rho_1 kR_0 \frac{I_0(kR_0)}{I_1(kR_0)} \right)} + \tag{21}$$

$$+ \frac{\rho_2 (kV_2)^2 kR_0 \frac{K_0(kR_0)}{K_1(kR_0)} + \rho_1 (kV_1)^2 kR_0 \frac{I_0(kR_0)}{I_1(kR_0)} - k^4 R_0 \sigma}{\left(\rho_2 kR_0 \frac{K_0(kR_0)}{K_1(kR_0)} + \rho_1 kR_0 \frac{I_0(kR_0)}{I_1(kR_0)} \right)} = 0$$

Let us consider the solution of equation (21) with no viscosity, i.e. assume $\mu_1 = \mu_2 = 0$. In this case the equation (21) takes the form:

$$Y(X,G) = \pm i \frac{X}{\sqrt{G}} \sqrt{ \frac{ \left(\frac{\rho_2 V_2^2}{\rho_1 V_1^2} \frac{K_0(X) I_1(X)}{K_1(X) I_0(X)} + 1 \right) - GX \frac{I_1(X)}{I_0(X)} }{ \left(\frac{\rho_2}{\rho_1} \frac{K_0(X) I_1(X)}{K_1(X) I_0(X)} + 1 \right) } } \tag{22}$$

where, $G = \frac{\sigma}{V_1^2 \rho_1 R_0}$, $X = kR_0$, $Y = \omega\sqrt{G}\sqrt{\frac{\rho_1 R_0^3}{\sigma}}$

The instability increment is determined by the expression:

$$\gamma_{KG}(X,G) = \mathrm{Im}(Y(X,G)) \tag{23}$$

and is realized at positive values of the radical expression (22).

The summands for water and air proportional to small values $\rho_2 V_2^2 / \rho_1 V_1^2 \ll 1$ and $\rho_2/\rho_1 \ll 1$ can be neglected in (23). As a result, we come to the following expression for the instability increment:

$$\gamma_{KG}(X,G) = \frac{X}{\sqrt{G}} \sqrt{1 - GX \frac{I_1(X)}{I_0(X)}}. \tag{24}$$

In (24) the constant G is specified by the system parameters at the initial time. Let us determine its value. From experimental studies of jet decomposition into droplets with no viscosity it follows that instability is possible for $X \leq 1$ [5]. Therefore, from the condition of stability $\gamma_{KG}(1,G) = 0$ it is easy to determine the value G: $G = I_0(1)/I_1(1) \approx 2.24$.

We compare the obtained expression for the increment (24) with the experimental data shown in Fig. 1 as well as with those given in the review [5]. Let us consider first the experimental data in Fig. 1. But first of all we note that the excitation wavelengths prescribed in the experiment do not correspond to the wavelengths in Fig. 1. For example, an excitation with a wavelength of 18.4 mm is prescribed for a lower jet and the excitation wavelength in the Fig. 1 is of the order of 12 mm.

The same can be seen on the second and third jets. At the second jet the excitation wavelength is 50 mm and the Fig. 1 shows the superposition of a prescribed wavelength and a wavelength close to the resonance one. At the third jet the excitation wavelength is equal to 168 mm and the Fig. 1 shows an evidence of shorter wavelengths, so that the prescribed wavelength does not have time to show itself. However, despite this we'll determine the comparative value of increments of jet decomposition into droplets.

The distance of jet decomposition for all images, as follows from Fig. 1, we will determine by a distance including several excitation wavelengths of the jet N. We assume that the instability increment of the lower jet decomposition in Fig. 1 is equal to γ_1. Then the distance of the lower jet decomposition is determined by the expression $\Delta l_1 = N\lambda_1 \approx V_1/\gamma_1$. The wavelength is $\lambda_1 = 4.6 \cdot 4 = 18.4$ mm and the corresponding wavenumber $X_1 \approx 2\pi \cdot 2/4.6 \cdot 4 = 0.68$.

The distance of the second jet decomposition is determined by the expression $\Delta l_2 = N\lambda_2 \approx V_1/\gamma_2$. The excitation wavelength is $\lambda_2 = 12.5 \cdot 4 = 50$ mm and the corresponding dimensionless wavenumber $X_2 \approx 2\pi \cdot 2/12.5 \cdot 4 = 0.25$.

Then, on the basis of given estimates, the instability increment of the second jet decomposition is smaller than the increment of the lower jet by a factor of $\Delta l_1/\Delta l_2 \approx 4.6/12.5 \approx 0.37$, i.e. is equal to $\gamma_2 \approx \gamma_1 \Delta l_1/\Delta l_2 = \gamma_1 \cdot 0.37$.

For the upper jet the instability increment of jet decomposition is less than the increment of the lower jet by a factor of $\Delta l_1/\Delta l_3 = 4.6/42 \approx 0.11$, i.e. it is equal to $\gamma_3 \approx \gamma_1 \Delta l_1/\Delta l_3 = \gamma_1 \cdot 0.11$ and the dimensionless wavenumber is of the order $X_3 \approx 2\pi \cdot 2/42 \cdot 4 = 0.08$.

If we assume that the lower jet is close to the resonant decomposition into droplets, this means that the value of the dimensionless increment is of the order of the maximum increment (24), which is realized at $X_1 = 0.7$. Numerical calculations show that the maximum increment (24) is reached at $G = 2.24$, which corresponds to the water velocity $V_1 = 12.6\,\text{cm/s}$. Based on the above reasoning we determine from (24) the value of the maximum increment $\gamma_{KG}^{\max} = 0.32479$.

Fig. 3 shows a dependence graph of the instability increment of jet decomposition (curve 1) obtained from the expression for the Rayleigh-Plateau instability increment (3). Dark markers on this graph indicate the values of instability increments obtained on the basis of the experimental data presented in Fig. 1. Light markers in Fig. 3 indicate the experimentally measured points describing the dependence of the dimensionless instability increment $Y(X)$ on the dimensionless wave number X for ideal liquids [5]. The dependence of the dimensionless increment on the dimensionless wavenumber (curve 2) described by expression (24) is presented in Fig. 3 for comparison.

It follows from Fig. 3 that the theoretical model of jet decomposition described by formula (24) with no media viscosity corresponds closely in quantitative sense to the experimental results. Taking account of media viscosity, as follows from the solution of the Kelvin-Helmholtz problem in viscous media [11], can lead to a quantitatively different result.

In the next section we present the solution of the Rayleigh-Plateau problem in the Kelvin-Helmholtz formulation with allowance for the viscosity of both media.
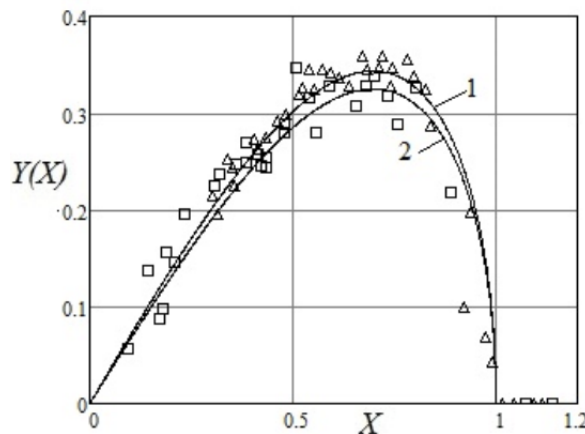
Figure 3. Dimensionless instability increment $Y(X)$ as a function of the dimensionless wavenumber X for ideal liquids. Curve 1 corresponds to the dimensionless increment of Rayleigh-Plateau instability (3), curve 2 is given by expression (24).

TAKING ACCOUNT OF MEDIA VISCOSITY EFFECT ON RAYLEIGH-PLATEAU INSTABILITY IN THE FORMULATION OF THE KELVIN-HELMHOLTZ PROBLEM
Low viscosity media

At dimensionless variables $G = \dfrac{\sigma}{V_1^2 \rho_1 R_0}$, $X = kR_0$, $Y = \omega\sqrt{G}\sqrt{\dfrac{\rho_1 R_0^3}{\sigma}}$ the dispersion equation (21) takes the form:

$$Y^2 + 2i\frac{YX}{\sqrt{G}}\frac{I_1(X)}{I_0(X)}\hat{\mu}_1\left(1 + X\frac{K_0(X)}{K_1(X)}\right) - 2i\frac{X^2}{G}\frac{I_1(X)}{I_0(X)}\hat{\mu}_2\left(1 - X\frac{I_0(X)}{I_1(X)}\right) + \frac{X^2}{G}\left(1 - GX\frac{I_1(X)}{I_0(X)}\right) = 0. \quad (25)$$

where, $\hat{\mu}_1 = \dfrac{\mu_1}{R_0 \rho_1 V_1}$; $\hat{\mu}_2 = \dfrac{\mu_2}{R_0 \rho_1 V_1}$ - dimensionless coefficients of dynamic viscosity of the media 1 and 2, respectively.

The relationship between the dynamic viscosities of air and water $\hat{\mu}_1 \gg \hat{\mu}_2$ and the relationship between velocities of media $V_1^2 \gg V_2^2$ are taken into account in the expression (25).

Using the reasoning of the previous section on ideal water-air jet decomposition we can determine the characteristic parameters of the jet decomposition of viscous water-air media, provided that the ow velocity of water in

the viscous case remains the same as in the ideal case. In numerical calculations of the increment in the expression (25) the following parameter values were chosen: $\widehat{\mu}_1 = 2.17 \cdot 10^{-3}$; $\widehat{\mu}_2 = 3.91 \cdot 10^{-5}$, which correspond to the viscosity of water and air under normal conditions. The numerical analysis (25) shows that taking account of water and air viscosities does not significantly change the value of the instability increment compared with their ideal analogue and the range of unstable wavenumbers remains as before.

Thus, when taking into account the viscosity of water and air, the jet decomposition into droplets is possible within the range of wavenumbers $0 < X \le 1$, which corresponds to the jet diameters. The obtained criterion corresponds to Plato's experimental conclusion that the instability of the jet occurs when the length of the liquid column satisfies the condition $\lambda \ge 3.13 \cdot D$. The maximum increment is equal to $Y(X_1) = 0.32391$, smaller in magnitude than for ideal media $Y(X_1) < \gamma_{KG}^{\max}$ and is achieved for perturbances with a wavelength $X_{\max} = 0.7$.

Thus, the proposed model of decomposition of the viscous fluid jet into droplets corresponds to the experimental data; makes it possible to take into account the effect of viscosity on the jet decomposition velocity and to estimate the characteristic parameters of the process.

As we see, the instability increments in media with low viscosity differ slightly from increments for ideal media. Let us consider the instability of jet decomposition in media with a finite viscosity.

The jet is characterized by a high viscosity and the ambient medium – by a low viscosity

Let us consider the jets whose viscosities are not small. The description of jet instability with the Ohnesorge number $Oh_1 = \mu_1 \rho_1^{-1} \sqrt{\rho_1 / (\sigma R_0)} = 0.58$ [5] by expression (25) shows that the curve with parameters $\widehat{\mu}_1 = 0.39 \gg \widehat{\mu}_2 \approx 7.0 \cdot 10^{-5}$ has the smallest departure from the experimental data. Based on the condition for the development of instability $0 < X \le 1$ an optimal value of the parameter $G = 0.45$ is calculated. Value of the increment determined by the equation (25) relative to the experimental data (curve 2) is shown in Fig. 4.
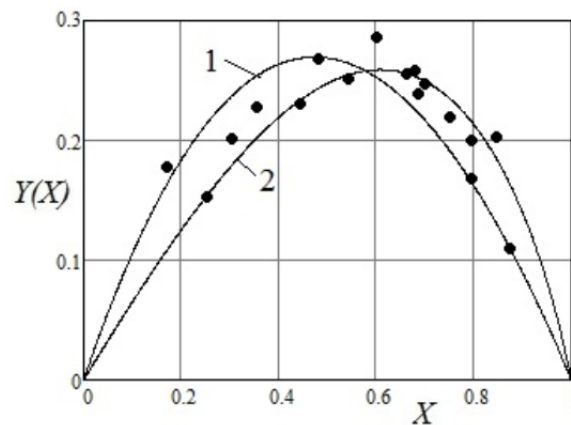
Figure 4. Dimensionless instability increment of decomposition of a viscous liquid jet in the air $Y(X)$ for $Oh_1 = 0.58$ as a function of the dimensionless wavenumber X (curve 1, [3]). Curve 2 corresponds to the increment (25). Experimental points are shown by markers [5].

From the comparison of curves 1 and 2 in Fig. 4 it follows that taking account of the high viscosity of the jet in the expression for the increment (25) makes it possible to describe the experimental results with a sufficiently high degree of accuracy. For liquid densities $\rho_2 \ll \rho_1$ the relationship $Oh_2 \ll Oh_1$ is satisfied. The interval of unstable wavenumbers remains the same $0 < X \le 1$.

The jet and the ambient medium are characterized by a high viscosity

In the case $\widehat{\mu}_1 > \widehat{\mu}_2 \sim 1$ the instability increment is determined by the expression (25), since we believe that $V_1^2 \gg V_2^2$ as before. The result of the numerical calculation of the instability increment of jet decomposition obtained from equation (25) with allowance for viscosity in both media is shown in Fig. 5. The Ohnesorge number $Oh_1 = 0.58$ and the following parameter values are used for calculations:

- $\widehat{\mu}_1 = 1.83$; $\widehat{\mu}_2 = 1.64$, $G = 10$ - follows from the condition for instability development $0 < X \le 1$ (curve 2, Fig. 5);
- $\widehat{\mu}_1 = 1.83$; $\widehat{\mu}_2 = 1.8$, $G = 16$ - follows from the condition for instability development $0 < X \le 1$ (curve 3, Fig. 5).
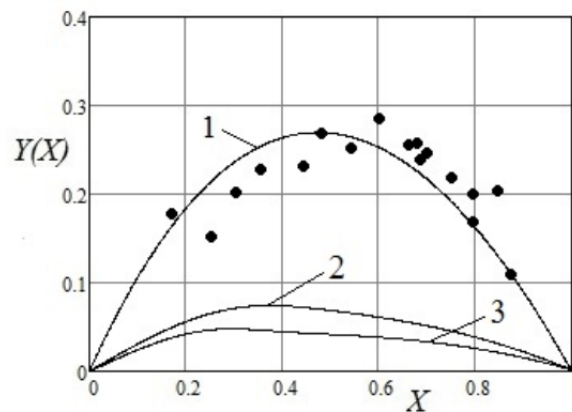
Figure 5. Dimensionless instability increment of viscous fluid jet decomposition in a viscous medium as a function of the dimensionless wavenumber X for $Oh_1 = 0.58$ and parameters: curve 2 - $\hat{\mu}_1 = 1.83$; $\hat{\mu}_2 = 1.64$; curve 3 - $\hat{\mu}_1 = 1.83$; $\hat{\mu}_2 = 1.8$. Curve 1 corresponds to curve 1 of Fig. 4.

From numerical calculations it follows that with the same Ohnesorge numbers for the jet Oh_1 the instability increment decreases with increasing viscosity of the ambient medium $\hat{\mu}_2$. At a constant viscosity of the ambient medium the instability increment is greater there, where the jet viscosity is greater. This conclusion is in contrast to the theoretically obtained conclusion about decrease in the instability increment with increase in the jet viscosity [5]. This contradiction is associated probably with the specificity of the boundary conditions used at derivation of the dispersion equation.

CONCLUSIONS

In this paper the theoretical solution of the Rayleigh-Plateau problem about the instability of a freely falling uid jet is compared with the available experimental results. The mismatch of the theory with the experiment was revealed. In this case taking account of the jet viscosity does not significantly improve the agreement of the theory with the experiment. Therefore, it was proposed to investigate the Rayleigh-Plateau instability in the formulation of the Kelvin-Helmholtz problem with percolation boundary conditions with allowance for the viscosity of the contacting media. A dispersion equation was obtained taking account of the viscosity of both media for percolation boundary conditions. It was shown that for viscous jets and a weakly viscous ambient medium the instability increment describes the experimental results with a sufficiently high degree of accuracy. Numerical calculations show that for jets with the same viscosity the instability increment decreases with increasing viscosity of the ambient medium. If the viscosity of the ambient medium is constant, then the instability increment will be greater where the viscosity of the jet is greater.

ORCID IDs
Oksana L. Andreeva, https://orcid.org/0000-0001-9757-8519; **Leonid A. Bulavin**, https://orcid.org/0000-0002-8063-6441
Viktor I. Tkachenko, https://orcid.org/0000-0002-1108-5842

REFERENCES
[1]   J. Plateau, *Experimental and Theoretical Statics of Liquids Subject to Molecular Forces Only*, (Memoires of the Academy of Belgium, 1873).
[2]   Lord Rayleigh F.R.S., Proc. Lond. Math. Soc. **1-10**(1), 4 (1878), https://doi.org/10.1112/plms/s1-10.1.4.
[3]   J.W. Strutt (Lord Rayleigh), Phil. Mag. **34**(5), 177 (1892), https://doi.org/10.1080/14786449208620301.
[4]   S.K. Aslanov, Technical Physics. The Russian Journal of Applied Physics. **44**, 1386 (1999).
[5]   J. Eggers, E. Villermaux, Rep. Prog. Phys. **71**, 1 (2008), http://dx.doi.org/10.1088/0034-4885/71/3/036601.
[6]   S.O. Shiryaeva, and A.I. Grigoriev, *Электронная библиотека материалов* [*Electronic Library of Materials*], **50**(5), 24 (2014).
[7]   W.V. Ohnesorge, Z. Angew. Math. Mech. **16**, 355 (1936), https://doi.org/10.1002/zamm.19360160611.
[8]   H. Helmholtz, Annalen der Physik, **277**, 641 (1890), https://doi.org/10.1002/andp.18902771202.
[9]   W. Thomson (Lord Kelvin), Phil. Mag. **42**, 362 (1871), https://doi.org/10.1080/14786447108640585.
[10] S. Chandrasekhar, *Hydrodynamic and Hydromagnetic Stability* (Dover publications Inc., New York, 1981).
[11] V.I. Tkachenko, The Journal of Kharkiv National University, physical series "Nuclei, Particles, Fields", **916**, 70-74 (2011), http://dspace.univer.kharkov.ua/handle/123456789/4736. (in Russian)
[12] M. van Dike, *Альбом течений жидкости и газа* [*Album of fluid and gas flows*], (Mir, Moscow, 1986). (in Russian)
[13] D.S. Kuznetsov, *Специальные функции*, [*Special functions*], (Vysshaya shkola, Moscow, 1962). (in Russian)
[14] I.K. Kikoin, (Ed.), *Таблицы физических величин. Справочник* [Tables of physical quantities. Reference book.], (Atomizdat, Moscow, 1976). (in Russian)

ДИСИПАТИВНА НЕСТІЙКІСТЬ РЕЛЕЯ-ПЛАТО
Оксана Л. Андрєєва[a,b]**, Леонід А. Булавін**[c]**, Віктор І. Ткаченко**[a,b]

[a]*ННЦ "Харківський фізико-технічний інститут"*
вул. Академічна, 1, 61108, Харків, Україна
[b]*Харківський Національний університет імені В.Н. Каразіна, Харків, Україна*
пл. Свободи, 4, 61022, Харків, Україна
[c]*Київський Національний університет імені Тараса Шевченка*
вул. Володимирська 64/13, 01601, Київ, Україна

Розглянуто нестійкість струменя рідини, що вільно падає, в повітрі при врахуванні в'язкості середовищ, що контактують. У нехтування в'язкості обох середовищ нестійкість досліджена в роботах Релея і Плато. Вони показали, що нестійкість розвивається в результаті дії поверхневих сил, і виражається в зміні циліндричної форми границі струменя рідини, що вільно падає, з повітрям на послідовність сферичних крапель. У наступних роботах, шляхом феноменологічного врахування в'язкості за допомогою числа Онзагера, показано, що на показники нестійкості впливає в'язкість кожної з контактуючих середовищ. Однак такий метод обліку в'язкості є не зовсім коректним, тому що не враховує специфіку граничних умов, існуючу на кордоні розділу середовищ. В роботі запропоновано використовувати перколяційні граничні умови, правомірність яких доведена на прикладі точного визначення порогової швидкості виникнення нестійкості Кельвіна-Гельмгольца. Для задачі Релея-Плато з перколяційними граничними умовами отримано дисперсійне рівняння, яке описує нестійкість при врахуванні в'язкості обох середовищ. Обґрунтовано дисипативний характер розвитку таких нестійкостей. Визначено інкремент розвитку нестійкості у випадках, коли: струмінь і середовище мають малу в'язкість (ідеальні рідини); струмінь характеризується великою в'язкістю, а навколишнє середовище - малою; струмінь і навколишнє середовище характеризуються великою в'язкістю. Показано, що теоретична модель краплинного розпаду струменя у відсутність в'язкості обох середовищ досить добре, в кількісному відношенні, відповідає експериментальним результатам. Максимальний інкремент дорівнює $\gamma_{KG}^{\max} \approx 0.32$, проти інкремента Релея-Плато $\gamma_{RP}^{\max} \approx 0.34$, для збурень з однаковим хвильовим числом $X_{\max} \approx 0.7$. Показано також, що для вузьких струменів і слабов'язкого навколишнього середовища інкремент нестійкості з досить високим ступенем точності описує експериментальні результати. Числові розрахунки показують, що для струменів з порівняною в'язкістю інкремент нестійкості зменшується з ростом в'язкості навколишнього середовища. У разі, якщо в'язкість навколишнього середовища постійна, то інкремент нестійкості буде більше там, де більше в'язкість струменя. Показано, що результати теоретичних розрахунків добре узгоджуються з наявними експериментальними даними.

КЛЮЧОВІ СЛОВА: нестійкість Релея-Плато, поверхневий натяг, в'язкість, перколяційні граничні умови, дисипативна нестійкість, інкремент нестійкості, хвильове число, інтервал нестійкості.

ДИССИПАТИВНАЯ НЕУСТОЙЧИВОСТЬ РЭЛЕЯ-ПЛАТО
Оксана Л. Андреева[a,b]**, Леонид А. Булавин**[c]**, Виктор И. Ткаченко**[a,b]

[a]*ННЦ "Харьковский физико-технический институт"*
ул. Академическая, 1, 61108, Харьков, Украина
[b]*Харьковский национальный университет имени В.Н. Каразина, Харьков, Украина*
пл. Свободы, 4, 61022, Харьков, Украина
[c]*Киевский Национальный университет имени Тараса Шевченко*
ул. Владимирская 64/13, 01601, Киев, Украина

Рассмотрена неустойчивость свободно падающей струи жидкости в воздухе при учете вязкости контактирующих сред. В пренебрежении вязкостей обеих сред неустойчивость исследована в работах Рэлея и Плато. Они показали, что неустойчивость развивается в результате действия поверхностных сил, и выражается в изменении цилиндрической формы границы свободно падающей струи жидкости с воздухом на последовательность сферических капель. В последующих работах, путем феноменологического учета вязкости посредством числа Онзагера, показано, что на характер неустойчивости влияет вязкость каждой из контактирующих сред. Однако такой метод учета вязкости является не совсем корректным, т.к. не учитывает специфику граничных условий, существующую на границе раздела сред. В работе предложено использовать перколяционные граничные условия, правомерность которых доказана на примере точного определения пороговой скорости возникновения неустойчивости Кельвина-Гельмгольца. Для задачи Рэлея-Плато с перколяционными граничными условиями получено дисперсионное уравнение, которое описывает неустойчивость при учете вязкости обеих сред. Обоснован диссипативный характер развития таких неустойчивостей. Определены инкременты развития неустойчивостей в случаях, когда: струя и среда имеют малую вязкость (идеальные жидкости); струя характеризуется большой вязкостью, а окружающая среда - малой; струя и окружающая среда характеризуются большой вязкостью. Показано, что теоретическая модель капельного распада струи в отсутствие вязкости обеих сред достаточно хорошо, в количественном отношении, соответствует экспериментальным результатам. Максимальный инкремент равен $\gamma_{KG}^{\max} \approx 0.32$, против инкремента Рэлея-Плато $\gamma_{RP}^{\max} \approx 0.34$, для возмущений с одинаковым волновым числом $X_{\max} \approx 0.7$.

Показано также, что для вязких струй и слабовязкой окружающей среды инкремент неустойчивости с достаточно высокой степенью точности описывает экспериментальные результаты. Численные расчеты показывают, что для струй с сравнимой вязкостью инкремент неустойчивости уменьшается с ростом вязкости окружающей среды. В случае, если вязкость окружающей среды постоянна, то инкремент неустойчивости будет больше там, где больше вязкость струи. Показано, что результаты теоретических расчетов хорошо согласуются с имеющимися экспериментальными данными.

КЛЮЧЕВЫЕ СЛОВА: неустойчивость Рэлея-Плато, поверхностное натяжение, вязкость, перколяционные граничные условия, диссипативная неустойчивость, инкремент неустойчивости, волновое число, интервал неустойчивости.

ON THE PERIODIC CHANGE OF THE LUMINOSITY
OF THE COSMIC SOURCES WITH AN ACTIVE MEDIUM

Vitaly V. Kostenko, ⬥Volodymyr M. Kuklin*, ⬥Eugen V. Poklonskiy
V.N. Karazin Kharkiv National University, Kharkiv, Ukraine
Svobody Sq. 4, Kharkiv, Ukraine, 61022
Corresponding Author: kuklinvm1@gmail.com
Received March 22, 2020; accepted March 27, 2020

The presence of an internal layer with an active medium in a hot radiation source is considered, which can be described by a quantum two-level system located near equilibrium. The population of the upper and lower levels is approximately equal. It is shown that during convection from deeper hot layers, which supports the inversion of the populations of the active system, generation of induced radiation pulses is possible, the intensity of which is comparable to or greater than the intensity of the background spontaneous radiation of the source. With a sufficient thickness of the surface layers due to the effects of radiation scattering in them, the emission spectrum of a completely black body may well form there. Pulse generation near a previously detected new threshold of induced radiation can lead to a periodic change in the radiation intensity of the source as a whole. This threshold is determined by the equality of the squared population inversion to the total number of states. The generation of pulses of induced radiation is considered both in Einstein's representation, on the basis of balanced equations, and using a semiclassical description for small values of population inversion and for low levels of electric field intensity, when the Rabi frequency is less than the line width. The description of the induced radiation process is reduced to a one-parameter system of equations. Periodic solutions are represented by closed trajectories on the phase plane (relative density of quanta, relative density of population inversion). A similar layer with an active medium, which can be described by a quantum two-level system located near equilibrium, can exist in stars and is most likely localized in the photosphere. If there is significant convection in the star's atmosphere, conditions can be realized for generating pulses of induced radiation. It turns out that one can see the similarity of the obtained solutions with known observations of changes in the luminosity of Cepheid stars (Cepheus delta and the North Star).
KEYWORDS: pulse generation of induced radiation, convective source of population inversion, periodic change in the luminosity of Cepheid stars.

Spontaneous and induced radiation. In the most general case, particle radiation can be either spontaneous, independent of external influence, or stimulated, imposed by an intense external field [1,2]. Consider a particle that has its own field. If this field or part of it is not able to propagate independently of the particle, accompany the particle, then there is no radiation. If, however, during particle motion, translational or vibrational, the particle field is considered, then under certain conditions there will be a part in it that will be able to propagate independently in the medium. The work of this part of the field on the particle will not be zero and will lead to its deceleration or to a decrease in the amplitude of the oscillations, respectively, which is a sign of the presence of radiation of field energy by the particle [3].

It is also important to note that the value of the work of the particle's own field on its own current is always sign-defined and describes only the radiation process, which is one of the important characteristic features of spontaneous processes. Another characteristic feature of spontaneous emission is the fact that its sources are independent and the radiation process is not imposed by a wave at this frequency existing in a given medium or system [4].

The induced radiation is due to the fact that an external field in the entire interaction space modulates the movement of particles of the medium. In this case, radiation (or absorption) of many particles located at different points in space may well occur in phase with this field. Ch. H. Townes drew attention to this in his Nobel lecture: "... the energy emitted by molecular systems has the same field distribution and the same frequency as the inducing radiation, and, consequently, a constant (possibly zero) difference phases" [5]. Such radiation synchronized by an external field, as well as particle absorption, leads to a sharp increase in the efficiency of interaction between particles and the field. The cause of the induced (stimulated) radiation, as it turned out, is the presence of population inversion (a positive definite difference of particles at higher and lower energy levels) [1].

Formulation of the problem. Consider the radiation source and select in it the layer where the medium is located, capable of generating periodic radiation pulses.

For example, such a layer in stars can be localized in the region of the photosphere. In some cases, there may be several such layers. It is possible to simulate the active zone of this layer by a two-level quantum system, and the populations of these two levels will be considered approximately equal. With a very insignificant excess of the upper level population (the population inversion is positive in this case), in addition to spontaneous emission, the generation of induced radiation is possible, the threshold of which was found in [6,7]. With a sufficient thickness of the overlying layers due to the effects of scattering of radiation emanating from the active zone of the two-level system in them, the emission spectrum of a completely black body may well form there [8].

In addition, we will assume the existence of strong convective flows emanating from layers closer to the hot region of the source of the source, which are capable of introducing a certain fraction of excited atoms of this active substance into the active zone. That is, such convective flows are able to increase the population inversion in the core.

One can verify that the intensity of the induced radiation of a given spectral line, described by a two-level system, can significantly exceed not only the spontaneous intensity of atoms of a given substance, but also the spontaneous emission of the entire spherical source as a whole.

The purpose of this work is to consider the generation of periodic pulses of induced radiation in a heated gas with a fraction of active particles in two states (two-level system). It is important that in a certain active zone of the radiation source, the number of active particles at two energy levels is approximately equal, the population inversion is much less than the total number of particles. Under these conditions, the intensity of the induced radiation is comparable to the intensity of spontaneous emission. It is assumed that in this active zone, which is transparent to radiation at the frequency of the energy transition, due to convection, active particles from the underlying dense layers enter the excited state. That is, in the core there is a source of inverted (excited) active particles.

MODEL OF PULSES GENERATION IN EINSTEIN REPRESENTATIONS

According to the ideas of A. Einstein, the description of the simplest one-dimensional two-level system in the presence of radiation at the transition frequency using the so-called balance equations is as follows [1]:

$$\partial n_2 / \partial t = -u_{21} \cdot n_2 - w_{21} \cdot \mu \cdot N_k, \tag{1}$$

$$\partial n_1 / \partial t = u_{21} \cdot n_2 - w_{12} \cdot \mu \cdot N_k, \tag{2}$$

moreover, the total number of particles of the system in the first and second levels is constant $N = n_2 + n_1 = Const$, u_{21} – is the rate of change in the number of quanta of the second excited level due to spontaneous emission processes, $\mu = n_2 - n_1$ - is the population inversion. The rate of change in the number of quanta (particles) at these levels due to the induced processes of radiation $w_{21} \cdot N_k \cdot n_2$ and absorption $w_{12} \cdot N_k \cdot n_1$. Here N_k is the number of radiation quanta (spectral density) at the transition frequency, for which the equation

$$\partial N_k / \partial t = -\delta_D N_k + u_{21} \cdot n_2 + w_{21} \cdot \mu \cdot N_k. \tag{3}$$

where δ_D – is the decrement of absorption (or radiation loss) of quantum energy. Generally speaking, the relationship between the coefficients u_{21} and w_{21} in the general case can be represented as follows

$$\frac{u_{21}}{w_{21}} = g = \frac{A_{21}}{\hbar\omega \cdot B_{21}} = \frac{2\omega^2}{\pi c^3}, \tag{4}$$

where A_{21} and B_{21} are the corresponding Einstein coefficients. The dimension of this ratio in the three-dimensional case is time per unit volume, since we are talking about the spectral density of quanta. For yellow light the numerical value $g \approx 0.25$, for violet at the edge of the visible spectrum $g \approx 0.6$.

The traditional idea of the instability threshold in neglecting spontaneous processes meets the requirement of positivity of the right-hand side of (3) or, what is the same

$$\mu = \mu_{TH1} = \delta_D / w_{21} \tag{5}$$

One can detect the threshold for the appearance of such radiation due to competition with spontaneous processes at a certain critical value of population inversion μ_{TH2} [6,7]. In the absence of absorption of quantum energy ($\delta_D = 0$), the new threshold for the generation of induced radiation is determined by the relation

$$\mu = \mu_{TH2} \approx (2N)^{1/2} = [2(n_2 + n_1)]^{1/2}. \tag{6}$$

Near this threshold $n_2 \geq n_1 \approx N/2$, the inversion value $\mu << n_2, n_1$ is very small. It is important to note that under these conditions the induced radiation is comparable to spontaneous. Collisions with fast electrons of the medium can provide a transition from the lower energy level of the quantum system to the upper energy level:

$$\partial\mu / w_{21}\partial t = 2[(v - u_{21}) / w_{21}] \cdot n_1 - 2\mu \cdot N_k, \tag{7}$$

where v is the effective frequency of collisions with fast electrons of the medium and $n_2 \approx n_1 \approx N/2$. In this case $v \approx u_{21}$, we can introduce into consideration the quantity

$$2[(v - u_{21}) / w_{21}] \cdot n_1 = \mu_0^2 I_0. \tag{8}$$

where $\mu_0 = \mu(t = 0)$ is some initial population inversion value that exceeds the threshold (6).

The condition $I_0 = 0$ describes the equilibrium state of collisional excitation by free electrons of the main gas of active atoms and their radiative relaxation (due to spontaneous emission). A transition from a higher nonradiative level

(in this case $V \cdot n_1 \approx u_{32} \cdot n_3$) can take an active part in the excitation of the upper working level, then a dark line (absorption line at the frequency of this transition) appears in the spectrum, which allows one to determine the sort of particles and the working levels of the quantum system.

Under the discussed conditions, at various levels of initial inversion both near the threshold (6) and far from it, equations (3), (7) are similar to the Statz-DeMars equations [9], which describe relaxation (that is, damped) oscillations with the establishment of a stationary state. The situation changes if transfer of population inversion from other, for example, inner layers of the radiation source, can occur

$$-V \cdot \partial \mu / \partial x \approx V \cdot \mu / l > 0 , \tag{9}$$

where $-V \cdot \nabla \mu \approx V \cdot \mu \cdot l^{-1}$ it is responsible for convective transfer of inversion with speed V from denser underlying source layers [10].

In these works, it was shown that the inversion flux into the region of the active medium can lead to a change in the relaxation nature of oscillations to periodic. In this case, one can observe the appearance of characteristic sawtooth periodic pulses of induced radiation against the background of the average radiation flux. It is important to note that such pulses occur only under equilibrium conditions $I_0 = 0$ and also in the case of proximity of the generation thresholds (5) and (6), and their repetition rate depends on the quantum absorption decrement δ_D and the rate of change of the inversion due to its transfer. In the discussed models, for convenience of description, the field quanta were divided by origin: $N_k^{(incoh)}$ - the density of the number of quanta of the incoherent radiation field and the density of the number of quanta of the field of induced radiation $N_k^{(coh)}$. The equations describing the generation of sawtooth pulses of induced radiation in a continuous medium can be written in the form [10]

$$\partial N_c / \partial T = M \cdot N_c - \theta \cdot N_c , \tag{10}$$

$$\partial M / \partial T = K \cdot M - 2M \cdot N_c + I_0 , \tag{11}$$

where $M = \mu / \mu_0$, is the relative population inversion, $T = w_{21} \cdot \mu_0 \cdot t$, $N_c = N_k^{(coh)} / \mu_0$ - is the relative number of quanta of induced radiation $\theta = \delta_D / w_{21}\mu_0$, $K = V / w_{21}\mu_0 l$, $N_0 = N / 2\mu_0^2$.

The change in the relative number of quanta of spontaneous emission $N_{inc} = N_k^{(incoh)} / \mu_0$ is described by the equation

$$\partial N_{inc} / \partial T = (N_0 / 2) - \theta \cdot N_{inc} . \tag{12}$$

When $I_0 > 0$, when the collisional excitation is large, the induced radiation is monotonic in nature, in the case of $I_0 < 0$ you can see that there is no induced radiation. That is, the generation of periodic pulses reveals itself only under conditions of equilibrium of the processes of collisional excitation by free electrons of the main gas of active atoms and their radiative relaxation mainly due to spontaneous emission $I_0 = 0$ [10]. In this case, the integrated radiation intensity during the appearance of a pulse can increase several times. It should be noted that the authors of [10] noticed the considered phenomenon only under the condition of equilibrium $I_0 = 0$ and also in the case of proximity of the generation thresholds (5) and (6).

DESCRIPTION OF THE PULSE GENERATION PROCESS USING THE QUASICLASSIC THEORY

With a higher field intensity or with a significant inversion, the induced radiation in a bounded waveguide system should be described by a semiclassical theory [11], where the medium is described quantum mechanically and the electric field in the classical representation. The nature of the process depends on the ratio of the line width of the wave packet to the Rabi frequency, which determines the probabilities of induced radiation or absorption of field quanta [12,13] in each region of the waveguide along its length. With a significant population inversion or in strong fields, the line width can be neglected. For small population inversions and for low electric field intensities, when the Rabi frequency is less than the line width of the wave packet, the behavior of a two-level system is similar to the description of the process presented in [1].

Let us consider a one-dimensional model for perturbations of the electric field, polarization, and population inversion slowly varying with time, which describe the excitation of electromagnetic waves in a two-level active medium, the equations of which can be represented as [11]

$$\frac{\partial^2 E}{\partial t^2} + \delta_D \frac{\partial E}{\partial t} - c^2 \frac{\partial^2 E}{\partial x^2} = -4\pi \frac{\partial^2 P}{\partial t^2} , \tag{13}$$

$$\frac{\partial^2 P}{\partial t^2} + \gamma_{12}\frac{\partial P}{\partial t} + \omega^2 \cdot P = -\frac{2\omega|d_{ab}|^2}{\hbar}\mu E ,$$ (14)

$$\frac{\partial \mu}{\partial t} = \frac{2}{\hbar\omega} < E\frac{\partial P}{\partial t} >,$$ (15)

where the transition frequency ω between the levels corresponds to the field frequency, we neglect the relaxation of the inversion due to external reasons, δ_D is the decrement of field absorption in the medium, and d_{21} is the matrix element of the dipole moment (more precisely, its projection on the direction of the electric field), $\mu = (n_2 - n_1)$ - the population difference per unit volume, n_2 and n_1 - levels populations in the absence of a field, γ_{12} - the width of the spectral line, $N = (n_1 + n_2)$ is the density of the dipoles of the active medium. Fields are represented as $E = [E(t)\cdot\exp\{-i\omega t\} + E*(t)\cdot\exp\{i\omega t\}]$ and $P = [P(t)\cdot\exp\{-i\omega t\} + P*(t)\cdot\exp\{i\omega t\}]$.

Wherein $< E^2 >= 2|E(t)|^2$. The number of field quanta is then determined as $< E^2 > /4\pi\hbar\omega = 2|E|^2/4\pi\hbar\omega = N_c$. Spontaneous emission is absent in this representation, but as shown above, it is not difficult to take into account, for example, using equation (12). For slowly varying amplitudes, the equations

$$\frac{\partial E}{\partial \tau} + \Theta\cdot E = \frac{i}{2}P ,$$ (16)

$$\frac{\partial P}{\partial \tau} + \Gamma_{12}P = -iM E ,$$ (17)

$$\frac{\partial M}{\partial \tau} = K\cdot M + \frac{i}{2}[EP* - E*P] ,$$ (18)

the notation is used here $\mu/\mu_0 = M$, $K = (V/\Omega_0 l)$, and we immediately note that changes in population inversions will be determined by the choice μ_0 and initial conditions, $\Omega_0 = |d_{ab}|\cdot|E_0|/\hbar = |d_{ab}|\cdot[4\pi\omega\cdot\mu_0/\hbar]^{1/2}$ is the Rabi frequency corresponding to the value of the electric field amplitude $|E_0| = [4\pi\hbar\omega\mu_0]^{1/2}$ $E = \dfrac{E(t)}{[4\pi\hbar\omega\mu_0]^{1/2}}$, $P = \dfrac{P(t)}{[4\pi\hbar\omega\mu_0]^{1/2}}\cdot\dfrac{4\pi\omega}{\Omega_0}$, $\tau = \Omega_0 t$, $\Gamma_{12} = \gamma_{12}/\Omega_0$, $\Theta = \delta/\Omega_0$.

At low field intensities or a large line width $\Gamma_{12} = \gamma_{12}/\Omega_0 >> 1$, using the notation $N_c = < E^2 >_c /4\pi\hbar\omega\mu_0$, $M = M = \mu/\mu_0$, $\tau_1 = \Omega_0^2 t/\gamma_{12}$, $K_1 = (V/\Omega_0 l)(\gamma_{12}/\Omega_0)$, $\Theta_1 = (\delta_D/\Omega_0)\cdot(\gamma_{12}/\Omega_0)$, we obtain the system of equations (10) - (11) when the equilibrium condition is satisfied $I_0 = 0$.

That is, it is easy to see that the previous description (10 - (11) corresponds to the equality, whence it follows. You can make the system of equations one-parameter by dividing the right and left parts by and passing to the values, write the equations in the form

$$\frac{\partial M}{\partial \tau_1} = K_1\cdot M - 2M\cdot N_c ,$$ (19)

$$\frac{\partial N}{\partial \tau_1} = M\cdot N_c - 2\Theta_1 N_c ,$$ (20)

That is, it is easy to see that the previous description (10 - 11) corresponds to the equality $T = \tau_1$, whence it follows $w_{21} = \Omega_0^2/\mu_0\cdot\gamma_{12}$. You can make the system of equations one-parameter by dividing the right and left parts by Θ_1^2 and passing to the value $N_c = \Theta_1\cdot N_2$, $M = \Theta_1\cdot M_2$, $\tau_2 = \Theta_1\cdot\tau_1$, $K_1 = \Theta_1\cdot K_2$, write the equations in the form

$$\frac{\partial M_2}{\partial \tau_2} = K_2\cdot M_2 - 2M_2\cdot N_2 ,$$ (21)

$$\frac{\partial N_2}{\partial \tau_2} = M_2\cdot N_2 - 2N_2 ,$$ (22)

where $\tau_2 = \Theta_1 \cdot \tau_1 = \delta_D t$, $M_2 = \dfrac{\mu}{\mu_0} \dfrac{\Omega_0^2}{\delta \cdot \gamma_{12}}$, $N_2 = \dfrac{<E^2>}{4\pi\hbar\omega} \dfrac{\Omega_0^2}{\delta \cdot \gamma_{12}}$.

These equations describe the generation of induced radiation, with the number of quanta per unit volume $N_c = N_k^{(coh)}$, which is the periodic pulses with some constant component.

In addition, there is a spontaneous incoherent component of the same source, the number of quanta of which is equal $N_{inc} = N_k^{(incoh)} / \mu_0$, described, for example, by equation (12). A significant part of the radiation of a quantum source is induced radiation, which is almost monochromatic. However, if the quantum source is surrounded by a fairly extended atmosphere, due to multiple scattering, as noted in [8], the radiation characteristics will approach the radiation characteristics of an absolute black body. The total number of radiation quanta per unit volume is equal to $N = N_{inc} + N_c$, and in spontaneous emission, all types of radiation should be taken into account, and not just the radiation of a quantum source. It is important to note that despite an extremely small population inversion, the intensity of the induced radiation may well exceed the spontaneous intensity.

System (21-22) has a singular point $(2, K_2 / 2)$ and a stationary solution: $M_2 = 2$, $N_2 = K_2 / 2$. In the case of small deviations M_2, N_2 from the singular point, the system can be linearized and the equation for the phase trajectory obtained: $K_2(M_2 - 2)^2 + 8(N_2 - K_2 / 2)^2 = Const$. The phase trajectory turns out to be a closed line, which indicates the presence of stable periodic solutions.

In Figure 1-3 shows the time dependences M_2, N_2 and phase trajectories for different cases of removal from the critical point at $K_2 = 20$. The initial values M_2 for were set constant $M_2(0) = 2$, the choice of the curve was controlled by removing the initial value $N_2(0)$ from its critical value equal to 10.
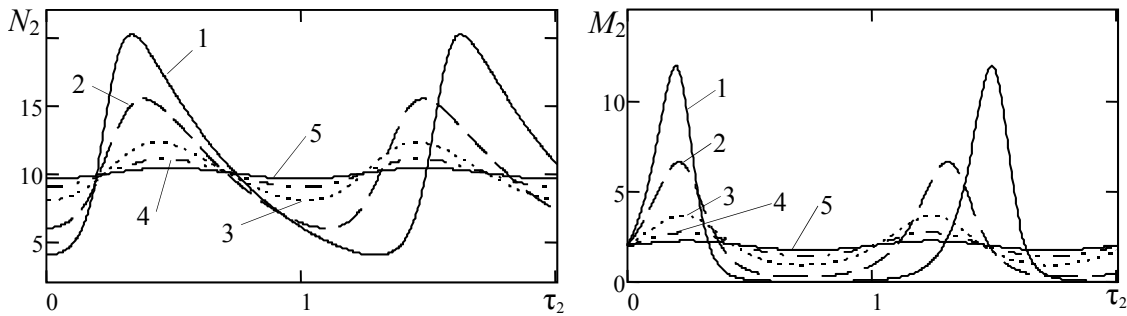
Figure 1. a). The behavior of the relative magnitude of the density of quanta as a function of time τ_2 b) The behavior of the relative density of the inversion of populations as a function of time τ_2, for 1 - $N_2(0) = 4$; 2 - $N_2(0) = 6$; 3 - $N_2(0) = 8$; 4 - $N_2(0) = 9$; 5 - $N_2(0) = 9.6$.
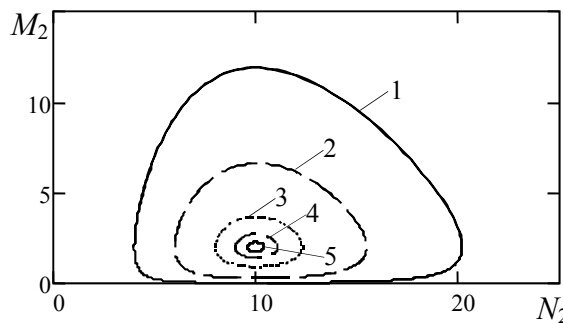
Figure 2. Phase diagrams for the system of equations (21) - (22) when choosing the initial conditions in the form 1 - $N_2(0) = 4$; 2 - $N_2(0) = 6$; 3 - $N_2(0) = 8$; 4 - $N_2(0) = 9$; 5 - $N_2(0) = 9.6$.

For clarity, Table 1 shows the minimum number of quanta $N_{2\min}$ (constant component in the induced radiation), the maximum number of quanta $N_{2\max}$, the average value of the number of quanta N_{2av}, the amplitude of oscillations $N_{2\max} - N_{2\min}$, and the period of oscillations T_2. It should be noted that the average value of the relative number of quanta N_{2av} depends only on the choice of the position of the center of the diagram - its critical value $K_2 / 2$.

The graph of the number of quanta N_2 changes has the form of a sinusoid for phase trajectories near the critical point (calculation 4 and 5). For phase trajectories far from the critical point (calculations 1, 2), the change graph N_2

takes the form of a saw: a sharp increase and a slow decrease. Such behavior is characteristic of the Cepheid luminosity, where fusion has reached its ultimate element – iron: significant sawtooth fluctuations in the luminosity of the Cephei delta and small sinusoidal oscillations of the North Star.

Table 1.

The results of the solution of equations (21)-(22)

N data	$N_{2\min}$	$N_{2\max}$	N_{2av}	$N_{2\max} - N_{2\min}$	T_2
1	4	20,188	10	16,188	1,289
2	6	15,474	10	9,474	1,0964
3	8	12,308	10	4,308	1,0147
4	9	11,071	10	2,071	0,9984
5	9,635	10,374	10	0,739	0,9941

ABOUT POSSIBLE APPLICABILITY OF THE MODEL

Indeed, such a generation may well occur in cosmic conditions, where their radiation is generated in the photosphere of stars. The presence of pulsations is possible if the conditions are met in the presence of convection, which ensures the delivery of inverted atoms of the active substance from the dense underlying layers, that is $-v \cdot \partial\mu / \partial x \approx v \cdot \mu / l$, convection should be quite intense $(v / l \cdot w_{21}) > \mu_{TH2}$. We show that the above-considered model of generation of pulses of induced radiation can be useful for describing a periodic change in the luminosity of Cepheid stars.

As noted above, N_2 can describe the generation of induced radiation, for example, in the photosphere of stars, which is a pulse with a certain constant component. In addition, there is a spontaneous incoherent component of the same source. To this radiation, it is necessary to attach the constant radiation of the rest of the heated material of the star, i.e. the total emission of the star takes the form

$$N(\tau) = N_b + N_2(\tau) \tag{23}$$

The value of the constant component N_b (the spontaneous incoherent component of a quantum source and the constant radiation of the rest of the warmed matter of the star) must be added to N_2. This addition can be estimated by knowing the relationship between the maximum and minimum luminosity of a star $k = (N_b + N_{2\max}) / (N_b + N_{2\min})$, on the other hand, the ratio of the maximum and minimum luminosities of a star is $k = L_1 / L_2 = 10^{0,4(m_2 - m_1)}$ [14], here m_1 is the apparent magnitude at the maximum luminosity of the star, m_2 - at the minimum luminosity. Below we will focus on the values of the apparent magnitude obtained from observations. Using the known apparent magnitude m, knowing the distance to the star d in parsec, we can calculate the luminosity [14]:

$$m = M_{l\odot} + 5\lg(d/10) - 2.5\lg(L). \tag{24}$$

To compare the luminosities of stars with each other, the absolute magnitude (apparent magnitude from a distance of 10 parsecs) $M_l = m - 5\lg(d/d_0)$, $d_0 = 10$ is used, d here is the distance in parsecs to the star, $d = 273$ for the Cephei delta and $d = 133$ for the North Star. Then the luminosity of the star in units of the luminosity of the Sun is equal to $L = 10^{0,4(M_\odot - M)} L_\odot$, $L_\odot = 1$, where $M_{l\odot} = 4.77$ is the absolute magnitude of the Sun. To obtain the dependence of the luminosity of the star on time $L(\tau)$, we multiply (23) by the coefficient A, i.e.

$$L(\tau) = A \cdot N(\tau) = A \cdot [N_b + N_2(\tau)]. \tag{25}$$

Table 2 shows the calculation results for the Cepheus delta and the North Star. For this, the values of Table 1 are taken from the first and fifth rows.

Table 2

The calculation results for the Cepheus delta and the North Star

Stars	m_1	m_2	k	$N_{2\min}$	$N_{2\max}$	N_{2av}	N_b	A	L_1	L_2
Cephei delta	3.48	4.37	2.27	4	20,188	10	8.748	84.507	2445.3	1077.3
North Star	2.092	2.125	1.031	9,635	10,374	10	14.315	84.412	2084	2021.6

You can make sure that the average value $\overline{L}$ is determined by the formula

$$\overline{L} = A \cdot \left(N_{2av} + N_b \right). \tag{26}$$

Fig. 4a and Fig. 4b show the time dependences of the number of quanta and the corresponding luminosity of the Cephei delta and the North Star. The bottom curve is the number of quanta of induced radiation. The upper curve takes into account the constant component of spontaneous emission due to other elements of the radiation source, in addition to the quantum system.
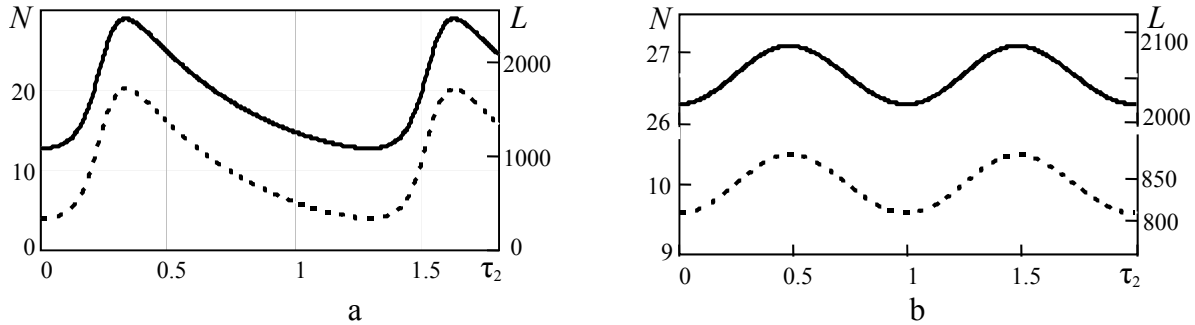
Figure 4. Time dependences of the relative number of quanta (left scale) and the corresponding luminosity (right scale) of the Cephei delta (a) and the North Star (b).

The lower curve on each fragment represents the number of quanta of induced radiation. The upper curve takes into account the constant component of spontaneous emission due to other elements of the radiation source, in addition to the quantum system.

Fig. 5 and Fig. 6 below show the change in the stellar magnitude of the star of the Cepheus delta [15] and the North Star with time [16]. The ordinate shows the values of the apparent magnitude, while the abscissa shows time in fractions of the period of change in the brightness of the star.
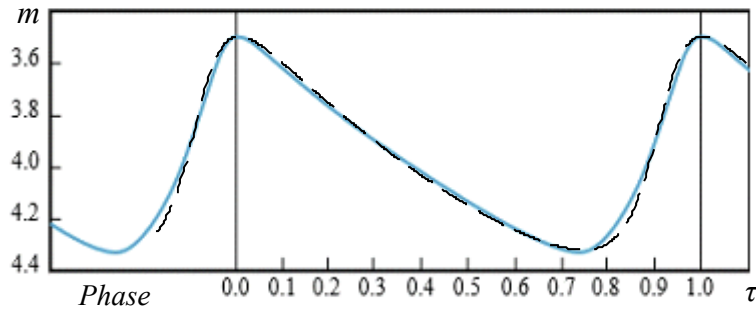
Figure 5. The change in the stellar magnitude of the star of the Cepheus delta with time. (solid curve received in the 1930s N.F. Florey using a visual photometer) see, for example, [17] and the solution of equations of system (21) - (22) in the same variables when choosing the level of spontaneous emission and scales (dashed line).
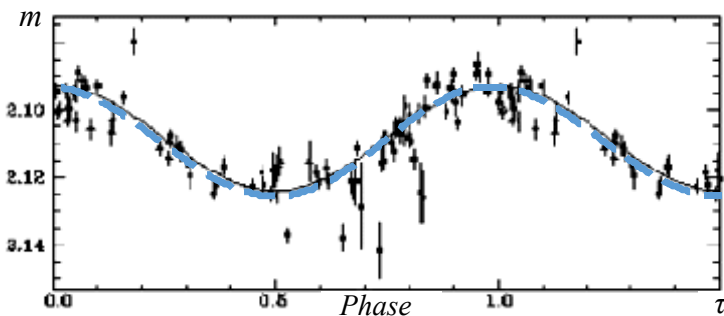
Figure 6. The change in the magnitude of the North Star with time. (solid curve) and the solution of the equations of system (20) - (21) in the same variables when choosing the level of spontaneous emission and scales (dashed line).

CONCLUSIONS

The state of a gas radiation source close to equilibrium under collisional excitation by free electrons of the main gas of active atoms and their radiative relaxation due mainly to spontaneous emission was considered [10]. In such a medium, for a two-level system, when the population inversion is much less than the total number of states, there are conditions for the generation of pulses of induced radiation.

Moreover, the intensity of such pulses is comparable with the intensity of spontaneous emission of the system. It was shown earlier that during convection from deeper hot layers, which supports (is the source) the population

inversion of the active system, it is possible to generate periodic pulses of induced radiation, the intensity of which is comparable to or greater than the intensity of the background spontaneous radiation of the source [10]. With a sufficient thickness of the surface layers due to the effects of scattering of radiation in them, the emission spectrum of a completely black body may well form there [8].

Pulse generation near a previously detected new threshold of induced radiation [10] under the conditions of such convection can lead to a periodic change in the radiation intensity of the source as a whole. This threshold is due to competition between spontaneous and induced radiation, which weaken the population inversion and is determined by the equality of the square of the population inversion to the total number of states. A consideration of the generation of pulses of induced radiation in the present work is carried out both using Einstein's balanced equations and on the basis of a semiclassical description for small population inversions and at low levels of electric field intensity, when the Rabi frequency is less than the width of the radiation line.

It is shown in the paper that the description of the induced radiation process reduces to a one-parameter system of two equations (21) - (22). Periodic solutions are represented by closed trajectories on the phase plane (relative density of quanta, relative density of population inversion). A similar layer with an active medium, which can be described by a quantum two-level system located near equilibrium, can exist in stars and is most likely localized in the photosphere. If there is significant convection in the star's atmosphere, conditions can be realized for generating pulses of induced radiation. It turns out that one can see the similarity of the obtained solutions with the well-known observations of changes in the luminosity of Cepheid stars (Cepheus delta and the North Star). Moreover, the ratio of periods of change in luminosity is (according to table 1.) also similar (accurate to 2.5%). It is important to note that the solutions of equations (21) - (22) for these two cases are on the same diagram in Fig. 3, which corresponds to one type of object. As well as small amplitude Cepheids (DCEPS) of the North Star type, they belong to the class of classical Cepheids, the brightest representative of which is the Cepheus delta.

ORCID IDs
Volodymyr M. Kuklin, http://orcid.org/0000-0002-0310-1582; **Eugen V. Poklonskiy**, https://orcid.org/0000-0001-5682-6694

REFERENCES
[1] A. Einstein, Mitteilungen, D. Phys. Ges. Zürich **18**, 47–62 (1916); Phys. Z. **18,** 121-128 (1917); UFN **86** (3)**,** 371–411 (1965), https://doi.org/10.3367/UFNr.0086.196507b.0371, in https://ufn.ru/ru/articles/1965/7/b/, (in Russian).
[2] R. Ladenburg, Rev. Mod. Phys. **4,** 243-260 (1933); UFN **14** (6)**,** 721–741 (1934), https://doi.org/10.3367/UFNr.0014.193406b.0721, in https://ufn.ru/ru/articles/1934/6/b/, (in Russian)
[3] L.D. Landau, and E.M. Livshits, *Electrodynamics of continuous media*. (Moscow, GIFLML, 1959), pp. 532, (in Russian).
[4] V.L. Ginzburg, UFN, **140** (4), 687–698 (1983), (in Russian)
[5] Ch.H. Townes, Science, **149** (3686), 831-841 (1965), https://doi.org/10.1126/science.149.3686.831; UFN. **88** (3), 461–483 (1966), (in Russian).
[6] A.G. Zagorodny, and V.M. Kuklin, in: *High-power pulsed electrophysics. International conference XIV Khariton's topical scientific readings. Digest of technical papers* (Sarov, 2013), pp. 38-43, (in Russian)
[7] A.V. Kirichok, V.M. Kuklin, A.V. Mischin, A.V. Pryjmak, and A.G. Zagorodny, VANT. Ser.: Plasma Electronics and New Methods of Acceleration, **4** (77), 267-271 (2013).
[8] S.B. Pickelner, *Atmospheres of stars*, (Physics of Space, 1986), http://www.astronet.ru/db/msg/1179555, (in Russian)
[9] C.L. Statz, and G. DeMars, *Quantum Electronics*, (N.Y., Columbia Univ. Press, 1960), pp. 530.
[10] A.V. Kirichok, V.M. Kuklin, and A.G. Zagorodny, VANT. Ser.: Plasma Electronics and New Methods of Acceleration, **4** (80), 9-11 (2015), https://arxiv.org/pdf/1610.04628v1.
[11] P.S. Landa, *Self-oscillations in distributed systems*, (Moscow, Nauka, 1983), pp. 320, in Russian
[12] A.S. Davydov, Quantum mechanics, (Fizmatgiz, Moscow, 1963), pp. 748, in Russian
[13] L. Allen, J. Eberly, *Optical resonance and two-level atoms*. (New York, Wiley-Interscience, 1975), pp. 222.
[14] A.S. Rastorguev, *Lectures on Galactic Astronomy*, in http://www.astronet.ru/db/msg/1228262, in Russian
[15] J. Kaler, *Stars and stars of the week*, (University of Illinois), in http://stars.astro.illinois.edu/sow/deltacep.html
[16] J. Kaler, *Stars and stars of the week*, (University of Illinois), in http://stars.astro.illinois.edu/sow/polaris.html
[17] N.N. Samus, and O.V. Durlevich, *GCVS - General Catalog of Variable Stars*, (Institute of Astronomy of Russian Academy of Sciences, Sternberg State Astronomical Institute of the Moscow State University), in: http://heasarc.gsfc.nasa.gov/W3Browse/all/gcvs.html.

ПРО ПЕРІОДИЧНІ ЗМІНИ СВІТНОСТІ КОСМІЧНИХ ДЖЕРЕЛ З АКТИВНИМ СЕРЕДОВИЩЕМ
В.В. Костенко, В.М. Куклін, Є.В. Поклонський
Харківський національний університет імені В.Н. Каразіна, Харків, Україна
пл. Свободи 4, Харків, Україна, 61022

Розглянуто наявність в гарячому джерелі випромінювання внутрішнього шару з активним середовищем, що знаходиться поблизу рівноваги і представлено квантовою дворівневою системою, населеністі верхнього і нижнього рівнів якої приблизно однакові. Показано, що при конвекції з більш глибоких гарячих шарів, яка підтримує інверсію населеністі активної системи, можлива генерація імпульсів індукованого випромінювання, інтенсивність яких порівнянна або

перевершує інтенсивність фонового спонтанного випромінювання джерела. При достатній товщині поверхневих шарів за рахунок ефектів розсіювання в них, там цілком може сформуватися спектр випромінювання абсолютно чорного тіла. Генерація імпульсів поблизу виявленого раніше нового порога індукованого випромінювання здатна привести до періодичної зміни інтенсивності випромінювання джерела в цілому. Цей поріг визначається рівністю квадрату інверсії населеності повному числу станів. Розгляд генерації імпульсів індукованого випромінювання проводиться як на основі балансних рівнянь, так і за допомогою напівкласичного опису при невеликих значеннях інверсії населеності і при низьких рівнях інтенсивності електричного поля, коли частота Рабі менше ширини лінії. Опис процесу індукованого випромінювання зводиться до однопараметричної системі рівнянь. Періодичні рішення представлені замкнутими траєкторіями на фазової площині (відносна щільність квантів, відносна щільність інверсії населеністі). Подібний шар з активним середовищем в вигляді квантової дворівневої системи може існувати в зірках і швидше за все локалізован в області фотосфери. При наявності в атмосфері зірки значною конвекції можуть бути реалізовані умови для генерації імпульсів індукованого випромінювання. Виявляється, що можна побачити подібність отриманих рішень з відомими спостереженнями змін світності зірок-цефеїд (дельти Цефея і Полярної зірки).

КЛЮЧОВІ СЛОВА: генерація імпульсів індукованого випромінювання, конвективне джерело інверсії населеністі, періодична зміна світності зірок-цефеїд.

О ПЕРИОДИЧЕСКОМ ИЗМЕНЕНИИ СВЕТИМОСТИ КОСМИЧЕСКИХ ИСТОЧНИКОВ С АКТИВНОЙ СРЕДОЙ

В.В. Костенко, В.М. Куклин, Е.В. Поклонский
Харьковский национальный университет имени В.Н. Каразина, Харьков, Украина
пл. Свободы 4, Харьков, Украина, 61022

Рассмотрено наличие в горячем источнике излучения внутреннего слоя с активной средой, которую можно описать находящейся вблизи равновесия квантовой двухуровневой системой, населенность верхнего и нижнего уровней которой примерно равна. Показано, что при конвекции из более глубоких горячих слоев, которая поддерживает инверсию населенностей активной системы, возможна генерация импульсов индуцированного излучения, интенсивность которых сравнима или превосходит интенсивность фонового спонтанного излучения источника. При достаточной толщине поверхностных слоев за счет эффектов рассеяния в них излучения, там вполне может сформироваться спектр излучения абсолютно черного тела. Генерация импульсов вблизи обнаруженного ранее нового порога индуцированного излучения способна привести к периодическому изменению интенсивности излучения источника в целом. Этот порог определяется равенством квадрата инверсии населенностей полному числу состояний. Рассмотрение генерации импульсов индуцированного излучения проводится как в представлении Эйнштейна, на основе балансных уравнений, так и с помощью полуклассического описания при небольших значениях инверсии населенностей и при низких уровнях интенсивности электрического поля, когда частота Раби меньше ширины линии. Описание процесса индуцированного излучения сводится к однопараметрической системе уравнений. Периодические решения представлены замкнутыми траекториями на фазовой плоскости (относительная плотность квантов, относительная плотность инверсии населенностей). Подобный слой с активной средой, которую можно описать находящейся вблизи равновесия квантовой двухуровневой системой может существовать в звездах и скорее всего локализован в области фотосферы. При наличии в атмосфере звезды значительной конвекции могут быть реализованы условия для генерации импульсов индуцированного излучения. Оказывается, что можно увидеть подобие полученных решений с известными наблюдениями изменениями светимости звезд-цефеид (дельты Цефея и Полярной звезды).

КЛЮЧЕВЫЕ СЛОВА: генерация импульсов индуцированного излучения, конвективный источник инверсии населенностей, периодическое изменение светимости звезд-цефеид.

INCOMMENSURATE CRYSTALLIZATION OF NEUTRON MATTER IN NEUTRON STARS

Kapil M. Khanna*, **David K. Kandie,** **Joel K. Tonui,** **Hezekiah K. Cherop**

Department of Physics, University of Eldoret
P.O. Box 1125-30100, Eldoret, Kenya
*Corresponding Author: Khannak700@gmail.com

The composition of the neutron stars from its surface region, outer-core, inner-core, and to its center is still being investigated. One can only surmise on the properties of neutron stars from the spectroscopic data that may be available from time to time. A few models have suggested that the matter at the surface region of the neutron star is composed of atomic nuclei that get crushed under extremely large pressure and gravitational stress, and this leads to the creation of solid lattice with a sea of electrons, and perhaps some protons, flowing through the gaps between them. Nuclei with high mass numbers, such as ferrous, gold, platinum, uranium, may exist in the surface region or in the outer-core region. It is found that the structure of the neutron star changes very much as one goes from the surface to the core of the neutron star. The surface region is extremely hard and very smooth. Surface irregularities are hardly of the order of 5 mm, whereas the interior of the neutron star may be superfluid and composed of neutron-degenerate matter. However, the neutron star is highly compact crystalline systems, and in terrestrial materials under pressure, many examples of incommensurate phase transitions have been discovered. Consequently, the properties of incommensurate crystalline neutron star have been studied. The composition of the neutron stars in the super dense state remains uncertain in the core of the neutron star. One model describes the core as superfluid neutron-degenerate matter, mostly, composed of neutrons (90%), and a small percentage of protons and electrons (10%). More exotic forms of matter are possible, including degenerate strange matter. It could also be incommensurate crystalline neutron matter that could be BCC or HCP. Using principles of quantum statistical mechanics, the specific heat and entropy of the incommensurate crystalline neutron star has been calculated assuming that the temperature of the star may vary between $10^6 K$ to $10^{12} K$. Two values for the temperature T that have been arbitrarily chosen for which the calculations have been done are $1.7 \times 10^6 K$ and $1.7 \times 10^{10} K$. The values of specific heat and entropy decrease as the temperature increases, and also, their magnitudes are very small. This is in line with the second law of thermodynamics.

KEYWORDS: terrestrial materials, incommensurate phase, incommensurate crystalline neutron star, superfluid, neutron-degenerate matter

An incommensurate quantum solid or crystalline solid is one that need not to have an integer number of atoms per unit cell [1]. For an HCP (Hexagonal Close Packed) lattice of volume V and lattice constant "*a*", the number of lattice sites N_s is written as,

$$N_S = V \frac{\sqrt{2}}{a^3} \tag{1}$$

If in the ground state the crystal is incommensurate, then its number N of atoms differs from its number of sites N_s such that $N \neq N_s$. To know how incommensurate the ground state actually is for the quantum solid, it is essential to know or measure the density and lattice constant "*a*" precisely and simultaneously. If the incommensurability is denoted by ε, then it is defined as,

$$\varepsilon = \frac{N_S - N}{N_S}, \quad (N_s > N) \tag{2}$$

The quantity ε is defined as the net fractional vacancy number. If ε_0 is the value of ε at absolute zero temperature, and δ is the change in the incommensurability away from its ground state value (ε_0), then,

$$\varepsilon = \varepsilon_0 + \delta \tag{3}$$

Staying at $T = 0$, the incommensurability is changed away from its ground state value (ε_0) by changing the number of lattice sites and consequently changes in lattice constant "*a*". Thus, if E_0 is the ground state energy, then E may be the harmonic increase in the crystal energy, when the crystal temperature stays at $T = 0$. At the ground state, (ε_0), $\delta = 0$, since $\varepsilon = \varepsilon_0$.

If however, the ground state of the crystalline state is commensurate, then there will be exactly one atom per lattice site $(N = N_S)$, and hence $\varepsilon = 0$. In fact, the value of ε depends on the magnitude of the difference between the

number of atoms (N) and the number of sites (N_s). It is well known that in the ground state of solid $_2^4He$, the difference in N and N_s is around 1%, whereas in the neutron stars it could be as much as 10% since in the crystalline state of the neutron stars, there could be roughly 10% protons and electrons, and the rest 90% could be neutrons. The structure of crystalline solids is based on a periodic repetition of a certain basic arrangement of atoms. In many solids or materials, this basic arrangement shows vibrations, which are also periodically repeated. If the periodicities of the repetition of the basic (structure) arrangement and that of the variation of this arrangement are commensurate, a super structure results. However, if there do exist solids where the periodicity of the repetition of the basic arrangement and that of its variations are not commensurate, in that case one gets an incommensurate or modulated structure [2, 3, 4a, 4b].

Neutron stars have overall densities of $3.7 \times 10^{17} kgm^{-3}$ to $5.9 \times 10^{17} kgm^{-3}$ which means 2.6×10^{14} to 4.1×10^{14} times the density of the Sun [5]. The density of $3.7 \times 10^{17} kgm^{-3}$ derives from mass $2.68 \times 10^{30} kg / volume$ of star of radius $12 km$ and $5.9 \times 10^{17} kgm^{-3}$ is derived from mass $4.2 \times 10^{30} kg / volume$ of star of radius $11.9 km$. These densities are comparable to the approximate density of an atomic nucleus which is of the order of $3 \times 10^{17} kgm^{-3}$. The neutrons star's density varies roughly from $1 \times 10^9 kgm^{-3}$ in the crust, then increases with depth to about 6×10^{17} or $8 \times 10^{17} kgm^{-3}$ (denser than the atomic nucleus) deeper inside the neutron star (the core of the neutron star) [6].

In terrestrial materials under pressure, many examples of incommensurate phase transitions have been discovered [4a]. Hence, we decided to study the properties of an incommensurate crystalline neutron star. It is still not known exactly whether the crystalline structure is BCC or HCP, and whether it is in the crust or interior (core) or both. However, it will be easier to study experimentally the neutron star crusts as compared to the study of the core or interior of the neutron star.

In neutron stars, which are very high density systems, an essential new concept will be the Fermi energy E_F. The quantum mechanical way to think about it is in terms of the uncertainty principle [7], which is expressed as,

$$\Delta x \Delta p = \hbar \qquad (4)$$

and thus in a dense system, like the neutron star, there is a finite momentum, and hence there is the definite energy associated with the confinement. Therefore, squeezing the neutron star increases its total energy, and hence the Fermi energy E_F acts as the pressure – called the degeneracy pressure. Now at the densities of neutron star, i.e., $\rho > 6 \times 10^{15} gcm^{-3}$ or so, the electrons are highly relativistic, whereas the neutrons and protons are $(m_N \cong m_P \cong 1837 m_e)$ slightly less relativistic since these are heavy particles when compared to the electrons. At very high densities, the neutron star has a smooth distribution of neutrons, plus a $5-10\%$ smattering of protons and electrons. Since the number of neutrons is comparatively very large, the neutron Fermi energy could become very high enough such that the other particles like protons and electrons could appear as separate entities. The composition of the super dense neutron star remains uncertain in the core of the neutron star. One model describes the core as superfluid neutron – degenerate matter, mostly composed of neutrons, and a small percentage (10%) of protons and electrons. More exotic forms of matter are possible, including degenerate strange matter [8a]. In the crystalline state, the neutron star is assumed to be composed of some 90% neutrons, and 10% protons. It is also surmised that when the temperature of the neutron star is $T = 100 KeV = 11.5942 \times 10^8 K$, the proton fraction (F_p) could have different values at different densities of the neutron star. It is proposed that F_p increases as the density ρ of the neutron star increases [8a]. This means that the neutron star in such a crystalline state is incommensurate, and this means that the number of sites (N_s) for the neutrons is more than the number of neutrons (N). If the number of neutrons is 90%, then 10% of the sites will be occupied by the protons. The incommensurability for neutrons and protons will be given by Eq.(2). Keeping this in mind, a theory is developed for the incommensurate neutron star, and its thermodynamic properties, especially specific heat (C_v) and entropy (S) are calculated.

SIGNIFICANCE OF THE RESEARCH WORK

Although several equations of state have been proposed, the exact equation of state for neutron star is still not known. Similarly, the exact composition of the neutron star from its surface region to the core is still not known. Some models indicate that the matter at the surface of the neutron star is composed of ordinary atomic nuclei crushed into a solid lattice with a sea of electrons flowing through the gaps between them, and there could also be some protons. Nuclei with very high binding fraction such as iron could exist in the surface region. The structure of the neutron star varies drastically and characteristically from the extremely hard and very smooth (with maximum surface irregularities of approximately 5mm) surface to the inner crystalline crust and core of the neutron star. Proceeding inwards, one can encounter superfluid neutron-degenerate matter, mostly composed of neutrons, some protons and electrons. Although

the inner crust and core have very high temperatures, of order of $10^7 K$ to $10^{10} K$; extremely high density results in extremely high gravitational field or stress, and extremely high pressure; and all put together can result in a crystalline structure of the neutron star with 90% neutrons and 10% protons. It is also not known exactly whether the outer crust and the inner crust are BCC or HCP and there are suggestions that the proton fraction could be more than 10%. Since the neutron star assumed to be composed of 90% of neutrons, 10% protons, is very compact, has very large density, has very large or extremely large gravitational stress and pressure; it can be safely assumed that it may be an incommensurate crystalline structure. It was therefore decided that, the crystalline state of a neutron star with 90% neutrons and 10% protons be studied to understand some thermodynamic properties of the neutron star, such as specific heat and entropy. A crystalline structure of this type is called incommensurate, and in this, the number of sites and the number of occupants of the sites are not equal, rather, the number of sites is more than the number of occupants [6, 8a, 8b, 8c, 8d].

The theory of quantum statistical mechanics; the method of calculating the activation energy of vacancy formation in crystalline neutron star, have been used to study the problem and the principles of thermodynamics have been used to calculate the specific heat (C_v), and the entropy (S), of the incommensurate crystalline state of the neutron star.

THE THEORY OF INCOMMENSURATE CRYSTALLINE NEUTRON STAR

A neutron star's almost incompressible structure results in very large density, even more than nuclear density, and this causes protons and electrons to combine into neutrons, the process that gives such stars their name. The composition of the cores of the neutron stars is still not exactly known, but they may consist of a neutron superfluid or some unknown state of matter, or have some crystalline structure [9, 10a, 10b].

It is possible that not all the neutrons may become part of the crystalline state of a neutron star. There may be some free neutrons whose lifetime may be about 15 minutes, and they can decay as,

$$n \rightarrow p + e^- + V_e \tag{5}$$

where, n = neutron, p = proton, e^- = electron or β-particle and V_e = neutrino associated with negative electron emission.

This shows that due to the β – decay, there will be electrons and protons in addition to the neutrons in the neutron star. The electron number density and the proton number density are small compared to the neutron number density [11]. The maximum number density of the protons cannot be more than $1/8$ of the total number of density in the neutron star [12]. Thus, it can be assumed that the crystalline state of a neutron star is incommensurate, i.e., the number of sites N_s is not equals to the number of neutrons, and that $N_S > N$.

It is to be emphasized that in terrestrial materials under pressure, many examples of in-commensurate phase transitions have been discovered [13]. Information so far indicates the existence of BCC structure in the crust of the neutron star. It is still not exactly known whether in the interior of the neutron star, the structure is BCC or HCP. However, it is easier to study experimentally the neutron star crust compared to the interior of the neutron star [14]. It seems quite certain that both the crust and the interior of the neutron star are in the crystalline state such that there may be 90% neutrons and 10% protons that may occupy the crystal sites, and hence the neutron star will be in the incommensurate crystalline state. Hence, we consider a crystalline system composed of 90% neutrons and 10% protons. For the lattice system for protons, only 10 out of 100 lattice sites will be occupied, the rest will be empty. Similarly for the lattice system for neutrons, 90 out of 100 lattice sites will be occupied, the rest will be empty. However, in the crystalline state, the difference between the neutrons and protons will be assumed to disappear, and even if they are at the same lattice site, they can co-exist on the same lattice site without disturbing each other or the rest of the system, or the particles on the rest of the lattice sites.

It is well known that in the crystalline state or a quantum solid, the system is intrinsically restless, and the energy it possesses is the zero-point energy that is calculated using the Heisenberg's Uncertainty principle [15,16]. In this manuscript, the crystalline state is assumed to be incommensurate such that the number of neutrons N_n is less than the number of sites (N_s) and also the number of protons (N_p) is less than N_s. Thus the ground state of the quantum state is incommensurate such that $N_n < N_s$ and $N_p < N_s$. The energy of such a system is calculated in this manuscript using the principles of quantum statistical mechanics.

Now we will write the incommensurability constant, ε_p for protons as,

$$\varepsilon_p = \frac{N_s - N_p}{N_s} \tag{6}$$

and the incommensurability constant, ε_n, for neutrons as,

$$\varepsilon_n = \frac{N_s - N_n}{N_s} \tag{7}$$

By definition ε_p and $\varepsilon_n \neq 1$, they are both less than 1 $(\varepsilon_p < 1, \varepsilon_n < 1)$. It is also assumed that there is no disorder (in the crystalline state) and no inter site interaction in the crystalline state. This would mean that the particles and sites can be freely permuted. The number of ways we can permute particles and sites will then be $(N_s + N_p + N_n)!$. Since in the crystalline state, the distinction between protons and neutrons is lost, permutation among them must be excluded by dividing by $(N_p + N_n)!$.

Similarly, the permutations among identical sites must also be excluded by dividing by $N_s!$. Thus the number of ways in which neutrons and protons can be distributed among the sites is given by P, such that,

$$P = \frac{\left(N_s + N_p + N_n\right)}{\left(N_s\right)\left(N_p + N_n\right)!} \tag{8}$$

Hence the statistical count, C, for the incommensurability of neutrons and protons in the crystalline neutron matter in a neutron star is,

$$P = \prod_S \frac{\left(N_s + N_p + N_n\right)}{\left(N_s!\right)\left(N_p + N_n\right)!} \tag{9}$$

Taking logarithms of both the sides, we can write,

$$\log C = \log \prod_S P = \log \prod_S \frac{(N_s + N_p + N_n)!}{(N_s!)(N_p + N_n)!}$$

$$= \sum_s \left[\log(N_s + N_p + N_n)! - \log N_s! - \log(N_p + N_n)! \right] \tag{10}$$

For large N, Stirling's theorem gives,

$$\log N! = N \log N - N \tag{11}$$

Using Eq. (11) in Eq. (10) and simplifying, we get,

$$\log C = \sum_s [(N_s + N_p + N_n)\log(N_s + N_p + N_n) - N_s \log N_s - (N_p + N_n)\log(N_p + N_n)] \tag{12}$$

Now we assume that N_s is uniquely determined for a given crystalline structure, and in that case, it will have only one value. We denote this by η_0 such that, $\eta_0 = N_S$, although we will continue with the notation N_s for the number of sites. Hence, the summation over S in Eq. (12) will have only one value on the right hand side, and we get,

$$\log C = (N_s + N_p + N_n)\log(N_s + N_p + N_n) - N_s \log N_s - (N_p + N_n)\log(N_p + N_n) \tag{13}$$

Now from Eq. (6), we can write,

$$N_s = \frac{N_p}{1 - \varepsilon_p} \tag{14}$$

In addition, from Eq. (7), we can write,

$$N_s = \frac{N_n}{1 - \varepsilon_n} \tag{15}$$

Combining Eqs. (14) and (15), we can write, for N_s,

$$N_s = \frac{(N_p N_n)^{\frac{1}{2}}}{\left[\left(1-\varepsilon_p\right)\left(1-\varepsilon_n\right)\right]^{\frac{1}{2}}} \tag{16}$$

Using Eqs. (14) and (15), we can write the values of $(N_s + N_p + N_n)$ and $(N_p + N_n)$ in Eq. (13), i.e.,

$$N_s + N_p + N_n = N_s + N_s(1-\varepsilon_p) + N_s(1-\varepsilon_n) = N_s(3-\varepsilon_p-\varepsilon_n) \tag{17}$$

and

$$N_p + N_n = N_s(1-\varepsilon_p) + N_s(1-\varepsilon_n) = N_s(2-\varepsilon_p-\varepsilon_n) \tag{18}$$

Substituting Eqs. (17) and (18) in Eq. (13) gives,

$$\log C = N_s\left\{\left(3-\varepsilon_p-\varepsilon_n\right)\left\{\log N_s + \log\left(3-\varepsilon_p-\varepsilon_n\right)\right\} - \log N_s - \left(2-\varepsilon_p-\varepsilon_n\right)\left\{\log N_s + \log\left(2-\varepsilon_p-\varepsilon_n\right)\right\}\right\} \tag{19}$$

Re-arranging terms in log N_s and the other terms gives,

$$\log C = N_s\left\{\left(3-\varepsilon_p-\varepsilon_n\right)\log\left(3-\varepsilon_p-\varepsilon_n\right) - \left(2-\varepsilon_p-\varepsilon_n\right)\times\log\left(2-\varepsilon_p-\varepsilon_n\right)\right\} \tag{20}$$

Eq. (20) will be used to calculate the thermodynamic properties, especially specific heat C_v and the entropy S of an incommensurate neutron star. Thus we have to fix the values of the incommensurability constants ε_p and ε_n.

In general, a neutron star is divided into many regions. The outer crust is supposed to be solid, and has nuclei and electrons. The inner crust is assumed to be solid-superfluid and composed of nuclei, neutrons and electrons; the outer core is supposed to be superfluid – superconductor and composed of neutrons, protons and electrons; the constitution of the inner core is still uncertain [17, 18, 19, 20, 21, 22, 23, 24, 25].The density of each region of the star also varies. Depending upon the types of excitations, the specific heat expression also changes. In another calculation the specific heat was also calculated in the different baryonic density conditions corresponding to the inner crust and in the temperature range $100 KeV$ $\left(T = 11.5942\times10^8 K\right)$ to $2MeV\left(T = 2.3188\times10^{10} K\right)$. Different values for the proton fraction against total baryonic density were obtained at $T = 100 KeV$ [26, 27, 28, 29]. However, we have assumed that in the incommensurate crystalline state of the neutron star, the number of neutrons is 90%, and the number of protons is 10%, and this will determine the values of ε_n and ε_p.

Now in the case of incommensurate quantum solid, vacancies can occur such that the number of particles that occupy the sites is less than the number of sites. In general, vacancies occur naturally in all crystalline materials. At any given temperature, up to the melting point of the material, there is what is called equilibrium concentration (ratio of vacant sites to those containing atoms [15, 16], is also called vacancy concentration). At the melting point of some metals, this ratio can be roughly 1:1000. Now the temperature dependence of the vacancy concentration, N_v, can be modeled by,

$$N_V = N_S\left(e^{-\frac{Q_V}{kT}}\right) \tag{21}$$

where, Q_V - energy required for vacancy formation, k - Boltzmann constant, T - Absolute temperature, N_S - concentration of atomic sites.
Here N_S is given by,

$$N_S = \frac{\rho N_A}{A} \tag{22}$$

where ρ - density, A - atomic mass, and N_A - Avogadro's number.
Vacancies are formed during solidification due to vibrations of atoms, plastic deformation, BCC and HCP.
To make the calculations more explicit, we write,

N_V = vacancy concentration,

N_S = number of sites,

N_p = number of protons

N_n = number of neutrons

Now for protons, vacancy concentration, v_p, is the ratio of vacant lattice sites to those containing protons [27] i.e.,

$$v_p = \frac{N_s - N_p}{N_p}.$$
(23)

Similarly, the vacancy concentration, v_n, for the neutrons is the ratio of vacant lattice sites to those containing neutrons [17], i.e.,

$$v_n = \frac{N_s - N_n}{N_n}$$
(24)

Now if Q_p is the energy required for proton vacancy formation, and Q_n is the energy required for neutron vacancy formation, then from Eq. (21), we can write,

$$v_p = \frac{N_s - N_p}{N_p} = N_s e^{-\left(\frac{Q_p}{kT}\right)}$$
(25)

$$v_n = \frac{N_s - N_n}{N_n} = N_s e^{-\left(\frac{Q_n}{kT}\right)}$$
(26)

Combining Eqs. (25) and (26), we can write,

$$N_s = \left(v_p v_n\right)^{\frac{1}{2}} e^{\left(\frac{Q_p + Q_n}{kT}\right)}$$
(27)

Substituting for N_s from Eq. (27) in Eq. (20), gives,

$$\log C = \left[\left(3 - \varepsilon_p - \varepsilon_n\right)\log\left(3 - \varepsilon_p - \varepsilon_n\right) - \left(2 - \varepsilon_p - \varepsilon_n\right) \times \log\left(2 - \varepsilon_p - \varepsilon_n\right)\right]\left(v_p v_n\right)^{\frac{1}{2}} e^{\left(\frac{Q_p + Q_n}{2kT}\right)}$$
(28)

Eq. (28) depends on the essential parameters of the incommensurate crystalline state of the neutron star in such a way that the N_s is eliminated. Now we can write,

$$\log C = \left[A - B\right]\left(v_p v_n\right)^{\frac{1}{2}} e^{\left(\frac{Q_n + Q_n}{kT}\right)}$$
(29)

where,

$$A = \left(3 - \varepsilon_p - \varepsilon_n\right)\log\left(3 - \varepsilon_p - \varepsilon_n\right)$$
(30)

$$B = \left(2 - \varepsilon_p - \varepsilon_n\right)\log\left(2 - \varepsilon_p - \varepsilon_n\right)$$
(31)

The Gibb's free energy of the incommensurate crystalline neutron star can be written as, G, i.e.,

$$G = -\int k \log C \, dT$$
(32)

Substituting for $\log C$ from Eq. (29) into Eq. (32) and integrating gives, G as,

$$G = 2k^2 \left[A - B\right]\left(v_p v_n\right)^{\frac{1}{2}} \left(\frac{T^2}{Q_p + Q_n}\right) e^{\left(\frac{Q_p + Q_n}{2kT}\right)}$$
(33)

$$G = \eta T^2 e^{\left(\frac{Q_p + Q_n}{2kT}\right)}$$
(34)

where,

$$\eta = 2k^2 \left[A - B\right]\left(v_p v_n\right)^{\frac{1}{2}} \left(\frac{1}{Q_p + Q_n}\right)$$
(35)

THE ENTROPY (S)

The entropy, *S*, of the system is given by,

$$S = -\left(\frac{\partial G}{\partial T}\right) \tag{36}$$

$$S = \eta \left(\frac{Q_p + Q_n}{2k} - 2T\right) e^{\left(\frac{Q_p + Q_n}{2kT}\right)} \tag{37}$$

Eq. (37) is obtained by substituting the value of *G* from Eq. (34) in Eq.(36).

THE SPECIFIC HEAT (C_V)

The specific heat C_v is given by,

$$C_v = T\left(\frac{\partial S}{\partial T}\right) \tag{38}$$

Substituting the value of S in Eq. (38) from Eq. (37), we obtain,

$$C_v = -\eta \left(\frac{Q_p + Q_n}{2k}\right)^2 \left(\frac{1}{T}\right) e^{\left(\frac{Q_p + Q_n}{2kT}\right)} - 2\eta Te^{\left(\frac{Q_p + Q_n}{2kT}\right)} + 2\eta \left(\frac{Q_p + Q_n}{2k}\right) e^{\left(\frac{Q_p + Q_n}{2kT}\right)} \tag{39}$$

CALCULATION OF THE ACTIVATION ENERGY OF VACANCY FORMATION IN CRYSTALLINE NEUTRON STAR

In the incommensurate crystalline neutron star, there will be activation energy (Q_n) for vacancy formation for neutrons and the activation energy (Q_p) for vacancy formation for protons. From Eq. (26), the vacancy formation activation energy, Q_n, for neutrons can be written as,

$$Q_n = -kT \log \frac{v_n}{N_s} \tag{40}$$

Similarly the activation energy, Q_p, for the vacancy formation for protons can be written from Eq.(25) as,

$$Q_p = -kT \log \frac{v_p}{N_s} \tag{41}$$

Thus in the crystalline neutron star in which 90% of the sites are assumed to be occupied by the neutrons, and 10% are occupied by protons, $v_n = 1/9$ and $v_p = 9$. Now, to get the values of the entropy S and specific heat C_v, we have to calculate the values of Q_n and Q_p from Eqs. (40) and (41), and to get the values of Q_n and Q_p, we need the value of N_s that is obtained from Eq.(22). To know the value of N_s, we need to know the value of the density ρ of the neutron star, and this is assumed to be,

$$\rho = 3.7 \times 10^{17} \, kg/m^3 \text{ to } 5.9 \times 10^{17} \, kg/m^3 \tag{42}$$

Now we have to calculate the activation energy for vacancy formation by first calculating the number of sites N_s given by Eq. (22). The general expression for the activation energy, Q_v, for vacancy formation is given by,

$$Q_v = -kT \log\left(\frac{N_v}{N}\right) = kT \log\left(\frac{N}{N_v}\right) \tag{43}$$

Knowing the temperature T of the star, Q_v can be calculated by knowing N_v which is the equilibrium number of vacancies at the temperature of the star. Thus, for neutron star with 90% neutrons, the vacancies at equilibrium will be 10%, and for on-site protons, which are 10%, the vacancies at equilibrium will be 90%. Hence for neutrons on-site, $N_v^n = \frac{10N}{100} = \frac{N}{10}$, and for protons on-site, $N_v^p = \frac{90}{100}N = \frac{9}{10}N$. Now we can calculate Q_v^n for neutrons on-site, and Q_v^p for protons on-site. Using Eq. (43) we get, for $T = 10^6 K$,

$$Q_v^n = kT \log 10 = 2.3kT = 198.375 eV \tag{44}$$

Similarly, we can write for Q_v^p as,

$$Q_v^p = kT \log \frac{10}{9} = kT[2.30 - 2.19] = 0.11kT = 24.30 eV \tag{45}$$

Eq. (44) gives the activation energy for the vacancy formation in the case of neutrons, and Eq. (45) gives the activation energy for vacancy formation in the case of protons when the temperature of the neutron star is $T \approx 10^6 K$. However, in literature different values for the temperature, T, of neutron stars are given. For instance in one calculation [26], T Variation is taken as $T = 100 KeV = 11.5942 \times 10^8 K$ to $T = 2 MeV = 2.3188 \times 10^{10} K$, and the specific heat was calculated for the inner crust of the neutron star. They also calculated the variation of the proton fraction with baryonic gas density at $T = 100 KeV$. Since there are large variations in the density, composition and temperature of the neutron star as we go from the core to the crust, all the values of different physical parameters will be approximate or speculative. In general thermodynamic calculations of the inner crust neglect temperature variation of the proton fraction since the chemical potentials of neutron (μ_n), proton (μ_p) and electron (μ_e) depend on the temperature via an equilibrium condition [27],

$$\mu_n(T) - \mu_p(T) = \mu_e(T) \tag{46}$$

Thus in our calculations, we have assumed that N_v^n and N_v^p will remain constant even if the value of T changes, and the value of Q_v^n and Q_v^p given in Eqns. (44) and (45) will be used to calculate the values of entropy S and specific heat C_v for different values of T that may vary between $10^6 K$ to $10^{12} K$.

CALCULATION OF ENTROPY (S)

In physics, entropy is defined as a mathematical function that describes the thermodynamic macro state of a physical system constituted from the statistical description of the system. Entropy describes the thermodynamic evolution of the system in time, and hence entropy plays a key role in any process in Universe, and this is particularly so in astrophysical objects in nature such as stars, neutron stars etc. Same is true of the specific heat since both specific heat and entropy are related to each other via a fundamental thermodynamic relation

$$TdS = du + pdv \tag{47}$$

The expression for entropy, S, is given by Eq. (37). In the expression for entropy, the values of Q_v^n and Q_v^p (or Q_n and Q_p) are given by the Eqns. (44) and (45). We have to calculate the value of η, which is given by Eq. (35). For $\varepsilon_n = \frac{1}{10}$ and $\varepsilon_p = \frac{9}{10}$, and $\nu_p = 9$ and $\nu_n = \frac{1}{9}$. The value of η will be written as,

$$\eta = 2k^2(1.386)\left(\frac{1}{198.375 eV + 24.3 eV}\right) \tag{48}$$

Thus the expression for entropy, S, is,

$$S = \frac{1.9125}{T} \times 10^{-16} erg\left(e^{\left(\frac{1.7 \times 10^6}{T}\right)}\right) \tag{49}$$

Now if we arbitrarily decide that the temperature T of the neutron star is $1.7 \times 10^6 K$, and this is being done for convenience of calculation (T can vary from $10^6 K$ to $10^{12} K$), we get,

$$S = 2.4435 \times 10^{-22} erg / K \tag{50}$$

We can go on increasing the value of T as, $2 \times 1.7 \times 10^6 K$, $3 \times 1.7 \times 10^6 K$, and so on to $10^4 \times 1.7 \times 10^6 K$ and we find that $\left(e^{\frac{1.7 \times 10^6}{T}}\right)$ keeps decreasing such that for $T = 10^4 \times 1.7 \times 10^6 K$ its value will be roughly 1.00007757, which can be approximated as unity. Hence, for $T = 1.7 \times 10^{10} K$, the value of the entropy will be,

$$S = 2.4435 \times 10^{-26} erg / K \tag{51}$$

CALCULATION OF SPECIFIC HEAT (C_V)

In the same manner, the specific heat C_v can be calculated from Eq. (39). For $T = 1.7 \times 10^6 K$, C_v is,

$$C_v = 2.875 \times 10^{-28} erg / K \tag{52}$$

and for $T = 1.7 \times 10^{10} K$, it will be,

$$C_v = 2.875 \times 10^{-32} \, erg / K \tag{53}$$

The values of entropy (S) and specific heat (C_v) obtained in Eqs. (51) and (53) respectively, are very small for an incommensurate crystalline structure of the neutron star.

RESULTS AND DISCUSSION

When the neutron star is formed, the proton – neutron phase is assumed to have a temperature of $T \cong 10^{11} K$, and this is called hot phase. Later a stationary hot phase gets established whose temperature $T \cong 10^9 K$. After a few hours of the formation of the neutron star, the final cold stationary phase is established and has a temperature $T \cong 1 \times 10^7 K$. All these temperatures have approximate magnitude [28, 29]. The change in entropy with time is a consequence of the very process of evolution of the star, and this is due to the attempt of the gravity of the system to sustain the star in a state of quasi – hydrostatic equilibrium. Distant observers on the Earth can only surmise or anticipate or do some approximate calculations about the properties of the neutron star from whatever data they can collect on the Earth. No actual experiments can be done, at least as of to – day, on the surface of the neutron star. Hence the data used and the results obtained in the calculations will be approximate or possible results.

Now the present understanding is that a neutron star has a mass of the order of $1.4 M_s$, where M_s is the mass of the Sun. This huge mass is contained in a comparatively (when compared to the size of the Sun) smaller radius of the order of $10 km$, hence the density of the neutron star is very large and very strong gravitational force exists in the neutron star. The composition of the neutron star with 90% neutrons and 10% protons is assumed to be a crystalline state resulting in incommensurate crystallization of the neutron star. Using these parameters, in this manuscript, calculations have been done for the entropy and specific heat of the neutron star. The state of crystallization is immensely rigid under very strong gravitational forces and hence the numerical values of the specific heat and entropy obtained in this paper are very small. Hence, we can write that very small specific heat means that the neutron star in the incommensurate crystalline state does not absorb heat or absorbs very small heat. Similarly, very small entropy means that there will be no disorder (except the zero-point-energy disorder) in the incommensurate crystalline state of the neutron star, and this again, could be due to very large density (more than the nuclear saturation density) and very strong gravitational force. Calculations show that both the specific heat (C_v) and entropy (S), decrease with increase in temperature of the neutron star.

Prevalent models suggest that the crust of the neutron star is extremely hard, but very smooth with maximum surface irregularities of the order of 5mm, and it is surmised that this is due to very large gravitational field [30]. The crust may be composed of very heavy elements like platinum, gold, uranium, iron etc. There Q values can be calculated by the methods outlined in this manuscript. Assuming that the neutron star is composed of these elements, the entropy and the specific heat can also be calculated. We will have to know or assume the comparative abundance of these elements to calculate S and C_v [31].

It is not known [31] what exactly is at the centre of the neutron star. Since Pressure is greatest at the centre, it may be composed of hyperons, kaons and pions. The outer 1 km is assumed to be solid although its temperature is of the order of 10^6K or 10^7K. There exists a very strong magnetic field of the order of 10^{12}gauss (the Earth's magnetic field is 0.5 gauss). In some cases the magnetic field could be 10^{14} and 10^{15}gauss. The gravity on a neutron star is roughly 2 billion times stronger than gravity on Earth. It is so strong that it can even bend radiation from the star, and this process is called gravitational lensing. There exist staggering pressures and incompressible density, and this may lead to a neutron superfluid, or an incommensurate crystalline state of the neutron star. It is this state that has been studied in this manuscript [32]. In fact, the entropy of cold crystallized and incommensurate lattice has been studied, and our calculations show that the entropy decreases with increase in temperature of neutron star, and this is in agreement with the second law of Thermodynamics.

In neutron stars, there is decrease of entropy due to gravitational contraction, and this is at the expense of increase in the entropy of the whole environment due to the release of very high – energy radiation (neutrinos) during the life of the stars in the main sequence.

Cumming [33] and his collaborators calculated that the core temperature after the accretion outburst constraints the core specific heat. It was found that the larger the specific heat, the smaller the rise in core temperature during the outburst. Alternatively, if the core temperature is large, the specific heat will be smaller, and this is the result of the calculations done in this manuscript. It may be a good idea to do the calculations by considering the existence of gold, platinum, uranium and silver as part of the lattice. (As a rule the existence of these heavy elements as a part of the incommensurate crystalline structure should lead to reduction of the specific heat C_V and entropy S).

In spite of high temperature of the core $\left(\approx 10^{10} K \right)$, due to large gravity stress and very high density in the core of the neutron star, the specific heat C_v and the entropy S are very small. This is due to the fact that the core is not able

to vibrate, and this also means the absence of conventional restlessness in the crystalline state, irrespective of whether we deal with the crystallization of the core or the crust of the neutron star. The study of incommensurate quantum crystal by Anderson [34] for systems on the Earth, $C_v = AT^3 + BT^7$, whereas the temperature variation for C_v for neutron stars as obtained in this paper is $(1/T)$.

There is a marked difference between the study of thermodynamics of an incommensurate quantum crystal by Anderson and his collaborators [34] and the study of incommensurate crystallization of neutron matter in neutron stars in this manuscript. In the phenomenological thermodynamic description of low temperature incommensurate quantum solid, Anderson et.al developed a theory in which the lattice constant and density can change independently. In the temperature range considered by them (T = 0K to T= 1.4K), the vacancies and interstitials are assumed to be incorporated in a highly correlated quantum state of the system. The temperature dependence is a consequence of the existence of only low frequency modes called phonons. Considering a given mass of helium at a fixed volume, they used the expansion of free energy at low temperature and obtained an expression for the specific heat; $C_v = AT^3 + BT^7$. The problem of incommensurate crystallization of neutron matter in neutron stars is quite different. Here the system is composed of 90% neutrons and 10% protons. The 90% neutron sites are considered as vacant sites for protons, and 10% proton sites are treated as vacant sites for neutrons. Both neutrons and protons are fermions and there are no such thing as low frequency modes of the type of phonons. The density of the helium system is very low, whereas a neutron star has very large density, more than the saturation nuclear density, and hence has extremely high gravitational stress. The core of the neutron star is said to be an isothermal system. The internal structure is extremely compact and strong that it does not permit any disorder. Due to these factors, our calculations lead to very small specific heat and entropy. The variation $(1/T)$ means that, as T increases, there is a very small variation in specific heat and entropy in line with the second law of thermodynamics.

The gravity stress, the very high density and the very high temperature at the core of the neutron star result in the lowering of the specific heat and the entropy compared to the values of C_v and S at the crust region of the neutron star. Although the core of the neutron star is extremely dense such that the core is not able to vibrate, it still sustains very high temperature, of the order of $10^9 - 10^{12}\,K$. However, the exact structure, density, gravitational stress and temperature of the core of the neutron star is open to discussion. Physicists cannot agree on what exactly happens inside the neutron star.

Once the neutron star is cooled from a temperature of the order of $10\,MeV\left(\cong 10^{10}\,K\right)$ which is the temperature of the neutron star when it is born and cooled by the emission of huge amount of energy via neutrino emission to temperatures of the order of $0.1\,MeV\left(\cong 10^6 \text{ to } 10^8\,K\right)$ or less, it becomes cold and crystalline. Due to very large density, even more than the density of nuclei, there is a huge gravitational stress in the crust to the core of the neutron star. The very large gravitational stress leads to the incommensurate structure of the neutron star. The crystalline structure may be such that, it will not permit any disorder and that means accepting no heat, which means very little entropy and specific heat. This is exactly the result of the calculations done in this manuscript.

Considering a uniform neutron matter inside the crust of the neutron star, calculations showed that the specific heat increases [35]. Whereas for an incommensurate crystalline structure of the neutron star, calculations in this manuscript show that the entropy S and the specific heat C_v are quite small.

ORCID IDs
Kapil M. Khanna, https://orcid.org/0000-0003-4311-9987; **David K. Kandie**, https://orcid.org/0000-0003-1894-239X
Joel K. Tonui, https://orcid.org/0000-0002-9860-4691; **Hezekiah K. Cherop**, https://orcid.org/0000-0002-0832-9340

REFERENCES
[1] A.F. Andreev and I.M. Lifshitz, JETP, **29**, 1107 (1969).
[2] U.Z. Dehlinger, Krist. **65**, 615 (1927).
[3] J.S. Moreno. *Progress in Statistical mechanics Research*. (Nova Science Pub. Inc., New York, 2008).
[4] (a) K.M. Khanna, J. Namwitako, T.W. Sakwa, Y.K. Ayodo, A. Sarai, G.O. Barasa and S.J. Prichani, International Journal of Physics and Mathematical Sciences, **5**(2), 34-39 (2015), http://www.cibtech.org/J-PHYSICS-MATHEMATICAL-SCIENCES/PUBLICATIONS/2015/Vol-5-No-2/03-JPMS-004-SAKWA-THERMODYNAMICS.pdf. (b) A. Lazarides, A. Das and R. Moessner, Phys. Rev. Lett. **112**, 150401 (2014), https://doi.org/10.1103/PhysRevLett.112.150401.
[5] NASA, Goddard Space Flight Center, RXTE Guest Observer Facility, (2001) https://heasarc.gsfc.nasa.gov/docs/xte/Greatest_Hits/khz.qpo.html.
[6] B.G. Todd-Rutel and J. Piekarewicz, Phys. Rev. Lett. **95**(12), 122501 (2005), https://doi.org/10.1103/PhysRevLett.95.122501.
[7] J.S. Namwetako, J.K. Tonui, G.S.W. Murunga and K.M. Khanna, Zero Point Energy as Sea of Energy, Journal of Materials Science & Nanotechnology, **7**(2), (2019).
[8] (a) H. Pawel, A.Y. Potekhin, and D.G. Yakovlev. *Neutron Stars 1*. Equation of state and structure, Springer science and Business media **326** (2007). (b) F. Özel, D. Psaltis, R. Narayan, A.S. Villareal, On the mass distribution and birth masses of neutron stars, the Astrophysical Journal, **757**(1), 55 (2012), https://doi.org/10.1088/0004-637X/757/1/55. (c) J. Timlin, Neutron

Degeneracy Pressure-Physics, Quantum Mechanics II, Spring (2013); (d) A.W Steiner, J. M. Lattimer and E.F. Brown, The Neutron Star mass radius relation and the Equation of State of dense matter. The astrophysical Journal Letters, **765**(1), 5 (2013).

[9] A. Gezerlis, C.J. Pethick and A. Schwenk,Pairing and superfluidity of nucleons in neutron stars (2014), https://arxiv.org/abs/1406.6109v2, (13 April 2015).

[10] (a) S. Jarman, Neutron star marger reveals secrets. Physics world, **31**(6), 4 (2018); (b) B. Haskell, N. Anderson, D.I Jones and L. Samuelsson, Are neutron stars with crystalline colour superconducting cores Interesting for the LIGO experiments? (2007), e-print arXiv: 0708.2984v2.

[11] A.G. Vorlesungskriptum, *Theoretische physic IV. Statistische physic*, (2006).

[12] N.K. Glendenning, *Compact stars*, (Springer, New York, 1997), pp. 390.

[13] M.I. McMahon and R.J. Nelmes, High pressure Structures and phase transformations in elemental metals, Chem. Soc. Rev. **35**, 943-963 (2006), https://doi.org/10.1039/B517777B.

[14] B. Posselt, G.G. Pavlov, Ü. Erta, S. Çalışkan, K.L. Luhman and C.C. Williams, Discovery of Extended Infrared Emission around the Neutron star RXJ0806. 4-4123, The Astrophysical Journal, **865**(1), 1-12 (2018), https://doi.org/10.3847/1538-4357/aad6df

[15] Superstructure Condensed Incommensurate Solids, in: https://en.wikipedia.org/wiki/Superstructure_(condensed matter).

[16] P. Ehrhart, *Properties and interaction of atomic defects in metals and alloys. Chapter 2. New series III*, **25**, (Springer. Berlin, 1991) pp. 88.

[17] M. Mortazavifar, and M. Oettel, Thermal vacancies in close-packing solids, https://arxiv.org/abs/1311.5093v1. (20 November 2013).

[18] D. Page and S. Reddy, in: https://arxiv.org/abs/1201.5602. (26 January 2012).

[19] P.F. Bedaque, https://arxiv.org/abs/1711.05868.

[20] B. Bertoni, S. Reddy and E. Rrapaj, https://arxiv.org/abs/1409.7750.

[21] C. Vincenzo, Low energy Probes of Physics beyond the Standard Model, https://arxiv.org/abs/1304.0017.

[22] S. Reddy, Thermal and transport properties of neutron star matter, http://www.int.washington.edu/talks/WorkShops/int_16_2b/People/Reddy_S/Reddy.pdf

[23] R. Wijnands, N. Degenaar and D. Page, Cooling of Accretion-heated neutron stars. Journal of Astrophysics and Astronomy, 38 (3) (2017) p.49, https://www.ias.ac.in/article/fulltext/joaa/038/03/0049.

[24] V. Cirigliano, S. Reddy and R. Sharma, Low energy theory for Superfluid and solid Matter and its application to the neutron star crust. Physical Review C, **84**(4), 045809 (2011), https://journals.aps.org/prc/issues/84/4.

[25] J.F. Acevedo, J. Bramante, R.K. Leane and N. Raj, Cooking Pasta with Dark Matter: Kinetic and Annihilation Heating of Neuton star Crusts, Nov.14, (2019), https://arxiv.org/abs/1911.06334.

[26] S. Burrello, F. Gulminelli, F. Aymard, M. Colonna, and Ad.R. Raduta, The Heat Capacity of the Neutron Star inner Crust within an extended NSE model. e-print Arxiv: 1511.00304v1, Nov.1, (2015), https://arxiv.org/abs/1511.00304v1.

[27] M. Fortin, F. Grill, J. Margueron, D. Page and N. Sandulescu, Phys. Rev. C, **82**(6), 065804 (2010), https://doi.org/10.1103/PhysRevC.82.065804.

[28] F. Barranco, R.A. Broglia, H. Eshenseu and E. Viggezzi, Phys. Rev. C, **58**, 1257 (1998), https://doi.org/10.1103/PhysRevC.58.1257.

[29] A. Pastore, Phys. Rev. **91**, 015809, 28 January (2015), in: https://doi.org/10.1103/PhysRevC.91.015809.

[30] J.M. Lattimer and M. Prakash, Astrophys. J. **550**, 426 (2001), https://doi.org/10.1086/319702.

[31] S.W.G. Murunga, J. Mater. Sci. Nanotech. **6**(3), 303 (2019), http://www.annexpublishers.com/articles/JMSN/6303-Estimation-of-the-Abundances-of-Heavy-Elements-Isotopes-in-Neutron-Stars.pdf.

[32] Neutron stars and how they cause Gravitational waves, https://www.nationalgeographic.com/science/space/solar-system/neutron-stars/.

[33] A. Cumming, E.F. Brown, F.J. Fattoyer, C.J. Horowitz, D. Page and S. Reddy. A lower limit on the Heat capacity of a Neutron star core. Phys. Rev. C, **95**(2), 025806 (2017), https://doi.org/10.1103/PhysRevC.95.025806.

[34] P.W. Anderson, W.F. Brinkman and D.A. Huse, Science, **310**(5751), 1164-1166 (2005), https://doi.org/10.1126/science.1118625.

[35] G. Lazzari and F.V. de Blasio, Astro. Lett. and Communications. **35**, 339-347 (1997), https://ui.adsabs.harvard.edu/#abs/1997ApL&C..35..339L/abstract.

НЕРОЗМІРНА КРИСТАЛІЗАЦІЯ НЕЙТРОННОЇ РЕЧОВИНИ У НЕЙТРОННИХ ЗІРКАХ

Капіл М. Ханна, Девід К. Канді, Джоел К. Тонуі, Хезекія К. Чероп
Фізичний факультет, Університет Елдорет
P.O. Box 1125-30100, Елдорет, Кенія

Склад нейтронних зірок від його поверхневої області, зовнішнього ядра, внутрішнього ядра і до його центру все ще досліджується. Можна тільки здогадуватися про властивості нейтронних зірок по спектроскопическим даними, які можуть бути доступні час від часу. У ряді моделей передбачається, що речовина в поверхневій області нейтронної зірки складається з атомних ядер, які руйнуються при надзвичайно великому тиску і гравітаційному напрузі, і це призводить до створення твердої решітки з морем електронів, і, можливо, деякої кількості протонів, що протікають через проломи в решітці. Ядра з високим масовим числом, такі як залізо, золото, платина, уран, можуть існувати в області поверхні або в області зовнішнього ядра. Встановлено, що структура нейтронної зірки дуже сильно змінюється при переході від поверхні до ядра нейтронної зірки. Поверхня дуже жорстка і дуже гладка. Поверхневі нерівності чи становлять близько 5 мм, тоді як внутрішня частина нейтронної зірки може бути сверхтекучей і складатися з виродженого нейтронного речовини. Однак нейтронна зірка є дуже компактні кристалічні системи, і в земних матеріалах, що знаходяться під тиском також було виявлено багато прикладів невідповідних фазових переходів. В результаті були вивчені властивості невідповідною кристалічної нейтронної зірки. Склад нейтронних зірок в сверхплотном стані залишається невизначеним в ядрі нейтронної зірки. Одна модель описує ядро як надплинну нейтронно-вироджену матерію, в основному складається з нейтронів (90%) і

невеликої відсотка протонів і електронів (10%). Можливі більш екзотичні форми матерії, включаючи вироджену дивну матерію. Це також може бути невідповідна кристалічна нейтронна матерія, яка може бути BCC або HCP. Використовуючи принципи квантової статистичної механіки, була розрахована питома теплоємність і ентропія невідповідною кристалічної нейтронної зірки виходячи з припущення, що температура зірки може змінюватися від до Були довільно обрані два значення для температури T - $1.7 \times 10^6 K$ і $1.7 \times 10^{10} K$ для яких були зроблені обчислення. Значення питомої теплоємності і ентропії зменшуються з ростом температури, а також їх величини дуже малі. Це відповідає другому закону термодинаміки.

КЛЮЧОВІ СЛОВА: земні матеріали, нерозмірна фаза, нерозмірна кристалічна нейтронна зірка, надтекучість, вироджена нейтронна матерія.

НЕСОРАЗМЕРНАЯ КРИСТАЛЛИЗАЦИЯ НЕЙТРОННОГО ВЕЩЕСТВА В НЕЙТРОННЫХ ЗВЕЗДАХ

Капил М. Ханна, Дэвид К. Канди, Джоэл К. Тонуи, Хезекия К. Чероп
Физический факультет, Университет Элдорет
P.O. Box 1125-30100, Элдорет, Кения

Состав нейтронных звезд от его поверхностной области, внешнего ядра, внутреннего ядра и к его центру все еще исследуется. Можно только догадываться о свойствах нейтронных звезд по спектроскопическим данным, которые могут быть доступны время от времени. В ряде моделей предполагается, что вещество в поверхностной области нейтронной звезды состоит из атомных ядер, которые разрушаются при чрезвычайно большом давлении и гравитационном напряжении, и это приводит к созданию твердой решетки с морем электронов, и, возможно, некоторого количества протонов, протекающих через бреши в решетке. Ядра с высоким массовым числом, такие как железо, золото, платина, уран, могут существовать в области поверхности или в области внешнего ядра. Установлено, что структура нейтронной звезды очень сильно меняется при переходе от поверхности к ядру нейтронной звезды. Поверхность очень жесткая и очень гладкая. Поверхностные неровности едва ли составляют порядка 5 мм, тогда как внутренняя часть нейтронной звезды может быть сверхтекучей и состоять из вырожденного нейтронного вещества. Однако нейтронная звезда представляет собой очень компактные кристаллические системы, и в земных материалах, находящихся под давлением также было обнаружено много примеров несоразмерных фазовых переходов. В результате были изучены свойства несоразмерной кристаллической нейтронной звезды. Состав нейтронных звезд в сверхплотном состоянии остается неопределенным в ядре нейтронной звезды. Одна модель описывает ядро как сверхтекучую нейтронно-вырожденную материю, в основном состоящую из нейтронов (90%) и небольшого процента протонов и электронов (10%). Возможны более экзотические формы материи, включая вырожденную странную материю. Это также может быть несоразмерная кристаллическая нейтронная материя, которая может быть BCC или HCP. Используя принципы квантовой статистической механики, была рассчитана удельная теплоемкость и энтропия несоразмерной кристаллической нейтронной звезды исходя из предположения, что температура звезды может изменяться от $10^6 K$ до $10^{12} K$. Были произвольно выбраны два значения для температуры $T - 1.7 \times 10^6 K$ и $1.7 \times 10^{10} K$ для которых были сделаны вычисления. Значения удельной теплоемкости и энтропии уменьшаются с ростом температуры, а также их величины очень малы. Это соответствует второму закону термодинамики.

КЛЮЧЕВЫЕ СЛОВА: земные материалы, несоразмерная фаза, несоразмерная кристаллическая нейтронная звезда, сверхтекучесть, вырожденная нейтронная материя.

STRUCTURAL, ELECTRONIC, OPTICAL AND MAGNETIC PROPERTIES OF Co$_2$CrZ (Z= Al, Bi, Ge, Si) HEUSLER COMPOUNDS

Sukhender[a], Lalit Mohan[a], Sudesh Kumar[b], Deepak Sharma[c], Ajay Singh Verma[a]*

[a]Department of Physics, Banasthali Vidyapith, Banasthali 304022, India
[b]Department of Chemistry, Banasthali Vidyapith, Banasthali 304022, India
[c]Department of Physics, IIMT College of Engineering, Greater Noida, 201306, India
*Corresponding author: ajay_phy@rediffmail.com
Received January 26, 2020; revised February 11, 2020; accepted February 17, 2020

In this paper, we have studied the structural, electronic, optical and magnetic properties of Co$_2$CrZ (Z= Al, Bi, Ge, Si) compounds by using two different methods one is full potential linearized augmented plane wave (FP-LAPW) method as implemented in WIEN2k and second is pseudo potential method as implemented in Atomistic Tool Kit-Virtual NanoLab (ATK-VNL). The respective band gaps in their minority-spin of Co$_2$CrZ (Z= Al, Bi, Ge, Si) are 0.696, 0.257, 0.602 and 0.858 eV near the Fermi level, which is implemented in WIEN2k code and showing 100% spin polarization. Further, these compounds have been found to be perfectly half-metallic ferromagnetic (HMF). However, above mentioned compounds shows zero band gaps in ATK-VNL code. The calculated magnetic moment of these compounds Co$_2$CrZ (Z= Al, Bi, Ge, Si) are 3.06, 4.99, 3.99 and 3.99μ$_B$ respectively in FP-LAPW method. However, the respective magnetic moment of these compounds is found to be 3.14, 5.08, 4.11 and 4.08μ$_B$ in ATK-VNL code. Optical properties play an important role to understand the nature of material whether it can be used as optoelectronics device. From the optical Spectra, complex dielectric functions calculated values are 312.370 and 141.991, 299.812 and 111.368, 288.127 and 106.342, 290.688 and 99.095 for the compounds Co$_2$CrZ (Z= Al, Bi, Ge, Si) respectively by using WIEN2k. The maximum energy loss is observed between 11.4 to 13eV for above these compounds. The refractive index values for the compounds Co$_2$CrZ (Z= Al, Bi, Ge, Si) are observed as 18.104, 17.602, 17.252 and 17.289 respectively. In the optical conductivity spectrum a sharp peak is observed at 1.6 - 2.3eV.
KEYWORDS: Half-metallic ferromagnetic, band gap, dielectric constant, magnetic moment

A German mining engineer and chemist Friedrich Heusler discovered the Heusler compounds [1]. The Full Heusler compounds are the ternary compounds of the composition 2:1:1 with chemical formula X$_2$YZ and having structure of the L2$_1$ formed by four interpenetrating FCC-lattices [2-3]. Heusler alloys shows half metallic ferromagnetism and was first predicted by de Groot [4]. Half metallic ferromagnets (HMFs) having band structure for majority spins is metallic and for minority spin is semiconducting presenting 100% spin polarization at Fermi level. Half metallicity attracted more attention due to its various applications in Spintronics devices, such as nonvolatile magnetic random access memories, magnetic sensors, spin-resonant tunneling diodes, spintronic transistors and spin light emitting diodes and so on [5-10]. Felser et al. [11] have studied the X$_2$RbCa (X = C, N, O) full-Heusler compounds showing the half-metallicity primarily originate from the spin-polarization of the p-like states of N and O atoms. Bai et al. [12] have presented a comprehensive review of the Heusler family with special focus on its broad applications in the field of magnetic data storage, ranging from CPP-GMR read heads, to MRAM arrays, and emerging SPRAMs. These compounds are outstanding functional building blocks for spintronics devices. Sharma et al**.** [13] have investigated that Fe$_2$CrAl compound has high density of states and shows a 100% spin polarization in the vicinity of the Fermi level. Rai et al. [14] have also proposed that Full-Heusler compound Co$_2$CrGe is half-metallic ferrimagnet using Generalized-gradient approximation for the structural and local spin density approximation for electronic calculation. It was found that the Co$_2$YZ compounds exhibit half-metallic ferromagnetic and an apparently linear dependence of the Curie temperature on the magnetic moment [15]. Among the Heusler compounds, Co-based compounds were investigated by ab initio techniques and most of them are found HMFs [16-17]. Seema et al. [18] had investigated the effect of disorder by using density functional theory on electronic, magnetic and optical properties of Co$_2$CrZ (Z= Al, Ga, Ge, Si) Heusler compounds. They consider three types of disorders DO$_3$, A2 and B2 in which B2 disorder retains the spin polarization whereas DO3 and A2 disorder leads decrease in the spin polarization value at Fermi level.

In this paper, we have calculated the structural, electronic, optical and magnetic properties of Co$_2$CrZ (Z= Al, Bi, Ge, Si) compounds, by using WIEN2k code and Atomistic Tool Kit-Virtual NanoLab (ATK-VNL) code within Generalized-gradient approximation (GGA) for exchange correlation functions.

COMPUTATION DETAILS

Wien2k code based on the full-potential linearized augmented plane wave (FP-LAPW) method [19,20,21] was applied for the fundamental physical properties calculations of Co$_2$CrZ (Z= Al, Bi, Ge, Si) compounds within

Generalized-gradient approximation (GGA) for exchange correlation functions. Wien2k is one of the most accurate methods for performing electronic structure calculations for solids. Core states are considered relativistically and valence states are considered as semi-relativistic way and energy between these two states was set -6.0Ry. We have used 1000 k-points in the first Brillouin zone for this code. For the calculation of optical properties we used here 10000 k-points. The convergence or cutoff parameter $R_{mt} K_{max}$ is set to 7.0, which is used to control the size of the basis sets. Here plane wave radius is denoted by R_{mt} and maximum modulus for reciprocal lattice vector is denoted by K_{max}. The energy convergence criterion was taken as 0.0001Ry. The angular momentum maximum (l_{max}) value is taken as 10. In the central region the charge density and potential were elaborated as a fourier series with wave vector up to G_{max}=10. For the each atom muffin tin sphere radii (R_{MT}) are tabulated in Table 1.

Table 1

Muffin tin radius (R_{MT}) for Co_2CrZ (Z= Al, Bi, Ge, Si).

R_{MT} (a.u.)	Compound			
	Co_2CrAl	Co_2CrBi	Co_2CrGe	Co_2CrSi
Co	2.38	2.22	2.28	
Cr	2.26	2.12	2.17	
Z	2.15	2.26	2.12	1.89

Pseudo-potential method has been carried out in the framework of density functional theory implemented in the commercially licensed Atomistic Tool Kit-Virtual NanoLab (ATK-VNL) package [22,23]. First-principles calculations was applied to investigate electronic and magnetic properties of Co_2CrZ (Z= Al, Bi, Ge, Si) using Pulay Mixer algorithm. For investigations, we use double-zeta (ζ) polarized basis set for electron wave function expanding and GGA for exchange-correlation functional [20]. For spin polarization, up and down initial state have been selected for the atoms. We used 10 x 10 x 10 Monkhorst-Pack k-mesh [24] for brillouin zone sampling to maintain balance between computational time and results accuracy. Further, for optimisation of structures we do not impose any constrain in x, y and z directions. The structures are permitted to optimized until each atom achieve force convergence criteria of 0.05 eV/Å.

RESULTS AND DISCUSSIONS:
Structural Study

The Full Heusler compounds have the composition 2:1:1 with chemical formula X_2YZ having structure of the $L2_1$ (space group: 225 Fm-3m) formed by four penetrating FCC-lattices with atomic positions at X_1 (1/4, 1/4, 1/4), X_2 (3/4, 3/4, 3/4), Y (1/2, 1/2, 1/2) and Z (0, 0, 0). Where X and Y atoms are transition metal and Z is main group metal or semimetal. The equation of state given by Murnaghan [25] gives the value of total energy & pressure as a function of volume is stated as:

$$E(V) = E_O + \left[\frac{BV}{B_P}\left(\frac{1}{(B_P-1)}\left(\frac{V_O}{V}\right)^{B_P}+1\right) - \frac{BV_O}{(B_P-1)}\right]$$

$$P(V) = \frac{B}{B_P}\left\{\left(\frac{V_O}{V}\right)^{B_P}-1\right\},$$

where

$$\text{Pressure } (P) = -\frac{dE}{dV}, B_P = -V\frac{dP}{dV} = V\frac{d^2E}{dV^2}$$

In the above equations E_0 is the minimum energy at T = 0K, B is the bulk modulus, B_P is the pressure derivative of the bulk modulus and V_o is the equilibrium volume. The structural optimization results are shown in Figure 1. The optimized lattice parameter in WIEN2k for Co_2CrBi is slightly higher than the ATK lattice parameters; but the optimized lattice parameters in WIEN2k for Co_2CrAl, Co_2CrGe and Co_2CrSi are slightly less than the lattice parameters optimized in ATK-VNL. Calculated values of the optimized lattice parameter, equilibrium energy and pressure derivative have been presented in Table 2.

71

Structural, Electronic, Optical and Magnetic Properties of Co$_2$CrZ...

EEJP. 2 (2020)

Lattice parameter, Bulk modulus, Equilibrium energy and Pressure derivative for Co$_2$CrZ (Z= Al, Bi, Ge, Si).

Compound	Lattice Constants a$_0$ (Å)		Bulk modulus (GPa)		Equilibrium	Pressure
	Calculated		Calculated		Energy (Ry)	derivative (GPa)
	WIEN2k	ATK	WIEN2k	ATK		
Co$_2$CrAl	5.712	5.843	195.42	172.96	-8161.392	4.842
Co$_2$CrBi	6.151	6.120	195.32	198.36	-50838.608	-0.832
Co$_2$CrGe	5.740	5.833	218.32	216.10	-11873.869	4.159
Co$_2$CrSi	5.633	5.794	191.00	215.75	-8255.854	4.054
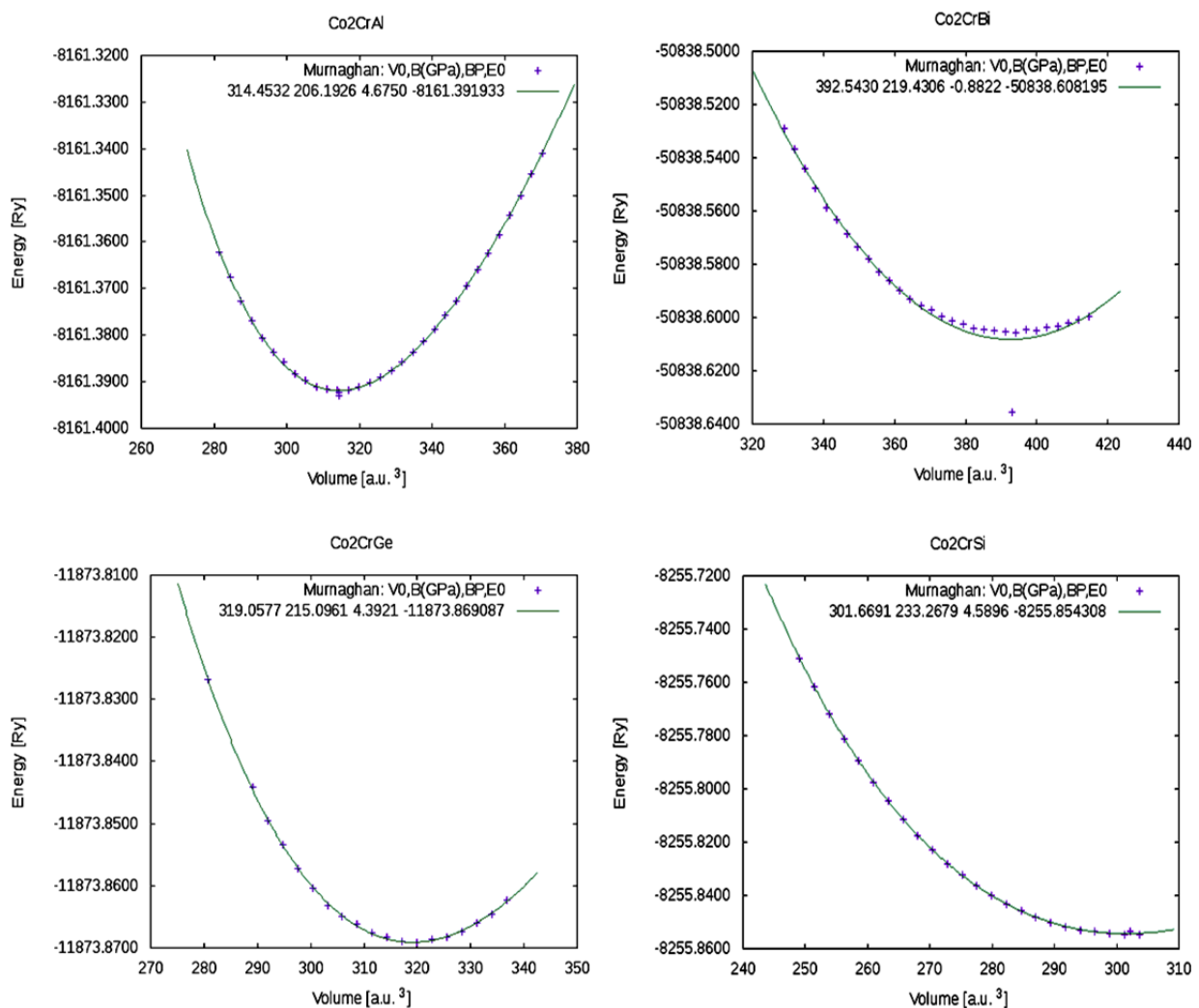
Fig. 1. Volume optimization for the lattice parameters

Electronic and magnetic properties

Spin polarized calculations of Co$_2$CrZ (Z= Al, Bi, Ge, Si) compounds within Generalized-gradient approximation (GGA) full Heusler have been carried out at the optimized lattice parameters. The calculations revealed a gap in the minority states and zero gaps in the majority states at the Fermi level resulting 100% spin polarized band structure at the Fermi level.

In Spintronics, magnetic moment is associated due to intrinsic spin of electron. By using the given formula the spin polarization has been calculated theoretically.

$$P_n = \frac{n\uparrow - n\downarrow}{n\uparrow + n\downarrow}$$

If $n_\uparrow = 0$ or $n_\downarrow = 0$; $P_n = 1$ or -1 in these cases only up or down spins are exist and the spin polarization is 100%. Such materials are known as half metals ferromagnetic or Heusler alloys with 100% spin polarization. If the value of P_n is vanishes then the materials are paramagnetic or anti-ferromagnetic even below the magnetic transition temperature [26]. This impressive category of materials has highly prospective for different application such as spintronics, magneto-electronic devices to increase data processing speed and integration density increasing etc. In Heusler alloy magnetic moment is key point in spintronics and obeys Slater-Pauling rule. This rule correlates the magnetic moment per atom of transition element alloys to the average number of valance electron per atom:

$$m = N_v - 2N_\downarrow$$

Where m is magnetic moment per atom in μ_B, N_v is average number of valence electron per atom & $N_\downarrow$ ($N_\uparrow$) shows the number of minority spin (majority spin) valence electron per atom. The component of spin degree of freedom creates non-volatility in materials [27]. The obtained energy gap and spin polarization for the above approximation is summarized as under in Table 3. The detailed results of band structures and density of states are shown in Figures 2-5.

Table 3

Energy gap and spin polarization for Co_2CrZ (Z= Al, Bi, Ge, Si)

Compound	Energy gap E_g (eV)				Spin polarization	
	WIEN2k		ATK		WIEN2k	ATK
	Up spin	Down spin	Up spin	Down spin		
Co_2CrAl	0.0	0.696	0.0	0.0	100%	P_n vanishing
Co_2CrBi	0.0	0.257	0.0	0.0	100%	P_n vanishing
Co_2CrGe	0.0	0.602	0.0	0.0	100%	P_n vanishing
Co_2CrSi	0.0	0.858	0.0	0.0	100%	P_n vanishing
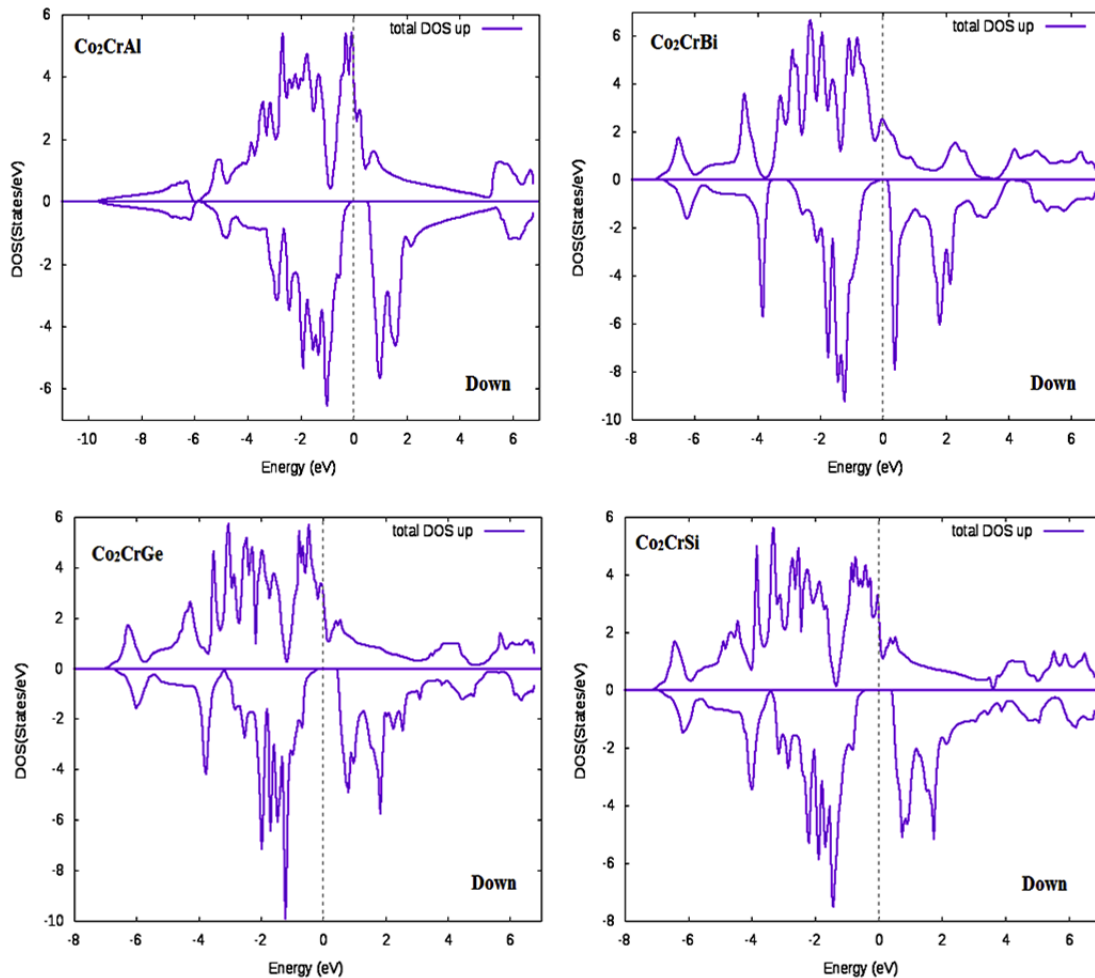
Fig. 2. DOS of Co_2CrZ (Z= Al, Bi, Ge, Si) using WIEN2K Code
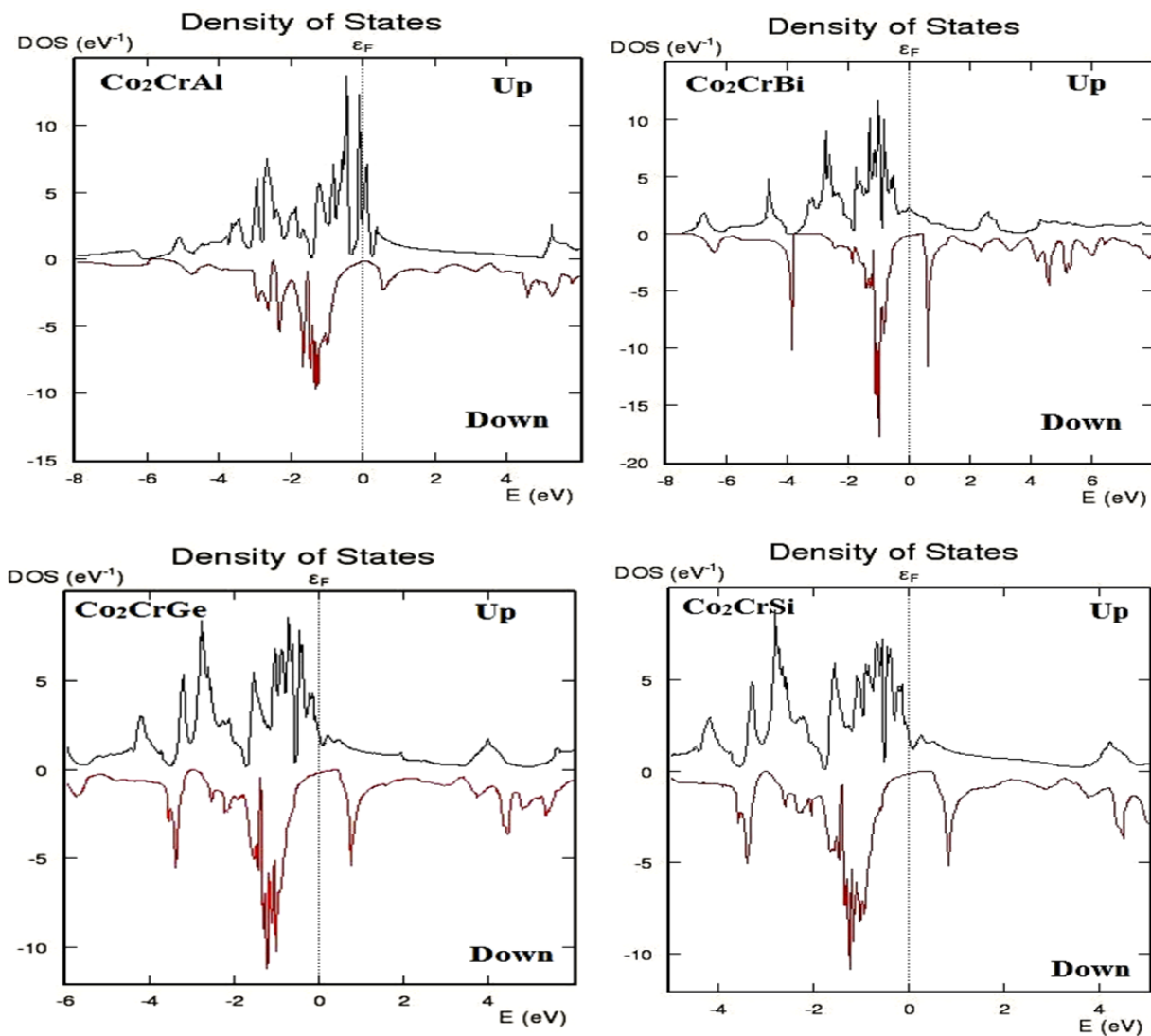
Fig. 3. DOS of Co₂CrZ (Z= Al, Bi, Ge, Si) using ATK-VNL Code.
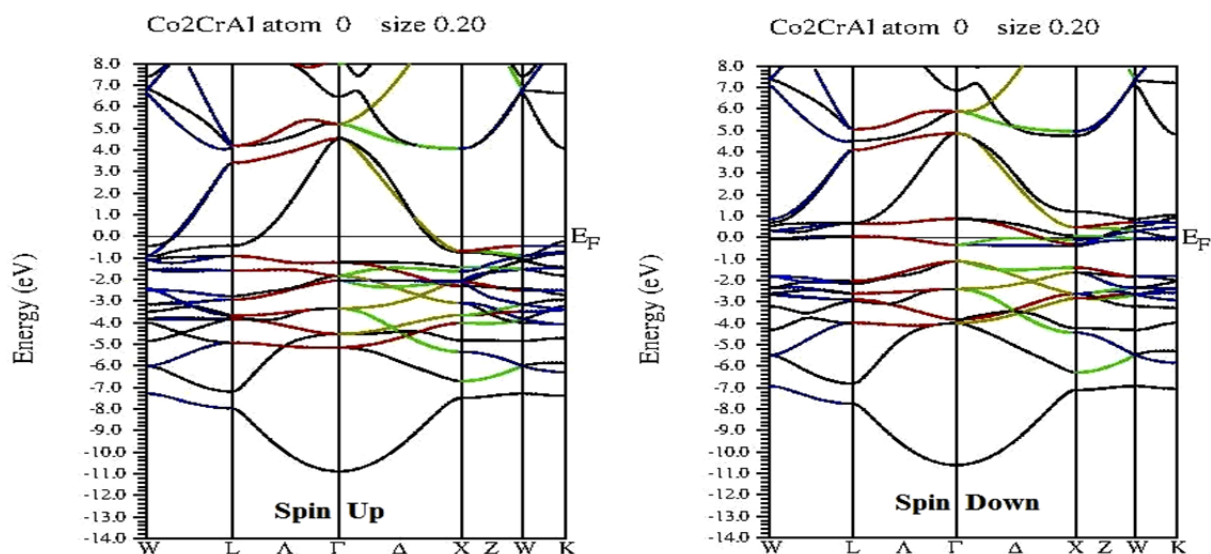
Fig. 4. Band Structure of Co₂CrZ (Z= Al, Bi, Ge, Si) using WIEN2K Code
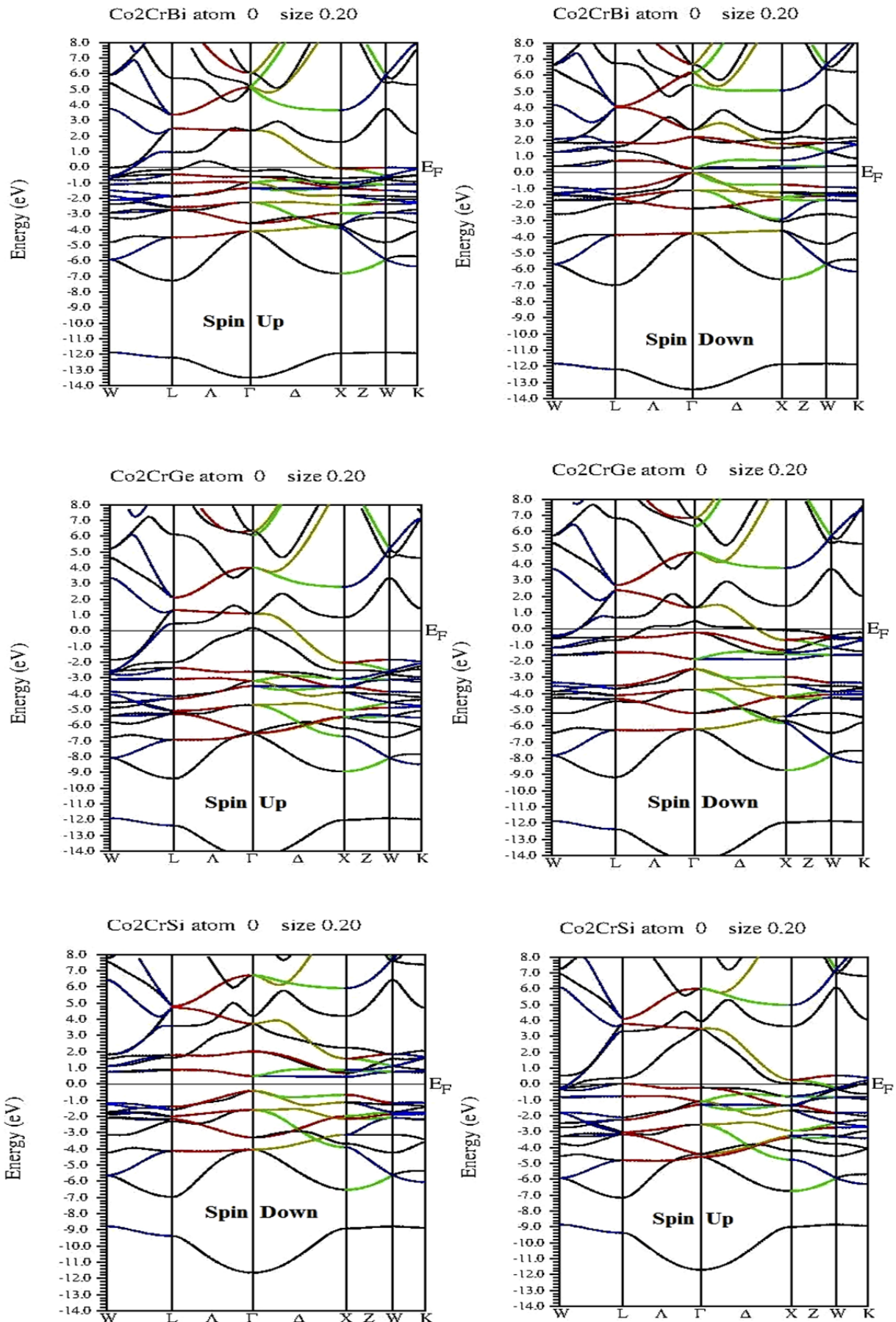
Fig. 4. Band Structure of Co$_2$CrZ (Z= Al, Bi, Ge, Si) using WIEN2K Code
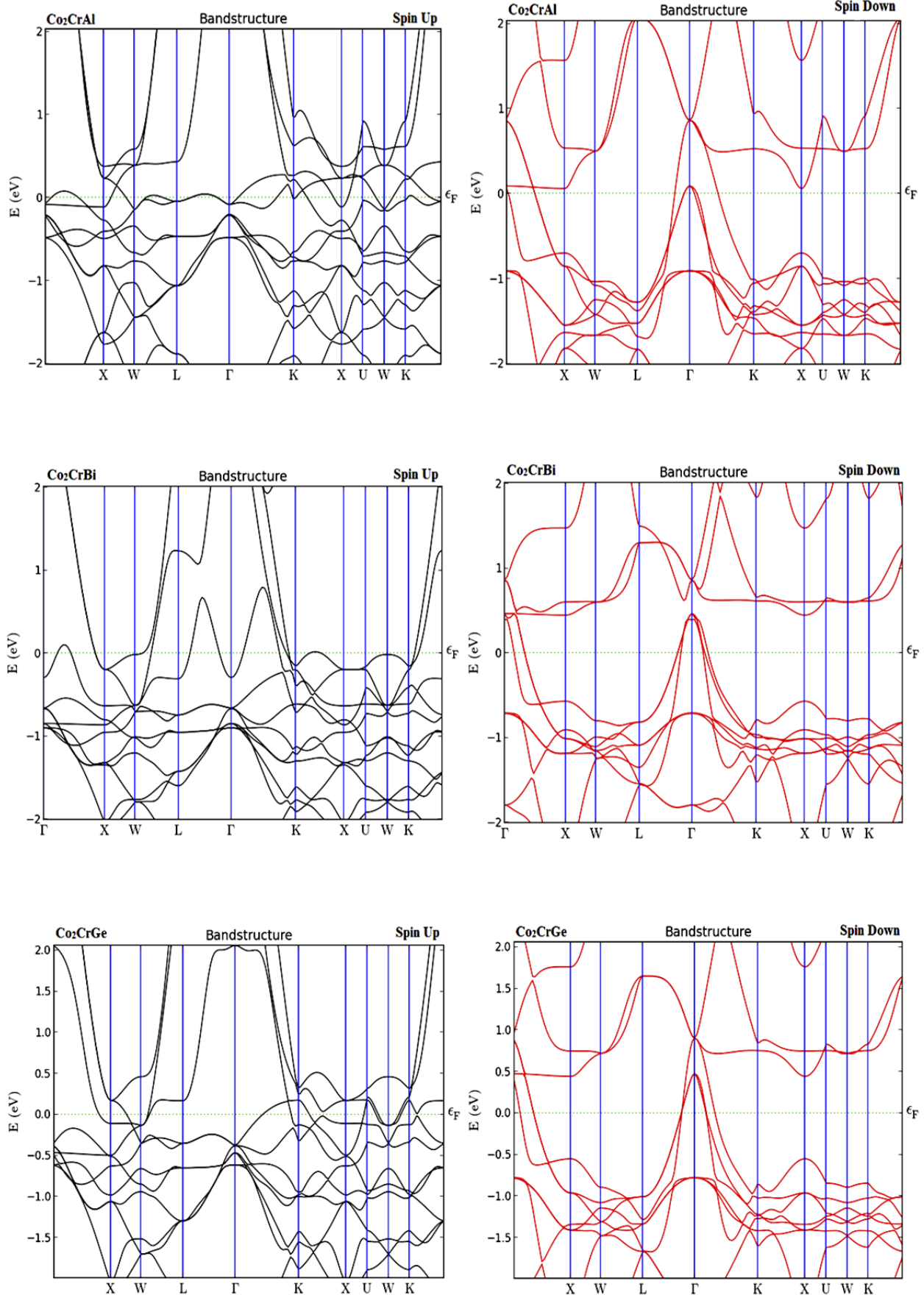
Fig. 5. *(continued)* Band Structure of Co$_2$CrZ (Z= Al, Bi, Ge, Si) using ATK-VNL Code
(continued on next page)
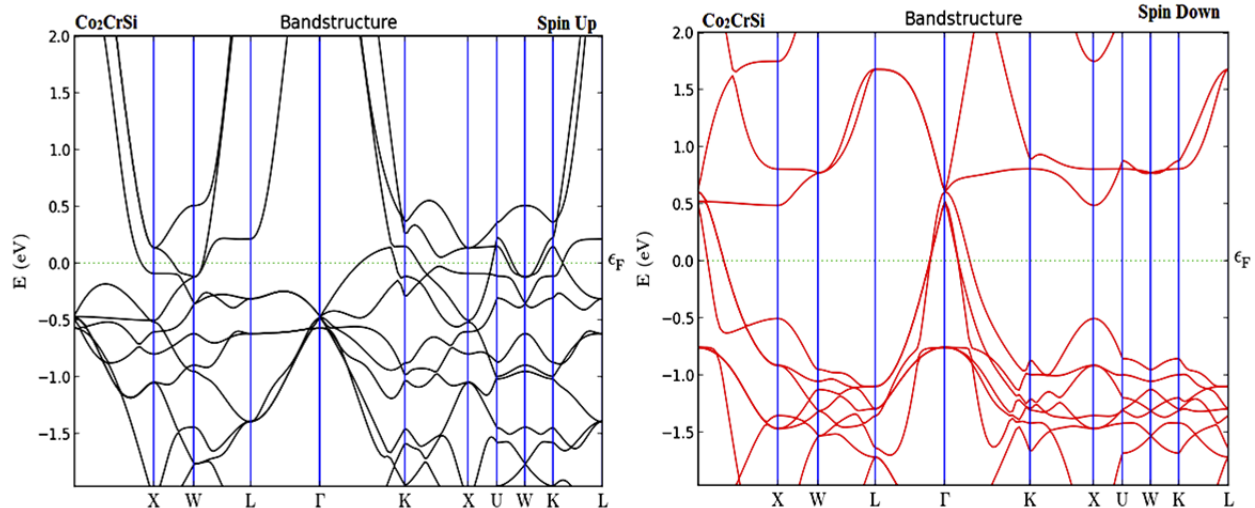
Fig. 5. *(continued)* Band Structure of Co_2CrZ (Z= Al, Bi, Ge, Si) using ATK-VNL Code

By counting the number of valence electrons of the Heusler alloys, it is possible to predict the magnetic properties of the alloys. Even 24 valence electron concentration semiconductors are possible in case of three transition metals per formula unit. For example Fe_2VaI is a non magnetic semiconductor with non-magnetic iron. Co_2YZ Heusler compounds have more than 24 valence electron concentration and follow the Slater-Pauling rule. If the numbers of valence electrons are differ from 24, and then these materials are magnetic, where the magnetic moment per formula unit is directly related to the number of valence electrons minus 24 ($M = Z_t - 24$). Here M denotes the total magnetic moment per unit cell and Z_t is the total number of valence electrons. An important distinction from the half Heusler compounds is that the full Heusler compounds have two distinct magnetic sub-lattices [17]. For the ferromagnetic half-metallic Heusler compounds, the Curie temperature increases by ~175 K per added electron. For example Co_2CrAl has 27 valence electrons with a saturation magnetization of 3 μ_B/formula unit is ferromagnetic with a magnetic moment that mainly resides on the Co sites with a Curie temperature of ~525 K [11]. From the results, it was observed that the magnetic moment exists mainly on Co and Cr positions, while the Z position atom has negligible small magnetic. It was observed that Z atom having more valence electrons increases more magnetic moments on both sits at Co and Cr. The results also revealed that when Al replaces by Si or Ge or Bi increases the localized magnetic moments on both sites at Co and Cr due to addition of increased valence electrons. As the electro-negativity increases localized magnetic moments are increases at X and Y site. There is a good agreement with the Slater-Pauling behavior. Here we have observed that there are very slight difference between full potential linearized augmented plane wave (FP-LAPW) method implemented in WIEN2k and pseudo-potentials method implemented in ATK-VNL. There is also good agreement between above these methods. The calculated results for magnetic moments for Co_2CrZ (Z= Al, Bi, Ge, Si) obtained using full potential linearized augmented plane wave (FP-LAPW) method implemented in WIEN2k and pseudo-potentials method implemented in Atomistic Tool Kit-Virtual NanoLab (ATK-VNL) within Generalized-gradient approximation (GGA) for exchange correlation functions is tabulated in Table 4.

Table 4.

Total magnetic moments of the compounds Co_2CrZ (Z= Al, Bi, Ge, Si).

Compound	Z_t	Magnetic moment (μ_B)		
		WIEN2k	ATK	Slater-Pauling (Z_t - 24)
Co_2CrAl	27	3.07	3.15	3.00
Co_2CrBi	29	5.00	5.08	5.00
Co_2CrGe	28	4.00	4.11	4.00
Co_2CrSi	28	4.00	4.08	4.00

Optical properties

Optical properties play an important role to understand the nature of material whether it can be used as optoelectronics device. In the present section, we discuss the optical properties of the compounds Co_2CrZ (Z= Al, Bi, Ge, Si). For the optical properties, we calculate the dielectric function, optical conductivity, reflectivity, excitation coefficient, absorption coefficient and electron energy loss as a function of photon energy for the above compounds. The complex dielectric function describes the optical response of a material on incident electromagnetic radiation.

$$\varepsilon(\omega) = \varepsilon_1(\omega) + i\varepsilon_2(\omega)$$

where $\varepsilon_1(\omega)$ real represents polarization and anomalous dispersion of medium and $i\varepsilon_2(\omega)$ corresponds imaginary part represents the absorption or loss of energy into the medium [28, 29]. The different optical spectra are shown in Figure 6.

The imaginary part of dielectric function for all four compounds shows the main peak in visible region, after that imaginary part of dielectric function decreases continuously. The zero frequency real (ε_1 (ω)) and imaginary part of complex dielectric functions values are 312.370 and 141.991, 299.812 and 111.368, 288.127 and 106.342, 290.688 and 99.095 for the compounds Co$_2$CrZ (Z= Al, Bi, Ge, Si) respectively as observed from the figure 6 (a) and 6 (b). Optical conductivity is an important optical parameter for conduction of electron due to an applied electromagnetic field. In the optical conductivity spectrum, several peaks are observed between 5.4 - 8.6eV and a sharp peak is observed at 1.6 - 2.3eV. As the material has high absorption coefficient means that they absorb more photon, which excite electron from valence band to conduction band.

The values of absorption coefficient are an increase along the values of energy is increases towards visible region to ultraviolet region as shown in the figure 6 (d). Electron energy-loss function gives the energy loss of a fast moving electron when passing through the medium. The plasma frequency is the frequency corresponding to plasma resonance at which sharp peaks are associated. As if the frequency is above the plasma frequency then the material showing the dielectric behavior and below which the material shows metallic behavior. The maximum energy loss is observed between 11.4 to 13eV for above these compounds as shown in figure 6 (e) and extinction coefficient spectra is displaced in the above figure 6 (h). A prominent peak is shown in the visible region and then value of extinction coefficient is decreases in the ultraviolet region. The values of zero frequency reflectivity are 0.810, 0.802, 0.799 and 0.798 for the compounds Co$_2$CrZ (Z= Al, Bi, Ge, Si) respectively as observed from figure 6 (f). Noticeably, from the absorption and reflection spectra relation, if the absorption is maximum then obviously reflectivity will be minimum. The region in which material substantially absorbs light and it cannot effectively reflect light in the same span. The refractive index is the important optical property due to wide applications because it determines the dispersive power of prisms, focusing power of lenses, light guiding, and critical angle for total internal reflection etc. How fast light is traveling through the materials is described by refractive index. The values for zero frequency refractive index for the compounds Co$_2$CrZ (Z= Al, Bi, Ge, Si) are observed as 18.104, 17.602, 17.252 and 17.289 respectively.
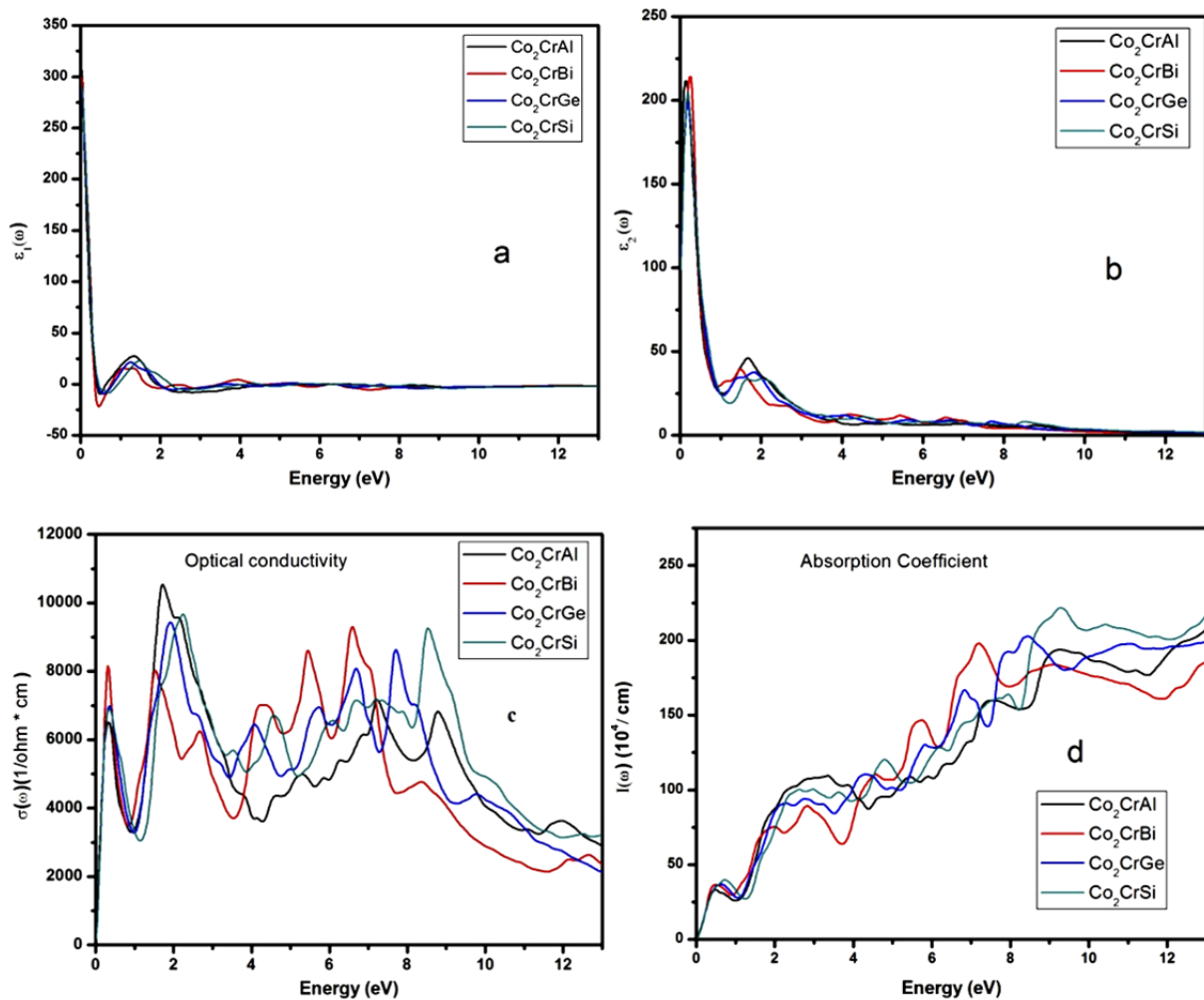
Fig. 6. Calculated optical parameters (a) real part of dielectric function, (b) imaginary part of dielectric function, (c) optical conductivity, (d) absorption coefficient, (e) electron energy-loss function, (f) reflectivity, (g) refractive index and (h) extinction coefficient for Co$_2$CrZ (Z= Al, Bi, Ge, Si).

(continued on next page)
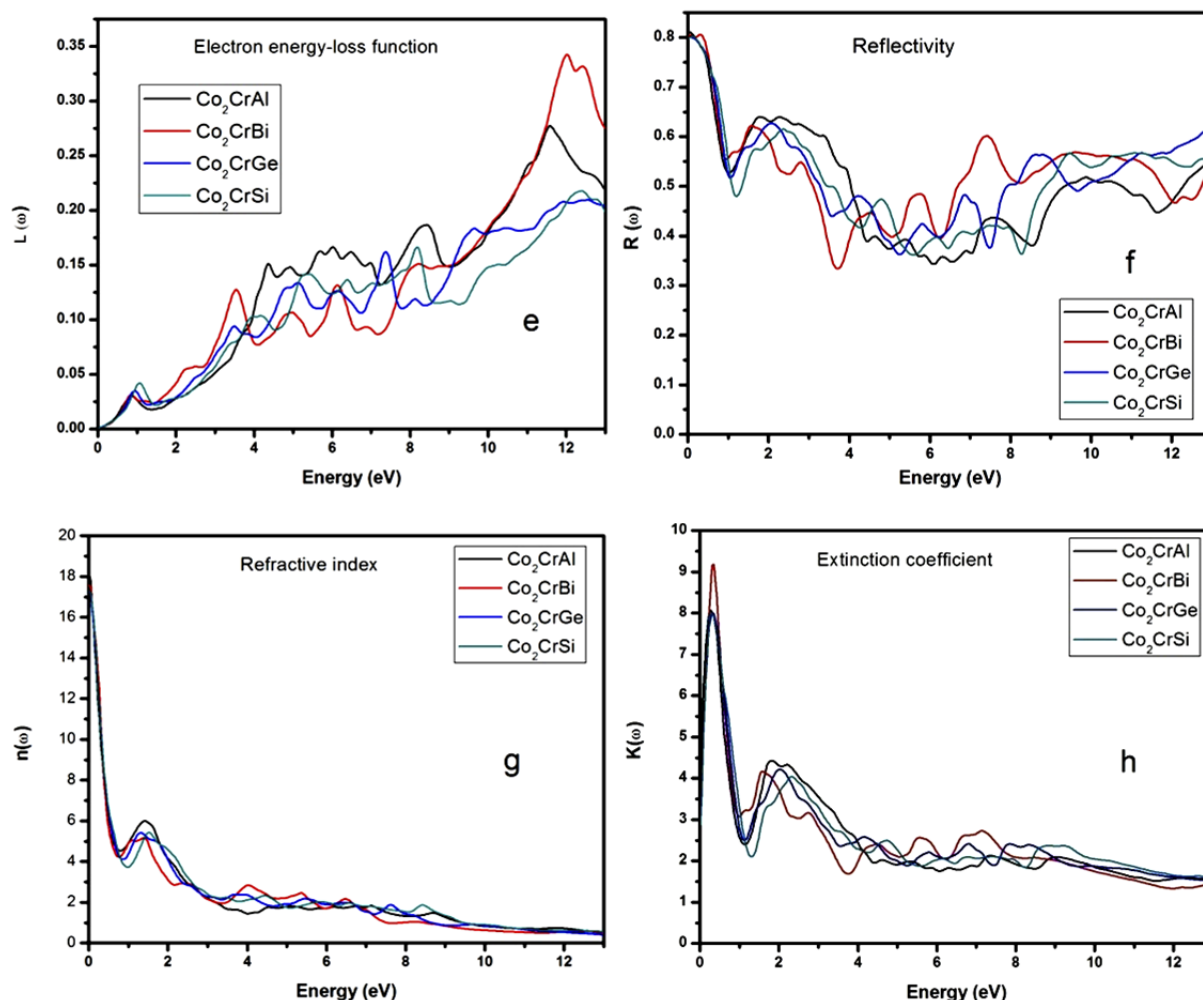
Fig. 6. *(continued)* Calculated optical parameters (a) real part of dielectric function, (b) imaginary part of dielectric function, (c) optical conductivity, (d) absorption coefficient, (e) electron energy-loss function, (f) reflectivity, (g) refractive index and (h) extinction coefficient for Co_2CrZ (Z= Al, Bi, Ge, Si).

CONCLUSIONS

　　　　Structural, electronic, optical and magnetic properties of Co_2CrZ (Z= Al, Bi, Ge, Si) compounds have been studied by using full potential linearized augmented plane wave (FP-LAPW) method implemented in WIEN2k and pseudo-potentials method implemented in Atomistic Tool Kit-Virtual NanoLab (ATK-VNL) within Generalized-gradient approximation (GGA) for exchange-correlation functional. From this study we have found that most of the compounds show half metallicity and 100% spin polarization with $L2_1$ ordered stable structures. Calculated magnetic moments have good agreement with the Slater-Pauling behavior. For above listed compounds, the optical properties named as reflectivity, refractive index, excitation coefficient, absorption coefficient, optical conductivity and electron energy loss have been calculated. Also, we have analyzed their optical spectra. The predicted results of Co_2CrZ (Z= Al, Bi, Ge, Si) are suitable for Spintronic applications.

ORCID IDs
Sukhender, https://orcid.org/0000-0002-2149-5669; **Lalit Mohan**, https://orcid.org/0000-0003-3323-8296
Sudesh Kumar, https://orcid.org/0000-0002-7507-4712; **Deepak Sharma**, https://orcid.org/0000-0001-9163-9050
Ajay Singh Verma, https://orcid.org/0000-0001-8223-7658

REFERENCES
[1]　Fr. Heusler, and E. Take, Trans. Faraday Soc. **8**, 169-184 (1912), http://dx.doi.org/10.1039/TF9120800169.
[2]　J. Li, Y. Li, G. Zhou, Y. Sun, and C. Q. Sun, Appl. Phys. Lett. **94**, 242502 (2009), https://doi.org/10.1063/1.3156811.
[3]　F. Casper, T. Graf, S. Chadov, B. Balke and C. Felser, Semicond. Sci. Technol. **27**, 063001 (2012), https://doi.org/10.1088/0268-1242/27/6/063001.
[4]　R.A. De Groot, F.M. Muller, P. G.Van Engen, and K.H.J. Buschow, Phys. Rev. Lett. **50**, 2024-2027 (1983), https://doi.org/10.1103/PhysRevLett.50.2024.
[5]　S. A. Khandy, I. Islam, D. C. Gupta, and A. Laref, Full Heusler alloys (Co_2TaSi and Co_2TaGe) as potential spintronic materials with tunable band profiles, J. Solid State Chem. **270**, 173-179 (2019), https://doi.org/10.1016/j.jssc.2018.11.011.

[6] T. Graf, C. Felser, and S.S.P. Parkin, Prog. Solid State Chem. **39**, 1-50 (2011), https://doi.org/10.1016/j.progsolidstchem.2011.02.001.

[7] M. Zipporah, P. Rohit, M. Robinson, M. Julius, S. Ralph and K. Arti, AIP Advances **7**, (2017) 055705, https://doi.org/10.1063/1.4973763.

[8] J. Kubler, G. H. Fecher, and C. Felser, Phys. Rev. B, **76**, 024414 (2007), https://doi.org/10.1103/PhysRevB.76.024414.

[9] Z.Q. Bai, Y.H. Lu, L. Shen, V. Ko, G.C. Han and Y.P. Feng, J. Appl. Phys. **111**, 093911 (2012), https://doi.org/10.1063/1.4712301.

[10] V. Ko, G. Han, J. Qiu, and Y. P. Feng, Appl. Phys. Lett. **95**, (2009) 202502, https://doi.org/10.1063/1.3263952.

[11] C. Felser, L. Wollmann, S. Chadov, G.H. Fecher, and S.S.P. Parkin, APL Mater. **3**, 041518 (2015), https://doi.org/10.1063/1.4917387.

[12] Z. Bai, L. Shen, G. Han, and Y.P. Feng, Spin **2**, 1230006 (2013), https://doi.org/10.1142/S201032471230006X.

[13] V. Sharma, and G. Pilania, J. Magn. Magn. Mater. **339**, 142150 (2013), https://doi.org/10.1016/j.jmmm.2013.03.008.

[14] D.P. Rai, A. Shankar, Sandeep, M.P. Ghimire, and R.K. Thapa, J. Theor. Appl. Phys. **7**, 1-6 (2013), https://doi.org/10.1186/2251-7235-7-3.

[15] G.H. Fecher, H.C. Kandpal, S. Wurmehl, and C. Felser, J. Appl. Phys. **99**, 08J106 (2006), https://doi.org/10.1063/1.2167629.

[16] M. Tas, E. Sasıoglu, C. Friedrich, S. Blugel, and I. Galanakis, J. Appl. Phys. **121** (2017) 053903, https://doi.org/10.1063/1.4975351.

[17] H.C. Kandpal, G.H. Fecher, and C. Felser, Journal of Physics D: Applied Physics, **40**(6), (2007), 1587-1592, https://doi.org/10.1088/0022-3727/40/6/S01.

[18] K. Seema, N.M. Umran, and R. Kumar, J. Supercond. Nov. Magn. **29**, 401-408 (2016), https://doi.org/10.1007/s10948-015-3271-7.

[19] P. Blaha, K. Schwarz, G.K.H. Madsen, D. Kvasnicka, and J. Luitz in: *WIEN2k, An Augmented Plane Wave+Local Orbitals Program for Calculating Crystal Properties*, editor: K. Schwarz (Technical Universitatwien, Austria, 2001), ISBN 3-9501031-1-2.

[20] J.P. Perdew, K. Burke, and M. Ernzerhof, Phys. Rev. Lett. **77**, 3865-3868 (1996), https://doi.org/10.1103/PhysRevLett.77.3865.

[21] E. Sjostedt, L. Nordstrom, and D.J. Singh, **114**, 15-20 (2000), https://doi.org/10.1016/S0038-1098(99)00577-3.

[22] Atomistix ToolKit-Virtual Nanolab (ATK-VNL), QuantumWise Simulator, Version. 2014.3, http://quantumwise.com/.

[23] Y.J. Lee, M. Brandbyge, J. Puska, J. Taylor, K. Stokbro and M. Nieminen, Electron transport through monovalent atomic wises, Phys. Rev. B, **69**, 125409 (2004), https://doi.org/10.1103/PhysRevB.69.125409.

[24] H.J. Monkhorst, and J.D. Pack, Phys. Rev. B, **13**, 5188-519 (1976), https://doi.org/10.1103/PhysRevB.13.5188.

[25] F.D. Murnaghan, Proc. Natl. Acad. Sci. USA, **30**, 244-247 (1944), https://doi.org/10.1073/pnas.30.9.244.

[26] D.P. Rai, and R.K. Thapa, J. Alloys Comp. **542**, 257-263 (2012), https://doi.org/10.1016/j.jallcom.2012.07.059.

[27] S. Wurmehl, G.H. Fecher, H.C. Kandpal, V. Ksenofontov and C. Felser, Appl. Phys. Lett. **88**, 032503 (2006), https://doi.org/10.1063/1.2166205.

[28] R. Jain, N. Lakshmi, V.K. Jain, V. Jain, A.R. Chandra, and K. Venugopalan, J. Magn. Magn. Mater. **448**, 278-286 (2018), https://doi.org/10.1016/j.jmmm.2017.06.074.

[29] S. Sharma, A.S. Verma, and V.K. Jindal, Materials Research Bulletin **53**, 218-233 (2014), https://doi.org/10.1016/j.materresbull.2014.02.021.

СТРУКТУРНІ, ЕЛЕКТРОННІ, ОПТИЧНІ ТА МАГНІТНІ ВЛАСТИВОСТІ СПОЛУК ХІСЛЕРА Co$_2$CrZ (Z = Al, Bi, Ge, Si)

Сухендер[a], Лаліт Мохан[a], Судеш Кумар[b], Діпак Шарма[c], Аджай Сінгх Верма[a]*

[a]Фізичний факультет, Банастхалі Відяпіт, Банастхалі 304022, Індія; [b]Хімічний факультет, Банастхалі Відяпіт, Банастхалі 304022, Індіят; [c]Фізичний факультет, Інженерний коледж ІІМТ, Велика Нойда, Індія

У цій роботі ми вивчили структурні, електронні, оптичні та магнітні властивості сполук Co$_2$CrZ (Z = Al, Bi, Ge, Si) за допомогою двох різних методів, один – це метод повноцінної лінеаризованої розширеної плоскої хвилі (FP-LAPW) реалізований у WIEN2k, а другий – псевдопотенційний метод, реалізований у Atomistic Tool Kit-Virtual NanoLab (ATK-VNL). Відповідні заборонені зони для Co$_2$CrZ (Z = Al, Bi, Ge, Si) знаходяться біля рівня Фермі 0,696, 0,257, 0,602 і 0,858 eB, що реалізовано в коді WIEN2k і показують 100% спінову поляризацію. Крім того, було виявлено, що ці сполуки є ідеально напівметалічними феромагнітами (HMF). Однак вищезгадані сполуки показують нульові заборонені зони в коді ATK-VNL. Обчислений методом FP-LAPW магнітний момент цих сполук Co$_2$CrZ (Z = Al, Bi, Ge, Si) становить 3,06, 4,99, 3,99 і 3,99 μ_B відповідно. Однак у коді ATK-VNL відповідний магнітний момент цих сполук становить 3,14, 5,08, 4,11 та 4,08 μ_B. Оптичні властивості відіграють важливу роль для розуміння природи матеріалу, чи можна його використовувати як пристрій оптоелектроніки. Обчислені з оптичних спектрів комплексні діелектричні функції з використанням WIEN2k становлять 312,70 і 141,991, 299,812 і 111,368, 288,127 і 106,342, 290,688 і 99,095 для сполук Co$_2$CrZ (Z = Al, Bi, Ge, Si) відповідно. Максимальні втрати енергії для вище зазначених сполук спостерігаються між 11,4 до 13eB. Значення показника заломлення для сполук Co$_2$CrZ (Z = Al, Bi, Ge, Si) спостерігаються як 18.104, 17.602, 17.252 і 17.289 відповідно. В спектрі оптичної провідності різкий пік спостерігається при 1,6 - 2,3eB.

КЛЮЧОВІ СЛОВА: напівметалічний феромагнетик, заборонена зона, діелектрична константа, магнітний момент

СТРУКТУРНЫЕ, ЭЛЕКТРОННЫЕ, ОПТИЧЕСКИЕ И МАГНИТНЫЕ СВОЙСТВА СОЕДИНЕНИЙ ХИСЛЕРА Co$_2$CrZ (Z = Al, Bi, Ge, Si)

Сухендер[a], Лалит Мохан[a], Судеш Кумар[b], Дипак Шарма[c], Аджай Сингх Верма[a]*

[a]Физический факультет, Банастхали Видяпит, Банастхали 304022, Индия; [b]Химический факультет, Банастхали Видяпит, Банастхали 304022, Индия; [c]Физический факультет Инженерный колледж ИИМТ, Большая Нойда, Индия

В этой работе мы изучили структурные, электронные, оптические и магнитные свойства соединений Co$_2$CrZ (Z = Al, Bi, Ge, Si) с помощью двух различных методов, один - это метод полноценной линеаризованной расширенной плоской волны (FP-LAPW) реализован в WIEN2k, а второй - псевдопотенцийный метод, реализованный в Atomistic Tool Kit-Virtual NanoLab

(ATK-VNL). Соответствующие запретные зоны для Co_2CrZ (Z = Al, Bi, Ge, Si) находятся около уровня Ферми 0,696, 0,257, 0,602 и 0,858 эВ, что реализовано в коде WIEN2k и показывают 100% спиновую поляризацию. Кроме того, было обнаружено, что эти соединения являются идеально напивметаличними ферромагниты (HMF). Однако вышеупомянутые соединения показывают нулевые запретные зоны в коде ATK-VNL. Исчисленный методом FP-LAPW магнитный момент этих соединений Co_2CrZ (Z = Al, Bi, Ge, Si) составляет 3,06, 4,99, 3,99 и 3,99 μ_B соответственно. Однако в коде ATK-VNL соответствующий магнитный момент этих соединений составляет 3,14, 5,08, 4,11 и 4,08 μ_B. Оптические свойства играют важную роль для понимания природы материала, можно ли его использовать как устройство оптоэлектроники. Вычисленные из оптических спектров комплексные диэлектрические функции с использованием WIEN2k составляют 312,70 и 141,991, 299,812 и 111,368, 288,127 и 106,342, 290,688 и 99,095 для соединений Co_2CrZ (Z = Al, Bi, Ge, Si) соответственно. Максимальные потери энергии для вышеуказанных соединений наблюдаются между 11,4 до 13эВ. Значение показателя преломления для соединений Co_2CrZ (Z = Al, Bi, Ge, Si) наблюдаются как 18.104, 17.602, 17.252 и 17.289 соответственно. В спектре оптической проводимости резкий пик наблюдается при 1,6-2,3эВ.
КЛЮЧЕВЫЕ СЛОВА: полуметаллический ферромагнетик, запретная зона, диэлектрическая постоянная, магнитный момент

SPEED MEASUREMENT IN AN ACCOMOVING REFERENCE SYSTEM

ⓘ**Volodymyr M. Svishch**
National Aerospace University "Kharkiv Aviation Institute"
17, Chkalova St., Kharkiv, 61070, Ukraine
Corresponding Author: vladimir.svishh@rambler.ru
Received February 13, 2020; revised March 2, 2020; accepted March 10, 2020

A method of direct measurement of the observer's velocity (peculiar velocity) relative to the accompanying reference system is proposed and investigated. To measure peculiar velocity, it is proposed to use the measurement of stellar light aberration. A comparison of the use of light aberration and the Doppler Effect for measuring velocity relative to relic radiation was made. When using the Doppler Effect, the total speed of the observer was measured - the Hubble speed and the radial component of the peculiar speed of the observer. As a result of the analysis of the components of the observer's velocity in the comoving reference frame, the Hubble and peculiar velocities of the observer, their essential features are formulated. The analysis of the shape of the wave fronts of the CMB radiation, the radiation of quasars, the radiation of stars and the radiation of ground sources is given. As a consequence of this analysis, the decisive influence of the shape of their wave fronts on the possibilities of measuring stellar aberration and the absence of such an effect when measuring velocity using the Doppler Effect are shown. Measurement of light aberration in an inertial system enables direct measurement of the observer's peculiar velocity in an comoving reference frame. Knowing the observer's peculiar velocity is important for increasing the accuracy of determining the Hubble velocity of especially objects of relatively small remoteness. The proposed structures of devices for measuring the peculiar velocity of an inertial reference system were investigated. Peculiar speed is determined by the measured light aberration without switching to another frame of reference. Their expected accuracy and reliability were evaluated. The practical use of the proposed structures is possible in astronomy and spacecraft.
KEYWORDS: relict radiation, stellar light aberration, comoving reference frame, Hubble velocity, peculiar velocity, collimator, photo detector.

The measurement of the observer's speed relative to other objects (stars, galaxies, blazars, relict background) is primarily associated with the characteristics of their radiation. The most ancient radiation that can be observed in general in the universe is relict. In accordance with the inflation hypothesis, this residual radiation fills the space of a constantly expanding universe after "separation" from the plasma of the Universe cooled to 3000K about 300,000 years after the Big Bang [1-4]. In fact relict radiation was discovered by Penzias and Wilson in the Laboratory named after Bell in 1964 [5]. In the early 80s with the development of the space industry, it was possible to establish the property of isotropy of relict radiation. In 2006, John Mather and George Smoot were awarded the Nobel Prize in Physics for their discovery of the blackbody shape of the spectrum and the anisotropy of cosmic microwave background radiation.

The results of J. Mather and J. Smoot were confirmation of the origin of the universe as a result of the Big Bang [6-10]. According to the observations of the COBE satellite and the calculations performed, all galaxies and constellations move relative to relict radiation with great speed, about hundreds of kilometers per second.

The measurement of our own velocity relative to relict radiation is an important task in understanding the structure of the Universe.

The temperature of the relict radiation in the direction of the constellation Leo is 0.1% higher, and in the opposite direction 0.1% lower [11-13]. This fact is interpreted because of the Doppler effect that occurs when the Sun moves relative to the "motionless" relict background at a speed of about 370 km/s towards the constellation Leo. That is, the Doppler shift of the radiation frequency caused by our own speed relative to the reference frame associated with relic radiation. These measurements allow better understanding both the structure of the modern Universe and the early moments of its history [12, 13].

Relict radiation is isotropic only in the coordinate system associated with the entire system of scattering galaxies, in the so-called "comoving reference frame", which expands with the Universe. In any other coordinate system, the relict radiation intensity depends on the direction, the so-called dipole component. The comoving reference system is thus distinguished from all other reference systems (a selected reference system - SRS), since only in it the proper, peculiar velocity of the observer and all objects of the universe is directly determined.

By the definition of an comoving reference system, only in it are states possible for a system A with a dipole component of relict radiation equal to 0 in any given point of space. This is the only "absolutely" resting frame of reference – SRS.

$$v_\Sigma = v_H + v_{p=0}, v_H = 0, v_p = 0. \tag{1}$$

Here, v_H - hubble velocity component of the total v_Σ velocity, determined by the expansion of the Universe; v_p-peculiar (intrinsic) system A speed.

The vector magnitudes of the velocities, in the SRS are always collinear due to the isotropy of the expansion of space. The collinearity of vectors allows us not to focus on this further when adding or subtracting them.

Measurements from artificial Earth satellites using the Doppler shift of the radiation frequency substantially refined the data of the dipole component [14].

However, the speed of the observer directly affects the observation of extraterrestrial objects. The effect of stellar aberration primarily manifested this influence. The expression of its magnitude directly includes the speed of the observer.

Light aberration was measured only with a relative change in the observer's speed relative to starlight, associated, for example, with the daily rotation of the Earth (daily), with the orbital movement of the Earth around the Sun (annual), of the Sun around the core of the Galaxy (secular). Their measurements are taken, passing from an inertial system with one speed to an inertial system with another speed [15]. These velocities, and the corresponding aberrations, are components of the observer's full, peculiar velocity and the corresponding complete aberration. Since it is not possible to change the completely peculiar velocity, complete aberration $\alpha = \arcsin\frac{v_p}{c}$ considers unobservable.

In any closed inertial reference system containing an observer and a radiation source (in a "car"), their mutual position is known. Therefore, if it is possible to measure the aberration of the source in this system, the peculiar velocity v_{pi} of the system is easily determined.

The possibility of measuring the full aberration of light and its observer's own motion velocity hasn't been previously considered.

The study of the possibility of measuring the speed of the observer relative to the selected reference system (SRS) associated with relic radiation, and the possibility of measuring the speed of the inertial reference system (IRS) relative to the SRS without moving to the SRS or any other IRS using full stellar aberration is the goal of this work.

FEATURES OF THE DOPPLER EFFECT AND STELLAR ABERRATION

We consider the components of the observer's velocity in the SRS v_Σ taking into account the features of this reference system associated with relic radiation.

Let's distinguish two components of the observer's velocity v_Σ, v_p - the peculiar, intrinsic velocity of the observer relative to the SRS, associated with a change in the position of the observer in space, and v_H − the Hubble velocity, associated with the expansion of the space of the Universe (inflationary, gamma) $v_\Sigma = v_H + v_p$.

The peculiar v_p and Hubble v_H speeds are fundamentally different.

If the observer's own peculiar velocity v_p can't exceed the light speed c ($v_p \le c$), then the (inflationary) Hubble expansion speed of space v_H can exceed it $c \ge v_H \ge c$.

The second fundamental difference: the peculiar velocity v_p is oriented in space (anisotropic) and does not depend on the distance of the observer to the beginning of the SRS, and the Hubble speed v_H is isotropic in direction (doesn't depend on the direction) and depends on the distance from the object to the beginning of the reference system $v_H = H(t)dl$. Hubble speeds v_{HA} of v_{HB} an equidistant from two points observer will be equal in magnitude, and points of space A and B located in the same direction will be equal in magnitude, but oppositely directed $v_{HA} = -v_{HB}$.

Because of measuring the Doppler shift of the relic radiation frequency will have common velocities $v_{\Sigma A} = v_{HA} + v_{pA}$, $v_{\Sigma B} = v_{HB} - v_{pB}$, $v_{HA} = -v_{HB}$ in opposite directions A, B. Half of the difference in these velocities is equal to the component of the peculiar velocity v_p of the observer in the direction A, B

$$v_{pAB} = \frac{v_{\Sigma A} - v_{\Sigma B}}{2}. \tag{2}$$

The maximum of this difference using the Doppler Effect allows you to determine the magnitude and direction of the Earth's own speed relative to the relict radiation. The search for the maximum of this difference is caused by the fact that the Doppler Effect determines the radial velocity directed along the propagation of the light wave.

Unlike the Doppler Effect, stellar aberration depends directly on observer's own speed v_p $\alpha = \arcsin\frac{v_p}{c}$. Measurement of stellar aberration of relict radiation sources would directly determine the peculiar velocity of the observer $v_p = c\sin\alpha$. However, measuring stellar aberration of relict radiation sources is difficult due to its significant features compared to the Doppler Effect.

Let consider the features of stellar aberration and the Doppler Effect as applied to the measurement of the observer's own speed, taking into account the previous analysis of the relic radiation features.

Let choose such stars from the set of stars A and B that their speeds v_A and v_B are equal in magnitude to observer' speed v_n and are multidirectional $v_n = v_A = -v_B$. However, their aberrations are equal $\alpha_A = \alpha_B = \arcsin\frac{v_n}{c}$.

This indicates that:

1) the speed of light c is independent of the speed v_A, v_B of the source [17];
2) stellar aberration depends on telescopes speed v_n relative to the speed of light flux inside the telescope [16];

3) stellar aberration is observed in an inertial system $v_A = v_n$ with a fixed source (star A) and an observer.

Similar conditions exist on the Earth with ground sources. However, stellar aberration of terrestrial sources is not observed.

Let's compare stellar aberration and the Doppler Effect in more detail.

First, stellar aberration does not depend on the source velocity [17]. The Doppler Effect depends on the relative velocity of the source and observer including the Hubble velocity. The Doppler Effect is absent with equal speeds of the observer and the source. That is, in a moving inertial system with a source and an observer, the Doppler Effect is not observed.

Aberration is also observed in a moving inertial system with a fixed source. (An example of a star having a speed equal to the speed of the observer during the radiation of the light flux entering the telescope input at the time of measurement - see above). However, only parts of its components (daily, annual) were measured.

This is because, since the position of the star is unknown, measurements have to be made when moving from one inertial system to an inertial system with another opposite speed. From the measured difference in the positions of the star at opposite speeds, double aberration $2\alpha_n$ is determined. The impossibility of practical independent determination of the position of the star at the time of measurement determines it.

Thus, having a fixed source, with its fixed position relative to the observer, the observer in the inertial system can measure the stellar aberration of the source without switching to another inertial system, as the deviation of the observation pipe from the known position of the source. Using the known aberration of the source α_n, the observer would determine the speed v_n of the inertial system during measurement relative to the light flux of the source without going beyond the inertial system $v_n = c \sin \alpha_n$.

However, we don't observe the aberration of ground sources.

Stellar aberration depends on the speed of the observer perpendicular to the propagation direction of the light wave of the remote radiation source ("very far from the origin") [17].

The condition of the distance of the radiation source from the observer actually determines the requirements for the wave front shape of the radiation source at the input of the stellar aberration-measuring device. That is, the light wave of a star has a plane wave front. A plane wave is characterized by the fact that the direction of its propagation and the amplitude are the same everywhere [18, 19]. When measuring using the Doppler Effect, such requirements for the shape of the wave front of the source do not arise.

Stellar aberration depends on the speed of the device relative to the propagating light wave in place and while the measuring device is in space (here and now).

Thus, stellar aberration depends on the peculiar velocity of the observer at a given time, at a given point in space and does not depend on its Hubble velocity. This allows determining the component of the current peculiar observer's velocity using the aberration value.

In measurements, using the Doppler Effect, we obtain the sum of the radial, peculiar, and Hubble velocities. The Doppler Effect of stationary ground sources and the observer is absent due to its physical nature. The stellar aberration of terrestrial sources should essentially be observed, but is not observable.

Let us consider the differences between the essential parameters of the radiation of the observed sources during measurements of stellar aberration and the Doppler Effect.

The frequency spectra of the sources are very diverse and their analysis allows you to get rich information about the sources, medium and space that their radiation passed to the observer. To measure speed using the Doppler Effect, the most important parameter is the frequency shift. Stellar aberration is independent of the radiation frequency of the source. Another parameter is the shape of the wave fronts of the sources.

SHAPE OF WAVE FRONTS OF SOURCES

The shape of the wave fronts does not significantly affect the Doppler Effect, but is very important when observing stellar aberration. The equality of the velocities of the relict radiation, the radiation of distant quasars, the radiation of the stars of our Galaxy and the radiation of ground sources follow based on the independence of the speed of light from the speed of the source and the constancy of its value in vacuum. However, the shapes of their wave fronts are significantly different.

The wave front of radiation of ground-based point sources has a spherical shape of positive curvature $\rho = \frac{1}{R}$, where R has a finite value. The direction of wave propagation at each point of the wave front coincides with the radius of this point from the center of the sphere at the time of wave emission [18]. The wave front of the emission of stars in our Galaxy is almost flat due to their remoteness $R \approx (4 - 300000)$ of light years and the curvature of their wave fronts $\rho \approx 0$. The wave front of the radiation of quasars (blazars) is also flat due to their even greater remoteness. Their distance at redshift is $z = (2 - 20)$. A plane wave differs by the property that its direction of propagation and amplitude are the same everywhere.

Sources of relict radiation are also removed even further. Their remoteness by redshift $z \geq 1000$ $R \approx \infty$, however, they were extremely specific. Sources of relict radiation are everywhere around us. They scatter in all directions from the observer with a Hubble speed v_H significantly exceeding the speed of light ($z \geq 1000$). The wave front of their

total radiation is similar to the wave front of a source of radiation of negative curvature $(-\rho \to -\infty - R \to 0)$ at the observation point.

Relict radiation is isotropic in all directions. This causes difficulties in increasing the accuracy of determination using the Doppler effect of the direction of the vector of our own velocity relative to the SRS, associated with relic radiation. Measuring aberration relative to relict radiation is impossible because of its isotropy and the curvature of its wave front.

Thus, aberration is not observed in relict radiation$(-\rho \to -\infty)$, ground-based sources stationary relative to the observer ($\rho = \frac{1}{R}$ - is the finite value of the spherical wave front) and is observed in stars and blazars (including stars that are stationary relative to the observer, $\rho \approx 0$ - a plane wave front).

That is, when observing a nearby (not remote) source located in the same inertial system with the observer, but having a plane wave front ($\rho \approx 0$) similar to a stellar one, it becomes possible to measure the aberration of such a source [18]. From the measured aberration of such a source, it is easy to determine the intrinsic speed v_p of the inertial system without going beyond this system.

Since the position of the source in the inertial system is known, there is no need to switch to another inertial system, for measure of full light aberration. There is the possibility of prolonged observation of the peculiar velocity of the Earth and its possible changes.

Let consider the possible structures of the peculiar velocity v_p meters of an inertial system without going beyond this system, for full aberration measure.

PECULIAR VELOCITY METERS

The measurement of the observer's own speed is important not only in cosmology. Such measurements are practically important for spacecrafts in deep space exploration. When accelerometers do not work for a long time, in addition to measurement accuracy, the reliability of the device is important. Let consider some measuring instruments of own speed.

The structure of possible peculiar velocity meters consists of blocks 1, 2, 3 measuring the velocity v_p components installed on the x, y, z axes of the observer's reference frame (Fig. 1). Blocks 1, 2, 3 (Fig. 2) associated with the block 4 of the processing of their output information.
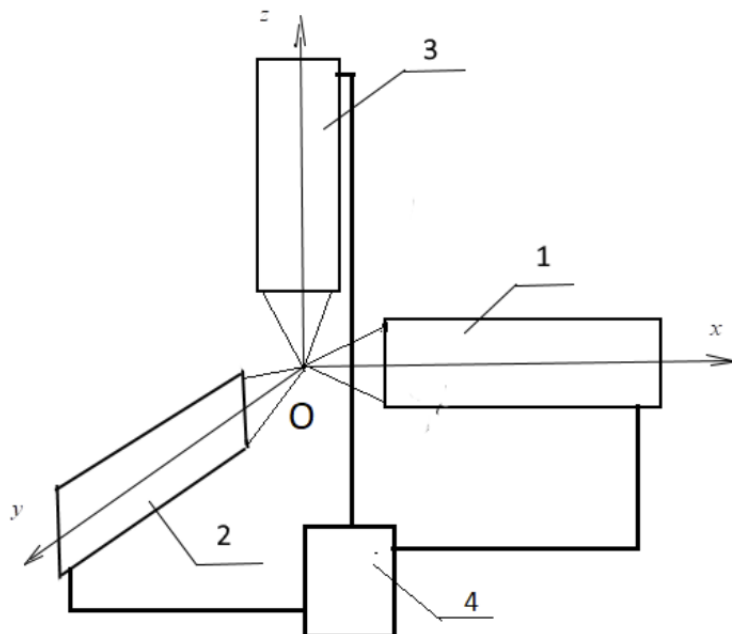
Fig 1. Peculiar velocity meters structure

Meters differ in the used measuring units. The simplest measurement unit 2.1 (Fig. 2) consists of a point radiation source 1, a collimator 2, a lens 3, a body 4, and a photo detector 5. The photo detector can be made in the form of a positional sensitive two-dimensional photo matrix or an analog two-dimensional sensitive element.

The photo detector 5 is installed in the perpendicular optical axis of the plane-measuring 2.1 unit with mutually perpendicular directions at a distance from the lens 3. Each measurement unit is mounted on the corresponding axis of the observer's reference system so that the selected directions of their photo detectors coincide with the direction of the axes perpendicular to the installation axis of the measurement unit. To increase the sensitivity, an eyepiece can be installed in front of the photo detector.

Thus, each photo detector 5 is a two-dimensional screen $s_z - x, y$; $s_x - z, y$; $s_y - z, x$ with axes perpendicular to the corresponding installation axis of the measuring unit z, x, y (Fig. 3).

The spherical waveform of a point source compensates for the aberration caused by the movement of the device with a ground source [18]. Therefore, when assembling each measurement unit, the relative position of the point source 1, lens 3 and photo detector 5 without collimator 2 is adjusted. The image of source 1 is focused at the beginning of the corresponding coordinates of photodetector 5. This alignment fixes the location of point source 1, lens 3 and the origin of photo detector 5 on the optical axis of the measurement unit.
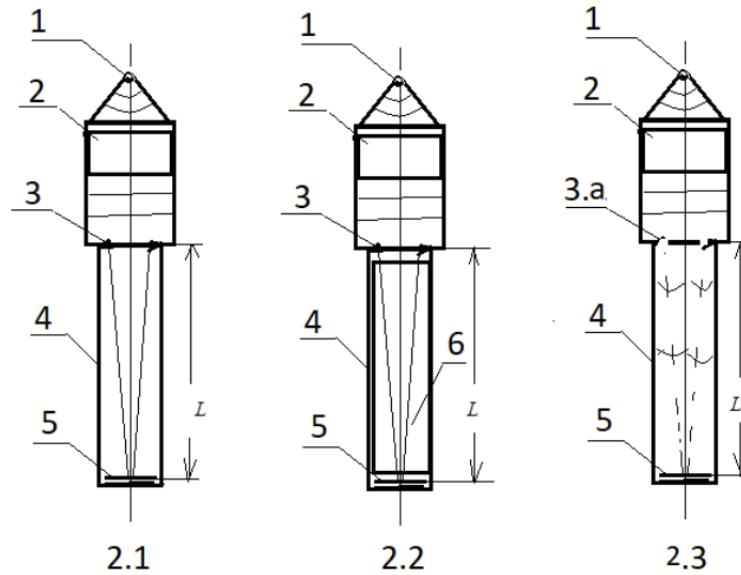
Fig.2. Measurement blocks 2.1, 2.2, 2.3.

Then, to form a plane wave front perpendicular to the optical axis of the measurement unit, a collimator 2 is installed and the image of source 1 is refocused without reference to the origin of the photo detector 5. Thus, the conditions for observing a "star" with a known fixed position on the optical axis of each measurement unit are created.
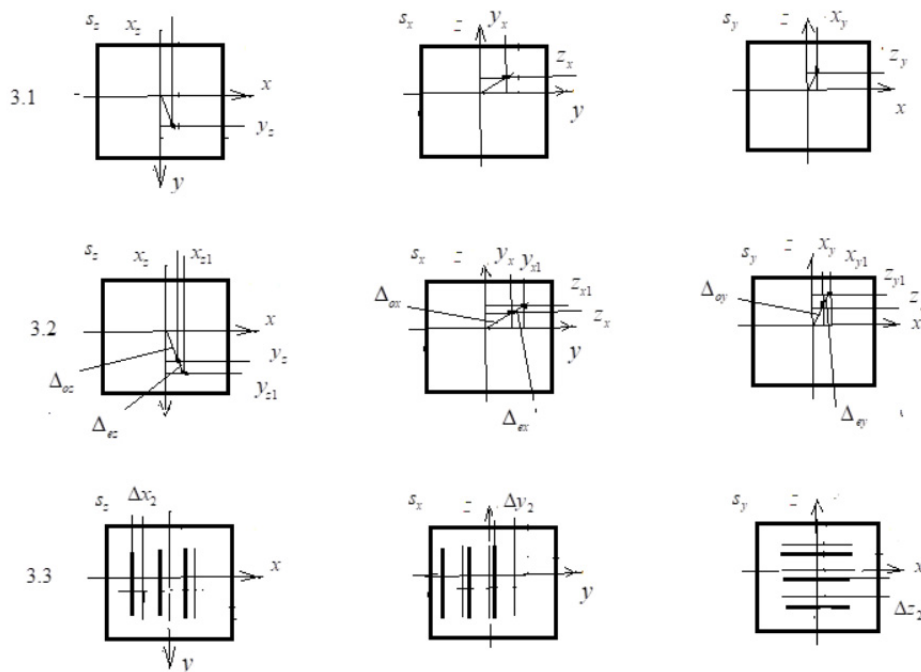
Fig. 3. Measurement screens

After installing the aligned measurement units along the axes z, x, y on the photo detectors s offsets Δ_i from Δ_z, Δ_x, Δ_y are proportional to the corresponding velocity v_{pi} component Δ_{ip}.

As shown in [18], aberration $\propto_{ip} = \frac{v_{ip}}{c} \sin \Psi_i \approx \frac{\Delta_i}{L}$. Hence, the velocity v_{pi} component v_{ip} is equal to

$$v_{ip} = c \frac{\Delta_i}{L} \frac{1}{\sin \Psi_i}, \tag{3}$$

where L – is the pipe length of the measuring unit, Ψ_i - is the angle between v_{ip} and the axis of the measuring unit.

According to the components v_{ip}, projections of the vector of the current peculiar velocity of the meter in the observer's reference system are obtained, proportional $s_z - x_z, y_z; s_x - y_x, z_x; s_y - x_y, z_y$ (Fig. 3.1). Projections of the peculiar velocity vector on the axes of the same name z, x, y on different photo detectors should be equal to $x_z = x_y, y_z = y_x, z_x = z_y$. Using these projection values, the processing unit calculates the magnitude and direction of the vector v_{pi} of the current peculiar velocity of the meter in the observer's reference system. Aberration measurements can be made using optically active materials [16]. The refractive indices of an ordinary ray and an extraordinary ray $n_e \neq n_o$ are different in the direction perpendicular to the optical axis of the uniaxial optically active substance 6 (2.2, Fig. 2). This leads to a difference in the aberration angles of the ordinary and extraordinary ray $\propto_e = \frac{n_o^2}{n_e^2} \propto_o$ and their displacements $\Delta_{oz} \Delta_{ox} \Delta_{oy} \Delta_{ez} \Delta_{ex} \Delta_{ey}$ [16]. Accordingly, the expressions for the projections of the velocity v_{pi} component v_{ip} along the ordinary v_{oip} and extraordinary v_{eip} rays will be $v_{oip} = c \frac{\Delta_{oi}}{L} \frac{1}{\sin \Psi_i}$ and $v_{eip} = c \frac{n_e^2}{n_o^2} \frac{\Delta_{ei}}{L} \frac{1}{\sin \Psi_i}$, where L is the length of the tube of the measuring unit with an optically active substance.

When using filled with a uniaxial optically active substance with an axis that coincides with the optical axis of the measurement units 2.2 (Fig. 2), they are aligned with the reference to the origin of the photo detectors without collimator 2 using an ordinary ray. Then, a collimator 2 is installed and focusing is again performed without reference to the origin of the photo detector 5. For installed aligned measurement units with optically active substance along the axes z, x, y the photo detectors receive double images of sources 1, according to ordinary $x_z x_y y_z y_x z_x z_y$ and extraordinary $x_{z1} x_{y1} y_{z1} y_{x1} z_{x1} z_{y1}$ rays (Fig. 3.2).

Projections of the current peculiar velocity $v_{oip} = c \frac{\Delta_{oi}}{L} \frac{1}{\sin \Psi_i}$ vector of the meter $s_z - x_z, y_z; s_x - y_x, z_x; s_y - x_y, z_y$ correspond to images of a source along an ordinary ray. Images of a source along an extraordinary ray $s_z - x_{z1}, y_{z1}; s_x - y_{x1}, z_{x1}; s_y - x_{y1}, z_{y1}$ also correspond to projections of the current peculiar velocity vector $v_{eip} = c \frac{n_e^2}{n_o^2} \frac{\Delta_{ei}}{L} \frac{1}{\sin \Psi_i}$.

Here, the difference in the refractive indices of the ordinary and extraordinary rays $n_e \neq n_o$ in the perpendicular optical axis of the measurement units is taken into account [16]. By these values of the projections, by the ordinary ray $s_z - x_z, y_z; s_x - y_x, z_x; s_y - x_y, z_y$ and on an extraordinary ray $s_z - x_{z1}, y_{z1}; s_x - y_{x1}, z_{x1}; s_y - x_{y1}, z_{y1}$, the processing unit calculates the magnitude and direction of the vector v_{pi} of the current peculiar speed of the meter on ordinary v_{oip} and extraordinary v_{eip} rays. Their values must be equal $v_{oip} = v_{eip}$.

To measure the peculiar velocity using a Young's interferometer [18], light sources 1 were installed in the measurement units 2.3 (Fig. 2), in the form of a brightly lit narrow gap. Instead of lenses 3, there are installed screens 3.a with narrow slots parallel to the slit of light source 1 so that the slits of light source 1 and screens are perpendicular to the corresponding axes x, y, z of photo detectors 3.3 $s_z s_x s_y$ in the observer's reference frame (Fig. 3).

When adjusting the measurement units, the position of the interference pattern on the photo detectors $s_z s_x s_y$ is fixed. The collimators 2 of the luminous flux of the source 1 are installed in the aligned measurement blocks 2.3. The collimators 2 provide the output of the luminous flux with a plane wave front parallel to the plane of the screen 3.a.

The interference patterns on the photo detectors 3.3 $s_z s_x s_y$ will shift to $\Delta i_2 = -L_2 \frac{v_{ip}}{c} \sin \Psi$ in the opposite direction to the corresponding components v_{ip} of the velocity v_{pi}. Based on these values $\Delta x_2 \Delta y_2 \Delta z_2$ projections, the processing unit calculates the components $v_{ip} = \frac{\Delta i_2}{L_2 \sin \Psi} c$ and from them the magnitude and direction of the vector v_{pi} of the current peculiar velocity of the meter [18].

To calculate the current peculiar velocity vector by processing unit 4 (Fig.1), the projection values of the measurement units along any two axes are sufficient. Projection values from the third measurement unit can be used to increase the accuracy and reliability of measurements.

The projection values for an ordinary ray and for an extraordinary ray when using measurement units filled with uniaxial optically active substance 6 (2.2, Fig. 2) can be used to further increase the reliability of measurements. This is especially important when measuring the current speed of vehicles in deep space.

The use of measurement 2.3 (Fig.3) units with a Jung's interferometer makes it possible to measure the velocity v_{pi} component v_{pi} along only one axis in the observer's reference frame. However, the use of a shift in the interference pattern on photodetectors can improve the accuracy of measuring the velocity component.

In all analysis results, first-order quantities $\frac{v}{c}$ are obtained. The influence of motion (second order $\Delta t, \Delta r$ magnitude $\frac{v^2}{c^2}$) determined by the Lorentz transformations here may not be taken into account when measuring order magnitudes $\frac{v}{c}$.

CONCLUSIONS

1. Measurement of light aberration in a closed inertial system enables direct measurement of the (peculiar) speed of the observer in a comoving, selected reference system (SRS) without the Hubble component.

2. By measuring the component of the current peculiar velocity vector v_H in the selected direction, and by the total speed v_Σ using the Doppler effect, it is easy to calculate the Hubble speed determined by Universe expansion v_H (averaged) by $z \geq 1000$ in the same direction.

3. The expected accuracy of measuring the speed of the inertial reference system is better for a device with measuring units based on Jung's interferometer.

4. In a device with blocks filled with a uniaxial optically active substance, we obtain double duplication of the measurement channels. This increases the reliability of the devices, which is important when used to track the peculiar speed of the Earth and in spacecrafts for deep research.

ORCID IDs

Volodymyr M. Svishch, https://orcid.org/0000-0003-2903-5744

REFERENCES

[1] Ya.B. Zeldovich, Hot model of the Universe. UFN, **89**, 647-668 (1966), https://doi.org/10.3367/UFNr.0089.196608e.0647.
[2] Ya.B. Zeldovich and R.A. Syunyaev, Astrophys. Space Sci. **6**, 358-376 (1970), https://doi.org/10.1007/BF00653855.
[3] Ya.B. Zeldovich and I.D. Novikov, *The structure and evolution of the Universe*, (Nauka, Moscow, 1975). (in Russian)
[4] S. Weinberg, *The First Three Minutes: A Modern View of the Origin of the Universe*, (Basic books, New York, 1977).
[5] A. Penzias, Rev. Mod. Phys. **51**, 425 (1979), https://www.nobelprize.org/uploads/2018/06/penzias-lecture.pdf.
[6] J. Silk, *The Big Bang. The birth and evolution of the Universe*. (Mir, Moscow, 1975), pp. 391. (in Russian)
[7] A.D. Dolgov, Ya.B. Zeldovich and M.V. Sagin, *Cosmology of the Early Universe*. (MSU, Moscow, 1988), pp. 199. (in Russian)
[8] I.D. Novikov, *Evolution of the Universe*, (Nauka, Moscow, 1990), pp. 192. (in Russian)
[9] D.I. Novikov, in: *Historical Development of Modern Cosmology, ASP Conference Series*, **252**, edited by V.J. Martínez, V. Trimble and M.J. Pons-Bordería, (ASP Publisher, San Francisco, 2001).
[10] Yu.N. Eroshenko, Physics-Uspekhi, **8**, 181 (2011), https://doi.org/10.3367/UFNe.0181.201108c.0858.
[11] R.J. Bouwens, P.A. Oesch, G.D. Illingworth, I. Labbe, P.G. van Dokkum, G. Brammer, D. Magee, L. Spitler, M. Franx, R. Smit, M. Trenti, V. Gonzalez and C.M. Carollo, https://doi.org/10.1088/2041-8205/765/1/L16.
[12] P.J.E. Peebles, *Principles of Physical Cosmology*, (Princeton University Press, Princeton, 1993), pp. 736.
[13] A. Kovács and J. García-Bellido, Monthly Notices of the Royal Astronomical Society, **462**(2), 1882–1893 (2016), https://doi.org/10.1093/mnras/stw1752.
[14] A.V. Zasov and K.A. Postnov, *General astrophysics*, (Fryazino, 2005), pp. 496. (in Russian)
[15] L.D. Landau and E.M. Lifshits, *The theory of field*, (Fizmatlit, Moscow, 2003), pp. 534.
[16] V.M. Svishch, East Eur. J. Phys. **4**(3), 71-77 (2017), https://doi.org/10.26565/2312-4334-2017-3-10.
[17] A. Einstein, *Collection of Transactions Vol.1*, (Nauka, Moscow, 1965), pp. 702. (in Russian)
[18] V.M. Svishch, East Eur. J. Phys. **5**(3), 24-31 (2018), https://doi.org/10.26565/2312-4334-2018-3-03.
[19] V.M. Svishch, Optics, **7**(2), 74-79 (2018), https://doi.org/10.11648/j.optics.20180702.13.

ВИМІРЮВАННЯ ШВИДКОСТІ В СУПУТНІЙ СИСТЕМІ ВІДЛІКУ
В.М. Свищ

Харківський національний аерокосмічний університет ім. М.Є. Жуковського «Харківський авіаційний інститут»
вул. Чкалова 17, Харків, Україна, 61070

Запропоновано та досліджено спосіб прямого виміру швидкості спостерігача (пекулярної швидкості) відносно супутньої системи відліку. Для виміру пекулярної швидкості пропонується використовувати вимірювання зіркової аберації світла. Проведено порівняння використання аберації світла та ефекту Допплера для вимірювання швидкості відносно реліктового випромінювання. При використанні ефекту Допплера вимірюється сумарна швидкість спостерігача – хабловська швидкість та радіальна складова пекулярної швидкості спостерігача. В результаті проведеного аналізу складових швидкості спостерігача в супутній системі відліку, хабловської та пекулярної швидкостей спостерігача, сформульовано їх суттєві особливості. Наведено аналіз форми фронтів хвиль реліктового випромінювання, випромінювання квазарів, випромінювання зірок та випромінювання наземних джерел. В наслідок цього аналізу, показано визначальний вплив форми їх хвильових фронтів на можливості вимірювання зіркової аберації та відсутність такого впливу при вимірюванні швидкості з використанням ефекту Доплера. Вимірювання аберації світла в інерційній системі надає можливість прямого вимірювання пекулярної швидкості спостерігача в супутній системі відліку. Знання пекулярної швидкості спостерігача важливе для підвищення точності визначення хабловської швидкості особливо об'єктів порівняно невеликої віддаленості. Досліджені запропоновані структури пристроїв вимірювання пекулярної швидкості інерційної системи відліку. Пекулярна швидкість визначається по виміренній аберації світла не переходячи до іншої системи відліку. Виконано оцінку їх очікуваної точності

та надійності. Практичне використання пропонованих структур можливе в астрономії та апаратах дослідження далекого космосу.

КЛЮЧОВІ СЛОВА: реліктове випромінювання, зіркова аберація світла, система відліку, хабловська швидкість, пекулярна швидкість, коліматор, фотоприймач.

ИЗМЕРЕНИЕ СКОРОСТИ В СОПУТСТВУЮЩЕЙ СИСТЕМЕ ОТСЧЕТА
В.М. Свищ

Харьковский национальный аэрокосмический университет им. М.Е. Жуковского «Харьковский авиационный институт»
Харьков, Украина, 61070

Предложен и исследован способ прямого измерения скорости наблюдателя (пекулярной скорости) относительно сопутствующей системы отсчёта. Для измерения пекулярной скорости предлагается использовать измерение звездной аберрации света. Проведено сравнение использования аберрации света и эффекта Доплера для измерения скорости относительно реликтового излучения. При использовании эффекта Доплера измеряется суммарная скорость наблюдателя – хабловская скорость и радиальная составляющая пекулярной скорости наблюдателя. В результате проведенного анализа составляющих скорости наблюдателя в сопутствующей системе отсчёта, хабловской и пекулярной скоростей наблюдателя, сформулированы их существенные особенности. Приведен анализ формы волновых фронтов реликтового излучения, излучения квазаров, излучения звезд и излучения наземных источников. Вследствие этого анализа, показано определяющее влияние формы их волновых фронтов на возможности измерения звездной аберрации и отсутствие такого влияния при измерении скорости с использованием эффекта Доплера. Измерение аберрации света в инерциальной системе дает возможность прямого измерения пекулярной скорости наблюдателя в сопутствующей системе отсчёта. Знание пекулярной скорости наблюдателя важно для повышения точности определения хабловской скорости особенно объектов сравнительно небольшой удаленности. Исследованы предложенные структуры устройств измерения пекулярной скорости инерциальной системы отсчета. Пекулярная скорость определяется по измеренной аберрации света без перехода в другую систему отсчёта. Оценена их ожидаемая точность и надежность. Практическое использование предложенных структур возможно в астрономии и аппаратах для исследования дальнего космоса.

КЛЮЧЕВЫЕ СЛОВА: реликтовое излучение, звездная аберрация света, система отсчёта, хабловская скорость, пекулярная скорость, коллиматор, фотоприемник.

COMPUTER SIMULATION OF THE ANGULAR DISTRIBUTION OF ELECTRONS AND BREMSSTRAHLUNG PHOTONS IN TANTALUM CONVERTER

Viktoriia V. Lisovska, Tetiana V. Malykhina*

Kharkiv V.N. Karazin National University
4, Svobody sq., 61022, Kharkiv, Ukraine
*Corresponding Author: malykhina@karazin.ua

The present work is dedicated to study of the possibilities of improving the production method of ^{11}C and ^{18}F medical isotopes using a linear electron accelerator. Experimental studies of ^{11}C and ^{18}F isotopes production by the photonuclear technique were carried out in [1]. Various targets were irradiated by bremsstrahlung photons following by measurements targets' activities. This experimental research has been carried out in the energy range from 10 to 40 MeV. The current work studies an angular distribution of bremsstrahlung photons in order to estimate the possibilities of producing maximum achievable levels of medical isotopes ^{18}F and ^{11}C activities. The angular distribution of bremsstrahlung photons is an important property of the irradiation stand which contains an assembly of targets. This important property allows designing necessary changes in the target assembly setup used to produce medical isotopes. The research presented in the current work was done as a computer simulation. The computer software package 'KIPT' was developed in C++ programming language, using the Geant4 toolkit in order to obtain the angular distribution of bremsstrahlung photons. Experimental setup materials as well as structural elements positions were defined in the DetectorConstruction class of our program. The parameters of an electron beam were defined in the PrimaryGeneratorAction class. The electron beam diameter was defined as 8 mm, energy E_e=36.7 MeV, corresponding to the real experiment carried out at the "Accelerator" Science and Research Establishment of Kharkiv Institute of Physics and Technology [1]. Models of physical processes occurring while the electron beam crosses the target assembly were defined in the PhysicsList class. All classes and modules necessary for the analysis of simulation results were included to our program together with visualization modules. Visualization modules use the OpenGL graphics library and the Qt5 software to represent the relative position of experimental setup parts and to visualize particle trajectories. As a result of this work, the angular distributions were obtained for the beam of electrons and bremsstrahlung photons directly before the target. This result will allow target assembly parameter optimization for optimal production of medical isotopes by the photonuclear technique.

KEY WORDS: bremsstrahlung converter, angular distribution, Geant4 simulation, medical isotopes production

The use of radionuclides in nuclear medicine, biology as well as to assess the state of the environment and in other areas is widespread. Many nuclear centers have reactors or accelerators. These centers have technologies for the development and research of radionuclides producing methods. Radiopharmaceuticals created on the basis of these radionuclides make it possible to obtain information about pathological changes in various organs of a person after the injection of radiopharmaceuticals into the patient's body. At present, scientists of leading scientific centers conduct research on the production of radiopharmaceuticals by the photonuclear technique [1-3].

Scientists of Kharkiv Institute of Physics and Technology are conducting research in the field of photonuclear isotope production technique [1]. The target irradiation by bremsstrahlung flux is carried out to study the possibility of obtaining the maximum achievable activity levels of medical isotopes (in particular, ^{11}C and ^{18}F) using a linear electron accelerator. Further research is planned for development of radiopharmaceuticals based on these isotopes.

The use of computer simulation tools allows one to conduct a preliminary virtual experiment. This work is an assessment of the method of computer simulation of electrons and bremsstrahlung photons angular distributions for the experimental setup described in [1].

FORMULATION OF THE PROBLEM

Radioisotopes (^{11}C and ^{18}F) can be obtained as a result of photonuclear reactions $_z^A X(\gamma, n)\,_z^{A-1}Y$ when using a linear electron accelerator. Lithium fluoride is used as a target in [1] to study the possibility of ^{18}F production. Fluorine interacts with incident gamma rays, and final products are formed as a result of a nuclear reaction – the fluorine isotope ^{18}F and a neutron:

$$_{8}^{19}F + \gamma \rightarrow\, _{8}^{18}F + n \ .$$
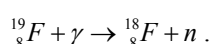
The energy of incident gamma rays must be above a threshold of 10.4 MeV to obtain the fluorine isotope ^{18}F [4]. Glucose $C_6H_{12}O_6$ is used as the target for labeling with ^{11}C isotope. The carbon isotope ^{11}C is formed in the reaction

$$_{6}^{12}C + \gamma \rightarrow\, _{6}^{11}C + n \ ,$$
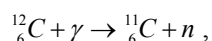
when glucose is irradiated by bremsstrahlung photons. The threshold of this nuclear reaction is 18.7 MeV [4].

The target is placed in an aluminum capsule located immediately after the water-cooled bremsstrahlung converter. The bremsstrahlung converter consists of several layers of refractory metal with a large atomic number z and atomic mass A. Tantalum was used in [1] as a suitable material with high density.

Incident electrons with initial energy $E_e = 36.7\,MeV$ undergo multiple scattering while passing through the convertor. Thus bremsstrahlung photons from scattered electrons can be directed into larger cone than ones produced by only incident beam. Therefore, it is advisable to preliminarily estimate the angular distribution of produced gamma rays by a simulation method. Such simulation helps to estimate the optimal size of the aluminum capsule, which contains the target for the production of isotopes.

RESEARCH METHODS

The computer program that uses the Geant4-10.5 toolkit was designed to evaluate the angular distribution of bremsstrahlung photons in experiments on the production of radioisotopes by the photonuclear method.

The program contains definitions of the DetectorConstruction class, which describes materials of the necessary components of the real experimental setup [1], as well as their sizes and structural elements relative positions. Fig. 1 shows a simplified diagram of a simulated experiment.
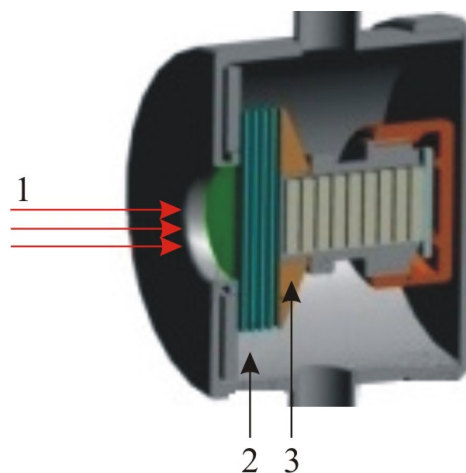
Fig. 1. The simplified diagram of the experiment [1]
1 – direction of primary electrons; 2– bremsstrahlung converter; 3 – target

Important parameters of the primary electron beam are described according to the real experiment conditions in the PrimaryGeneratorAction class, which is a part of the program. The beam diameter is described using the G4UniformRand() method [5]. The beam diameter value is 8 mm. The energy of primary electrons is described using the G4RandGauss::shoot method. The beam energy is 36.7 MeV. Models of all necessary physical processes that occur when an electron beam passes through a converter and target assembly are described in the PhysicsList class. The program also has all classes and modules necessary for the analysis of simulation results as well as visualization modules.

The PhysicsList class of our program describes physical processes using the Livermore model of low-energy electromagnetic processes. The Livermore low-energy electromagnetic process model implements the interaction of electrons and photons with matter down to energies of 250 eV. The Livermore model describes the following processes: photoelectric effect, Compton scattering, Rayleigh scattering, electron-positron pair formation, bremsstrahlung, and ionization. Realization of electromagnetic processes at low energies is valid for elements with atomic number up to 99, and a minimal energy 10 eV [6]. Data used to implement low-energy processes is collected in a set of evaluated data libraries, such as EEDL (Evaluated Electrons Data Library), EPICS2017 (Evaluated Photons Data Library) [4], etc. Multiple electron and positron scattering is implemented using the G4eMultipleScattering class and the G4GoudsmitSaundersonModel model. The G4GoudsmitSaundersonModel model was implemented in 2017, and today provides the best accuracy in the transport of electrons with energies below 100 MeV [6]. Description of photonuclear processes in the PhysicsList model of our program contains a parameterization that uses the G4PhotoNuclearCrossSection class.

Figure 2 shows fragments of preliminary Geant4 modeling in an interactive mode. This figure represents the OpenGL visualization of 10 electrons passage through one layer of 1 mm tantalum and 1 mm of water. The energy of electrons is 36.7 MeV. Primary electrons are directed at normal to the converter. The trajectories of electrons and bremsstrahlung photons are presented in Fig. 2 (a, b).

It is noticeable (Fig. 2) that electrons deviate from the original direction of motion even when passing through the first layer of tantalum. Therefore, bremsstrahlung photons are spread by some angle.

Computer simulation of the passage of 10000 primary electrons with an initial energy of 36.7 MeV was carried out in a batch mode in order to analyze the bremsstrahlung photons angular distribution in details. Electrons and

bremsstrahlung photons were monitored at the moment of crossing the target boundary. Coordinates of electrons and bremsstrahlung photons that crossed the target boundary with energies above the threshold were written to a file for further processing.
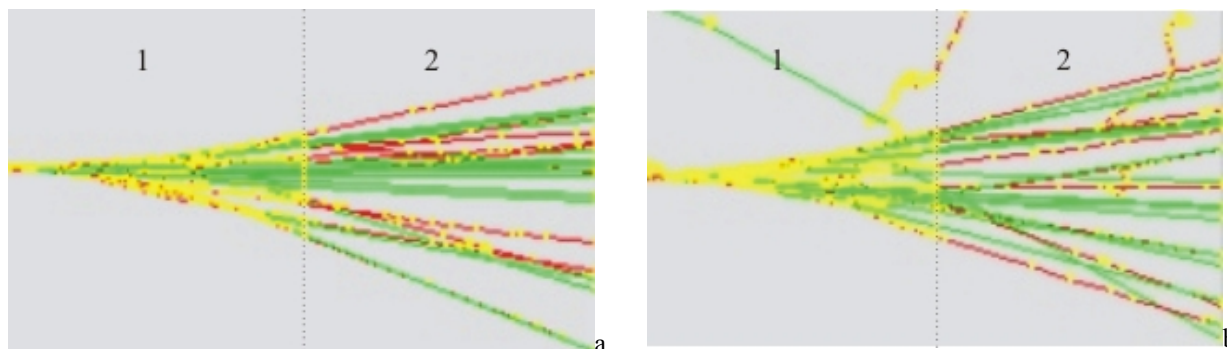
Fig. 2. The passage of 10 electrons with an energy of 36.7 MeV through one layer of 1 mm tantalum and 1 mm of water:
1 – tantalum layer; 2 – water

Figure 3 shows the results of data processing of primary electrons (Fig. 3a and Fig. 3b) and bremsstrahlung photons (Fig. 3c and Fig. 3d) passage through four layers of the converter.

a

b

c

c
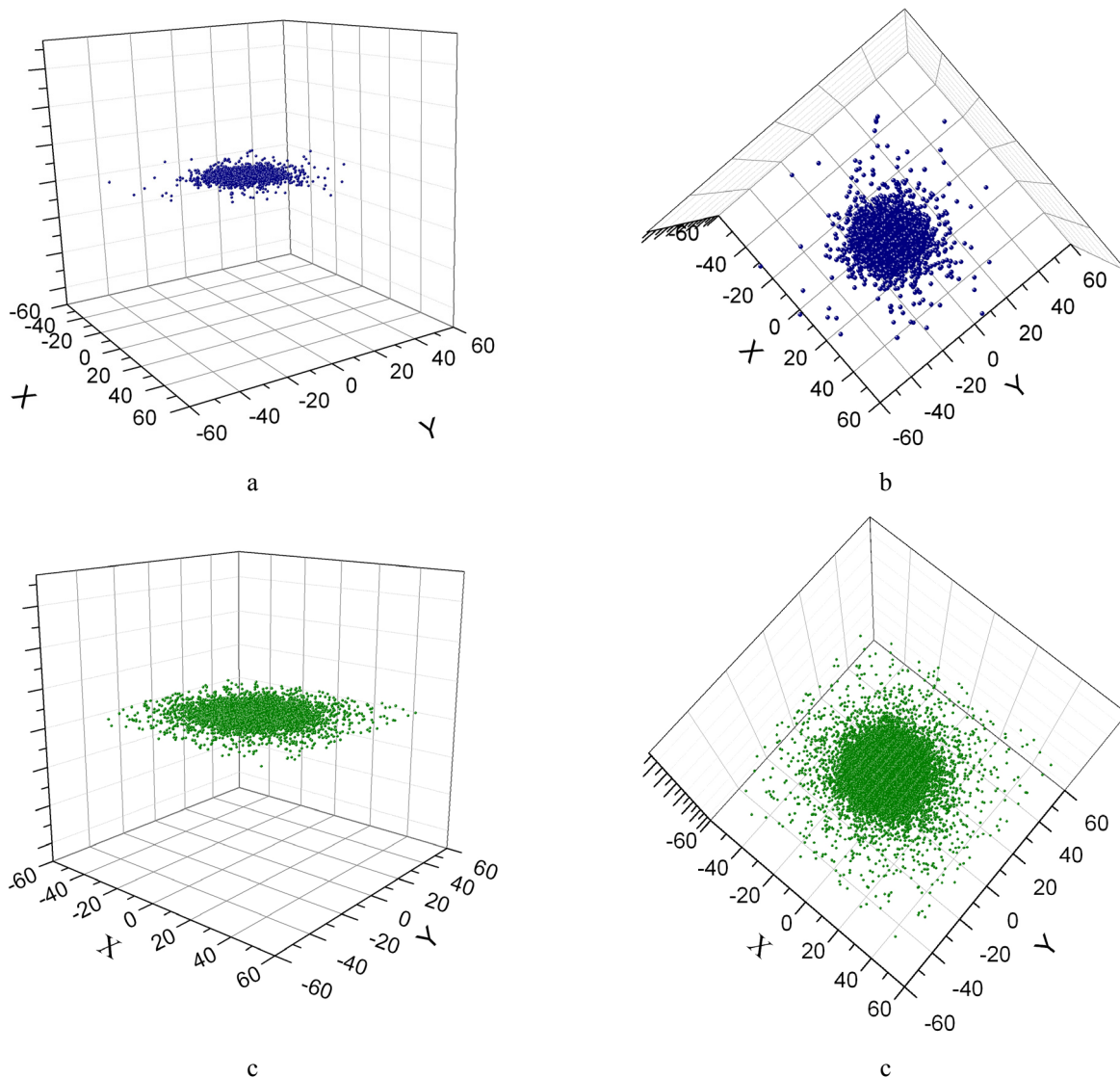
Fig. 3. The angular distribution of primary electrons (Fig. 3a and Fig. 3b) and bremsstrahlung photons (Fig. 3c and Fig. 3d) after passing through four layers of the converter

Fig. 4a and Fig. 4b present histograms obtained by calculating the frequency characteristics of the radii of the electron beam and bremsstrahlung photons after passing through four layers of tantalum and water. The graph does not show single events with radius values above 40 mm.

Model	GaussAmp	
Equation	y=y0+A*exp(-0.5*((x-xc)/w)^2)	
Reduced Chi-Sqr	729,28315	
Adj. R-Square	0,98261	
		Value	Standard Error
Count	y0	24,82446	8,84736
Count	xc	7,00854	0,10278
Count	w	3,71736	0,12966
Count	A	549,54096	14,84452
Count	FWHM	8,75371	
Count	Area	5120,64016	

Model	GaussAmp	
Equation	y=y0+A*exp(-0.5*((x-xc)/w)^2)	
Reduced Chi-Sqr	28617,37658	
Adj. R-Square	0,98831	
		Value	Standard Error
Count	y0	208,19503	44,8929
Count	xc	6,88095	0,07753
Count	w	3,43365	0,09128
Count	A	4350,68956	91,98545
Count	FWHM	8,08563	
Count	Area	37445,67526	

a   b

Fig. 4. Frequency characteristics of the radii of the electron beam (a) and bremsstrahlung photons (b) after passing through 4 layers of tantalum and water

The most probable value of the scattering radius of bremsstrahlung photons was obtained as a result of processing the statistical data: $X_C = 6.85\,mm$, and $\sigma = 3.2\,mm$ (Fig. 4b). Therefore, there is a significant deviation of scatter radii of bremsstrahlung photons. We can obtain the value of the circle radius into which bremsstrahlung photons hit with a probability of 68% when crossing the capsule boundary using the "Three sigma rule" [7]:

$$3.65\,mm \leq R \leq 10\,mm .$$

Therefore, the maximum probability diameter of the bremsstrahlung photons scatter circle is 20 mm. This means that the capsule containing the target must have a diameter of at least 20 mm if located directly behind the tantalum converter.

A series of virtual nuclear physical experiments are being conducted to determine the ^{18}F and ^{11}C isotope yeild after increasing the diameter of the target to 20 mm.

CONCLUSION

As a result of the work, the angular characteristics of the primary electrons beam and bremsstrahlung photons directly in front of the target were obtained. This allows optimal placement of the target assembly for the medical isotopes production by the photonuclear method. It was found that the maximum diameter of the circle into which bremsstrahlung photons hit with a probability of 68% when crossing the target boundary is 20 mm. Consequently, with the increase of the target diameter from 10 mm [1] to 20 mm, it will be possible to increase the activity level of medical isotopes due to more proper size of the target.

ORCID IDs
Viktoriia V. Lisovska, https://orcid.org/0000-0003-1237-7959
Tetiana V. Malykhina, https://orcid.org/0000-0003-0035-2367

REFERENCES
[1] A.N. Dovbnya, R.N. Dronov, V.A. Kushnir, V.V. Mitrochenko, S.A. Perezhogin, L.I. Selivanov, V.A. Shevchenko, and B.I. Shramenko, East Eur. J. Phys. **4**, 77-86 (2018), https://doi.org/10.26565/2312-4334-2018-4-09.
[2] M. Fujiwara, K. Nakai, N. Takahashi, T. Hayakawa, T. Shizuma, S. Miyamoto, G.T. Fan, A. Takemoto, M. Yamaguchi, and M. Nishimura, Physics of Particles and Nuclei, **48**(1), 124-133 (2017), https://doi.org/10.1134/S1063779617010075.
[3] D. Nabs, and U. Köster, Applied Physics B, **103**(2), 501-519 (2011), https://doi.org/10.1007/s00340-010-4278-1.
[4] Geant4 Collaboration, Book For Application Developers Release 10.5, https://geant4-userdoc.web.cern.ch/geant4-userdoc/UsersGuides/ForApplicationDeveloper/BackupVersions/V10.5-2.0/fo/BookForApplicationDevelopers.pdf.
[5] Geant4 Collaboration, Physics Reference Manual, https://geant4-userdoc.web.cern.ch/geant4-userdoc/UsersGuides/PhysicsReferenceManual/BackupVersions/V10.5-2.0/fo/PhysicsReferenceManual.pdf
[6] NEA: Electron photon interaction cross section library. https://www.oecd-nea.org/tools/abstract/detail/iaea1435/
[7] V.M. Kalinin, S.R. Tikhomirov, Lectures on Theory of Probability and Mathematical Statistics, (Saint-Petersburg State Institute of Technology, 2002), pp. 90. (in Russian)

КОМП'ЮТЕРНЕ МОДЕЛЮВАННЯ КУТОВОГО РОЗПОДІЛУ ЕЛЕКТРОНІВ ТА ГАЛЬМІВНИХ ГАММА-КВАНТІВ У ТАНТАЛОВОМУ КОНВЕРТОРІ

В.В. Лісовська, Т.В. Малихіна

Харківський національний університет імені В.Н. Каразіна
майдан Свободи, 4, 61022, Харків, Україна

Представлена робота присвячена дослідженню можливості удосконалення методів отримання медичних ізотопів ^{11}C та ^{18}F із використанням лінійного прискорювача електронів. У роботі [1] проводилися експериментальні дослідження напрацювання фотоядерним способом ізотопів ^{18}F та ^{11}C у різних мішенях при опроміненні потоком гальмівного випромінювання цільових мішеней. Експериментальні дослідження проведені в діапазоні енергій від 10 MeB до 40 MeB. У представленій роботі проводяться дослідження кутового розподілу гальмівних гамма-квантів з метою з'ясування можливостей отримання максимально досяжних рівнів активності медичних ізотопів ^{18}F та ^{11}C. Кутовий розподіл гальмівних гамма-квантів є важливою характеристикою випромінювального стенду, що містить збірку цільових мішеней, тому що знання цих важливих параметрів дозволяє внести необхідні зміни до конструкції збірки мішеней для напрацювання медичних ізотопів. Дослідження, представлені в даній роботі, виконувалися засобами комп'ютерного моделювання. Для вирішення задачі про кутовий розподіл гальмівних гамма-квантів була розроблена комп'ютерна програма KIPT мовою C++ з використанням бібліотеки класів Geant4. Програма містить визначення класу DetectorConstruction, в якому описуються матеріали необхідних складових елементів реальної експериментальної установки, а також взаємне розташування всіх елементів конструкції. У класі PrimaryGeneratorAction, що входить до складу програми, описані параметри пучка первинних електронів. Діаметр пучка електронів дорівнює 8 мм, енергія E_e = 36.7 MeB, відповідно до умов реального експерименту, проведеного в Науково-дослідному комплексі «Прискорювач» ННЦ ХФТІ [1]. У класі PhysicsList описувалися моделі фізичних процесів, що відбуваються при проходженні пучка електронів через мішень. Програма також містить всі класи і модулі, необхідні для аналізу результатів моделювання, а також модуль візуалізації. Модулі візуалізації використовують графічну бібліотеку OpenGL, а також програмний сервіс Qt5 для більш наочного уявлення взаємного розташування елементів експериментальної установки і візуалізації траєкторій електронів, позитронів, гамма-квантів. У результаті виконання роботи отримані кутові характеристики пучка первинних електронів і гальмівних гамма-квантів безпосередньо перед цільовою мішенню, що дозволить оптимізувати параметри збірки цільових мішеней для напрацювання медичних ізотопів фотоядерним способом.

КЛЮЧОВІ СЛОВА: конвертер гальмівного випромінювання, кутовий розподіл, Geant4-моделювання, виробництво медичних ізотопів

КОМПЬЮТЕРНОЕ МОДЕЛИРОВАНИЕ УГЛОВОГО РАСПРЕДЕЛЕНИЯ ПЕРВИЧНЫХ ЭЛЕКТРОНОВ И ТОРМОЗНЫХ ГАММА-КВАНТОВ В ТАНТАЛОВОМ КОНВЕРТЕРЕ

В.В. Лисовская, Т.В. Малыхина

Харьковский национальный университет имени В.Н. Каразина
майдан Свободы, 4, 61022, Харьков, Украина

Данная работа посвящена исследованию возможности совершенствования методов получения медицинских изотопов ^{11}C и ^{18}F с использованием линейного ускорителя электронов. В работе [1] проводились экспериментальные исследования наработки фотоядерным способом изотопов ^{18}F и ^{11}C в различных мишенях, при облучении потоком тормозного излучения целевых мишеней. Экспериментальные исследования проведены в диапазоне энергий от 10 МэВ до 40 МэВ. В представленной работе проводятся исследования углового распределения тормозных гамма-квантов с целью выяснения возможностей получения максимально достижимых уровней активности медицинских изотопов ^{18}F и ^{11}C. Угловое распределение тормозных гамма-квантов является важной характеристикой облучательного стенда, содержащего сборку целевых мишеней, т.к. знание этих важных параметров позволяет внести необходимые изменения в конструкцию сборки мишеней для наработки медицинских изотопов. Исследования, представленные в данной работе, выполнялись средствами компьютерного моделирования. Для решения задачи об угловом распределении тормозных гамма-квантов была разработана компьютерная программа KIPT на языке C++ с использованием библиотеки классов Geant4. Программа содержит определения класса DetectorConstruction, в котором описываются материалы необходимых составных элементов реальной экспериментальной установки, а также взаимное расположение всех элементов конструкции. В классе PrimaryGeneratorAction, входящем в состав программы, описаны параметры пучка первичных электронов. Диаметр пучка электронов был задан 8 мм, энергия E_e=36.7 МэВ, согласно условиям реального эксперимента, проводимого в Научно-исследовательском комплексе «Ускоритель» ННЦ ХФТИ [1]. В классе PhysicsList описывались модели физических процессов, происходящих при прохождении пучка электронов через сборку мишеней. Программа также содержит все классы и модули, необходимые для анализа результатов моделирования, а также модуль визуализации. Модули визуализации используют графическую библиотеку OpenGL, а также программный сервис Qt5 для более наглядного представления взаимного расположения элементов экспериментальной установки и визуализации траекторий электронов, позитронов, гамма-квантов. В результате выполнения работы получены угловые характеристики пучка первичных электронов и тормозных гамма-квантов непосредственно перед целевой мишенью, что позволит оптимизировать параметры сборки целевых мишеней для наработки медицинских изотопов фотоядерным способом.

КЛЮЧЕВЫЕ СЛОВА: конвертер тормозного излучения, угловое распределение, Geant4-моделирование, производство медицинских изотопов

TUNING OF SnS THIN FILM CONDUCTIVITY ON ANNEALING IN AN OPEN AIR ENVIRONMENT FOR TRANSISTOR APPLICATION

Thomas Daniel[a,b]*, **Uno Uno[b],** **Kasim Isah[b],** **Umaru Ahmadu[b]**

aDepartment of Physics/Geology/Geophysics, Alex Ekwueme-Federal University Ndufu-Alike Ikwo, P.M.B 1010, Ebonyi state, Nigeria
bDepartment of Physics, Federal University of Technology Minna P.M.B 065, Minna, Niger state, Nigeria
*Corresponding Author: danielojonugwathomas@gmail.com & daniel.thomas@funai.edu.ng
Received November 30, 2019; revised January 24, 2020; accepted March 12, 2020

The study aimed at enhancement and optimisation of SnS conductivity via annealing for field effect transistor's semiconductor channel layer application. Interstitials and vacancies in SnS films are known to cause carrier traps which limit charge carriers and hence limit the achievement of the threshold voltage for a field effect transistor operation. Tuning of SnS conductivity for transistor application is of emerging interest for novel device operation. SnS thin film semiconductors of 0.4 μm thickness were deposited using Aerosol assisted chemical vapour deposition and annealed in open air at annealing temperatures of150, 200, 250, 300 and 350℃. Variation of the annealing temperature from 150 through 250℃ enhances the crystallinity of the annealed thin film samples by increasing the number of crystallites of the annealed films which is also buttress by the decreasing values of FWHM. However a further decrease in crystallite size at higher annealing temperature of 300 to 350 ℃ was observed which could be attributed to the fragmentation of clusters of crystallites at higher annealing temperature. Increase in annealing temperature increases grain size leading to the reduction in grain boundaries and potential barrier thereby changing the structure and phase of the films which in essence affects the electrical conductivity of the SnS thin films. The films annealed at 250 ℃ exhibited optimum conductivity. The average hall coefficients of the samples deposited at 150 to 250℃ were positive which indicates that the films annealed at this temperature range are of p type conduction while the average hall coefficients of the samples deposited at 300 and 350 ℃ were negative indicating that the films are of n type conduction. The conductivity change is essential for the use of SnS as a semiconductor channel layer especially in a field effect transistor where the device can be tuned to work as a p type or n type semiconductor channel layer.
KEY WORDS: SnS thin film, annealing, conductivity, grain size, transistor, semiconductor

Metal chalcogenides such as Tin(II) sulphide (SnS) and metal dichalcogenides such as Tin(IV) sulphide (SnS$_2$) are of interest as potential candidates for the semiconductor transport channel of field effect transistor and has been previously used in an electric double layer field effect transistor [1]. Chalcogenides consist of a transition element and one or more chalcogenides elements. SnS thin film is abundance in the earth's crust with an orthorhombic crystal structure. It has been reported to be of p type conductivity with a carrier concentration on the order of 10^{16}cm^{-3} and hole mobility of 1.4 cm^{2}V^{-1}s^{-1} [2].

The operation of a field effect transistor is essentially dependent on the choice of semiconductor channel layer material since the voltage required in switching a transistor and also the minimum gate to source voltage differential that is needed to create a charge carrier conducting path between the source and drain is dependent on the transistor semiconductor channel layer [3].

However, oxides, nitrides, carbon nanotubes and organic semiconductor have been the widely reported materials [4]. Therefore, the investigation of other semiconductor materials such as SnS thin film is of interests for novel field effect transistor performances. An essential factor to be considered in the investigation of SnS as a semiconductor material for transistor application is the conductivity and conductivity type since a field transistor can operate as p-type or n-type carrier channel. Optimisation of conductivity is essential for attainment of transistor threshold voltage, easy reproducibility of film properties and simplicity in device design.

The electrical conductivity of semiconductor thin films strongly depends on the preparation conditions and techniques. Low resistive films are often obtained by the creation of excess metal atoms through heat treatment called annealing to fill up interstitials and vacancies which are structural defects in an SnS thin film or by the incorporation of suitable and control amount of dopants [5].

Annealing is the method of conductivity tuning or control employ in this research which is dependent on the choice of annealing temperature and annealing environment. For the choice of annealing temperature, it is generally recommended that the annealing temperature of any material should be less than one-third of its melting point [5]. Since the melting point of SnS is approximately 900 ℃, the annealing temperature for SnS should be ≤ 300 ℃. As such the annealing was carried out at a choice temperature range of 150 to 350℃ (150, 200, 250,300 and 350 ℃). A starting annealing temperature of 150 was chosen to allow for minimum temperature required for reacting components. Open air annealing in atmosphere oxygen was chosen due to its cost effectiveness in set up and acquisition which could scale down the deposition cost.

Hence, we report for the first time the tuning of SnS carrier conductivity and conductivity type with variation of annealing temperature in an open air environment for field effect transistor application.

EXPERIMENTAL PROCEDURE

Soda lime glass substrates were cleaned using the cleaning methods described as follows: (a). The substrates were washed in sodium lauryl sulphate (SLS) solution to remove oil and protein. (b). To remove the organic contaminants, the substrates were immersed in piranha solution (H_2SO_4: H_2O_2 (3:1)) for 30 minutes. (c). The substrates were then ultrasonically cleaned in distilled water using a sonicator and kept in methanol until it is ready to be used. (d). Finally, to use the substrate for deposition process, the substrate were taken from the methanol and dried in air at 150 ℃. Six samples of as deposited SnS semiconductor thin films were deposited individually using 0.1 M Tin chloride dehydrates and 0.2 M of Thiourea which was weighed in stoichiometric proportion and dissolve in ethanol solvent (0.2M of Thiourea (CH_4N_2S) solution was prepared with 0.60896g of CH_4N_2S salt made up to 10 ml of ethanol as solvent while 0.1 M $SnCl_2.2H_2O$ solution was prepared with 0.90252 g of $SnCl_2.2H_2O$ salt made up to 10 ml of ethanol as solvent). The two solutions were mixed and stirred for 1 hour using a magnetic stirrer at room temperature, after which the resulting solution was then deposited on the substrate by aerosol assisted chemical vapour deposition (AACVD) at a constant substrate temperature of 258 ℃. Five out of the six as-deposited samples of SnS thin film were annealed in open air at annealing temperatures of 150, 200, 250, 300 and 350℃ while one of the samples was left unannealed. The as deposited and the annealed samples were allowed to cool to room temperature before undergoing film characterisation.

The crystal phase analysis was carried out at room temperature using X-ray diffractometry (D8 Advance, Bruker AXS, 40Kv, 40 mA) with monochromatic CuKα (λ=1.540598 Å) over a scan mode of step size 0.034˚ and counts accumulated for 192.1 s at each step for 2θ ranging from 20˚ to 80˚.The XRD diffractogram was obtained using OriginPro 2018 software with the FWHM for the peaks estimated using a Gaussian function. Results were analysed with the scientific graphing analysis software and phase identification was done using the inorganic crystal structure data (ICSD) pattern [6] after which the crystallite size, d-spacing, lattice parameter, dislocation density and micro strain were analysed respectively.

The lattice parameters a, b and c value for the orthorhombic crystallographic system of SnS thin film was calculated from the observed values of 2θ using d values (interplaner spacing) for the orthorhombic structure [7]

$$1/{d^2}_{hkl} = h^2/a^2 + k^2/b^2 + l^2/c^2 \qquad (1)$$

XRD pattern of the films were first indexed after which three peaks whose (hkl) is known were selected and resolved for a, b and c lattice constants of the SnS thin film which is also equivalent to:

$$a = \frac{1}{d_{101}} = \frac{bc\sin\alpha}{V}; \ b = \frac{1}{d_{040}} = \frac{ac\sin\beta}{V}; \ c = \frac{1}{d_{002}} = \frac{ab\sin\gamma}{V}.$$

Where V (unit cell volume)=abc (for orthorhombic), d is the space between lattice planes, h k l are the miller indices while α, β, γ are the diffraction angles. Where d is the space between lattice planes and h k l are the miller indices. The atomic spacing parameter d was estimated from the Bragg's equation [8]:

$$2d \sin\theta = n\lambda \qquad (2)$$

$$d = \frac{\lambda}{2\sin\theta} \qquad (3)$$

where n=1, λ=1.5406A^0. The average crystallite size of the films were calculated using the equation:

$$D = \frac{0.9\lambda}{\beta\cos\theta} \qquad (4)$$

β = full width at half maximum (FWHM), θ = diffraction angle, k = Shape factor and λ = wavelength of the X-rays (1.5406 Å) and D= average crystallite size respectively.
Dislocation density δ was calculated using D [7]:

$$\delta = \frac{1}{D^2} \qquad (5)$$

D is the grain size of the film. The micro-strain ε was estimated using the equation [8],

$$\varepsilon = \frac{\beta}{4\tan\theta} \qquad (6)$$

Quantitative information about the preferential crystallite orientation of the SnS thin films were obtained from the texture coefficient (TC) using the relation [6]:

$$TC = \frac{I/I_o}{(1/N)\Sigma_N(I/I_o)} \qquad (7)$$

I is the measured intensity of the intense peak in the XRD spectrum, I_o is the intensity for completely random sample or the standard intensity of the hkl plane taken from the JCPDS 00-039-0354 card and N is the number of reflections considered in the analysis.

The morphology and the microstructure of the SnS thin film was characterized using High Resolution Scanning Electron Microscopy (HR-SEM, Zeiss) while the elemental composition of the as deposited and the annealed films were characterised by an Energy dispersive X-ray spectroscopy (EDS; Oxford instrument) attached to the SEM. The instrument was operated at a voltage of 20 kV while the images were captured at 5 kV. A Profilometer (VEECO

DEKTAK 150) was used to carry out measurement of the thickness of the as deposited and the annealed SnS thin films. After which the carrier density, carrier mobility and carrier type were determined by an ECOPIA Hall Effect measurement system (HMS 3000 Hall measurement system) based on Van der pauw configuration. The current was varied from ± 1 mA to 1 mA at room temperature. A magnetic field of 8000 gauss was employed for the Hall Effect measurement.

RESULTS AND DISCUSSION
Thickness measurement and compositional analysis of the annealed SnS thin films

The thickness of the as deposited and the annealed films were found to be 0.4 μm. The main constituents' elements and their relative concentrations are given in Table 1.The SnS thin film annealed at the different annealing temperatures were smooth, pin hole free and adheres firmly to the soda lime glass substrate surface. The films were all brown in colour without any significant colour change. The composition of the SnS thin films varied with the increase in annealing temperature as shown in Table 1.

Table 1

SnS thin film elemental composition (atomic percent) at varied annealing Temperatures.

T_A(℃)	Sn (at. %)	S (at. %)	Ca (at. %)	Na (at. %)	Cl (at. %)	Si (at. %)	O (at. %)	TOTAL 100
0	29.851	52.154	8.352	1.044	5.620	1.740	1.250	100
150	29.804	52.203	8.345	1.040	5.624	1.743	1.249	100
200	29.873	52.131	8.350	1.041	5.622	1.744	1.248	100
250	30.572	51.432	8.346	1.042	5.623	1.742	1.248	100
300	29.634	52.374	8.349	1.044	5.621	1.741	1.247	100
350	29.770	52.233	8.347	1.043	5.622	1.743	1.251	100

Figure 1 gives the EDX spectrum of the as deposited SnS thin film and the SnS samples annealed at annealing temperatures of 150, 200, 250,300 and 350℃. From the figures, it is evident that the film contained Tin (Sn) and Sulpur (S) elements which are as labelled. However minute quantity of Na, Ca, Si, Cl and Ca were also observed which could be attributed to their presence in the glass substrates. The decrease in sulphur content at 150 to 250 ℃ could be attributed to the rate of re-evaporation of sulphur from the SnS film layers with increase in annealing temperature due to the high vapour pressure of Sulpur or the loss of Sulpur during annealing at higher temperatures [5,9].
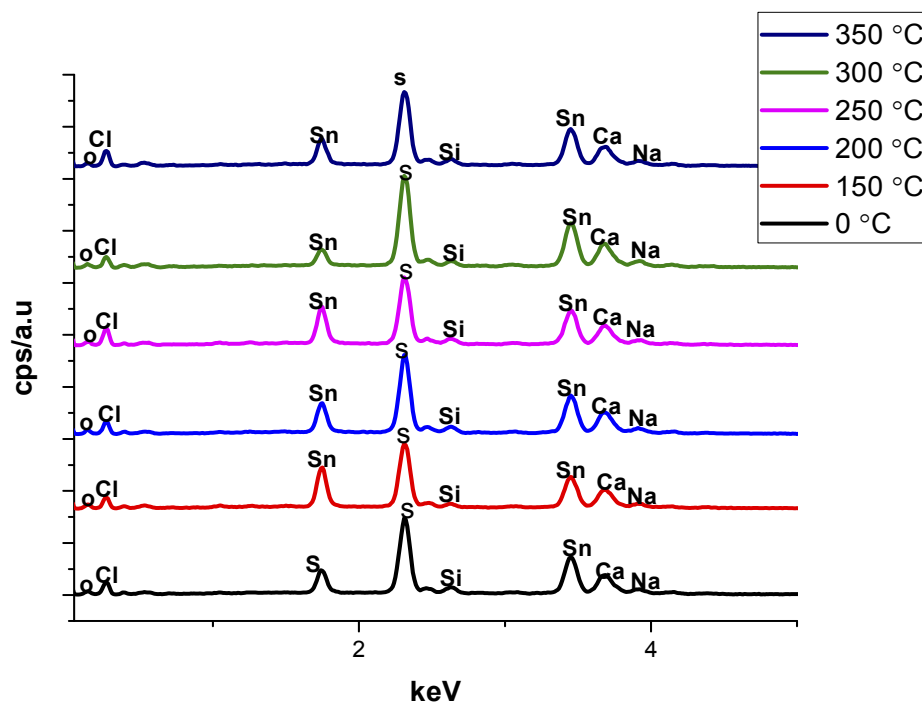
Figure 1. EDS spectrum of the SnS thin film semiconductor annealed at 0,150, 200, 250,300 and 350 ℃.

X-ray diffractomer (XRD) Analysis

Figure 2. Show the XRD pattern of SnS thin film annealed at different annealing temperatures. The peaks were identified using the JCPDS card number 39-0354 data and are labelled with corresponding orientations. All reflections were indexed to orthorhombic SnS phase as compared with the standard JCPDS card. The X-ray diffractogram or

spectrum of the annealed films exhibited peaks of different orientations at 2Θ values of approximately 31.7° and 66.8° corresponding to (040) and (080) peaks for samples annealed at 0 (as deposited), 150, 200, 300 and 350 °C annealing temperature. The position of the (040) peak shifted with annealing to higher 2Θ values from initial value of 31.71° for as deposited to a maximum value of 31.74℃ for the annealed films which could be due to the release of intrinsic strain through annealing.

No impurities peaks of elemental sulphur, tin or other tin sulphide phases were identified in the XRD pattern of the annealed films which buttress the formation of pure SnS phase and absence of oxidation of SnS with annealing in open air. The as deposited film possess a broad peak being characteristics for an amorphous material or one with very small nano-crystals. The annealed SnS films exhibited an orthorhombic structure with calculated lattice parameters of a = 0.429 nm, b=1.123 nm and c=0.399 nm with no change in the structure of SnS films with changes in annealing temperature. The observed d spacing as compared to the standard d spacing is shown in table 2.
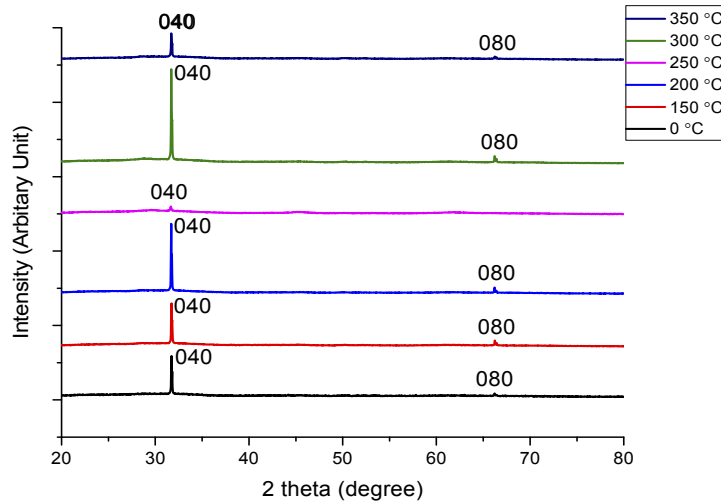
Figure 2. XRD pattern for SnS thin film at annealing temperatures of 150, 200, 250,300 and 350℃.

Table 2.

Observed and standard d spacing for annealed SnS thin films

S/N	Annealing Temperature (℃)	2Θ (°)	Observed D spacing ($\AA$)	Standard D spacing ($\AA$)
1	0	31.73912	2.8201	2.8000
2	150	31.74278	2.8167	2.8000
3	200	31.7253	2.8182	2.8000
4	250	31.71153	2.8194	2.8000
5	300	31.72585	2.8181	2.8000
6	350	31.72785	2.8180	2.8000

The calculated d spacing are closely related to the standard JCPDS data. Although a slight difference occurs in the values which could be attributed to the presence of unit cell volume contraction that might signify the presence of strain in the annealed films [5]. The calculated texture coefficient values of the five annealed samples is given in Table 3.

Table 3.

Calculated texture coefficient for the annealed SnS thin films

S/N	Annealing Temperature ℃	Texture coefficient (TC)	
		TC (040)	TC (080)
1	150	1.09	0.10
2	200	1.17	0.83
3	250	2.52	_
4	300	1.05	0.95
5	350	1.40	0.60

The value obtained shows that all the TC values of (040) plane of the annealed SnS thin film component are larger than 1 which indicates that all the SnS films are polycrystalline with preferred orientation along the (040) plane and denotes that the number of grains along the (040) plane is more than that on the other planes [9, 10]. The degree of

preferential orientation initially increased with increase in annealing temperature for samples annealed at 150 to 250 ℃ with a maximum value at the sample annealed at 250 ℃ for each plane after which it decreases.

At annealing temperature of 150℃, it could be inferred that the SnS thin film undergoes incomplete recrystallization giving rise to a peak with similar intensity to that of the as deposited film. The orientation and intensity of the film increases with increase in annealing temperature to 200 ℃ which could be attributed to improvement in crystallinity and signifies decrease in dislocation density and density of grain boundaries as a result of decrease of donor sites that are trapped at the dislocation and grain boundaries. However with increase in annealing temperature to 250 ℃, the intensity of SnS thin film of (040) preferencial orientation decreases which could be attributed to the decomposition and re-evaporation of adsorption atoms away from the surface as the SnS becomes thermodynamically unstable at high annealing temperatures which leads to increase in the speed of atoms so as to look for a site of lowest surface energy structure leading to a formation of a more improved crystalline film. A further increase in the intensity and crystallinity of the SnS films occurred at annealing temperature of 300-350 ℃ which could be attributed to the increase in thermal oscillation of atoms in their lattice position at high temperatures.

The peak associated with the (040) plane was used to calculate the structural parameters of the films been the preferred orientation of the annealed SnS thin films. The summarised structural parameters are given in in table 4 while figure 3 shows the variation of average crystallite size with annealing temperatures of 150, 200, 250,300 and 350℃.

Table 4.

Summary of calculated structural parameters for the annealed SnS thin films

Annealing Temperature (℃)	Full width half maximum β(°)	2Θ (°)	Average crystallite size D (nm)	Dislocation density $\delta \times 10^{14}$(Lines/m^2)	Micro strainε $\times 10^{-4}$
0 (as deposited)	0.13633	31.73912	60.57	2.73	5.72
150	0.14008	31.74278	58.95	2.88	5.88
200	0.13139	31.72530	62.94	2.52	5.52
250	0.12644	31.71153	65.30	2.35	5.31
300	0.13343	31.72585	61.89	2.61	5.60
350	0.15962	31.72785	51.73	3.74	6.70
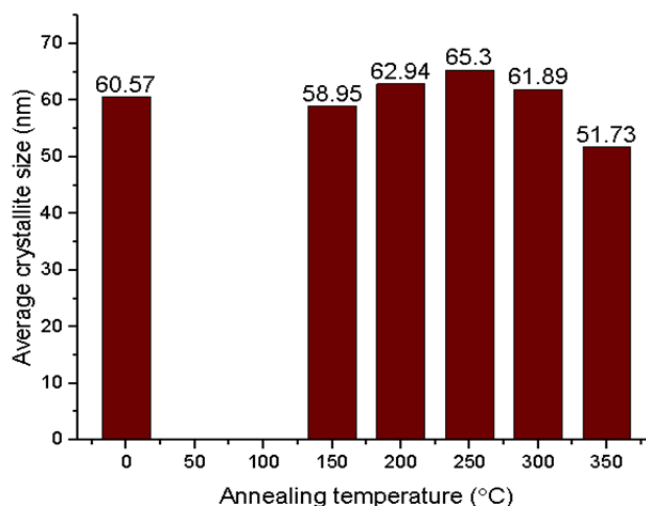
Figure 3. Composite variation of average crystallite size with annealing temperatures

Figure 3 shows the variation of average crystalline size evaluated. The crystallite size initial decreased to 58.95 nm from the value of 60.57 nm of the as deposited SnS thin film at 150 ℃ annealing temperature which could be as a result of the insufficient temperature to move grain boundaries or the fragmentation of clusters of SnS crystals to initiate recrystallization [5]. The crystallite size however increases with increase in annealing temperature from 58.95 nm for SnS film annealed at 150 ℃ to 62.94 nm for the film annealed at 200 ℃ and to 62.94 nm for the film annealed at 250 ℃. Increasing the annealing temperature from 150 through 250 ℃ enhances the crystallinity of the annealed thin film samples by increasing the number of crystallites of the annealed films which is also buttress by the decreasing values of FWHM and correlates with the report of [11]. Annealing enables Oswald ripening which is the consolidation and growth of larger grains at the expense of smaller ones with a rate of occurrence aided by temperature. The increase in crystallite size could also be attributed to the decrease in grain boundary and reduction in deformation as well as defects in the crystals which signifies increase of degree of perfection of grains with the removal of defects and the reduction of pores.

However a further decrease in crystallite size at higher annealing temperature of 300 to 350 °C was observed which could be attributed to the fragmentation of clusters of crystallites at higher annealing temperature. The sample annealed at 250 °C exhibits the best crystallinity with the largest grain size and decrease in defects density and decrease in donor sites trapped at the dislocation and grain boundaries.

Micro strain ε and dislocation density δ which are crystal defect parameters exhibits a reducing trend for the samples annealed at 150 to 250°C with increase in annealing temperature and with increase in average crystallite size. The decrease of dislocation density for SnS thin films annealed at 150 to 250 °C indicates the presence of higher crystallinity of SnS films than the samples annealed at 300 to 350 °C where the dislocation density and micro strain increases further.The change in the strain may be due to the recrystallization process in the SnS films. Also micro strain is an inherent and natural component of nano grained materials due to the large number of grain boundaries and the short spacing between them. Increase in crystal size with annealing temperature causes increase in surface energy which causes the varying magnitude of the strain [12].

SEM Analysis

The scanning electron microscopy micrograph at magnification of 20000 x for all the annealed samples of SnS thin film at various annealing temperature as compared to the as deposited is shown in Fig. 4.
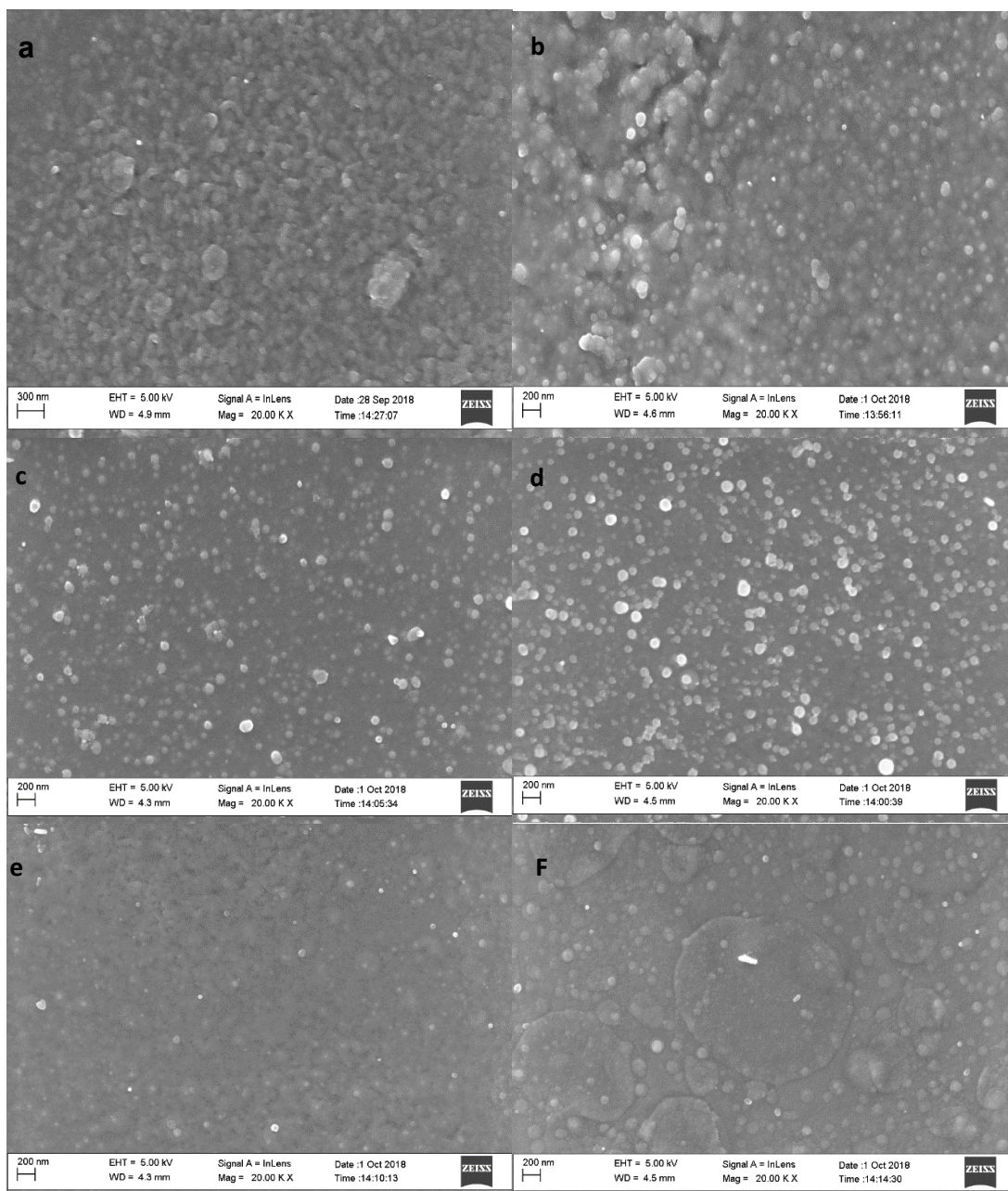
Figure 4. The surface morphology of SnS thin films annealed at 0, 150, 200, 250, 300 and 350°C.

A gradual change was observed from the micrograph in the growth of grains of SnS films from island nature to a more densely packed thin film nature as the annealing temperature increases from 150 to 350 ℃. The grains lie randomly oriented with a decrease in grain boundaries with increase in annealing temperature. Similar results have been reported by [5]. Figure 5 shows that the grain size which is as labelled on each column increases with increase in annealing temperature.
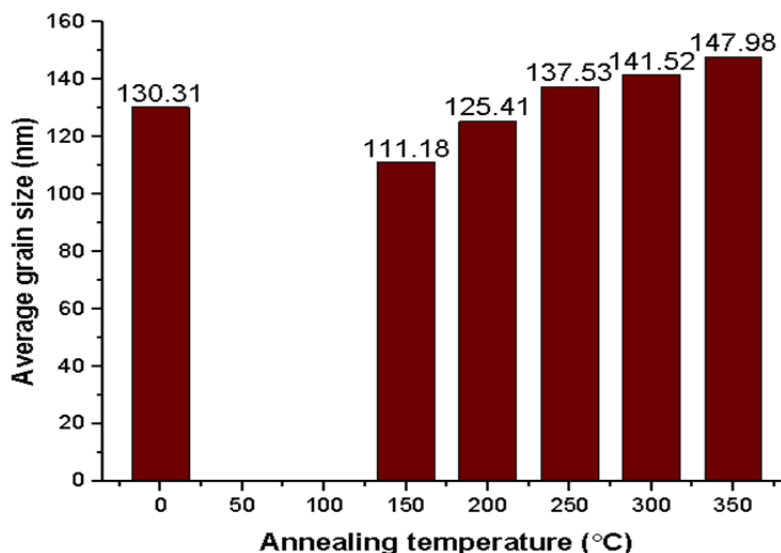
Figure 5. Composite average grain size plot for annealing temperatures of 150 to 350℃.

Increasing the annealing temperature increases grain size leading to the reduction in grain boundaries and potential barrier which enhances the release of trap carriers thereby increasing the conductivity of the SnS thin film with annealing.

Hall Effect measurement

The Hall Effect measurement showing carrier concentration, average hall coefficient, carrier mobility, resistivity, conductivity and sheet resistance is shown in table 5.

Table 5.

Electrical parameters for annealed SnS thin films using Hall Effect measurement

Annealing Temperature (℃)	Bulk concentration N_b (cm^{-3})	Average Hall coefficient R_H (cm^3/c)	Carrier mobility μ (cm^2/Vs)	Resistivity ρ (Ωcm)	Conductivity σ (Ωcm)$^{-1}$
0	2.238×10^{10}	6.928×10^9	4.337×10^3	3.612×10^5	2.768×10^{-6}
150	2.850×10^{10}	1.795×10^{10}	1.523×10^5	1.217×10^4	8.214×10^{-5}
200	3.010×10^{10}	1.833×10^{10}	1.571×10^5	1.121×10^4	8.921×10^{-5}
250	3.167×10^{10}	1.971×10^{10}	1.619×10^5	1.025×10^4	9.756×10^{-5}
300	-3.721×10^9	-8.678×10^9	1.692×10^4	1.249×10^5	8.008×10^{-6}
350	-6.664×10^9	-9.367×10^9	3.905×10^4	1.241×10^5	8.057×10^{-6}

Compared to the as deposited SnS thin film annealed at 0 ℃, the annealed samples showed improvement in their semiconducting properties. The average hall coefficients of the samples deposited at 150 to 250 ℃ are positive which indicates that the films annealed at this temperature range are of p type (with holes as majority carriers) conduction while the average hall coefficients of the samples deposited at 300 and 350 ℃ are negative indicating that the films are of n-type conduction. The change in conductivity could be attributed to the release of tin atoms with annealing at higher temperature. The inversion (transmutation) in type of carrier charge could also be related to impact defect due to crystal growth in material with changes in annealing temperature or the thermal oscillation of atoms in their lattice position at high temperature which may cause a release of atom from its location to filled space left behind. Annealing enhances increase carrier concentration, reduction in resistivity due to improvement in crystallisation and increase in grain size leading to decrease in defects density and crystal boundary which enhances increase in the SnS thin film conductivity.

With the increase of annealing temperature, the carrier concentration and mobility increases while the film resistivity decreases except that of films annealed at 300 and 350 ℃. The carrier concentration and mobility reached a maximum of $3.167 \times 10^{10} N_b$ (cm^{-3}) and 1.619×10^5 (cm^2/Vs) with a p type conductivity. This could be explained by the fact that increase of annealing temperature leads to improved crystallisation and increase in grain size in the films which could enhance the decrease of crystal defects, grain boundary and crystal bonding reduction, hence the release of the

electrons that are trapped at the grain boundary thereby decreasing resistivity and increasing conductivity. However above 250 ℃, higher temperatures enhance stronger crystal lattice vibration which could results in crystal lattice defects. Such defects become dispersion centres leading to increase of films resistivity. Similar reports have been reported by [13].

Temperature dependence of electrical conductivity

A deposited film of 0.40 μm thickness which was annealed at 250 °C was used to study the temperature dependence of electrical conductivity of the deposited SnS thin film by heating to a temperature of 300 °C after which the resistivity/conductivity was measured as the temperature reduced by 5 ℃ intervals. The obtained data was analysed using Arrhenius equation [14]. A plot of $\ln (\sigma/\sigma_0)$ versus (1/T) is given in Figure 7.
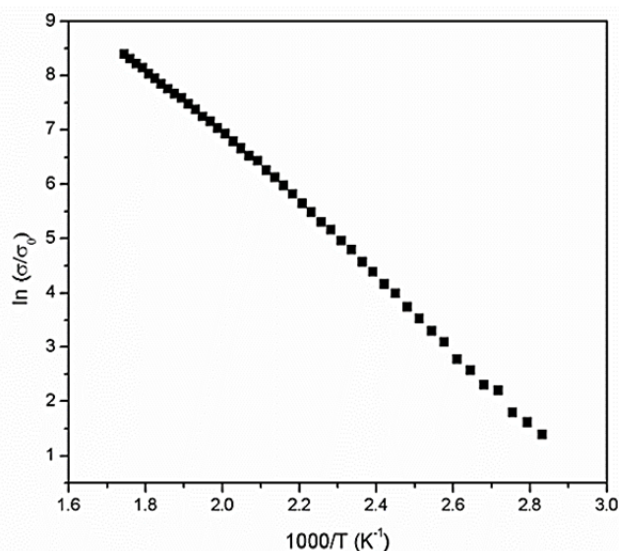
Fig. 7. The dependence of $\ln (\sigma/\sigma_0)$ versus (1000/T) for SnS thin film

The activation energy of the charge carriers evaluated from the slope of the curve was obtained as 0.520 eV. The value of the activation energy may be attributed to the deep acceptor states arising from the Sn vacancy which plays significant role in the p type carrier conductivity of the SnS semiconductor. The excess of non-metallic atoms (Sulpur) which is also evident in the elemental composition of the film, induces a proportionate Sn vacancy sites such that every anion would introduce two positive type (p-type) conductor which is supported by the fact that the activation energy of the SnS thin film depends on elemental ratio, presence of crystal defect and the deposition method used. It is also evident from the graph that the conductance increases with temperature which indicates the semiconducting behaviour of the thin film [10].

CONCLUSION

The SnS thin film semiconductors of 0.4 μm thickness were deposited using aerosol assisted chemical vapour deposition (AACV) and annealed in open air at annealing temperatures of 150, 200, 250, 300 and 350℃. The annealed SnS thin film was found to be polycrystalline consisting of Sn and S elements in varying composition with increase in annealing temperature. No noticeable change was noticed in the crystal structure of the films while the change in the lattice parameters was marginal. No impurities peaks of elemental sulphur, tin or other tin sulphide phases were identified in the XRD pattern of the annealed films which signifies the formation of pure SnS phase. The preferred orientation of all the annealed films was found to be along the (040) plane. Increasing the annealing temperature from 150 through 250℃ enhances the crystallinity of the annealed thin film samples by increasing the number of crystallites of the annealed films which is also buttress by the decreasing value of FWHM. However a further decrease in crystallite size at higher annealing temperature of 300 to 350℃ was observed which could be attributed to the fragmentation of clusters of crystallites at higher annealing temperature. A decrease of dislocation density and micro strain for SnS thin film samples annealed at 150 to 250 ℃ was noticed indicating the presence of higher crystallinity of SnS films than the samples annealed at 300 to 350 ℃ where the dislocation density and micro strain increases further. A gradual change was observed from the SEM micrographs in the growth of grains of SnS films from island nature to a more densely packed thin film nature as the annealing temperature increases from 150 to 350 ℃. Increase in annealing temperature increases grain size leading to the reduction in grain boundaries and potential barrier thereby changing the structure and phase of the films which in essence affects the electrical conductivity of the SnS thin films. The films annealed at 250 ℃ showed an optimum film property for in terms of the conductivity and band gap which are essential for application as a semiconductor channel layer in a field effect transistor. The average hall coefficients of the samples deposited at 150 to 250℃ were positive which indicates that the films annealed at this temperature range are of p type (with holes as

majority carriers) conduction while the average hall coefficients of the samples deposited at 300 and 350 ℃ are negative indicating that the films are of n type conduction.

To the best of our knowledge and within the limit of available literature, no report has been made on the tuning of SnS thin film semiconductor properties with annealing in an open air environment for transistor application, hence turning the results described here innovative to the scientific community.

ORCID IDs

Thomas Daniel, https://orcid.org/0000-0002-5176-9181; **Uno Uno,** https://orcid.org/0000-0001-6693-5894
Kasim Isah, https://orcid.org/0000-0002-9670-7697; **Umaru Ahmadu,** https://orcid.org/0000-0001-5966-0853

REFERENCES

[1] T.O. Daniel, Uno EU, K.U. Isah, and U. Ahmadu, EEJP, **3**, 71-80 (2019), https://doi.org/10.26565/2312-4334-2019-3-09.
[2] P. Thiruramanathan, G.S. Hikku, R. Krishna-Sharman, and S.M. Siva, International Journal of Technochem Research, **1**(1), 59-65 (2015).
[3] Du H, Lin Xi, Xu Z, and Chu D, J. Mater. Sci. **50,** 5641-5673 (2015), https://doi.org/10.1007/s10853-015-9121-y.
[4] H. Yuan, X. Wang, and B. Lian, National Nanotechnology, **9**, 851-857 (2014), https://doi.org/10.1038/nnano.2014.183.
[5] M. Devika, N.R. Koteeswara, K. Ramesh, K.R. Gunasekhar, E.S.R. Gopal, and R.K.T. Ramakrishna, **21**, 1125-1131 (2006), https://doi.org/10.1088/0268-1242/21/8/025.
[6] A. Sugaki, A. Kitakaze, and H. Kitazawa, Science Reports of the Tohoku University, Series III, **16**(2), 199–211 (1985), https://www.researchgate.net/profile/Arashi_Kitakaze/publication/307507517_Synthesized_tin_and_tin-silver_sulfide_minerals_Synthetic_sulfide_minerals_XIII/links/5a268779aca2727dd88136bd/Synthesized-tin-and-tin-silver-sulfide-minerals-Synthetic-sulfide-minerals-XIII.pdf.
[7] T.H. Patel, The open surface science journal, **4**, 6-13 (2012), http://dx.doi.org/10.2174/1876531901204010006.
[8] B.J. Babu, A. Maldonado, S. Velumani, and R. Asomoza, Material Science and Engineering B, **174**, 31-37 (2010), https://doi.org/10.1016/j.mseb.2010.03.010.
[9] M. Safonova, P.P.K. Nair, E. Mellikov, R. Aragon, K. Kerm, R. Naidu, and O. Volobujeva, Proceedings of the Estonian academy of sciences, **64**(4), 488-494 (2015), http://www.kirj.ee/26577/?tpl=1061&c_tpl=1064.
[10] E. Guneri, F. Gode, C. Ulutas, F. Kirmizigul, G. Altindemir, and C. Gumus, Chalcogenides letters, **7**(12), 685-694 (2010), http://chalcogen.ro/685_Guneri.pdf.
[11] K. Nadarajah, C.Y. Chee, and C.Y. Yan, Journal of Nanomaterials, **2013**, 146382 (2013), http://dx.doi.org/10.1155/2013/146382.
[12] Rasband WS, ImageJ, National institute of health, Bethesda, Maryland, USA, http://imagej.nih.gov/ij/1997-2014.
[13] G. Julio, M.D. Merindano, M. Canals and M. Rallo, Journal of anatomy, **212**, 879-886 (2008), https://doi.org/10.1111/j.1469-7580.2008.00898.X.
[14] T.S. Reddy and M.C. Kumar, RSC Adv. **6**, 95680-95692 (2016). https://doi.org/10.1039/C6RA20129F.

ТЮНІНГ ПРОВІДНОСТІ ТОНКОЮ ПЛІВКИ SnS ПРИ ВІДПАЛІ У ВІДКРИТОМУ ПОВІТРЯНОМУ СЕРЕДОВИЩІ ДЛЯ ЗАСТОСУВАННЯ В ТРАНЗИСТОРАХ

Томас Даніел[a,b], Уно Уно[b], Касим Ісах[b], Умару Ахмаду[b]
*[a]Кафедра фізики / геології / геофізики, Алекс Еквеуме, Федеральний університет Ндуфу Аліке
Ікво, P.M.B 1010, штат Ебоній, Нігерія*
*[b]Кафедра фізики, Федеральний технологічний університет, Мінна
P.M.B 065, Мінна, штат Нігер, Нігерія*

Дослідження спрямоване на покращення та оптимізацію провідності SnS за допомогою відпалу для застосування в напівпровідниковому шарі польового транзистора. Відомо, що міжвузлові атоми і вакансії в плівках SnS викликають пастки, які обмежують носії заряду і, отже, обмежують досягнення порогової напруги для роботи польового транзистора. Налаштування провідності SnS для застосування у транзисторах викликає інтерес для роботи нових пристроїв. Тонкоплівкові напівпровідники SnS товщиною 0,4 мкм були осаджались методом хімічного аерозольного осадження та відпалені на відкритому повітрі при температурі відпалу 150, 200, 250, 300 та 350°C. Зміна температури відпалу від 150 до 250°C підвищує кристалічність відпалених зразків тонкої плівки за рахунок збільшення кількості кристалітів відпалених плівок, що також підкріплюється зменшенням значень FWHM. Однак спостерігалося подальше зменшення розміру кристаліту при більш високій температурі відпалу від 300 до 350°C, що можна було пояснити фрагментацією скупчень кристалітів при більш високій температурі відпалу. Збільшення температури відпалу збільшує розмір зерна, що призводить до зменшення меж зерна та потенційного бар'єру, тим самим змінюючи структуру та фазу плівок, що по суті впливає на електропровідність тонких плівок SnS. Плівки, відпалені при 250°C, демонстрували оптимальну провідність. Середні коефіцієнти Холла на зразках, осаджених від 150 до 250°C, були позитивними, що вказує на те, що плівки, відпалені в цьому діапазоні температур, мають p-тип провідності, тоді як середні коефіцієнти Холла для зразків, осаджених при 300 і 350°C, були негативними, що свідчить про те, що плівки мають n-тип провідності. Зміна електропровідності має важливе

значення для використання SnS як шару напівпровідникового каналу, особливо в польовому транзисторі, де пристрій може бути налаштований на роботу типу напівпровідникового каналу типу p або n-типу.

КЛЮЧОВІ СЛОВА: тонка плівка SnS, відпал, провідність, розмір зерна, транзистор, напівпровідник

НАСТРОЙКА ПРОВОДИМОСТИ ТОНКОЙ ПЛЕНКИ SnS ПРИ ОТЖИГЕ В ОТКРЫТОЙ ВОЗДУШНОЙ СРЕДЕ ДЛЯ ПРИМЕНЕНИЯ В ТРАНЗИСТОРАХ

Томас Даниэль[a,b], Уно Уно[b], Касим Исах[b], Умару Ахмаду[b]

*[a]Кафедра физики/геологии/геофизики, Федеральный университет Алекса Эквуэме, Ндуфу-Алике
Икво, Р.М.В 1010, штат Эбони, Нигерия*
*[b]Кафедра физики, Федеральный технологический университет, Минна
Р.М.В 065, Минна, штат Нигер, Нигерия*

Исследование было направлено на улучшение и оптимизацию проводимости SnS посредством отжига для применения в полупроводниковом канале полевого транзистора. Известно, что междоузельные атомы и вакансии в пленках SnS вызывают ловушки носителей, которые ограничивают носители заряда и, следовательно, ограничивают достижение порогового напряжения для работы полевого транзистора. Тюнинг проводимости SnS для применения в транзисторах представляет интерес для работы новых устройств. Тонкопленочные полупроводники SnS толщиной 0,4 мкм осаждались методом аэрозольного химического осаждения из паровой фазы и отжигались на открытом воздухе при температурах отжига 150, 200, 250, 300 и 350°C. Изменение температуры отжига от 150 до 250°C повышает кристалличность отожженных образцов тонких пленок за счет увеличения количества кристаллитов отожженных пленок, что также подкрепляется уменьшением значений FWHM. Однако наблюдалось дальнейшее уменьшение размера кристаллитов при более высокой температуре отжига от 300 до 350°C, что можно объяснить фрагментацией кластеров кристаллитов при более высокой температуре отжига. Повышение температуры отжига увеличивает размер зерна, что приводит к уменьшению границ зерен и потенциального барьера, тем самым изменяя структуру и фазу пленок, что по существу влияет на электропроводность тонких пленок SnS. Пленки, отожженные при 250°C, показали оптимальную проводимость. Средние коэффициенты Холла образцов, нанесенных при температуре от 150 до 250°C, были положительными, что указывает на то, что пленки, отожженные в этом диапазоне температур, имеют проводимость p-типа, в то время как средние коэффициенты Холла образцов, нанесенных при 300 и 350°C, были отрицательными, что указывает на то, что пленки имеют проводимость n-типа. Изменение проводимости является существенным для использования SnS в качестве слоя полупроводникового канала, особенно в полевом транзисторе, где устройство может быть настроено для работы в качестве слоя полупроводникового канала p-типа или n-типа.

КЛЮЧОВІ СЛОВА: тонкая пленка SnS, отжиг, проводимость, размер зерна, транзистор, полупроводник

PACS: 29.30.Ep

DETERMINATION OF ^{234}U/^{238}U, ^{235}U/^{238}U, ^{236}U/^{238}U ISOTOPE RATIOS IN URANIUM OXIDE BY SECTOR-FIELD ICP-MS

Dmytro V. Kutnii*, Dmytro D. Burdeynyi, Stanislav A. Vanzha, Natalia V. Rud

National Science Center "Kharkiv Institute of Physics and Technology" of NAS of Ukraine
Corresponding Author: d_kutniy@kipt.kharkov.ua, tel. +380-50-628-06-31
Received March 20, 2020; accepted March 27, 2020

Influence of mass bias effect, isobaric and polyatomic interferences on the results of $^{234}U\big/^{238}U$, $^{235}U\big/^{238}U$, $^{236}U\big/^{238}U$ isotope ratio determination in uranium oxide by sector-field ICP-MS was studied. Uranium isotopic standards CRM U100, CRM U200 based on triuranium octoxide (U_3O_8) and single-collector mass spectrometer ICP-SFMS ELEMENT 2 were used for research. It has been demonstrated that the mass bias effect has most influence on the results of uranium isotope ratios determination. To investigate the influence of the mass bias effect on the determinations of uranium isotope ratios, the external standardization calibration was used with three models (linear, power, exponential) describing the behavior of the specific discrimination coefficient β versus the mass of measured isotopes. The mass discrimination factor has been found to vary from 6.00×10^{-3} to 1.20×10^{-2}. The advantage for using the (power/exponential)-law models of the $\beta = F(\Delta m)$ relationship for correcting measured isotope ratios was justified. In case of polyatomic interferences, the efficiency of uranium hydride ion ($^{235}U^1H^+$) formation is 3.54×10^{-5}, while the impact of isobaric overlapping due to the contribution of scattered $^{238}U^+$ ions to the intensities of less abundant ^{236}U and ^{235}U ions reaches 8.17×10^{-6}. The relative measurement error for the $^{234}U\big/^{238}U$, $^{236}U\big/^{238}U$ ratios was found to be < 0.5 %, and for the $^{235}U\big/^{238}U$ ratio less than 0.1 %. The calculated standard uncertainty u of the $^{234}U\big/^{238}U$, $^{235}U\big/^{238}U$, $^{236}U\big/^{238}U$ isotope ratio measurements in the CRM U100 was 0.563, 0.322 and 0.856 %, respectively. These are reasonable estimates in comparison with the uncertainties of certified values of 0.296, 0.097 and 0.265 %.

KEY WORDS: inductively coupled plasma mass spectrometry, uranium oxide, mass bias effect, polyatomic interferences, isobaric overlapping, uranium isotope ratios

The mass-spectrometry methods are intended for isotopic and elemental analysis of materials and applied at atomic industry plants for providing in-process control, as well as quality control and end products certification [1]. The in-process monitoring of nuclear fuel and constructional materials processing is extremely important for predicting the products behavior under irradiation conditions, where even a minor change in the element concentration may lead to a significant property changes [2].

The quality of uranium products (uranium ore concentrate, uranium hexafluoride, uranium dioxide) is regulated by international standards, whereby one of the most important quality characteristics is the isotopic composition of uranium [3]. The analytical methodology of isotope ratio measurements of depleted, enriched, and natural uranium is determined by the ASTM standard (ASTM C 1477-08), which also sets limits on the relative measurement error: less than 0.1 % for ^{235}U, and less than 1 % for ^{234}U, ^{236}U.

For precise determination of the uranium isotopes abundance, the following types of multi-collector mass spectrometers are mainly used (in accordance with the substance ionization method): the thermal ionization mass spectrometer (TIMS) and the inductively-coupled plasma mass spectrometer (ICP-MS). The presence of several collectors allows simultaneous measurement of a few isotopes at a time, thereby offsetting the influence of signal intensity variations with time, and considerably improving the accuracy of isotope ratio measurements. According to various literature data, the relative measurement error for those mass spectrometers may vary from 0.05 to 0.002 % [4,5,6].

The main application of single-collector sector-field ICP-MS is the analysis of extremely low contents of elements (elemental analysis) with the detection limit at level of ppq (10^{-13} %) [7]. This is due to high resolution of such mass spectrometers and their high sensitivity ($\sim 10^6$ cps per 1 ppb ^{115}In). The application of ICP-SFMS in the uranium isotope analysis calls for an additional consideration of the following effects that may affect the measurement results.

The mass bias effect occurs in the interface part of the mass-spectrometer due to the space-charge effect in the skimmer cone region, and promotes a higher heavy-ion transfer efficiency. Thus, two isotopes of the same element in the same concentrations will induce a signal of different intensity.

Isobaric overlapping of the high-intensity peak tail with the mass m on the peak intensities with the masses $(m-1)$, $(m-2)$, $(m-3)$. This effect is associated with ion scattering by the molecules of the residual gas in the vacuum system, and it is referred to as the abundance sensitivity. Its value becomes critical during measuring the extreme isotope ratios (higher than 10^5), uranium isotopes being an example [8, 9].

Polyatomic interferences is caused by the formation of Ar^+, H^+, O^+ ions in plasma, which in their transit through the interface part of the mass spectrometer enter into the plasma-chemical reactions with the result that polyatomic ions

Determination of $^{234}U/^{238}U$, $^{235}U/^{238}U$, $^{236}U/^{238}U$ Isotope Ratios in Uranium Oxide...   **EEJP. 2 (2020)**

105

are produced. In this case, to estimate the $m = 236$ peak intensity, it is necessary to take into account the contribution of the $^{235}U\,^1H^+$ hydride ions formation [10, 11].

With due regard for the above-mentioned peculiarities in the application of ICP-SFMS for the uranium isotope analysis the following research tasks were formulated:
- to study the influence of ion interaction processes in the ICP SFMS (mass bias effect, isobaric and polyatomic interferences) on the measurement results for the $^{234}U/^{238}U$, $^{235}U/^{238}U$ and $^{236}U/^{238}U$ isotope ratios in uranium oxide;
- to estimate metrological characteristics of the measured data with regard to the applicability of the ICP-SFMS method for the quality control and certification of uranium products in nuclear power industry.

MATERIALS AND METHODS

Studies were carried out using uranium isotopic standards based on triuranium octoxide (U_3O_8) CRM U100 and CRM U200, made by the U.S. National Bureau of Standards (since 1988 – National Institute of Standards and Technology of the U.S. Department of Commerce). Each standard represents 10 mg of highly purified U_3O_8 powder, certified values of the isotope ratios were obtained using multi-collector TIMS and are given in Table 1.

Table 1. Certified isotope ratio in uranium isotopic standards CRM U100 and CRM U200

$^{234}U/^{238}U$	$^{235}U/^{238}U$	$^{236}U/^{238}U$
CRM U100		
$0.00075359 \pm 0.00000223$	0.11359 ± 0.00011	$0.00042250 \pm 0.00000112$
CRM U200		
$0.00156432 \pm 0.00000378$	0.25126 ± 0.00026	$0.00265659 \pm 0.00000757$

The isotope ratios were measured using single-collector mass spectrometer ICP-SFMS ELEMENT 2 (Thermo Fisher Scientific GmbH, Germany), technical characteristics are given in Table 2.

The mass spectrometer resolution represents the value equal to $M/\Delta M$, where ΔM is the minimum distance (in a.m.u.) between two adjacent peaks at their overlapping at 10 % peak height. For example, the resolution of 1000 means that the peaks with masses of 100.0 a.m.u. and 100.1 a.m.u. are resolved, i.e., not overlapped up to 10 % of their height.

Table 2. Technical characteristics of ICP-SFMS ELEMENT 2

Mass range	from 2 to 264 a.m.u.
Sensitivity	$\sim 10^6$ cps for 1 ppb ^{115}In
Detection limit	1 ppq for non-interfering elements
Dark noise	< 0.2 cps
Dynamic range	$> 10^9$
Mass resolution	low (300), middle (4000), high (10000) at 10 % peak height
Signal stability	better than 1 % for 10 min.

The ions were registered at two modes of mass-spectrometer detecting system operation, namely, in the counting mode with the maximum counting rate of $\leq 10^6$ cps for the measurements of signal intensities from the ^{234}U, ^{235}U, ^{236}U isotopes; and in the analog mode with the maximum counting rate of $\leq 10^9$ cps for the measurements of signal intensities from the ^{235}U, ^{238}U isotopes. The comparison between the analytical signal values, measured in both the counting and analog modes of detector operation, was performed by means of cross-calibration according to the multielement standard ICP-MS-68A.

The aliquots for the analysis were prepared with the use of deionized water (HIGH PURITY STANDARDS, High Purity DI 18 MΩ Water) and nitric acid solutions (HIGH PURITY STANDARDS, Subboiled Distilled Nitric Acid). For preparation of the basis solution with 10 ppm ^{238}U content, 2.4 mg U3O8 CRM U100 and 2.8 mg U3O8 CRM U200 in powder form were dissolved in 15 % HNO3 under heated in a boiling-water bath. The final aliquots with the 50 ppb ^{238}U content were obtained through the basis solution dilution with 2 % HNO3. The aerosols of final solutions were introduced into the ionization region of the mass spectrometer with the speed-controlled peristaltic pump.

RESULTS AND DISCUSSIONS

The ion current contribution of uranium hydrides to the intensity of analytical signals from the isotopes ^{234}U, ^{235}U, ^{236}U, ^{238}U was estimated by measuring the mass spectra of the uranium ore concentrate CRM 124-1 with the use of the masses $m = 236$ (ion current contribution from $^{235}U\,^1H^+$) and $m = 239$ (ion current contribution from $^{238}U\,^1H^+$) on the assumption that there are no ^{236}U and ^{239}Pu isotopes in the measured sample. The efficiency of hydride ion

formation was calculated as the intensity ratios of $^{235}U\,^{1}H^{+}\,/\,^{235}U$ and $^{238}U\,^{1}H^{+}\,/\,^{238}U$. Then the analytical signal intensities of the isotopes in CRM U100 and CRM U200 were corrected and the isotope ratios $R_{meas.}$ were calculated with and without regard for the hydride ion current contribution. Obtained data were compared with the certified isotope ratio values $R_{cert.}$ given in Table 1.

The efficiency of the uranium hydride ion formation was found to be 3.54×10^{-5}, this corresponding to the $^{235}U\,^{1}H^{+}$ hydride ion current of 1 cps at the ^{235}U analytical peak current intensity of 3.54×10^{5} cps.

In the studies of the sample CRM U100, the analytical peak intensities were determined to be 8.53×10^{6} cps and 3.16×10^{4} cps for ^{235}U and ^{236}U , respectively, then the ion current contribution of $^{235}U\,^{1}H^{+}$ hydride to the analytical signal intensity at $m = 236$ (polyatomic interference effect) was determined to be 24 cps or ~ 0.1 %.

Fig. 1 shows the calculated isotope ratios $R_{cert.}\,/\,R_{meas.}$ as a functions of the difference of the isotope mass numbers (Δm) in the CRM U100 isotope standard, with and without regard for the ion current contribution of the $^{235}U\,^{1}H^{+}$ hydride.
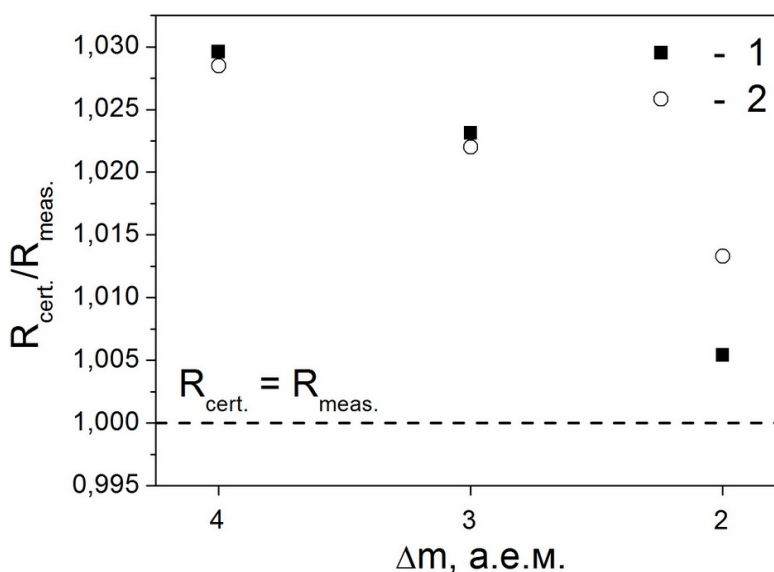
Figure 1. Isotope ratios versus their mass number difference Δm in the isotope standard CRM U100: 1 – initial value $R_{cert.}\,/\,R_{meas.}$ without regard for the ion current contribution from $^{235}U\,^{1}H^{+}$ hydride; 2 – corrected value $R_{cert.}\,/\,R_{meas.}^{corr.}$ with due regard for the ion current contribution from $^{235}U\,^{1}H^{+}$ hydride

From the data given at Fig. 1 it is evident that the polyatomic interference effect is the most significant during measuring the $^{236}U\big/^{238}U$ isotope ratios, i.e., at $\Delta m = 2$ a.m.u.; for the ratios $^{234}U\big/^{238}U$ ($\Delta m = 4$ a.m.u.) and $^{235}U\big/^{238}U$ ($\Delta m = 3$ a.m.u.) the given effect is less pronounced. Nevertheless, the values of all measured isotope ratios $R_{meas.}$ appear underestimated by 1…3 % relative to their certified values (the underestimating increases with increase in Δm), this bearing witness to the influence of other factors on the measurement results, one of which is mass bias effect.

To investigate the influence of the mass bias effect on the determinations of uranium isotope ratios, the external standardization calibration was used with three models (linear, power, exponential) describing the behavior of the specific discrimination coefficient β versus the mass of measured isotopes. The external standardization calibration implies that on measuring the ion signal ratios of isotopes in the probe, the parallel measurement of ion signals from the certified isotope standard is performed. After that, based on the measured isotope ratio and the exactly known isotope ratio in the standard the mass discrimination factor B and the specific discrimination coefficient β is calculated and the correction for the mass bias effect is introduced [12].

The mass discrimination factor characterizes the magnitude of the mass bias effect, and in the case of light-to-heavy isotope ratio measurements is determined as:

$$B = R_{cert.}\,/\,R_{meas.}\,. \qquad (1)$$

In addition to the mass discrimination factor, for quantitative description of the mass bias effect (the degree of ion mass discrimination in % $a.m.u.^{-1}$) the specific discrimination coefficient β is also used:

$$\beta = \big[(B-1)\cdot 100\big]/\Delta m\,. \qquad (2)$$

107

Determination of $^{234}U/^{238}U$, $^{235}U/^{238}U$, $^{236}U/^{238}U$ Isotope Ratios in Uranium Oxide...   **EEJP. 2 (2020)**

Formula (2) describes the linear model dependence of the specific discrimination coefficient β from the measured isotope masses. Then the isotope ratio value in the sample under study, corrected for the mass bias effect, is determined as:

$$R_{corr.}^{lin.} = R_{meas.}(1 + \beta \cdot \Delta m). \quad (3)$$

For the power and exponential models, the dependence of the specific discrimination coefficient β from the measured isotope masses is written as:

$$\beta = \ln B / \Delta m \quad\quad (4)$$

and the isotope ratios in the sample, corrected for the mass bias effect, are given by equations (5) and (6), respectively:

$$R_{corr.}^{pow.} = R_{meas.}(1 + \beta)^{\Delta m}, \quad (5)$$

$$R_{corr.}^{exp.} = R_{meas.} \cdot \exp(\beta \cdot \Delta m). (6)$$

In the present studies, the isotope standard CRM U200 was chosen as an external standard for taking into account the mass bias effect in the CRM U100 sample (conditionally unknown).

Table 3 lists the values of measured isotopic ratios in the sample CRM U100, which were corrected for the mass bias effect with the use of the linear, power and exponential dependence models of the specific discrimination coefficient β from the measured isotope masses (eqs. (3), (5) and (6), respectively). The table also gives the calculated values $R_{cert.} / R_{corr.}$ and the relative measurement error δ.

Table 3.

Results of isotope ratio determinations in the CRM U100 adjusted for mass bias effect

	$^{234}U/^{238}U$	$^{235}U/^{238}U$	$^{236}U/^{238}U$
$R_{cert.}$	0.00075359	0.11359	0.00042250
$R_{corr.}^{lin.}$	0.00076296	0.11444	0.00042583
$R_{corr.}^{pow.}$	0.00075613	0.11361	0.00042371
$R_{corr.}^{exp.}$	0.00075647	0.11364	0.00042380
$R_{cert.} / R_{corr.}^{lin.}$	0.988	0.993	0.992
$R_{cert.} / R_{corr.}^{pow.}$	0.997	0.999	0.997
$R_{cert.} / R_{corr.}^{exp.}$	0.996	0.999	0.997
$\delta^{lin.}$, %	1.243	0.746	0.788
$\delta^{pow.}$, %	0.338	0.015	0.287
$\delta^{exp.}$, %	0.382	0.047	0.308

The degree of ion mass discrimination calculated by formula (2) varies from от 6.00×10^{-3} (0.6 %) at $\Delta m = 4$ a.m.u. to 1.20×10^{-2} (1.2 %) at $\Delta m = 2$ a.m.u. Dependences of the specific discrimination coefficient β versus Δm, calculated by formulas (2) and (4), as well as the results of their approximation by linear and exponential functions are shown at Fig. 2.

It can be seen that at determining the uranium isotope ratios the mass bias effect can be compensated through their correction by means of the linear, power and exponential models of the $\beta = F(\Delta m)$ relationship. Nevertheless, taking into account the need for fulfillment of the conditions $(R_{cert.} / R_{corr.}) \rightarrow 1$ and $\delta \rightarrow 0$, the application of the power/exponential models is preferable. Besides, the approximation data in Fig. 2 confirm the advantage of the exponential function by the coefficient of determination $R^2 = 1$, that can be treated as full correspondence of the regression model to the experimental data.

Fig. 3 a-c shows the results of isotope ratio determination in the CRM U100 during seven consecutive measurements. The relative error of $^{234}U/^{238}U$, $^{236}U/^{238}U$ isotope ratio measurements was < 0.5 %, while for the $^{235}U/^{238}U$ ratio it was less than 0.1 %.

Mass spectra of the uranium ore concentrate CRM 124-1 on the mass $m = 237$ (contribution of the $^{238}U^+$ ion peak "tail") were measured to estimate the effect of isobaric overlapping of the "tail" of the high-intensity peak of mass m on the intensities of the peaks of masses ($m-1$), ($m-2$), ($m-3$). The estimated value was found to be 8.17×10^{-6}, this being in agreement with the data [13]. Thus, the contribution of scattered $^{238}U^+$ ions to the intensities of less abundant $^{236}U^+$ and $^{235}U^+$ is insignificant and can be neglected.
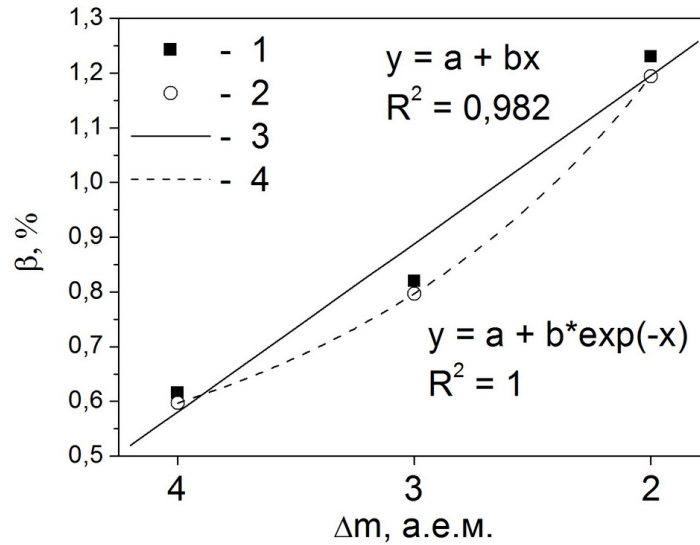
Fig. 2. Specific discrimination coefficient β versus mass numbers difference of the measured isotopes Δm : 1 – linear model calculated data; 2 – exponential model calculated data; 3 – approximation of points 1 by the linear function; 4 – approximation of points 2 by the exponential function
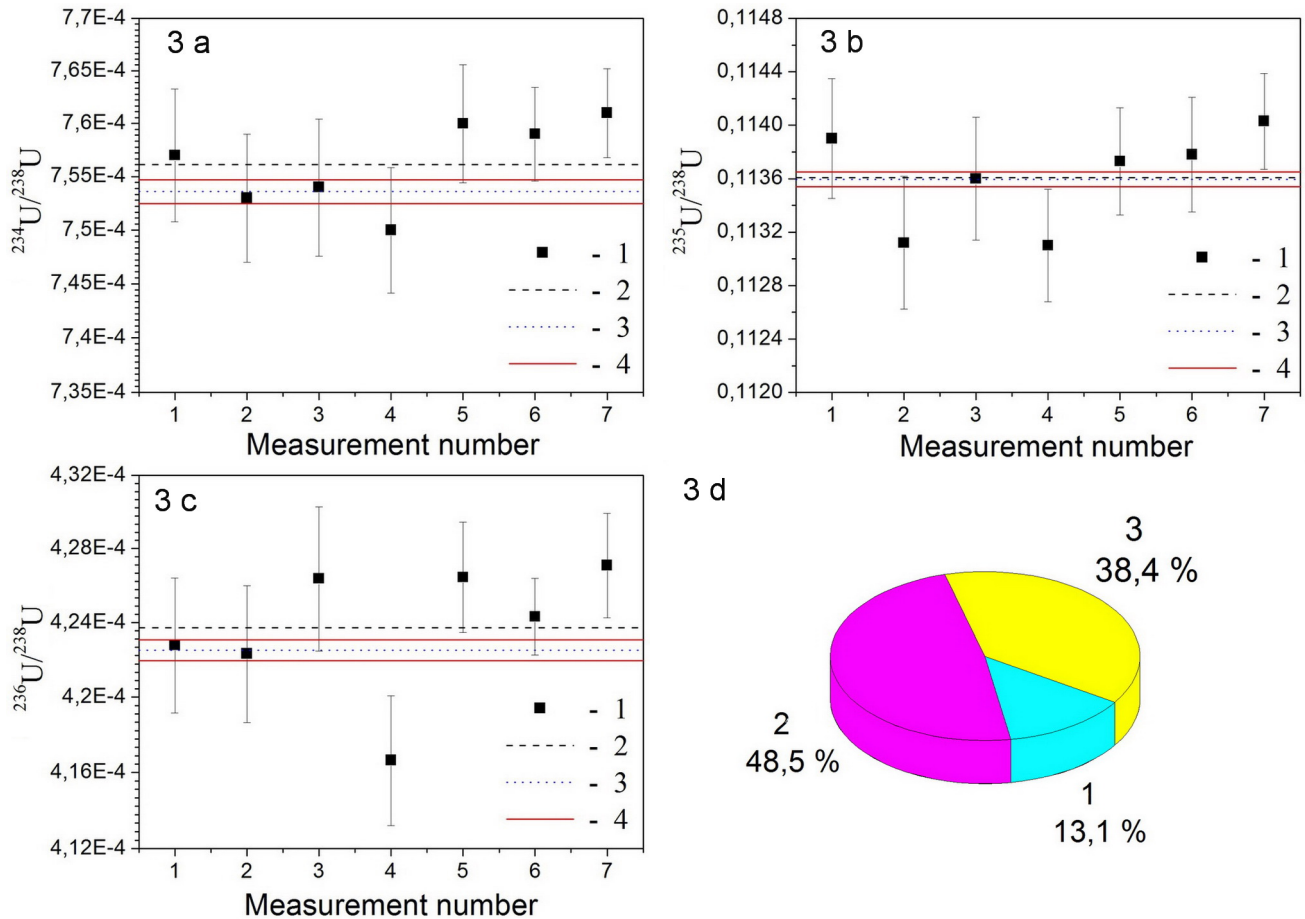
Fig. 3 a, 3 b, 3 c. Isotope ratios $^{234}U\big/^{238}U$, $^{235}U\big/^{238}U$, $^{236}U\big/^{238}U$ in the CRM U100, corrected for the mass bias effect using exponential model for $\beta = F(\Delta m)$: 1 – experimental data; 2 – mean value of experimental data; 3 – certified value; 4 – certified value uncertainty bounds

Fig. 3 d. Measurement uncertainty budget for the $^{235}U\big/^{238}U$ isotope ratio in the CRM U100: 1 – contribution of the certified value $^{235}U\big/^{238}U$ uncertainty; 2 – contribution of intensity measurement uncertainty for the analytical ^{235}U and ^{238}U peaks in the CRM U100; 3 –contribution of intensity measurement uncertainty for the analytical ^{235}U and ^{238}U peaks in the external standard CRM U200

109

Determination of $^{234}U/^{238}U$, $^{235}U/^{238}U$, $^{236}U/^{238}U$ Isotope Ratios in Uranium Oxide...   **EEJP. 2 (2020)**

In addition to the relative error, another metrological characteristic of the measurements is uncertainty, i.e., the parameter, which characterizes the spread of measured values. The calculated standard uncertainty u of the $^{234}U/^{238}U$, $^{235}U/^{238}U$, $^{236}U/^{238}U$ isotope ratio measurements in the CRM U100 was 0.563, 0.322 and 0.856 %, respectively. These are reasonable estimates in comparison with the uncertainties of certified values of 0.296, 0.097 and 0.265 %.

Finally, the uncertainty budgets of the $^{234}U/^{238}U$, $^{235}U/^{238}U$, $^{236}U/^{238}U$ isotope ratios measurements were calculated for the CRM U100, i.e., the contribution values of the uncertainty components (see Fig. 3 d).

The major contribution to the measurement uncertainty of the $^{235}U/^{238}U$ isotope ratio comes from the intensity measurement uncertainties for the analytical ^{235}U and ^{238}U peaks. For the other ratios under study, the measurement uncertainty budget is similar to that given at Fig. 3 d.

CONCLUSIONS

The influence of the ion interaction processes in the sector-field mass spectrometer (ICP-SFMS) on the measurements of $^{234}U/^{238}U$, $^{235}U/^{238}U$ and $^{236}U/^{238}U$ isotope ratios in uranium oxide was studied.

It has been demonstrated that the mass bias effect has most influence on the results of uranium isotope ratios determination. The degree of discrimination has been found to vary from 6.00×10^{-3} to 1.20×10^{-2}, and the grounds have been given for the use of the power/exponential models of the relationship $\beta = F(\Delta m)$ for correction of the measurement results.

Consideration has been given to the influence of the effects of isobaric and polyatomic interferences on the results of uranium isotope ratios determination. The efficiency of uranium hydride ion ($^{235}U^1H^+$) formation has been calculated to be 3.54×10^{-5}, while the contribution of scattered $^{238}U^+$ ions to the intensities of less abundant ^{236}U and ^{235}U reached 8.17×10^{-6}.

Metrological characteristics of analytical results have been analyzed, in particular, the relative measurement error for $^{234}U/^{238}U$, $^{236}U/^{238}U$ isotope ratios has made < 0.5 %, while for the $^{235}U/^{238}U$ ratio it was less than 0.1 %. This points to the applicability of the ICP-SFMS method for the quality control and certification of uranium products in nuclear power industry.

ORCID IDs

Dmytro V. Kutnii, https://orcid.org/0000-0001-9591-4013; **Dmytro D. Burdeynyi**, https://orcid.org/0000-0003-4431-7264
Stanislav A. Vanzha, https://orcid.org/0000-0003-0949-947X; **Natalia V. Rud**, https://orcid.org/0000-0002-2958-3524

REFERENCES

[1] V.A. Kalashnikov, Synopsis of Ph.D. dissertation, Federal State Unitary Enterprise Ural Electromechanical Plant, 2006. (in Russian)

[2] G.V. Shishalova, M.A. Kulakova, and E.E. Varlashova, Analytics and Control. **7**(2), 186-189 (2003) (in Russian)

[3] A.V. Saprygin, V.M. Golik, A.A. Makarov, B.G. Dzhavayev, and V.N. Kudryavtsev, Standard Samples. **2**, 39-48 (2007). (in Russian)

[4] I.T. Platzner, *Modern isotope ratio mass-spectrometry*. (Chichester, Wiley, 1997), pp. 83-108.

[5] A.V. Saprygin, B.G. Dzhavayev, and A.A. Makarov, Analytics and Control. **7**(1), 68-73 (2003). (in Russian)

[6] A.V. Saprygin, B.G. Dzhavayev, and A.A. Makarov, Analytics and Control. **7**(1), 64-67 (2003). (in Russian)

[7] S. Lapshin, O. Proshenkina, Equipment and materials. **3**, 28-36 (2012). (in Russian)

[8] A.V. Khoroshilov, E.L. Silakova, and P.I. Ivanov, Advances in Chemistry and Chemical Technology, **29**(6), 56-58 (2015). (in Russian)

[9] A.N. Baranova, in: *Материалы Конференции «Современные Проблемы Геохимии» [Materials of the Conference "Contemporary Issues of Geochemistry"]* (Irkutsk, Russia, 2011), pp. 84-86. (in Russian)

[10] M. Zoriy, L. Halicz, M. Ketterer, C. Pickhardt, P. Ostapczuk, and J. Becker, J. Anal. At. Spectrom. **19**, 362-367 (2004).

[11] A.Yu. Leikin, and P.V. Yakimovich, Journal of Analytical Chemistry, **67**(8), 752-762 (2012). (in Russian)

[12] A.A. Pupyshev, and B.A. Sermyagin, *Дискриминация ионов по массе при изотопном анализе методом масс-спектрометрии с индуктивно-связанной плазмой [Ion mass discrimination in the isotope analysis by the method of inductively coupled plasma mass spectrometry]* (Ural State Technical University, Yekaterinburg, Russia, 2006), pp. 16-68. (in Russian)

[13] V.A. Stebel'kov, O.V. Erokhin, N.R. Stankov, and A.I. Yermakov, Mass-Spectrometry. **1**(3), 221-230 (2004). (in Russian)

ВИЗНАЧЕННЯ ІЗОТОПНИХ СПІВВІДНОШЕНЬ ^{234}U/^{238}U, ^{235}U/^{238}U, ^{236}U/^{238}U В ОКСИДІ УРАНУ МЕТОДОМ МАС-СПЕКТРОМЕТРІЇ З ПОДВІЙНИМ ФОКУСУВАННЯМ (ICP-SFMS)

Д.В. Кутній, Д.Д. Бурдейний, С.О. Ванжа, Н.В. Рудь

Національний науковий центр «Харківський фізико-технічний інститут» НАН України

Досліджено вплив ефектів дискримінація іонів по масах, ізобарних і поліатомних інтерференцій на результати вимірювань ізотопних співвідношень $^{234}U\big/^{238}U$, $^{235}U\big/^{238}U$, $^{236}U\big/^{238}U$ в оксиді урану методом мас-спектрометрії з подвійним фокусуванням. Для проведення досліджень використовували сертифіковані ізотопні стандарти на основі октаоксида тріурана (U_3O_8) CRM U100, CRM U200 і одноколлекторний мас-спектрометр ICP-SFMS ELEMENT 2. Показано, що основним ефектом, що впливає на результати визначення ізотопних співвідношень урану, є дискримінація іонів по масах. Для вивчення впливу ефекту дискримінації іонів по масах на результати визначення ізотопних співвідношень урану, застосовували спосіб зовнішнього стандарту з трьома моделями (лінійної, степеневої та експоненціальної) залежності питомого коефіцієнта дискримінації β від мас вимірюваних ізотопів. Розрахований коефіцієнт ступеня дискримінації для лінійної, степеневої та експоненціальної моделей залежності питомого коефіцієнта дискримінації від мас ізотопів варіюється від $6,00 \times 10^{-3}$ до $1,20 \times 10^{-2}$. Обгрунтовано перевагу використання степеневої або експоненційної моделей залежності $\beta = F(\Delta m)$ для коригування ізотопних співвідношень, що вимірюються. При виникненні поліатомних інтерференцій ефективність утворення іонів гідриду урану ($^{235}U{}^{1}H^{+}$) становить $3,54 \times 10^{-5}$, а величина ефекту ізобарних накладень внаслідок вкладу розсіяних іонів $^{238}U^{+}$ в інтенсивності менш розпросторених $^{236}U^{+}$ і $^{235}U^{+}$ — $8,17 \times 10^{-6}$. Проаналізовано метрологічні характеристики аналітичних результатів, зокрема, відносна похибка вимірювань ізотопних співвідношень $^{234}U\big/^{238}U$, $^{236}U\big/^{238}U$ склала $< 0,5\,\%$, а для співвідношення $^{235}U\big/^{238}U$ — менше $0,1\,\%$. Розрахована стандартна невизначеність вимірювань ізотопних співвідношень u в стандарті CRM U100 склала 0,563; 0,322 і 0,856% відповідно, що виглядає задовільно в порівнянні з величинами невизначеності сертифікованих значень: 0,296; 0,097 і 0,265%.

КЛЮЧОВІ СЛОВА: мас-спектрометрія з індуктивно-зв'язаною плазмою, оксид урану, ефект дискримінації іонів по масах, поліатомні інтерференції, ізобарні накладення, співвідношення ізотопів урану

ОПРЕДЕЛЕНИЕ ИЗОТОПНЫХ ОТНОШЕНИЙ ^{234}U/^{238}U, ^{235}U/^{238}U, ^{236}U/^{238}U В ОКСИДЕ УРАНА МЕТОДОМ МАСС-СПЕКТРОМЕТРИИ С ДВОЙНОЙ ФОКУСИРОВКОЙ (ICP-SFMS)

Д.В. Кутний, Д.Д. Бурдейный, С.А. Ванжа, Н.В. Рудь

Национальный научный центр «Харьковский физико-технический институт» НАН Украины

Исследовано влияние эффектов дискриминация ионов по массам, изобарных и полиатомных интерференций на результаты измерений изотопных отношений $^{234}U\big/^{238}U$, $^{235}U\big/^{238}U$, $^{236}U\big/^{238}U$ в оксиде урана методом масс-спектрометрии с двойной фокусировкой. Для проведения исследований использовали сертифицированные изотопные стандарты на основе октаоксида триурана (U_3O_8) CRM U100, CRM U200 и одноколлекторный масс-спектрометр ICP-SFMS ELEMENT 2. Показано, что основным эффектом, влияющим на результаты определения изотопных отношений урана, является дискриминация ионов по массам. Для изучения влияния эффекта дискриминации ионов по массам на результаты определения изотопных отношений урана, применяли способ внешнего стандарта с тремя моделями (линейной, степенной и экспоненциальной) зависимости удельного коэффициента дискриминации β от масс измеряемых изотопов. Рассчитан коэффициент степени дискриминации для линейной, степенной и экспоненциальной моделей зависимости удельного коэффициента дискриминации от масс измеряемых изотопов, который варьируется от $6,00 \times 10^{-3}$ до $1,20 \times 10^{-2}$. Обосновано преимущество использование степенной либо экспоненциальной моделей зависимости $\beta = F(\Delta m)$ для корректирования измеряемых изотопных отношений. При возникновении полиатомных интерференций эффективность образования ионов гидрида урана ($^{235}U{}^{1}H^{+}$) составляет $3,54 \times 10^{-5}$, а величина эффекта изобарных наложений вследствие вклада рассеянных ионов $^{238}U^{+}$ в интенсивности менее распространенных $^{236}U^{+}$ и $^{235}U^{+}$ — $8,17 \times 10^{-6}$. Проанализированы метрологические характеристики аналитических результатов, в частности, относительная погрешность измерений изотопных отношений $^{234}U\big/^{238}U$, $^{236}U\big/^{238}U$ составила $< 0,5\,\%$, а для отношения $^{235}U\big/^{238}U$ — менее $0,1\,\%$. Рассчитанная стандартная неопределенность u измерений изотопных отношений $^{234}U\big/^{238}U$, $^{235}U\big/^{238}U$, $^{236}U\big/^{238}U$ в стандарте CRM U100 составила 0,563; 0,322 и 0,856 % соответственно, что выглядит удовлетворительно по сравнению с величинами неопределенности сертифицированных значений: 0,296; 0,097 и 0,265 %.

КЛЮЧЕВЫЕ СЛОВА: масс-спектрометрия с индуктивно-связанной плазмой, оксид урана, эффект дискриминации ионов по массам, полиатомные интерференции, изобарные наложения, отношения изотопов урана

EFFECT OF THERMAL-VACUUM DISPERTION OF GRAPHITE

Volodymyr O. Kutovyi*, Dmitry G. Malykhin, Olexandr S. Kalchenko
Ruslan L. Vasilenko, Volodymyr D. Virych, Olexandr O. Germanov
National Scientific Center "Kharkov Institute of Physics & Technology" NASU,
Kharkiv, 61108, Akademicheskaya st. 1, Ukraine
*Corresponding Author: kutovoy@kipt.kharkov.ua, Tel.: +38-057-349-10-82
Received February 24, 2020; revised March 27, 2020; accepted March 29, 2020

A scientific and technical development of a high-performance thermal-vacuum method, which is an environmentally friendly process based on combination of vacuuming and high-speed thermal heating, was carried out with non-stop production of nanodispersed carbon. A review of physical processes that affect a powder material has been carried out. Thermal-vacuum treatment of C1 grade graphite 1…2 mm of size was carried out. To study the structural composition of the material in initial state and processed in a thermal-vacuum installation, X-ray diffraction analysis and electron microscopy were used. According to results of X-ray analysis, the original C1 grade graphite has two known structural modifications: hexagonal one with lattice periods $a_o = 0.2461$ nm, $c_o = 0.6705$ nm, and rhombohedral structure about 30% – with $a = 0.2461$ nm and $c = (3/2)c_o = 1.003$ nm. In graphite treated in a thermal-vacuum installation, these components have been detected as the main composition. Additionally, a super-structural rhombohedral phase with periods $a = 2a_o = 0.492$ nm and $c = (3/2)c_o = 1.003$ nm has been detected. A monoclinic phase with parameters $a_1 = 0.6075$ nm, $b_1 = 0.4477$ nm, $c_1 = 0.4913$ nm, and $\beta = 99.6°$ has also been detected, probably with the presence of iron atoms in structure. The results of analysis and calculations are generally consistent with TEM images of the reciprocal lattice of processed graphite. As a result, it was noted that the initial graphite powder was crushed to 2…40 nm with a partial change in the structure, formation of objects like multilayer nanotubes and fullerenes. It was noted that thermal deformations are involved in this effect, what can significantly accelerate the process of obtaining nanodispersed carbon material with new physicochemical and mechanical properties. The results could be widely used for industrial production of nanosized materials.
KEY WORDS: carbon, thermal-vacuum dispersion, nanotubes, fullerenes.

Recently, it has become increasingly important to solve the problems of energy and resource conservation and intensification in production processes of nanodispersed materials. When dispersing materials in order to improve production cycle, in particular, several technological processes are combined in one installation. This leads to intensification of the production process and to lower capital costs. So, in some installations, the mechanical process of grinding and drying is used simultaneously [1]. In this case, preheated air is used for drying, what leads to essential energy demands. As a result of an analysis of the methods of fine grinding of materials, it was found that the most rational way is a combination of shock loads and erasure [2, 3]. Shock and erasure loads, which act in the field of intense turbulent flows, lead to destruction of the material with manifestation of new properties [4-7].

Due to the fact that among the tasks noted, much attention of the world community is paid to the use of carbon nanostructures in the industrial production, it would be advisable to test here similar dispersion methods with studying the properties of the obtained materials.

In this regard, the aim of this work is to investigate an effect of a thermal-vacuum dispersion process on state of C1 grade graphite.

SCHEME OF THERMAL-VACUUM INSTALLATION FOR DISPERSION
Used in this work, the thermovacuum method of non-stop dispersion of the material was developed on the basis of theoretical and experimental studies [8,9]. Its principle is based on the combination of fast vacuuming processes and contact heating of the surface of the particles of material inside a spiral heater, what provides instant heating of the surface layer of particles in vacuum to a predetermined temperature. Contact of the particles with the wall of the heater causes heat transfer to their surface layer, and the reduced pressure inside the heating element ultimately allows grinding the material layer by layer.

Figure 1 shows the thermal-vacuum installation designed for non-stop dispersing of powder materials [8].

The installation consists of a feed hopper (1), a hollow heater, (2), a vacuum pump (3), pipelines (4, 11), a cyclone (5), a dried raw material receiver (6), and a lock-gate (7). It has thermocouples (8, 13), a control panel (9), a conveyor (10), a filter (12), a level sensor for dried raw materials (14), and a vacuum gauge (15).

This design of the installation is able to provide non-stop dispersing of powder material in a space thermally insulated from the external environment.

REGULARITIES OF HEAT-MASS-EXCHANGE PROCESSES IN THERMAL-VACUUM INSTALLATION
An original coarse-grained material with ordinary humidity enters with the air inside the hollow spiral heater (2) (Fig. 1), and passes it for 15 s at a speed of ~10 m/s. This is provided by creating a pressure gradient in the hollow heating element using a vacuum pump. Due to this, centrifugal force acts on the particles in the spiral hollow of the

heater, and between the surface of particles and the wall of the heater at shortest times a dense shock contact is formed with an effective heat transfer. Instantaneous transfer of thermal energy from the heater wall to the surface layer of particles occurs [9,10]. The temperature change (dT/dt) on the particle surface is determined by the temperature gradient dT/dx at the moment of heat transfer from the heater in close contact with it:

$$\frac{\partial T}{\partial t} = -\kappa \frac{dT}{dx} \qquad (1)$$

where κ is a coefficient of thermal conductivity in the surface layer of the particle.
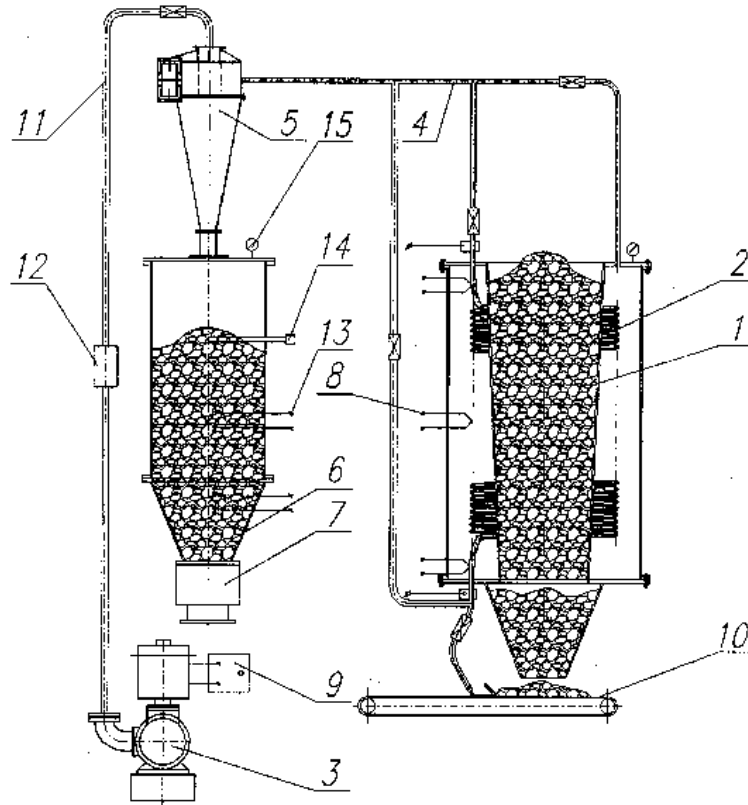
Fig.1. Scheme of thermal-vacuum installation.

A change in temperature leads to a change in the size of the heated section along the temperature front, i.e. along the contact surface: $\Delta l/l_0 = \alpha \Delta T/T$, where α is the thermal coefficient of linear expansion of the material. The velocity of the medium at the conditional boundary of the heated section of radius $l_0/2$ will eventually have the following expression:

$$v_l = \frac{1}{2}\frac{dl}{dt} = \alpha \frac{l_0}{2}\frac{\partial T}{\partial t} = -\alpha\kappa \frac{l_0}{2}\frac{dT}{dx}. \qquad (2)$$

As is known from field theory and continuum mechanics, all field perturbations are described by functions of a type $f(x,t) = f(x - v_s \cdot t)$ and propagate with speed v_s. The time derivative of the argument $v_s \cdot t - x$ is here the "Doppler" sound speed in the coordinates of the boundary of that section: $v_s - v_l$. Its relationship with the sound speed $v_s - v_l \leftrightarrow v_s$ indicates the compression degree of that boundary medium, and a rough estimate of the stress in this section can be represented by the following formula:

$$\sigma \sim C_{11}\frac{v_l}{v_s - v_l}, \qquad (3)$$

where C_{11} is an uniaxial compression module of the medium.

Thus, the effect of particle crushing, similar to the action of a shock wave, manifests itself at $v_l \sim v_s$ and even at lower v_l speeds. In addition, since the temperature gradient dT/dx (1-2) depends on the initial moment of contact inversely with t^n, where $n \sim 1$, this effect can occur in the shortest initial time intervals and with sufficiently small fragments of particles [11]. Such effects are known to be accompanied by audible characteristic crackles. At the same time, high stresses arising in such a process can significantly affect the crystalline structure of materials, like martensitic transformations.

It is known that the powders of many materials are hygroscopic and can contain from percent to tens of percent humidity. Then, since with sharp contact heating, the dispersion effect comprises microscopic sections of the material, the residual humidity in such cases can significantly affect the process. The essence of this is a sharp thermal expansion of water particles during the formation of water vapor – in a vapor explosion, which can significantly intensify the dispersion effect [11].

In general, the effectiveness of dispersion in a thermal-vacuum installation depends on the thermophysical properties of material and its state: on the relationships between thermal conductivity, heat capacity and thermal expansion, on dispersion and humidity of original material, on temperature of heater and pressure inside the channel.

MATERIAL AND METHODS

For processing in the thermal-vacuum installation, we chose the C1 grade graphite with 1...2 mm size of particles (Fig. 2a) and 1.0…1.5% total impurity according mass spectrometry.

X-ray diffraction analysis was used to investigate the structural composition of the graphite material in the original and processed state. The samples were made in the form of briquettes $\varnothing 25.0 \times 5 \dots 10$ mm² by pressing with 250 MPa pressure. The measurements were carried out by the DRON4-07 diffractometer according to the Bragg-Brentano X-ray optical scheme with a proportional counter. To eliminate the vertical divergence of the X-ray beam, a pair of Soller slits was used in the measurement scheme. In the initial processing of the obtained data, the reflection angles were corrected by eliminating the effect of the depth of reflection of radiation, which for dense graphite gives an X-ray line shift in order of part of degree, and this effect is enhanced when measuring the powder with a lower density.

For electron-optical studies of structure of the material, the JEM-100CX transmission microscope was used. For this, a light fraction of the material was released by aquatic flotation.

The chemical composition was determined using the EMAL-2 laser mass spectrometer.

RESULTS AND DISCUSSION

Table 1 shows the mass-spectrometric data on the chemical composition of the treated graphite.

Table 1.

Chemical composition of treated the C1 grade graphite.

element	Fe	Ca	Si	Al	K	Na	Mg	Ti	S	Mn	rest
% wt	3,1	2,9	0,94	0,7	0,68	0,5	0,47	0,3	0,24	0,1	<0.2

The bulk density of the material is 0.316 g/cm³.

By thermal-vacuum treatment, a nanodispersed graphite powder was obtained with decreasing in particle size to nanometer. Aggregations of particles with 10...40 nm size were also detected (Fig. 2b). It is considered that these are particles of an intermediate state that have been granulated during processing.
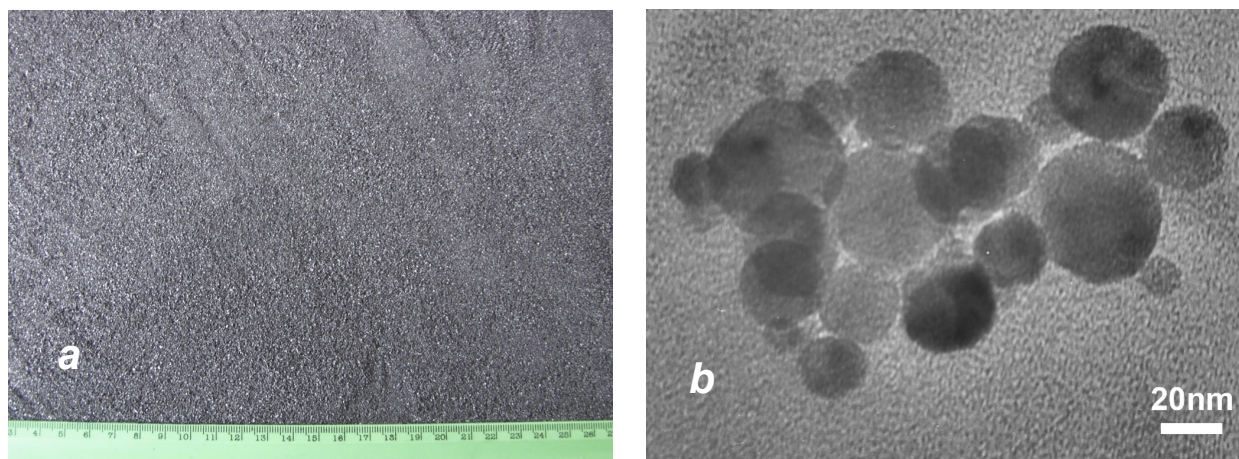
Figure 2. C1 graphite in the initial state (a) and after treatment (b; SEM image).

Figure 3 presents TEM images of the reciprocal lattice of the heat-treated graphite. Figure 3a shows it for a graphite particle having the ordinary hexagonal or rhombohedral lattice with its reflection here in the basal crystallographic plane (Fig. 3a). This particle also includes a coherent phase with a double period a, which follows from the hexagonal arrangement of small points in close proximity to the center of the electron-diffraction scan. The reciprocal lattice of the monoclinic modification with an angle $\beta = 99.5°$ was also recorded (Fig. 3b).

From these results it follows that, during processing, some of the graphite is transformed to a new modification.

According to Figure 4, in the heat-treated graphite C1, formations similar to multilayer nanotubes and fullerenes with sizes of 2 ... 5 nm and 2 nm, respectively, are observed.

Figure 5 presents fragments of 2θ-angular CuK_α diagrams of intensity of X-ray reflections of the C1graphite in the initial and heat-treated state. According to the results of measurements and calculations, the original graphite consists of two known components: the hexagonal phase with periods $a_o = 0.2461 \pm 0.0002$ nm, $c_o = 0.6705 \pm 0.0007$ nm, the rhombohedral component with periods $a = a_o = 0.2461 \pm 0.0001$ nm and $c = (3/2)c_o = 1.0030 \pm 0.0002$ nm with a content of about 30% (Fig. 5a).

As the main composition, these phases have also been detected with the same mutual proportion in the heat-treated graphite. Additionally, a modified (superstructural) rhombohedral phase was found in it with the double period a: $a_1 = 2a_o = 0.492 \pm 0.0001$ nm and $c_1 = c_o = 1.0030 \pm 0.0002$ nm. According to Figure 3a, this phase is coherent with the main graphite modification. A monoclinic phase was also found with the following lattice periods: $a_2 = 0.6075 \pm 0.0001$ nm; $b_2 = 0.4477 \pm 0.0002$ nm; $c_2 = 0.4913 \pm 0.0003$ nm and $\beta = 99.6 \pm 0.1°$. Probably, this structure was formed with the participation of iron atoms. The proportions and the angle value are consistent with the results of a TEM scan of the reciprocal lattice of the treated graphite (Fig. 3b).
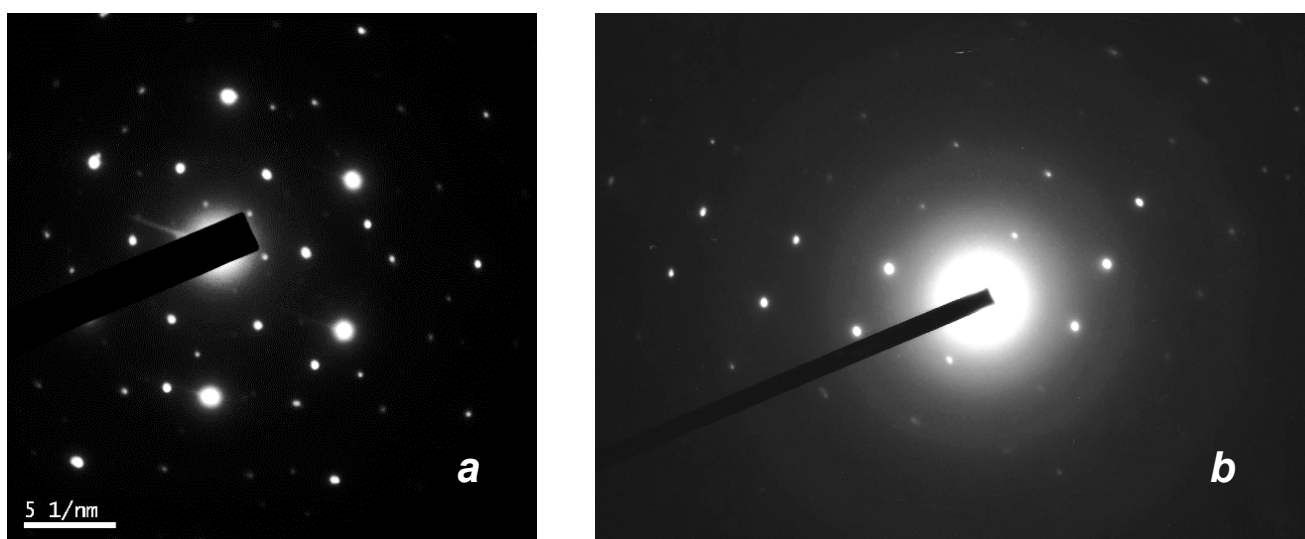
Figure 3. Electron-diffraction scans of hexagonal (a) and monoclinic (b) reciprocal lattices in the C1graphite after treatment.
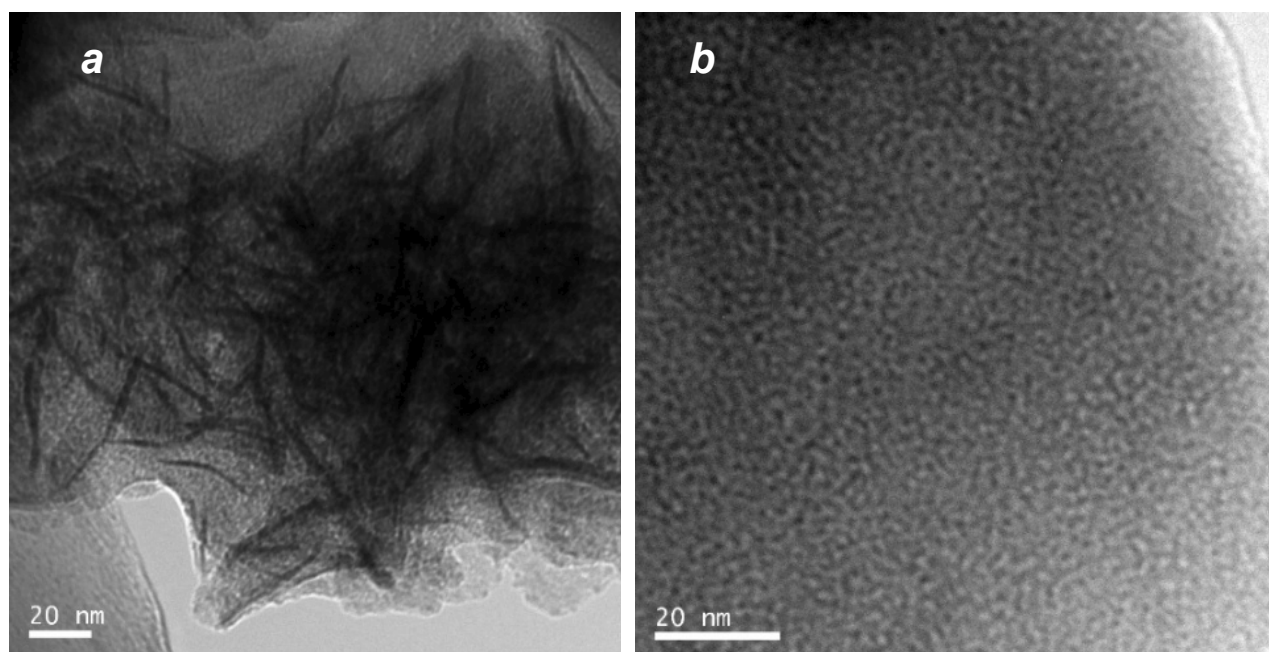
Figure 4. TEM illustrations of multilayer nanotubes (a) and fullerene-like formations (b) in the treated C1 graphite.

Table 2 presents the results of calculations of structures, including interplanar distances and reflection indices (in increasing angle): initial graphite with hexagonal and rhombohedral structure, as well as phases formed with superstructural rhombohedral and monoclinic systems.

Table 2.

Interplanar spacing (*d*) on the measurements of the treated graphite C1, and (*hk.l*) indices of the found phases: hexagonal, rhombohedral (RE), modified (superstructural) rhombohedral (RE'), and monoclinic system.

d (nm)	Structure; (*hk.l*)				*d* (nm)	Structure; (*hk.l*)				*d* (nm)	Structure; (*hk.l*)			
	Hex.	RE	RE'	Mono.		Hex.	RE	RE'	Mono.		Hex.	RE	RE'	Mono.
0,4265			(10.0)		0,2084		(10.1)	(20.1)		0,1816			(10.5)	
0,3932				(1-10)	0,2083				(1-12)	0,1800	(10.2)			
0,3925			(10.1)		0,2036				(021)	0,1739				(310)
0,3355	(00.2)				0,2033	(10.1)				0,1693				(212)
0,3345		(00.3)	(00.3)	(110)	0,2026				(1-21)	0,1678	(00.4)			
0,3249			(10.2)		0,2025				(300)	0,1672		(00.6)	(00.6)	(220)
0,3069				(1-11)	0,1994				(120)	0,1645				(3-20)
0,3037			(200)		0,1983			(11.3)		0,1625		(10.4)	(20.4)	
0,2462			(11.0)		0,1973				(3-10)	0,1560				(3-21)
0,2455			(002)		0,1979				(112)	0,1544	(10.3)			
0,2390			(2-11)		0,1966				(2-20)	0,1538				(3-12)
0,2276			(102)		0,1963		(10.2)	(20.2)		0,1537				(013)
0,2237			(020)		0,1909				(202)	0,1535			(21.2)	
0,2133	(10.0)				0,1872				(301)	0,1535				(2-22)
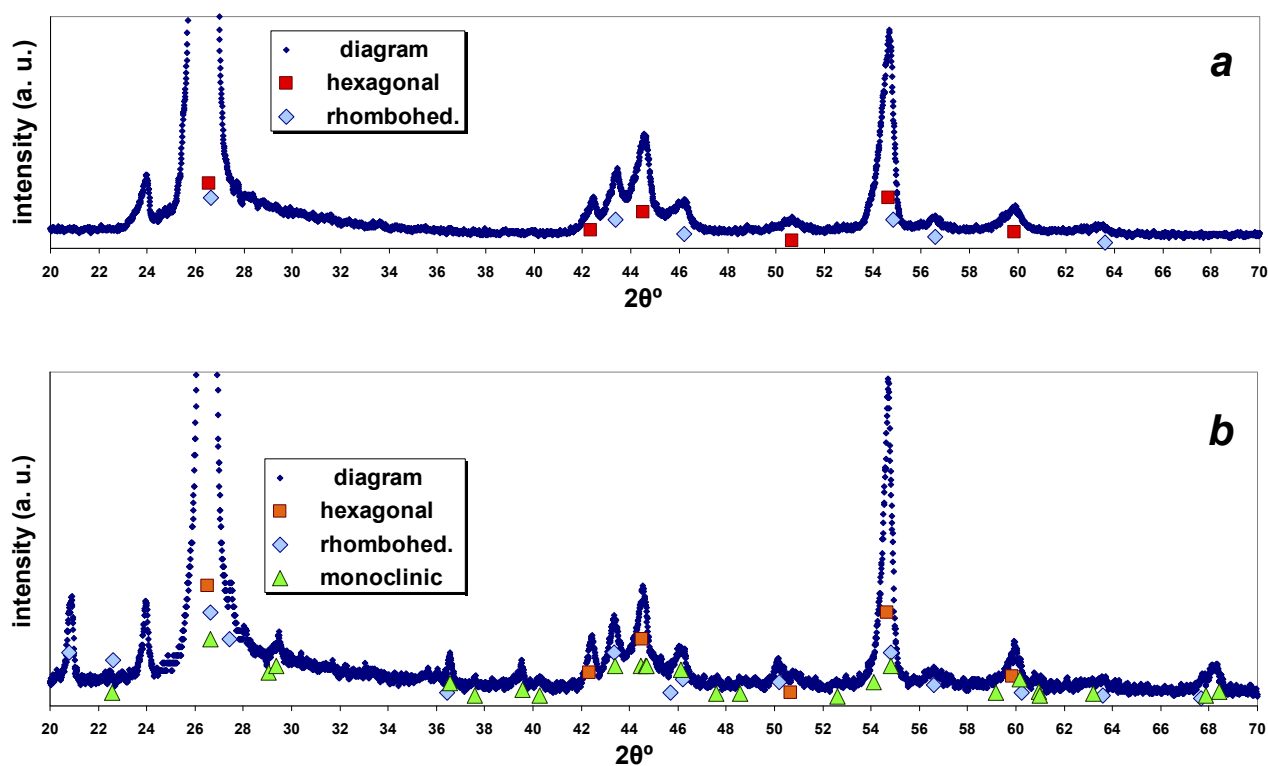
Figure 5. Fragments of X-ray scans with the designations of calculated reflection angles for the components of the C1 graphite in the original (a) and processed state (b).

Thus, movement of carbon powder in the hollow of the spiral heating element of the thermal-vacuum installation leads to its dispersion, converting the original material for 15 s (with a productivity of 8...9 g/s) into nanodispersed state with order of 2...40 nm particle sizes and with modification of structure of some part material.

It should be noted that the total continuance of the production of nanodispersed carbon in the thermal-vacuum installation counts some seconds, due to rapid heating and reduced ambient pressure. For the effective intake of carbon in the installation, a stream of air is necessary such that will ensure its continuous movement inside the spiral heating element.

CONCLUSION

The process of high-speed dispersion of powders, based on the combination of mechanics of particle motion under conditions of rapid evacuation, and thermal effects on particles, has been described and analyzed. A thermal-vacuum installation in which these processes are combined has been described.

By combining these processes in the thermal-vacuum installation, the processing of C1 grade graphite powder with an initial particle size of 1...2 mm was carried out. The following results were obtained:

As a result of the dispersion process, a powder is formed with particle sizes of the order of a nanometer with 10...40 nm residual granular particles. It has been established that the nanometer sizes are both nanotubes forming multilayer complexes and fullerene-like formations.

In addition to the ordinary phases of the original graphite, which have a hexagonal and a rhombohedral lattices, and are detected in the treated powder as the main composition, a superstructural-rhombohedral phase was also found in the treated powder, as well as a monoclinic phase was with the probable participation of iron atoms.

As a result, in the graphite's example, it was shown that the described thermal-vacuum treatment of coarse-grained materials is capable of dispersing them rapidly and energy-efficiently with a partial change in the crystalline structure and even in particle shape.

ORCID IDs
Dmitry Malykhin, https://orcid.org/0000-0003-0259-0211

REFERENCES

[1] N.I. Shishkov, S.A. Oparin, P.I. Soroka, and V.I. Zrajevsky, in: *Proceedings of V International research-to-practice conference Science and Education*, (Dnepropetrovsk – Donetsk, 2002). **19**, pp. 49-50.

[2] S.A. Oparin, and P.I. Soroka, Наукові праці Одеської національної академії харчових технологій [Scientific works of Odessa National academy of food technology], **45**(3), 4-9 (2014).

[3] S.A. Oparin, Ye.V. Leshchenko, and P.I. Soroka, Наукові праці Одеської національної академії харчових технологій [Scientific works of Odessa National academy of food technology], **37**, 118-122 (2010).

[4] A.V. Mikhailenko, S.Yu. Smyk, and Yu.A. Kunitsky, Поверхность [Surface], **3**(18), 50-102 (2011).

[5] Brychka S.Ya. Наноструктурное материаловедение [Nanostructured materials science], **2**, 40-53 (2009).

[6] Q. Zhang, S.F. Yoon, J. Ahn et al. Journal of Physics and Chemistry of Solids, **61**(7), 1179-1183 (2000), https://doi.org/10.1016/S0022-3697(99)00383-2.

[7] Y.S. Woo, N.S. Lee, D.Y. Han et al. Diamond and Related Materials, **11**, 59-66 (2002). https://doi.org/10.1016/S0925-9635(01)00519-2.

[8] V.O. Kutovoy, Patent of Ukraine No 81138, (27 July 2005). Vacuum drying device, N a200507488; stated 27 July 2005; publ. 10 December 2007. Bull. N 20, pp. 5.

[9] V.O. Kutovoy, and I.S. Mysak, East-European Journal of Advanced Technology, **6/8**(72), 35-40 (2014).

[10] V.I. Isachenko, V.A. Osipova, A.S. Sukomel, *Теплопередача* [*Heat conductance*]. (Energoizdat, Moscow, 1981), pp. 417.

[11] V.O. Kutovoy, D.G. Malykhin, O.S. Kalchenko, and R.L. Vasilenco, *Digest of scientific papers, Поверхность* [*Surface*], **11**(26), 508-520 (2019).

ЕФЕКТ ТЕРМОВАКУУМНОГО ДИСПЕРГУВАННЯ ГРАФІТУ
Кутовий В.О., Малихін Д.Г., Кальченко О.С., Василенко Р.Л., Вірич В.Д., Германов О.О.
Національний науковий центр «Харківський фізико-технічний інститут» НАНУ
Харків, 61108, вул. Академічна 1, Україна.

Здійснено науково-технічну розробку екологічно чистого, високопродуктивного термовакуумного методу безперервного виробництва нанодисперсних порошків, що виконано на підставі об'єднання процесу вакуумування і швидкісного термічного нагріву. Проведено аналіз фізичних процесів в термовакуумній установці, що впливають на частинки вихідного матеріалу. Проведено термовакуумну обробку графіту марки C1 з вихідним розміром частинок у 1…2 мм. Для дослідження структурного складу матеріалу в початковому стані і обробленого в термовакуумній установці застосовано рентгеноструктурний аналіз та електронну мікроскопію. Згідно з результатами рентгеноструктурних досліджень, вихідний графіт марки C1 має дві відомі структурні модифікації: гексагональну з періодами решітки $a_o = 0.2461$ нм, $c_o = 0.6705$ нм і ромбоедричну з вмістом близько 30% та з періодами $a = 0.2461$ нм и $c = 1.003$ нм (полуторне значення періоду c_o основної структури графіту). Поєднання цих фаз спостерігалося в основі складу графіту C1 після обробки в термовакуумній установці. Крім цього додатково виявлено надструктурну ромбоедричну фазу з періодами $a = 2a_o = 0.492$ нм і $c = (3/2)c_o = 1.003$ нм. Виявлено також фазу з моноклінною структурою і з параметрами $a_1 = 0.6075$ нм; $b_1 = 0.4477$ нм; $c_1 = 0.4913$ нм; $\beta = 99.6°$ – імовірно, з наявністю в структурі атомів заліза. Результати аналізу і розрахунків в цілому узгоджуються з ПЕМ-знімками зворотної кристалічної гратки обробленого графіту. В результаті відзначено, що вихідний порошок графіту піддався дробленню до розмірів 2…40 нм з частковою зміною структури та з проявом форм, подібних багатошаровим нанотрубкам і фулеренам. Також відзначається, що в цьому процесі беруть участь термодеформаційні ефекти, що дозволяє значно прискорити процес отримання нанодисперсного вуглецевого матеріалу з новими фізико-хімічними і механічними властивостями. Отримані результати можуть знайти широке застосування для промислового виробництва нанодисперсних матеріалів.

КЛЮЧОВІ СЛОВА: вуглець, термовакуумне диспергування, нанотрубки, фулерени

ЭФФЕКТ ТЕРМОВАКУУМНОГО ДИСПЕРГИРОВАНИЯ ГРАФИТА

Кутовой В.А., Малыхин Д.Г., Кальченко А.С., Василенко Р.Л., Вирич В.Д., Германов А.А.

Национальный научный центр «Харьковский физико-технический институт» НАНУ

Харьков, 61108, ул. Академическая 1, Украина

Осуществлена научно-техническая разработка экологически чистого, высокопроизводительного термовакуумного метода непрерывного производства наноодисперсных порошков, выполненная на основании объединения процесса вакуумирования и скоростного термического нагрева. Проведен анализ физических процессов в термовакуумной установке, которые воздействуют на частицы исходного материала. Проведена термовакуумная обработка графита марки С1 с исходным размером частиц 1…2 мм. Для исследования структурного состава материала в исходном состоянии и обработанного в термовакуумной установке использован рентгеноструктурный анализ и электронная микроскопия. Согласно результатам рентгеноструктурных исследований, исходный графит марки С1 имеет две известные структурные модификации: гексагональную с периодами решётки $a_o = 0.2461\pm0.0002$ нм, $c_o = 0.6705\pm0.0007$ нм и ромбоэдрическую с содержанием порядка 30% – с периодами $a = 0.2461\pm0.0001$ нм и $c = 1.003\pm0.0002$ нм (полуторное значение периода c_o основной структуры графита). Сочетание этих фаз наблюдалось в основе состава графита С1 после обработки в термовакуумной установке. Помимо этого дополнительно обнаружена сверхструктурная ромбоэдрическая фаза с периодами $a = 2a_o = 0.492\pm0.0001$ нм и $c = (3/2)c_o = 1.003\pm0.0002$ нм. Обнаружена также фаза с моноклинной структурой и с параметрами $a_1 = 0.6075\pm0.0001$ нм; $b_1 = 0.4477\pm0.0002$ нм; $c_1 = 0.4913\pm0.0003$ нм; $\beta = 99.6\pm0.1°$ – предположительно, с наличием в структуре атомов железа. Результаты анализа и расчётов в целом согласуются с ПЭМ-снимками обратной решётки обработанного графита. В результате отмечено, что исходный порошок графита подвергся дроблению до размеров 2…40 нм с частичным изменением структуры и с проявлением форм, подобных многослойным нанотрубкам и фуллеренам. Отмечается также, что в этом процессе участвуют термодеформационные эффекты, что позволяет значительно ускорить процесс получения нанодисперсного углеродного материала с новыми физико-химическими и механическими свойствами. Полученные результаты могут найти широкое применение для промышленного производства нанодисперсных материалов.

КЛЮЧЕВЫЕ СЛОВА: углерод, термовакуумное диспергирование, нанотрубки, фуллерены

NANOMECHANICAL CHARACTERIZATION OF APOLIPOPROTEIN A-I AMYLOID FIBRILS

Valeriya Trusova[a*], Kateryna Vus[a], Olga Zhytniakivska[a], Uliana Tarabara[a], Hiroyuki Saito[b], Galyna Gorbenko[a]

[a]Department of Medical Physics and Biomedical Nanotechnologies, V.N. Karazin Kharkiv National University
4 Svobody Sq., Kharkiv, 61022, Ukraine
[b]Department of Biophysical Chemistry, Kyoto Pharmaceutical University
5 Misasagi-Nakauchi-cho, Yamashina-ku, Kyoto, 607-8414, Japan
*Corresponding Author: valerija.trusova@karazin.ua
Received March 26, 2020, revised March 29, 2020; accepted March 30, 2020

Amyloid fibrils represent a special type of protein aggregates that are currently receiving enormous attention due to their strong implication in molecular etiology of a wide range of human disorders. Amyloid fibrils represent highly ordered self-assemblies sharing a core cross-β-sheet structure. Such organization of the fibrils is responsible for amyloid insolubility and exceptional mechanical properties. The remarkable rigidity of the protein fibrillar aggregates is due to intra- and interstrand hydrogen bonds which stabilize the β-strand scaffold of amyloid fibrils. Increasing evidence indicates that physical properties of amyloid assemblies, especially their mechanical characteristics, play essential role in determining their cytotoxic action. This highlights the necessity of deciphering the correlation between the elastic properties of amyloid aggregates and their cytotoxicity. In the present paper we utilized the atomic force microscopy (AFM) to visualize and analyze the amyloid fibrils of G26R/W@8 mutant of N-terminal fragment of human apolipoprotein A-I (apoA-I). The examination of AFM images revealed the existence of two polymorphic forms of apoA-I fibrils – twisted ribbon and helical ribbon. The quantitative analysis of apoA-I elastic properties was performed within the framework of worm-like model of polymer chain using the Easyworm software. The Easyworm package analyzes the images of individual polymer chains obtained by the atomic force microscopy and allows calculation of the persistent length of a chain in three regimes depending on the ratio between the contour and persistent lengths of the polymer. The set of evaluated parameters included the Young's modulus, persistent length, bending rigidity and the second moment of inertia. All parameters calculated for the helical ribbon conformation were higher than those of the twisted ribbon. These findings suggest that helical ribbon represents a more rigid and mechanically stable configuration. The results obtained may prove of importance for a deeper understanding the mechanics-driven pathological activities of amyloid fibrils.

KEYWORDS: amyloid fibrils, mechanical properties, worm-like model, atomic force microscopy, Easyworm

A fundamental propensity of polypeptide chain for self-assembly has a dual nature reflected in protein folding into a functionally active native state and misfolding that provokes protein oligomerization and aggregation [1,2]. All these processes are driven by the common forces and crucially depend on the environmental conditions. The intermolecular noncovalent interactions may stabilize a diversity of supramolecular assemblies whose structures range from disordered amorphous aggregates to the crystals with strictly defined three-dimensional symmetry. Along with a naturally occurring protein self-association, there exists a so-called pathological aggregation leading to the formation of amyloid fibrils. During the past decades amyloid protein aggregates remain a focus of extensive research activities due to their involvement in the development of numerous human disorders, including neurodegenerative diseases, type II diabetes, spongiform encephalopathies, etc [3]. Increasing evidence from both theoretical and experimental *in vitro* and *in vivo* studies suggests that amyloid proteins and peptides can self-associate into fibrillar structures of different morphologies [4]. This gives rise to variability in amyloid fibril conformations and distinctions in their toxic potential and pathology-spreading properties. Accordingly, it was shown that various fibril polymorphs are characterized by different ability to act as a catalytic surface for secondary nucleation [5], as well as by distinct biological activities, such as propagation in a prion-like manner or association with cytotoxic active species [6]. Furthermore, a polymorphic behavior is believed to be a fundamental characteristic of a protein fibrillar state. The existence of different polymorphs was reported for Aβ-peptide, prion proteins, α-synuclein, albumin, insulin, β-lactoglobulin, just to name a few. One of the most popular type of polymorphism is called lateral, or morphological one, and involves the transition from so-called twisted ribbon (TR) conformation to nanotube-like (NT) structure through the intermediate state called helical ribbon (HR) [7]. The driving force for the polymorphism is thought to be the variations in the number of protofilaments composing the fibril, that results in different twist and curvature of the final protein fibrillar assembly [8].

In general, characterization of the protein polymorphs is performed in a qualitative manner using the different microscopic techniques [9-11]. However, due to well-established key role of structural polymorphism in determining the amyloid cytotoxic activity, evaluation of the quantitative parameters of different amyloid conformations seems to be of great importance. In view of this, the aim of the present study was the examination of the polymorphic behavior of G26R/W@8 mutant of human apolipoprotein A-I (apoA-I) and analysis of its mechanical properties. The atomic force microscopy (AFM) was used in order to visualize, identify, classify and quantify in detail the distinct polymorphic species of apoA-I.

EXPERIMENTAL SECTION
Materials

G26R/W@8 mutant of N-terminal fragment (1-83) of human apoA-I was obtained as described previously [12]. To prepare the amyloid fibrils, apoA-I variant was freshly dialyzed from 6M guanidine hydrochloride solution into 10 mM Tris buffer, 150 mM NaCl, 0.01 % NaN$_3$, pH 7.4 before use. The reaction of protein fibrillization was conducted at 37 °C in the above buffer with constant agitation on an orbital shaker. The amyloid nature of fibrillar aggregates was confirmed in Thioflavin T (ThT) assay [13]. All other reagents were used without further purification.

Atomic force microscopy

AFM imaging was carried out with a NanoScope IIIa scanning probe work station equipped with a MultiMode head using an E-series piezoceramic scanner (Digital Instruments, Santa Barbara, CA, USA). AFM probes were single-crystal silicon microcantilevers with 300 kHz resonant frequencies and 26 N/m spring constant model OMCL-AC160TS-R3 (Olympus, Tokyo, Japan). 10 µl of each sample solution was spotted on freshly cleaved mica (The Nilaco Co., Tokyo, Japan). After washing the mica with distilled water (20 µl), samples were imaged under ambient conditions at room temperature at scan rates of 0.5 Hz by tapping mode.

RESULTS AND DISCUSSION

Among a wide variety of different filamentous morphologies which can be adopted by protein aggregates, the configurations such as twisted ribbon, helical ribbon and nanotubes (NT) are among the most frequently appeared. TR conformation is characterized by a saddle-like curvature, straight central axis and a constant pitch. In turn, HR and NT represent the polymorphs with a high mean curvature but zero Gaussian curvature, helical centerline and a constant tilt angle. The transition from a twisted ribbon to a helical ribbon occurs at increasing number of protofilaments, and the accompanying rise in the width-to-thickness ratio, resulting from the protein tendency to minimize the bending and torsional energy. A further transformation of HR into a nanotube is associated with extra energy due to the edge line tension. The surface curvatures of the twisted (κ_{TR}) and helical (κ_{HR}) ribbons are given by:

$$\kappa_{TR} = \frac{0.5w - d_{TR}}{\left(0.5w - d_{TR}\right)^2 + \left(P_{TR}/2\pi\right)^2} ; \qquad \kappa_{HR} = \frac{r_h}{r_h^2 + \left(P_{HR}/2\pi\right)^2} ; \qquad P_{HR} = 2\pi r_h \tan\psi \qquad (1)$$

where w is the width of fibril core, d_{TR} stands for the distance from the ribbon edge; P_{TR}, P_{HR} denote fibril pitch either in TR or in HR conformation, respectively; r_h is the helix radius; ψ is the pitch angle. In our previous study [13] we derived the structural parameters of the twisted and helical ribbon polymorphs of G26R/W@8 fibrils from the AFM data, that were found to be: $w = 10$ nm, $P_{TR} = 50$ nm for the twisted ribbon, and $r_h = 5$ nm, $\psi = 70°$ for the helical ribbon.

Fig. 1 represents the AFM image of fibrillar G26R/W@8 mutant of apoA-I. As seen from this figure, the amyloid fibrils are visualized as smoothed or twisted structures. This observation suggests the existence of at least two different polymorphic forms of fibrillar polypeptide. The analysis of height profiles along the contour length showed that these polymorphs correspond to TR and HR configurations.

From the physical viewpoint amyloid fibrils are considered as supramolecular semi-elastic polymers which are not subject to Gaussian statistics. The reason of non-Gaussian nature of amyloid fibrils lies in their increased rigidity which results in the lack of the number of independent segments for application of the Gaussian statistics. An increased rigidity of polymeric chains may originate from several factors, among which are: i) sterical restrictions arising from the repulsion of atoms which are getting closer upon segment rotation; ii) electrostatic interactions; iii) H-bond formation. The description of rigid polymer molecules is generally based on the worm-like model which represents the continuous version of the Kratky-Porod model [14]. Within the framework of this approach, the following conditions are valid for a persistent chain: i) the segment length $l \to 0$, ii) the angle between the segments $\alpha \to \pi$, so the chain is characterized by a continuous curvature equal to the mean value of the cosine of the angle ψ between the tangents to the chain at a given point and a starting point.

The curvature of the persistent chain is given by:

$$\langle \cos\psi \rangle = \exp(-s/l_p) \qquad (2)$$

where s is a contour length of a chain (i.e. the length from the beginning of a chain to a given point), l_p is a persistent length. As follows from the eq. (2), the curvature changes e times along a chain of a length l_p. If Λ is a total contour length and $\vec{u}(s)$ represents a unit vector characterizing the direction of the chain at a given point, which is at a distance s from the beginning of the chain, the vector $\vec{R}$ connecting the starting and ending points of a chain can be described as:

$$\vec{R} = \int_0^\Lambda \vec{u}(s)ds \qquad (3)$$

The root mean square value of this parameter is given by:

$$\left\langle \vec{R}^2 \right\rangle = \int_0^{\Lambda} \vec{u}(s_1) ds_1 \int_0^{\Lambda} \vec{u}(s_2) ds_2 \qquad (4)$$

The scalar product of unit vectors equals to:

$$\vec{u}(s_1)\vec{u}(s_2) = \cos(d\vec{s}_1, d\vec{s}_2) = \exp\left(\frac{-(s_1 - s_2)}{l_p} \right); \quad s_1 > s_2 \qquad (5)$$

Finally, one obtains:

$$\left\langle \vec{R}^2 \right\rangle = \int_0^{\Lambda}\int_0^{\Lambda} \exp\left(-\frac{(s_1 - s_2)}{l_p} \right) ds_1 ds_2 = 2\int_0^{\Lambda}\int_0^{s_1} \exp\left(-\frac{(s_1 - s_2)}{l_p} \right) ds_2 ds_1 \qquad (6)$$

$$\int_0^{s_1} \exp\left(-\frac{s_1}{l_p} \right) \exp\left(\frac{s_2}{l_p} \right) ds_2 = \exp\left(-\frac{s_1}{l_p} \right) l_p \exp\left(\frac{s_2}{l_p} \right) \Big|_0^{s_1} = l_p \left(1 - \exp\left(-\frac{s_1}{l_p} \right) \right) \qquad (7)$$

$$\left\langle \vec{R}^2 \right\rangle = 2l_p \int_0^{\Lambda} \left(1 - \exp\left(-\frac{s_1}{l_p} \right) \right) ds_1 = 2l_p \Lambda + 2l_p^2 \exp\left(-\frac{s_1}{l_p} \right) \Big|_0^{\Lambda} = 2l_p^2 \left\{ \frac{\Lambda}{l_p} - 1 + \exp\left(-\frac{\Lambda}{l_p} \right) \right\} \qquad (8)$$
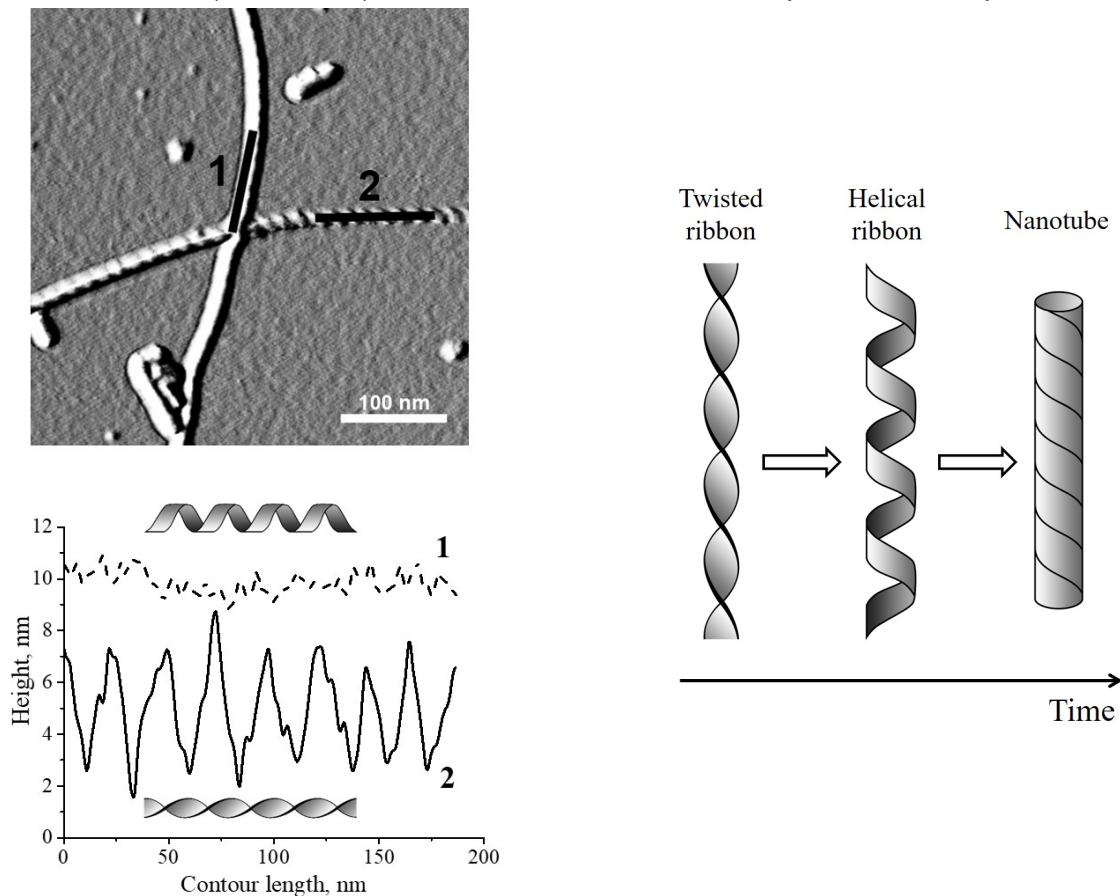
Fig. 1. Height profiles of G26R/W@8 amyloid fibrils along the contour length (left panel). Schematic representation of different polymorphs of amyloid fibrils (right panel).

It should be noted that the expression for the root mean square distance between the ends of a persistent chain may be used for the estimation of the root mean square distance between any points of a chain, s_1 and s_2:

$$\left\langle \vec{R}^2 \right\rangle = f(s_1 - s_2) = 2l_p^2 \left\{ \frac{|s_1 - s_2|}{l_p} - 1 + \exp\left(-\frac{|s_1 - s_2|}{l_p} \right) \right\} \qquad (9)$$

From the other hand, the persistent length relates to the two important elastic characteristics of amyloid fibrils:

$$l_p = EI/k_B T \qquad (10)$$

where E is the modulus of elasticity (the Young's modulus), I is the second moment of inertia. While the Young's modulus is determined mainly by the amino acid sequence of monomeric polypeptide chain, the second moment of inertia is a geometric factor which depends on the shape and size of fibril cross section [15]. Given that the cross section of the amyloid fibril in a twisted ribbon configuration is a rectangle, while that in the configuration of helical ribbon is a circle, the second moments of inertia for TR (I_{TR}) and HR (I_{HR}) may be written as:

$$I_{TR} = \frac{wh^3}{12}, \qquad\qquad I_{HR} = \frac{\pi h^4}{64} \qquad\qquad (11)$$

In turn, the Young's modulus and the second moment of inertia are interrelated by the following equation:

$$E = B/I \qquad\qquad (12)$$

where B is the bending rigidity coefficient.

For the quantitative estimation of the mechanical properties (persistent length, Young's modulus, second moment of inertia) of the G26R/W@8 amyloid fibrils within the framework of the worm-like model, the AFM image presented in Fig. 1 was analyzed using the Easyworm software [16]. The calculations were made separately for TR and HR conformations.
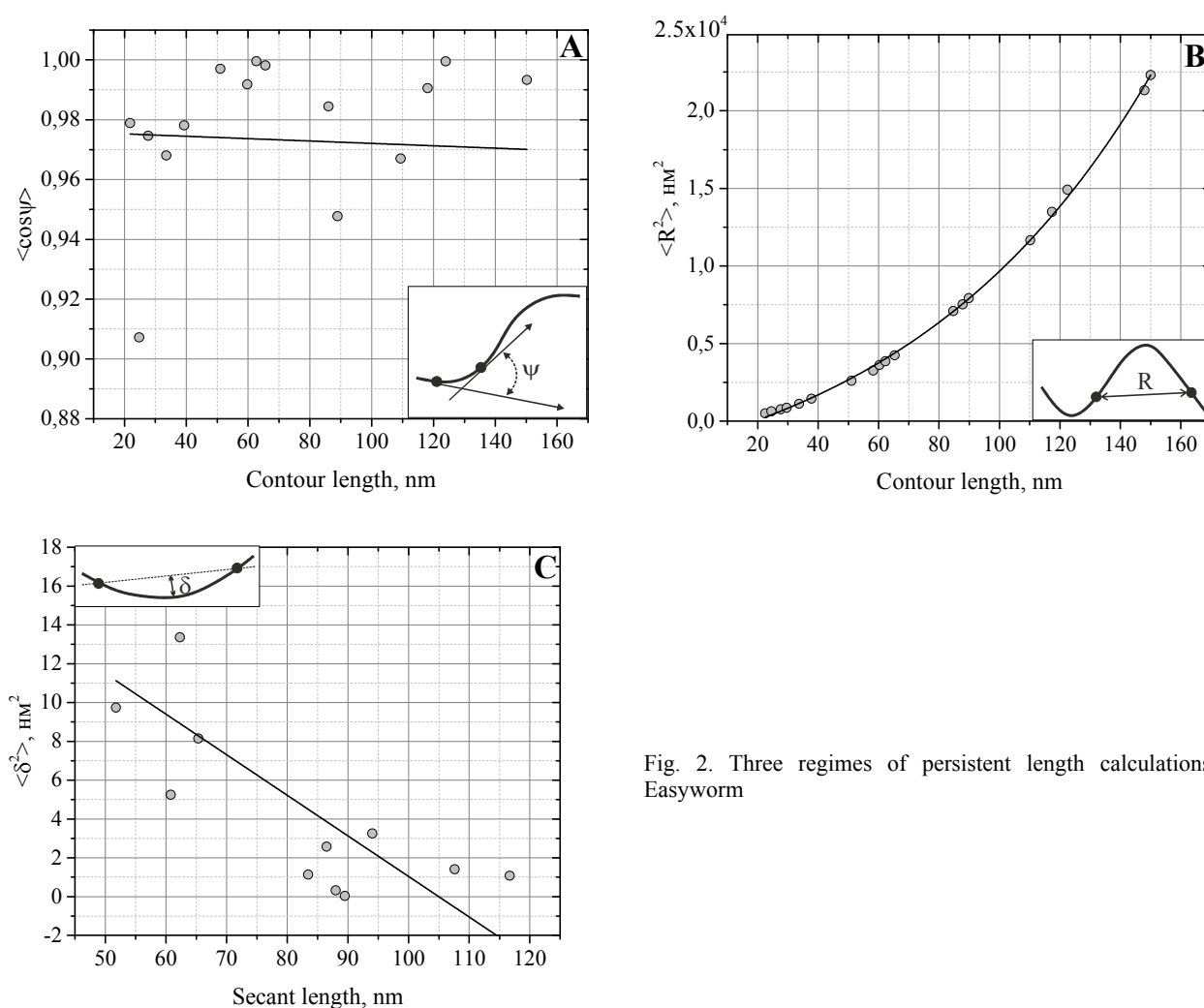
Fig. 2. Three regimes of persistent length calculations in Easyworm

The Easyworm represents the graphical interface of the algorithm of AFM data treatment, whose mathematical basis was created in MATLAB. The three regimes of persistent length calculations are available in Easyworm (Fig. 2):

Regime 1 – the measurement of the angle between the tangents at two points of the fibril segments. Persistent length is determined by eq. (2).

Regime 2 – the calculation of the mean square end-to-end distance of the fibril. Persistent length is determined by eq. (8).

Regime 3 – the determination of mean square of the deviations δ to secant midpoints at two points of the fibril segments. Persistent length is determined as:

$$\left\langle \delta^2 \right\rangle = \frac{L^3}{24 l_p} \qquad\qquad (13)$$

Table

Mechanical properties of two polymorphic forms of G26R/W@8 amyloid fibrils

Parameter	TR	HR
Persistent length, μm	2.23±0.24	4.17±0.61
Bending rigidity, N·m^2	$(9.17\pm1.07)\times10^{-27}$	$(17.15\pm2.11)\times10^{-27}$
Second moment of inertia, m^4	$(2.91\pm0.93)\times10^{-35}$	$(4.91\pm0.93)\times10^{-34}$
Young's modulus, GPa	3.15±0.72	3.54±0.77

Fig. 2 represents the approximation of the AFM data acquired for G26R/W@8 amyloid fibrils in TR configuration, by the eqs. (2), (8), (13). As seen from this figure, the best fit between the theory and experiment is achieved in the **Regime 2** (Fig. 2, B). An analogous result was obtained also for HR configuration. Therefore, the values of persistent length, derived from eq. (8), were used for the estimation of E, I and B. The mechanical characteristics of fibrillar G26R/W@8 calculated in such a way are summarized in Table 1. The results obtained show that the amyloid fibrils represent rigid, mechanically stable structures. For the sake of comparison, the elastic modulus of rubber is 0.005 GPa, of glass and aluminum is 70 GPa, of bones is 30 GPa, and that of steel is 200 GPa [17]. Another mechanical peculiarity of the examined amyloid fibrils is the fact that the aggregates in a HR conformation have the persistent length twice higher than that in a TR conformation. This finding reflects the expected increase of fibril rigidity upon topological evolution from a twisted to a helical ribbon during fibril maturation and thickening. Using the theoretical approaches of polymer statistics, Adamcik and co-workers have analyzed the nanomechanical properties of amyloid fibrils based on the AFM images [18]. The authors postulated that any fibrillar aggregate may be described as a multistranded fibril composed of $1 - 5$ filaments. The helicity of the resulted fibril depends on the interactions between the filaments, while the persistent length is determined by the number of protofilaments. More specifically, the rise in persistent length with the number of filaments is supposed to be due to the increase in cross-sectional moment of inertia.

The exceptional mechanical characteristics of amyloid fibrils are explained by their unique highly ordered structure, the main element of which is represented by the β-strands. A high density of the inter-backbone H-bonds which stabilize the integrity of the fibril plays a decisive role in determining the rigidity of fibrillar aggregates. Furthermore, the remarkable elastic properties of amyloid fibrils were reported to be a crucial factor underlying their cytotoxic potential. In particular, it was supposed that the mechanical disruption of cell membranes by amyloids arises from the fact that the Young's modulus of protein aggregates ($1 - 10$ GPa) substantially exceeds that of cellular membranes (~100 kPa). Thus, the findings presented here may help in creating the basis for understanding the mechanics-driven cytotoxic activities of amyloid fibrils.

CONCLUSIONS

In summary, the atomic force microscopy was utilized to perform the mechanical characterization of the apolipoprotein A-I amyloid fibrils. The set of elastic parameters, including the Young's modulus, persistent length, bending rigidity and the second moment of inertia was calculated for the two polymorphic forms of fibrillar aggregates − twisted ribbon and helical ribbon. A helical ribbon configuration was found to possess a higher mechanical strength and stiffness as compared to a twisted ribbon state. Given that the amyloid elastic characteristics correlate with its pathogenic potential, the results obtained highlight the key role of fibril maturation in determining its cytotoxicity.

ORCID IDs
Valeriya Trusova, https://orcid.org/0000-0002-7087-071X; **Kateryna Vus**, http://orcid.org/0000-0003-4738-4016
Olga Zhytniakivska, https://orcid.org/0000-0001-9554-0090; **Uliana Tarabara**, https://orcid.org/0000-0002-7677-0779
Hiroyuki Saito, https://orcid.org/0000-0003-1497-1425; **Galyna Gorbenko**, http://orcid.org/0000-0002-0954-5053

REFERENCES
[1] J. Vaquer-Alicea, and M. Diamond, Annu. Rev. Biochem. **88**, 785-810 (2019), https://doi.org/10.1146/annurev-biochem-061516-045049.
[2] S. Khatun, A, Singh, D. Mandal, A. Chandra, and A. Gupta, Phys. Chem. Chem. Phys. **21**, 20083-20094 (2019), https://doi.org/10.1039/C9CP03238J.
[3] A. Buell, Biochem. J. **476**, 2677-2703 (2019), https://doi.org/10.1042/BCJ20160868.
[4] O. Galzitskaya, Curr. Protein Pept. Sci. **20**, 630-640 (2019), https://doi.org/10.2174/1389203720666190125160937.
[5] P. Arosio, T. Knowles, and S. Linse, Phys. Chem. Chem. Phys. **17**, 7606-7618 (2015), https://doi.org/10.1039/c4cp05563b.
[6] M. Jucker, and L. Walker, Nature **501**, 45-51 (2013), https://doi.org/10.1038/nature12481.
[7] S. Zhang, M. Andreasen, J. Nielsen, L. Liu, E. Nielsen, J. Song, G. Li et al., Proc. Natl. Acd. Sci. USA **110**, 2798-2803 (2013), https://doi.org/10.1073/pnas.1209955110.
[8] V. Trusova, Biophys. Rev. Lett. **10**, 135-156 (2015), https://doi.org/10.1142/S1793048015300029.
[9] J. Liu, M. Tian, and L. Shen, Chem. Commun. **56**, 3147-3150 (2020), https://doi.org/10.1039/C9CC10079B.
[10] R. Tycko, Neuron **86**, 632-645 (2015), https://doi.org/10.1016/j.neuron.2015.03.017.
[11] M. Kollmer, W. Close, L. Funk, J. Rasmussen, A. Bsoul, A. Schierhorn, M. Schmidt et al., Nat. Commun. **10**, 4760-4767 (2019), https://doi.org/10.1038/s41467-019-12683-8.
[12] E. Adachi, H. Nakajima, C. Mizuguchi, P. Dhanasekaran, H. Kawashima, K. Nagao, K. Akaji et al., J. Biol. Chem. **288**, 2848-2856 (2013), https://doi.org/10.1074/jbc.M112.428052.
[13] M. Girych, G. Gorbenko, V. Trusova, E. Adachi, C. Mizuguchi, K. Nagao, H. Kawashima et al., J. Struct. Biol. **185**, 116-124 (2014), https://doi.org/10.1016/j.jsb.2013.10.017.

[14] C. Bouchiat, M. Wang, J.-F. Allemand, T. Strick, S. Block, and V. Croquette, Biophys. J. **76**, 409-413 (1999), https://doi.org/10.1016/S0006-3495(99)77207-3.

[15] I. Usov, and R. Mezzenga, ACS Nano **8**, 11035-11041 (2014), https://doi.org/10.1021/nn503530a.

[16] G. Lamour, J. Kirkegaard, H. Li, T. Knowles, and J. Gsponer, Source Code Biol. Med. **9**, 16-21 (2014), https://doi.org/10.1186/1751-0473-9-16.

[17] B. Choi, G. Yoon, S. Lee, and K. Eom, Phys. Chem. Chem. Phys. **17**, 1379-1389 (2015), https://doi.org/10.1039/c4cp03804e.

[18] J. Adamcik, J.-M. Jung, J. Flakowski, P. Rios, G. Dietler, and R. Mezzenga, Nat. Nanotech. **5**, 423-428 (2010), https://doi.org/10.1038/NNANO.2010.59.

НАНОМЕХАНІЧНІ ХАРАКТЕРИСТИКИ АМІЛОЇДНИХ ФІБРИЛ АПОЛІПОПРОТЕЇНУ А-I

Валерія Трусова[a], Катерина Вус[a], Ольга Житняківська[a], Уляна Тарабара[a], Хіроюкі Сайто[b], Галина Горбенко[a]

[a]Кафедра медичної фізики та біомедичних нанотехнологій, Харківський національний університет імені В.Н. Каразіна
м. Свободи 4, Харків, 61022, Україна
[b]Кафедра біофізичної хімії, Фармацевтичний університет
Місасагі-Накаучі-чо 5, Ямашина-ку, м. Кіото, 607-8414, Японія

Амілоїдні фібрили – це особливий тип білкових агрегатів, який привертає невпинно зростаючу увагу завдяки їх важливій ролі в молекулярній етіології широкого кола захворювань. Амілоїдні фібрили представляють собою високовпорядковані самоасоціати, що характеризуються крос-β-складчатою структурою. Така організація фібрил відповідальна за їх нерозчинність та особливі механічні властивості. Висока жорсткість фібрилярних білкових агрегатів забезпечується великою кількістю водневих зв'язків, які стабілізують β-складчастий каркас амілоїдних фібрил. Все більшого обґрунтування набуває припущення, що фізичні властивості амілоїдів, особливо їх механічні характеристики, відіграють ключову роль у визначенні їх цитотоксичної дії. У зв'язку із цим, встановлення кореляції між еластичними властивостями амілоїдних агрегатів та їх цитотоксичністю є вельми необхідним. У даній роботі з використанням атомної силової мікроскопії (АСМ) були проаналізовані амілоїдні фібрили мутанту G26R/W@8 N-термінального фрагменту аполіпопротеїну А-I (апоА-I). Аналіз АСМ мікрофотографій виявив наявність двох поліморфних форм фібрил апоА-I – закрученої стрічки та спіральної стрічки. Кількісна характеризація еластичних властивостей апоА-I була проведена у рамках моделі персистентного ланцюга Порода-Краткі, з використанням програмного пакету Easyworm. Цей пакет дозволяє аналізувати зображення окремого поліпептидного ланцюга, отримані за допомогою АСМ, та визначати персистентну довжину ланцюга у трьох режимах в залежності від співвідношення контурної та персистентної довжини. Набір параметрів, отриманих внаслідок такого аналізу, включав модуль Юнга, персистентну довжину, жорсткість при вигині та другий момент інерції. Виявилось, що розраховані параметри мали більші значення для конфігурації спіральної стрічки у порівнянні із конфігурацією закрученої стрічки. Це свідчить про те, що спіральна стрічка є більш жорсткою та механічно стабільною конфігурацією. Отримані результати є важливими для більш глибокого розуміння механічно-контрольованої патологічної дії амілоїдних фібрил.

КЛЮЧОВІ СЛОВА: амілоїдні фібрили, механічні властивості, персистентний ланцюг, атомно-силова мікроскопія, Easyworm

НАНОМЕХАНИЧЕСКИЕ ХАРАКТЕРИСТИКИ АМИЛОИДНЫХ ФИБРИЛЛ АПОЛИПОПРОТЕИНА А-I

Валерия Трусова[a], Екатерина Вус[a], Ольга Житняковская[a], Ульяна Тарабара[a], Хироюки Сайто[b], Галина Горбенко[a]

[a]Кафедра медицинской физики и биомедицинских нанотехнологий
Харьковский национальный университет имени В.Н. Каразина
пл. Свободы 4, Харьков, 61022, Украина
[b]Кафедра биофизической химии, Фармацевтический университет,
Мисасаги-Накаучи-чо 5, Ямашина-ку, Киото, 607-8414, Япония

Амилоидные фибриллы – это особый тип белковых агрегатов, которые привлекают все большее внимание благодаря их важной роли в молекулярной этиологии широкого круга заболеваний. Амилоидные фибриллы представляют собой высокоупорядоченные самоассоциаты, которые характеризуются кросс-β-складчатой структурой. Такая организация фибрилл ответственна за их нерастворимость и особые механические свойства. Высокая жесткость фибриллярных агрегатов белков обеспечивается большим количеством водородных связей, которые стабилизируют β-складчатый каркас амилоидных фибрилл. Все большее обоснование получает предположение о том, что физические свойства амилоидов, особенно их механические характеристики, играют ключевую роль в определении их цитотоксического действия. В связи с этим, установление корреляции между эластическими свойствами амилоидных агрегатов и их цитотоксичностью является актуальной задачей. В данной работе с использованием атомно-силовой микроскопии (АСМ) были проанализированы амилоидные фибриллы мутанта G26R/W@8 N-терминального фрагмента аполипопротеина А-I. Анализ АСМ изображений выявил наличие двух полиморфных форм фибрилл апоА-I – закрученной ленты и спиральной ленты. Количественная характеристика эластических свойств апоА-I была проведена в рамках модели персистентной цепи Порода-Кратки, с использованием программного пакета Easyworm. Данный пакет позволяет анализировать фотографии отдельной полипептидной цепи, полученные с помощью АСМ, и определять персистентную длину цепи в трех режимах в зависимости от соотношения между контурной и персистентной длиной. Набор параметров, полученных в результате такого анализа, включал модуль Юнга, персистентную длину, жесткость при изгибе и второй момент инерции. Оказалось, что рассчитанные параметры были выше для конфигурации спиральной ленты, чем для конфигурации закрученной ленты. Это свидетельствует в пользу того, что спиральная лента представляет собой более жесткую и механически стабильную конфигурацию. Полученные результаты являются важными для более глубокого понимания механически-контролируемого патологического действия амилоидных фибрилл.

КЛЮЧЕВЫЕ СЛОВА: амилоидные фибриллы, механические свойства, персистентная цепь, атомно-силовая микроскопия, Easyworm

NONLINEAR EFFECTS IN THE PHONON SYSTEM OF DIAMOND CRYSTAL

Artem S. Naumovets[a], Yurii M. Poluektov[a,b], Valery D. Khodusov[a]*

aV.N. Karazin Kharkiv National University
4 Svobody Sq., Kharkov, 61022, Ukraine
bNational Science Center "Kharkov Institute of Physics and Technology", National Academy of Sciences of Ukraine
1 Akademicheskaya St., Kharkov 61108, Ukraine
Corresponding Author: vdkhodusov@karazin.ua

Thermodynamic properties of diamond are theoretically investigated on the ground of self-consistent description of a phonon gas in lattice, which generalizes the Debye model with taking into account the phonon-phonon interaction. In many cases properties of crystals of certain symmetry can be well approximated by a model of an isotropic continuous medium, if its elastic moduli are chosen optimally. They should be found for a crystal of each symmetry from the condition of their proximity to the exact elastic moduli, which are measured experimentally and are given in the corresponding tables. At high temperatures, the nonlinear phonon interaction takes into account both three- and four-phonon interactions. In this reason we take into account not only the second-order elastic moduli tensor in the reduced isotropic crystal model, but also the third- and fourth-order elastic moduli tensors, which are all together characterized by nine independent components. Account of the phonon-phonon interaction leads to the redefinition of the phonon's speed and of the Debye energy. Their dependence on the temperature occurs. In the absence of interaction and neglecting the nonlinear effects, the phonons are the same as that of the Debye model. They are called "bare" or "Debye". Phonons whose speed is renormalized due to the interaction are called the "self-consistent" ones. It is shown that, at high temperatures, the theory predicts the linear in the temperature deviation of the isochoric heat capacity from the Dulong-Petit law. Unlike for the most crystals, where the decrease in the isochoric heat capacity is observed, our calculations for diamond and crystals with diamond structure predict the linear increase of the isochoric heat capacity with the temperature, viewed experimentally. The isobaric heat capacity of diamond, similar to other substances, linearly increases with the temperature.

KEYWORDS: phonons; thermal properties; phonon-phonon interaction; Debye energy; elastic moduli

The Debye model [1] is the simplest way to described thermodynamic properties of dielectric crystals. In this approximation a crystal is considered as a continuous elastic isotropic medium in which oscillations propagate with the average speed c_D. At temperatures of the order of the Debye temperature Θ_D and higher, the phonon density in a crystal becomes higher than the particle number density, so nonlinear effects get appeared due to phonon interactions. A generalization of the Debye model which takes into account the phonon-phonon interaction was proposed in [2,3].

In many cases properties of crystals of certain symmetry can be well approximated by a model of an isotropic continuous medium, if its elastic moduli are chosen optimally [4]. A similar approach for an approximate account of nonlinear effects, which are cubic in the strain tensor degree, was used in [5]. In this model, a nonlinear elastic medium is characterized by five elastic moduli. In many cases, for a more complete description of the nonlinear effects, it is necessary to take into account fourth-order terms by the strain tensor in the free energy as well. For these cases, the nonlinear elastic properties of the medium are characterized by nine elastic moduli [6–9].

The behavior of the heat capacity of diamond at high temperatures differs from the behavior of the heat capacity of most crystals of other symmetry. Here it is necessary to distinguish the heat capacity at a constant volume C_V (isochoric) and the heat capacity at a constant pressure C_p (isobaric). The isochoric heat capacity is a more fundamental characteristic [10], but the isobaric heat capacity is usually determined experimentally. In the high temperature limit in accordance to the Dulong - Petit law [1],

$$C_V = 3N\left[1 - \frac{1}{20}\left(\frac{\Theta_D}{T}\right)^2\right],\tag{1}$$

the isochoric heat capacity tends to a constant value. The difference between the heat capacities in the high-temperature limit is proportional to the temperature [1]:

$$C_p - C_V = 9n^2\gamma_T\Gamma^2VT,\tag{2}$$

where $n = N/V$ is the particle number density; $\Gamma = \partial\ln\Theta/\partial\ln n$ is the Grüneisen parameter; $\gamma_T = n^{-1}\left(\partial n/\partial p\right)_T$ is the coefficient of isothermal compressibility. Thus, in the high-temperature limit the experimentally observed heat capacity C_p grows linearly with increasing the temperature, but C_V tends to a constant value. Equation (2) allows one to find the isochoric heat capacity using the measured isobaric heat capacity and the quantities n, Γ, γ_T.

It turns out that at high temperature the heat capacity C_V contains a linear in the temperature correction to the Dulong-Petit law $C_V = 3N$. This deviation can be explained by taking into account the interaction of phonons. Note that an early attempt to explain the high temperature deviation in the behavior of the diamond heat capacity from the standard Dulong – Petit law was made in [11]. The proposed therein explanation is based on the choice of the anharmonic potential of atomic interaction, in the same way as in a diatomic molecule.

The self-consistent approach to the description of the phonon system is fundamentally non-linear, and initially takes into account anharmonic effects. Moreover, this approach is also correct in the case when nonlinear corrections are not small corrections to the harmonic approximation. For getting results of the self-consistent description of phonons one should add together an infinite number of corrections of the standard perturbation theory based on the harmonic approximation. A comparison of the self-consistent description with the standard perturbation theory was carried out in [12,13] using the example of an anharmonic oscillator. It is shown that the standard perturbation theory has a small range of applicability, and this region narrows with increasing of energy level. The field of applicability of the self-consistent description is much wider, even when anharmonisms is not small. Therefore, the proposed approach to the description of the nonlinear properties of crystals is fundamentally new and cannot be reduced to [14-17] in which the effect of phonon anharmonicity was studied.

For the most crystals, the isochoric heat capacity C_V obeys the deviation from the Dulong – Petit law: it linearly decreases with increasing the temperature. In diamond-like crystals, such a deviation receives the opposite sign. In this paper we show how these features in the behavior of the high-temperature heat capacity of diamond can be described in framework of the many-particle approach.

In section 2 we briefly comment on the basic equations of [2,3]. Expression for the free energy and equation for the speed of interacting phonons are obtained there in the general form. In section 3 these expressions are calculated for the isotropic medium, and the nonlinearity parameter is introduced. Section 4 describes how to obtain the elastic moduli of the approximate isotropic medium from the elastic moduli of a crystal. Section 5 contains calculations of the high-temperature heat capacity of diamond. For comparison, same calculation is given for NaCl as a typical crystal of the cubic crystal system. Our conclusions bring together in the last section.

SELF-CONSISTENT DESCRIPTION OF INTERACTING PHONONS

We present relations on which the approach developed in [2,3] is based. Let phonons in the crystal lattice be described by the Hamiltonian density operator

$$H(\mathbf{r}) = \frac{\pi_a(\mathbf{r})^2}{2\rho} + U_2(\mathbf{r}) + U_3(\mathbf{r}) + U_4(\mathbf{r}), \tag{3}$$

where quadratic, cubic, and fourth-order in the strain tensor $u_{ij} = \frac{1}{2}\left(\nabla_j u_i + \nabla_i u_j + \nabla_i u_a \nabla_j u_a\right)$ terms have the form

$$U_2 = \frac{1}{2}\lambda_{aibj} u_{ai} u_{bj}, \qquad U_3 = \frac{1}{6}\lambda_{aibjck} u_{ai} u_{bj} u_{ck}, \qquad U_4 = \frac{1}{24}\lambda_{aibjckdl} u_{ai} u_{bj} u_{ck} u_{dl}, \tag{4}$$

and ρ is the density, $u_i(\mathbf{r})$ is the displacement vector field, $\pi_a(\mathbf{r}) = \rho \dot{u}_a(\mathbf{r})$ is the canonical momentum. Here and further on, the standard agreement on the summation over repeated indices is used. Due to the symmetry of the strain tensor $u_{ij} = u_{ji}$, the elastic moduli satisfy the known symmetry conditions for both permutations of pairs of indices and permutations of indices within the each pair [18]. With the fourth order in the displacement vector gradients accuracy, the Hamiltonian density takes the form

$$H(\mathbf{r}) = \frac{\pi_a(\mathbf{r})^2}{2\rho} + \frac{1}{2}\lambda_{aibj}\nabla_i u_a \nabla_j u_b + \tilde{U}_3 + \tilde{U}_4, \tag{5}$$

where

$$\tilde{U}_3 = \frac{1}{2}\lambda_{aibj}\nabla_i u_a \nabla_j u_c \nabla_b u_c + \frac{1}{6}\lambda_{aibjck}\nabla_i u_a \nabla_j u_b \nabla_k u_c,$$

$$\tilde{U}_4 = \frac{1}{8}\lambda_{aibj}\nabla_a u_c \nabla_i u_c \nabla_b u_s \nabla_j u_s + \frac{1}{4}\lambda_{aibjck}\nabla_i u_a \nabla_j u_b \nabla_k u_s \nabla_c u_s + \frac{1}{24}\lambda_{aibjckdl}\nabla_i u_a \nabla_j u_b \nabla_k u_c \nabla_l u_d. \tag{6}$$

In the quantum description, the displacement and the canonical momentum should be considered as operators for which the well-known commutation relations are valid:

$$\pi_a(\mathbf{r}) u_b(\mathbf{r}') - u_b(\mathbf{r}')\pi_a(\mathbf{r}) = -i\hbar\delta_{ab}\delta(\mathbf{r} - \mathbf{r}'),$$

$$u_a(\mathbf{r}) u_b(\mathbf{r}') - u_b(\mathbf{r}') u_a(\mathbf{r}) = 0, \qquad \pi_a(\mathbf{r})\pi_b(\mathbf{r}') - \pi_b(\mathbf{r}')\pi_a(\mathbf{r}) = 0. \tag{7}$$

In general the elastic moduli are functions of the temperature. Here as well as in the standard Debye model, we will neglect this effect, as well as the difference between the isothermal and adiabatic modules. In what follows we will take into account only the temperature dependence of the observed values, associated with the phonon excitation. The total Hamiltonian $H = \int H(\mathbf{r})d\mathbf{r}$ is the sum of the free phonon Hamiltonians and their interactions $H = H_0 + H_I$, where

$$H_0 = \int\left[\frac{\pi_a(\mathbf{r})^2}{2\rho} + \frac{1}{2}\lambda_{aibj}\nabla_i u_a \nabla_j u_b\right]d\mathbf{r}, \qquad H_I = \int\left[\tilde{U}_3(\mathbf{r}) + \tilde{U}_4(\mathbf{r})\right]d\mathbf{r}. \tag{8}$$

To describe the system of interacting phonons, we use the self-consistent field method in the formulation developed for fermionic [19] and for bosonic [20, 21] systems. The implementation of this method on the example of the anharmonic oscillator was demonstrated in [22, 23]. In the proposed formulation, the method of a self-consistent field is introduced at the level of the Hamiltonian, rather than at the level of the equations of motion. This makes possible to achieve the fulfillment of all thermodynamic relations. In this method, the total Hamiltonian is represented as the sum of two terms

$$H = H_S + H_C. \tag{9}$$

Here, the approximating self-consistent Hamiltonian

$$H_S = \int\left[\frac{\pi_a^2}{2\rho} + \frac{\tilde{\lambda}}{2}\nabla_i u_a \nabla_i u_a\right]d\mathbf{r} + \varepsilon_0 \tag{10}$$

describes "free" phonons with renormalized speed, and the correlation Hamiltonian

$$H_C = \int\left[\frac{1}{2}\left(\lambda_{aibj} - \tilde{\lambda}\delta_{ij}\delta_{ab}\right)\nabla_i u_a \nabla_j u_b + \tilde{U}_3 + \tilde{U}_4\right]d\mathbf{r} - \varepsilon_0 \tag{11}$$

describes the interaction of these phonons. The self-consistent Hamiltonian (10) contains the only one effective modulus of elasticity $\tilde{\lambda}$ and describes the phonon system in the isotropic approximation when phonons with arbitrary polarization have the same speed. In addition, H_S includes ε_0, which does not contain operators. The inclusion of this term is essential, since it describes the change in the ground state during the transition from the exact Hamiltonian to the self-consistent one. Thus, by means of the renormalization of the elastic modulus, the main interaction between the original phonons in the isotropic approximation is taken into account in Hamiltonian (10), and Hamiltonian (11) describes the residual interaction, which is not included in the self-consistent field method. The self-consistent Hamiltonian (10) in the representation of phonon creation and annihilation operators, which satisfy the standard commutation relations $\left[b_{k\alpha}, b_{k'\alpha'}^+\right] = \delta_{kk'}\delta_{\alpha\alpha'}$, $\left[b_{k\alpha}, b_{k'\alpha'}\right] = \left[b_{k\alpha}^+, b_{k'\alpha'}^+\right] = 0$, takes the form

$$H_S = \hbar\sum_{k,\alpha}\omega(k)b_{k\alpha}^+ b_{k\alpha} + \frac{3}{2}\hbar\sum_k\omega(k) + \varepsilon_0, \tag{12}$$

where $\omega(k) = c_S k$, and the phonon speed with arbitrary polarization is $c_S = \sqrt{\tilde{\lambda}/\rho}$. The free energy of the system with Hamiltonian (12) is given by

$$F = \varepsilon_0 + \frac{3\hbar}{2}\sum_k\omega(k) + 3T\sum_k\ln\left(1 - e^{-\beta\hbar\omega(k)}\right). \tag{13}$$

The value ε_0 is found from the condition $\langle H\rangle = \langle H_S\rangle$, where the average is carried out with the statistical operator $\hat{\rho} = \exp\beta(F - H_S)$, $\beta = 1/T$ is the inverse temperature. The result is [3]

$$\varepsilon_0 = \frac{3\hbar}{2c_S}\left[\frac{1}{3\rho}\sum_k\frac{k_i k_j \lambda_{aiaj}}{k}\left(f_k + \frac{1}{2}\right) - c_S^2\sum_k k\left(f_k + \frac{1}{2}\right)\right] + \frac{\hbar^2}{8V\rho^2 c_S^2}I, \tag{14}$$

where

$$I \equiv \sum_{k_1,k_2}\frac{(f_{k_1} + 1/2)(f_{k_2} + 1/2)}{k_1 k_2}\Big\{\lambda_{aiajbkbl}k_{1i}k_{1j}k_{2k}k_{2l} +$$

$$+2\lambda_{aiajck}\left[3k_{1i}k_{1j}k_{2k}k_{2c} + 2k_{1i}k_{1k}k_{2j}k_{2c}\right] + 3\lambda_{aibj}\left[3k_{1i}k_{1a}k_{2b}k_{2j} + 2k_{1i}k_{1b}k_{2a}k_{2j}\right]\Big\}, \tag{15}$$

and $f_k = \left[e^{\beta \hbar \omega(k)} - 1 \right]^{-1}$ is the phonon distribution function. The phonon speed c_S, renormalized due to the interaction, can be found from the requirement of the free energy (13) minimum, $\partial F / \partial c_S = 0$. As a result, we obtain a nonlinear equation, which determines the speed of "new" phonons

$$c_S^2 = \frac{2\pi^2}{3\rho V} J^{-1} \sum_k \frac{k_i k_j \lambda_{aiaj}}{k} \left(f_k + \frac{1}{2} \right) + \frac{\hbar \pi^2}{6\rho^2 V^2 c_S} \frac{I}{J} \tag{16}$$

where $J = \int_0^{k_D} \left(f_k + \frac{1}{2} \right) k^3 dk$, and the upper integration limit is the Debye wave number $k_D = \left(6\pi^2 N/V \right)^{1/3}$ [24]. Equation (16) is valid for the self-consistent description of the nonlinear properties of crystals of arbitrary symmetry.

In the absence of interaction and neglecting the nonlinear effects, the phonons are the same as that of the Debye model. They are naturally called "bare" or "Debye". Phonons whose speed is renormalized due to the interaction in accordance with (16) will be called the "self-consistent" ones. Even in the case of neglecting the dependence of the modules λ_{aiaj} on the temperature, that is assumed in the ordinary Debye model, the renormalized speed c_S of our approach depends substantially on the temperature, since it is expressed in terms of integrals of the distribution function. In the considered approach, the parameter $\tilde{\lambda}$ is chosen so that Hamiltonian (10) is as close as possible to the exact Hamiltonian $H = H_0 + H_I$ and therefore describes the phonon system with the best approximation with the quadratic Hamiltonian [3].

THERMODYNAMIC PROPERTIES OF NONLINEAR CRYSTALS
IN THE ISOTROPIC MEDIUM APPROXIMATION

Calculations of the renormalized speed (16) and of the thermodynamic properties of a certain symmetry nonlinear crystal is a complicated and cumbersome procedure that should be separately performed for each crystal class. In many cases, properties of the crystal can be described qualitatively, and even quantitatively, once anisotropy is not strong enough, in the isotropic medium approximation. In [4] such a method was developed to describe elastic waves in crystals. To account of nonlinear effects, that are cubic in the strain tensor, such a method was used in [5]. For a more consistent description of thermodynamic, and in some cases, kinetic properties of the crystal, fourth-order terms in the strain tensor should also be taken into account. The model of the isotropic medium that describes properties of a crystal allows one to substantially simplify the results and to generalize the method to crystals of arbitrary symmetry. In this case, parameters of the isotropic medium model should be found for a crystal of each symmetry from the coincidence with the exact moduli of elasticity condition.

Let us consider the interacting phonons in the isotropic medium in more detail. In this case, the second-order elastic modulus tensor is

$$\lambda_{aibj} = \lambda \delta_{ai} \delta_{bj} + \mu \left(ij, ba \right), \tag{17}$$

where λ, μ are the Lame coefficients. For brevity, we have used the symbol $(ij, ab) \equiv \delta_{ij} \delta_{ab} + \delta_{ia} \delta_{jb}$. The third and fourth order anharmonic elastic moduli tensors in the isotropic elastic medium have the form

$$\lambda_{aibjck} = A \delta_{ai} \delta_{bj} \delta_{ck} + B \left[\delta_{ai} \left(jk, cb \right) + \delta_{bj} \left(ik, ca \right) + \delta_{ck} \left(ij, ba \right) \right] + $$
$$+ C \left[\delta_{ac} \left(ij, bk \right) + \delta_{ak} \left(ij, bc \right) + \delta_{ic} \left(jk, ab \right) + \delta_{ik} \left(ab, jc \right) \right], \tag{18}$$

$$\lambda_{aibjckdl} = C_1 \delta_{ai} \delta_{bj} \delta_{ck} \delta_{dl} + C_2 \lambda_{aibjckdl}^{(2)} + C_3 \lambda_{aibjckdl}^{(3)} + C_4 \lambda_{aibjckdl}^{(4)} + C_5 \lambda_{aibjckdl}^{(5)}, \tag{19}$$

where

$$\lambda_{aibjckdl}^{(2)} \equiv \delta_{ai} \delta_{bj} \left(lk, cd \right) + \delta_{ai} \delta_{ck} \left(jl, db \right) + \delta_{ai} \delta_{dl} \left(jk, cb \right) + $$
$$+ \delta_{bj} \delta_{ck} \left(il, da \right) + \delta_{bj} \delta_{dl} \left(ik, ca \right) + \delta_{ck} \delta_{dl} \left(ij, ba \right), \tag{20}$$

$$\lambda_{aibjckdl}^{(3)} \equiv \delta_{ai} \left[\delta_{bd} \left(jk, cl \right) + \delta_{bl} \left(jk, cd \right) + \delta_{jd} \left(kl, bc \right) + \delta_{jl} \left(bc, kd \right) \right] + $$
$$+ \delta_{bj} \left[\delta_{ac} \left(kl, di \right) + \delta_{ci} \left(kl, da \right) + \delta_{ka} \left(li, cd \right) + \delta_{ik} \left(ad, lc \right) \right] + $$
$$+ \delta_{ck} \left[\delta_{bd} \left(il, ja \right) + \delta_{dj} \left(il, ba \right) + \delta_{lb} \left(ij, da \right) + \delta_{jl} \left(ab, di \right) \right] + $$
$$+ \delta_{dl} \left[\delta_{ac} \left(ij, bk \right) + \delta_{ak} \left(ij, bc \right) + \delta_{ic} \left(jk, ab \right) + \delta_{ik} \left(ab, jc \right) \right], \tag{21}$$

$$\lambda_{aibjckdl}^{(4)} \equiv \left(il, da \right) \left(jk, cb \right) + \left(ik, ca \right) \left(jl, db \right) + \left(ij, ba \right) \left(kl, dc \right), \tag{22}$$

$$\lambda^{(5)}_{aibjckdl} \equiv (ab,ci)(jl,dk)+(ij,ca)(kl,db)+(ik,ba)(jl,dc)+(ij,ka)(bl,dc)+$$
$$+(ab,jc)(il,dk)+(ij,bc)(kl,da)+(ab,jk)(il,dc)+(ij,bk)(cl,da)+ \tag{23}$$
$$+(ad,ci)(jk,lb)+(jl,cb)(ik,da)+(jk,db)(il,ca)+(il,ka)(cj,bd).$$

The sixth-order tensor (18) is determined by three elastic moduli A, B, C, and the eighth-order tensor (19) is determined by five elastic moduli $C_1 \div C_5$. When taking into account effects of the order not higher than four, four invariants can be constructed from the strain tensor:

$$J_1 = u_{ii}, \quad J_2 = u_{ai}u_{ia}, \quad J_3 = u_{ai}u_{ib}u_{ba}, \quad J_4 = u_{ai}u_{ib}u_{bj}u_{ja}. \tag{24}$$

These invariants are not independent due to the relation

$$J_4 = \frac{1}{6}J_1^4 - J_1^2 J_2 + \frac{4}{3}J_1 J_3 + \frac{1}{2}J_2^2. \tag{25}$$

The contribution to the free energy of the third and fourth order terms in the strain tensor is given by equations

$$F_3 = \frac{1}{3!}\left(AJ_1^3 + 5BJ_1 J_2 + 8CJ_3\right), \tag{26}$$

$$F_4 = \frac{1}{4!}\left(C_1 J_1^4 + 12C_2 J_1^2 J_2 + 32C_3 J_1 J_3 + 12C_4 J_2^2 + 48C_5 J_4\right). \tag{27}$$

Taking into account the relation (25), equation (27) can be written in the form

$$F_4 = \frac{1}{4!}\left(DJ_1^4 + 12EJ_1^2 J_2 + 32FJ_1 J_3 + 12GJ_2^2\right), \tag{28}$$

where

$$D = C_1 + 8C_5, \quad E = C_2 - 4C_5, \quad F = C_3 + 2C_5, \quad G = C_4 + 2C_5. \tag{29}$$

Thus, there are two elastic moduli in the linear theory λ, μ, three third order modules A, B, C and four fourth order modules D, E, F, G [6–9]. In the considered case, the value (15) is determined in terms of the elastic moduli as

$$I \equiv \sum_{k_1, k_2} \frac{(f_{k_1} + 1/2)(f_{k_1} + 1/2)}{k_1 k_2}\left[V_0 k_1^2 k_2^2 + V_1 (\mathbf{k}_1 \mathbf{k}_2)^2\right], \tag{30}$$

where

$$V_0 = 9\lambda + 6\mu + 6A + 32B + 32C + D + 8E + 8F + 18G,$$
$$V_1 = 6\lambda + 24\mu + 4A + 48B + 88C + 8E + 40F + 10G. \tag{31}$$

Taking into account these relations, after integrating (30) over the angles, we arrive at the following equation, which determines the speed of self-consistent phonons in the isotropic elastic medium

$$c_S^2 = c_0^2 + \frac{\hbar}{24\pi^2 \rho^2 c_S}\left(V_0 + \frac{V_1}{3}\right)J, \tag{32}$$

where the average speed of the "bare" phonons is defined by

$$c_0^2 = \frac{1}{3}\left(2c_t^2 + c_l^2\right) = \frac{(\lambda + 4\mu)}{3\rho}, \tag{33}$$

and the longitudinal and transverse velocities of sound are determined by the known relations $c_l^2 = (\lambda + 2\mu)/\rho$, $c_t^2 = \mu/\rho$ [18]. Note that the definition (33) differs from the definition of the average Debye rate [1]:

$$\frac{1}{c_D^3} = \rho^{3/2}\left[\frac{2}{\mu^{3/2}} + \frac{1}{(\lambda + 2\mu)^{3/2}}\right]. \tag{34}$$

In the model, where the average speed or the Debye energy are phenomenological parameters, this difference in the definition is not significant. However, since the average velocities (33) and (34) are expressed differently through the elastic moduli, this distinction should be taken into account in a more exact description. The standard Debye energy is determined by the relation $\Theta_D \equiv \hbar c_D k_D$ [24], but in the considered approach, as it can be seen from equation (32), the natural definition of the Debye energy is $\Theta_0 \equiv \hbar c_0 k_D$. Since now, besides the speed of the "bare" phonons c_0, there arises the speed of the self-consistent phonons c_S, so it is natural to define the "self-consistent Debye energy" $\tilde{\Theta}_D \equiv \hbar c_S k_D$, which, unlike the standard definition of the Debye energy $\tilde{\Theta}_D$ or Θ_0, is a function of the temperature. Note, however, that although in its original formulation the Debye energy is assumed to be independent on the

temperature, in practice experiments (e.g. [25–27]) reveal the temperature dependence of the Debye energy. In the considered approach, the self-consistent Debye energy $\tilde{\Theta}_D$ significantly depends on the temperature due to the phonon-phonon interaction already at the starting point and, therefore, this approach better reflects the real situation. Although the shortcomings of the Debye model, associated with a very simplified choice of the spectral density which does not take into account the details of the structure of the lattice, remain also in our approach.

For the further reference, it is convenient to introduce the symbol σ for the ratio of the renormalized due to the phonon-phonon interaction sound speed c_S to the original average sound speed c_0, or, which is the same, ratio of the self-consistent Debye energy to the standard one:

$$\sigma \equiv c_s/c_0 = \tilde{\Theta}_D/\Theta_0 . \tag{35}$$

Equation (32), on account of the introduced quantity (35), can be written in the dimensionless form [3,4]

$$\left(\sigma^2 - 1\right)\sigma = \Lambda\Phi\left(\frac{\sigma}{\tau}\right), \tag{36}$$

where $\tau \equiv T/\Theta_0$ is the dimensionless temperature. We have taken into account that $J = \frac{k_D^4}{8}\Phi\left(\frac{\sigma}{\tau}\right)$, where $\Phi(x) \equiv 1 + \frac{8}{3x}D(x)$, $D(x) = \frac{3}{x^3}\int_0^x \frac{z^3 dz}{e^z - 1}$ is the Debye function. Equation (36) contains a single dimensionless parameter that characterizes the system:

$$\Lambda \equiv \frac{\Theta_0}{32\rho M c_0^4}\left(V_0 + \frac{V_1}{3}\right), \tag{37}$$

where M is the mass of the lattice atom. In general, there are no restrictions on the sign of this parameter. However, calculations show that for the most substances the sign of Λ is positive. This leads to the fact that in most cases the phonon speed c_S and the self-consistent Debye energy $\tilde{\Theta}_D$ increase with the temperature [2, 3]. For diamond and crystals with the similar structure, such as germanium and silicon, this parameter turns out to be negative. Further on we will study the solely diamond crystal case.

APPROXIMATION OF NONLINEAR CHARACTERISTICS OF CRYSTALS BY THE ELASTIC MODULI OF THE ISOTROPIC MEDIUM

A large number of elastic moduli describe the nonlinear elastic properties of crystals of different symmetry. Most simply is to describe nonlinear properties of the isotropic medium, where there are nine modules upon the expansion of the free energy up to the fourth power in the strain tensor. In most cases, crystals can also be well described using the isotropic medium model, if its parameters are optimally selected. In [4] it was proposed to choose the elastic moduli of the approximating linearized isotropic medium from the requirement of the minimum of the quantity

$$I_2 \equiv \left|\lambda_{aibj} - \lambda_{aibj}^{(0)}\right|^2, \tag{38}$$

where λ_{aibj} is the modulus of elasticity of a crystal, $\lambda_{aibj}^{(0)}$ is the elastic modulus of the isotropic medium. As it was shown in [28], the free energy of the isotropic medium turns out to be as close as possible to the free energy of the crystal in the case. It is natural for the approximation of nonlinear elastic moduli to use the analogous condition (38) [5], minimizing the quantities

$$I_3 \equiv \left|\lambda_{aibjck} - \lambda_{aibjck}^{(0)}\right|^2, \qquad I_4 \equiv \left|\lambda_{aibjckdl} - \lambda_{aibjckdl}^{(0)}\right|^2, \tag{39}$$

where λ_{aibjck}, $\lambda_{aibjckdl}$ are the elastic moduli tensors of the crystal, $\lambda_{aibjck}^{(0)}$, $\lambda_{aibjckdl}^{(0)}$ are the elastic moduli tensors of the isotropic medium. Taking the derivatives of I_2, I_3, I_4 with respect to the elastic moduli of the isotropic medium and setting them to zero, we obtain the systems of equations whose solutions are the elastic moduli of a reduced isotropic medium, expressed in terms of the following convolutions of the elastic tensors of a real crystal:

$$\begin{array}{c}
\lambda_1^{(2)} \equiv \lambda_{iikk}, \quad \lambda_2^{(2)} \equiv \lambda_{ikik}, \\
\lambda_1^{(3)} \equiv \lambda_{iikkll}, \quad \lambda_2^{(3)} \equiv \lambda_{ikklli}, \quad \lambda_3^{(3)} \equiv \lambda_{iikllk}, \\
\lambda_1^{(4)} \equiv \lambda_{iikkllpp}, \quad \lambda_2^{(4)} \equiv \lambda_{iikklppl}, \quad \lambda_3^{(4)} \equiv \lambda_{iikllppk}, \quad \lambda_4^{(4)} \equiv \lambda_{ikkilppl}, \quad \lambda_5^{(4)} \equiv \lambda_{ikkllppi}.
\end{array} \tag{40}$$

In terms of these quantities, the reduced elastic moduli are

$$\lambda = \frac{1}{15}\left(2\lambda_1^{(2)} - \lambda_2^{(2)}\right), \qquad \mu = \frac{1}{30}\left(-\lambda_1^{(2)} + 3\lambda_2^{(2)}\right), \tag{41}$$

$$A = \frac{1}{105}\left(8\lambda_1^{(3)} + 8\lambda_2^{(3)} - 15\lambda_3^{(3)}\right), \quad B = \frac{1}{210}\left(-15\lambda_1^{(3)} - 12\lambda_2^{(3)} + 19\lambda_3^{(3)}\right),$$
$$C = \frac{1}{210}\left(2\lambda_1^{(3)} + 9\lambda_2^{(3)} - 9\lambda_3^{(3)}\right), \tag{42}$$

$$D = \frac{1}{56700}\left(1123\lambda_1^{(4)} - 618\lambda_2^{(4)} - 2296\lambda_3^{(4)} - 1671\lambda_4^{(4)} + 3522\lambda_5^{(4)}\right),$$
$$E = \frac{1}{113400}\left(-103\lambda_1^{(4)} + 438\lambda_2^{(4)} + 376\lambda_3^{(4)} + 411\lambda_4^{(4)} - 1002\lambda_5^{(4)}\right),$$
$$F = \frac{1}{226800}\left(-287\lambda_1^{(4)} + 282\lambda_2^{(4)} + 1184\lambda_3^{(4)} + 39\lambda_4^{(4)} - 978\lambda_5^{(4)}\right),$$
$$G = \frac{1}{226800}\left(-557\lambda_1^{(4)} + 822\lambda_2^{(4)} + 104\lambda_3^{(4)} + 2469\lambda_4^{(4)} - 2598\lambda_5^{(4)}\right). \tag{43}$$

For the cubic crystals, to which diamond belongs, the following components are selected as the independent components of the elasticity tensors of the fourth, sixth and eighth ranks in the matrix representation [4,6]: 1) c_{11}, c_{12}, c_{44}; 2) $c_{111}, c_{112}, c_{155}, c_{123}, c_{144}, c_{456}$; 3) $c_{1111}, c_{1112}, c_{1166}, c_{1122},$ $c_{1266}, c_{4444}, c_{1123}, c_{1144}, c_{1244}, c_{1456}, c_{4466}$. In this case, equations (41)-(43) for the elastic moduli of the reduced isotropic medium take the form

$$\lambda = \frac{1}{5}\left(c_{11} + 4c_{12} - 2c_{44}\right), \qquad \mu = \frac{1}{5}\left(c_{11} - c_{12} + 3c_{44}\right), \tag{44}$$

$$A = \frac{1}{35}\left(c_{111} + 18c_{112} + 16c_{123} - 30c_{144} - 12c_{155} + 16c_{456}\right),$$
$$B = \frac{1}{35}\left(c_{111} + 4c_{112} - 5c_{123} + 19c_{144} + 2c_{155} - 12c_{456}\right),$$
$$C = \frac{1}{35}\left(c_{111} - 3c_{112} + 2c_{123} - 9c_{144} + 9c_{155} + 9c_{456}\right), \tag{45}$$

$$D = \frac{1}{315}\left(c_{1111} + 32c_{1112} + 36c_{1122} + 204c_{1123} - 132c_{1144} - 24c_{1166} - 312c_{1244} - 36c_{1266} + 240c_{1456} + 6c_{4444} + 12c_{4466}\right),$$
$$E = \frac{1}{315}\left(c_{1111} + 14c_{1112} + 9c_{1122} - 3c_{1123} + 21c_{1144} - 6c_{1166} + 48c_{1244} - 48c_{1456} - 3c_{4444} - 6c_{4466}\right),$$
$$F = \frac{1}{630}\left(2c_{1111} + 10c_{1112} - 9c_{1122} - 24c_{1123} + 6c_{1144} + 6c_{1166} + 78c_{1244} + 36c_{1266} - 6c_{1456} - 15c_{4444} - 30c_{4466}\right),$$
$$G = \frac{1}{630}\left(2c_{1111} - 8c_{1112} + 27c_{1122} - 42c_{1123} + 96c_{1144} + 24c_{1166} + 60c_{1244} - 54c_{1266} - 168c_{1456} + 39c_{4444} + 78c_{4466}\right). \tag{46}$$

Equations (44) - (46) are used here for computing the parameters of the proposed model for diamond crystals. The values of the independent components of the elasticity tensors of the fourth, sixth, and eighth ranks, which are given in Tables 1 and 2, are either measured experimentally or calculated theoretically [26,27]. As it has been noted, when the approximate description is used, the temperature dependence of the elastic moduli and the difference between the isothermal and adiabatic modules could be ignored.

Table 1

Independent components of the fourth and sixth elasticity tensors of diamond (10^{11} dyn cm^{-2})

C_{11}	C_{12}	C_{44}	C_{111}	C_{112}	C_{155}	C_{123}	C_{144}	C_{456}
108	12.4	57.8	-761	-226	-280	210	-178	-82.0

Table 2

Independent components of the eighth rank elastic tensor of diamond (10^{11} dyn cm^{-2})

C_{1111}	C_{1112}	C_{1166}	C_{1122}	C_{1266}	C_{4444}	C_{1123}	C_{1144}	C_{1244}	C_{1456}	C_{4466}
2669	946	1074	607	819	1132	-42.5	-138.5	-26.4	48.7	52.8

Using the data given in Tables 1, 2, equations (44) - (46) result in the elastic coefficients of the reduced isotropic medium for diamond (Table 3).

Table 3

The nine reduced moduli of elasticity of diamond (10^{11} dyn cm^{-2})

λ	μ	A	B	C	D	E	F	G
8.4	53.8	169.1	-162.1	-37.7	637.5	186.8	-280.3	183.9

Using these data together with values of the density ρ and of the atomic mass M makes possible to calculate the parameters of the generalized Debye theory for the self-consistent phonons [2,3] in diamond, which are listed in Table 4.

Table 4

Values of the parameters V_0, V_1 (31) и Λ (37), which determine the nonlinear properties of diamond crystal.

ρ, g/cm^3	M, 10^{-23} g	V_0, 10^{11}dyn/cm^2	V_1, 10^{11}dyn/cm^2	Λ
3.5	1.99	-1784.98	-2030.2	-0.00817

The values of the temperature independent longitudinal and transverse sound velocities, the average velocities of (33), (34) and, the corresponding Debye temperatures, are given in Table 5.

Table 5

Temperature independent longitudinal, transverse and average sound speeds
and the Debye temperature of diamond.

c_t 10^5 sm/c	c_l 10^5 sm/c	c_D 10^5 sm/c	c_0 10^5 sm/c	k_D 10^8 cm^{-1}	Θ_D K	Θ_0 K
12.31	18.09	9.37	14.59	2.18	1560.6	2430.0

THE TEMPERATURE DEPENDENCES OF THE DEBYE ENERGY. HEAT CAPACITY

Account of the phonon-phonon interaction leads to the appearance of the dependence of the average phonon speed on the temperature (32), (36) even if such a dependence was absent in the linear approximation. If we determine the Debye energy or the Debye temperature through this speed $\tilde{\Theta}_D \equiv \hbar c_S k_D$, the Debye energy will also depend on the temperature. Figure 1 shows the temperature dependence of the self-consistent phonon velocity and the Debye energy of diamond, calculated with the nonlinearity parameter Λ given in Table 4.

For most solids the nonlinearity parameter Λ is positive, and the average speed of the self-consistent phonons increases with the temperature [3]. For diamond and some other diamond-like crystals, the parameter Λ turned out to be negative, so that the phonon speed and the Debye energy decrease with the temperature for them (Fig. 1).
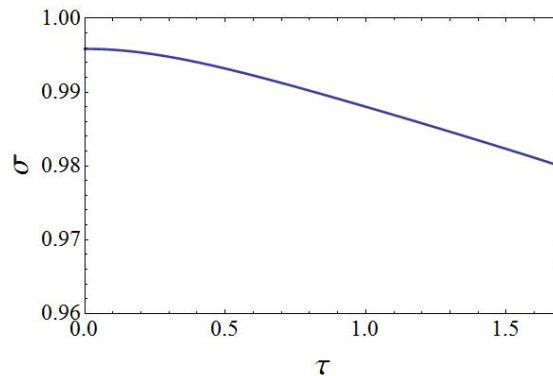

Figure 1. Dependence of the self-consistent phonon speed and the Debye energy of
diamond $\sigma \equiv c_s/c_0 = \tilde{\Theta}_D/\Theta_0$ on the temperature $\tau \equiv T/\Theta_0$.

Entropy can be obtained by the well-known expression $S = -(\partial F/\partial T)_V$ with the free energy (13), (14). Computing the derivative, the speed c_S, in view of $\partial F/\partial c_S = 0$, could be treated as a constant [2,3], then:

$$S = -N\left[3\ln\left(1 - e^{-\frac{\sigma}{\tau}}\right) - 4D\left(\frac{\sigma}{\tau}\right)\right]. \tag{47}$$

From the expression for entropy (47) it follows the expression for the isochoric heat capacity $C_V = T(\partial S/\partial T)_V$ [2,3]:

$$C_V = 3N\left[4\frac{\tau}{\sigma}D\left(\frac{\sigma}{\tau}\right) - \frac{3}{e^{\sigma/\tau} - 1}\right]\left(\frac{\sigma}{\tau} - \frac{d\sigma}{d\tau}\right). \tag{48}$$

The temperature derivative in (48) can be found from equation (36) [3]. As it is known, in the Debye model there is the law of the corresponding states, consisting in the fact that the heat capacity is a function of the dimensionless temperature $\tau = T/\Theta$ [1]. Account of the phonon-phonon interaction leads to the violation of this law, and every specific phonon system is additionally characterized by its dimensionless parameter Λ. The calculation of the parameter Λ shows that it is positive for the most substances. Consequently, we get increasing the self-consistent phonon speed with the temperature and the linear in the temperature deviation of the heat capacity C_V from the Dulong-Petit law [3]. Since experimentally it is usually measured the heat capacity C_p, which linearly grows at high temperatures (see eq. (2)), to identify the decrease of C_V experimentally, it is necessary to use the equation (2) upon processing the experimental data.

Figure 2 shows, using NaCl as an example, the typical behavior of the isochoric heat capacity at high temperatures, characterizing the most substances. The experimental data are taken from [29].
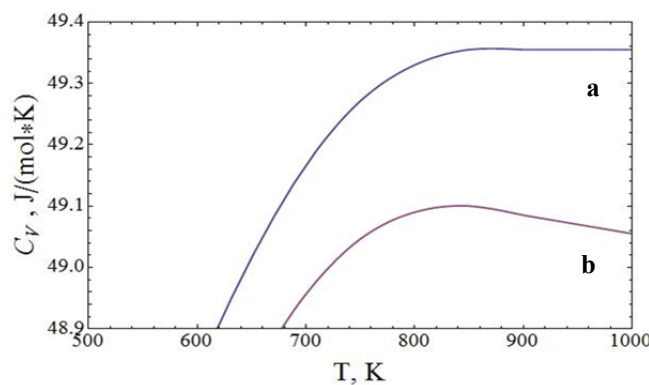

Figure 2. The molar heat capacity of NaCl at a constant volume: (a) constructed from the experimental data;
(b) subjected to equation (2).

Figure 3 shows the temperature dependence of the isochoric heat capacity of diamond, plotted by use of the experimental data from [30, 31]. As we can see, the behavior C_V of diamond at high temperatures is qualitatively different from the behavior of this quantity for the most crystals of the cubic crystal system (Fig. 2).
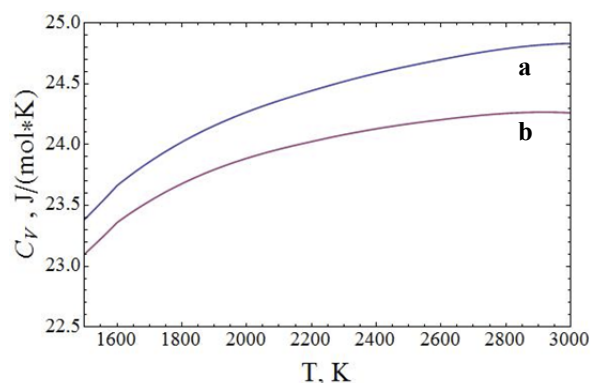

Figure 3. The molar heat capacity of diamond at a constant volume: (a) constructed from the experimental data; (b) calculated by equation (2).

CONCLUSIONS

For the most substances, the linear in the temperature decrease of C_V is observed with increasing the temperature. For crystals with diamond cubic crystal structure, this deviation occurs in the direction of increasing the heat capacity. In the framework of the approach of the self-consistent phonons, using the approximation of the elastic properties of crystals by the reduced isotropic medium, it is possible to clarify formulae for the isochoric heat capacity and the Debye energy.

Account of the phonon-phonon interaction leads to the redefinition of the phonon's speed and of the Debye energy. Their dependence on the temperature occurs. The isochoric heat capacity is no longer a constant. At low temperatures, the corrections to C_V are insignificant (the phonon gas can be considered as ideal). At high temperatures, the sign of the correction depends on the sign of the non-linearity parameter Λ. It is convenient to calculate it for the isotropic medium (see eq. (37), (31)). Calculations show that for all crystals of the cubic system Λ is positive, except of diamond and crystals with diamond structure. Figures 4, 5 show the difference in the behavior of C_V for diamond and NaCl (as an example of crystals of cubic crystal system).
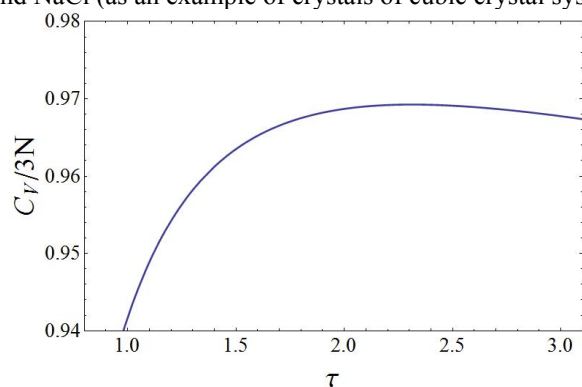
Figure 4. The normalized heat capacity of NaCl at a constant volume, calculated from equation (48), ($\Lambda = 0.007$).
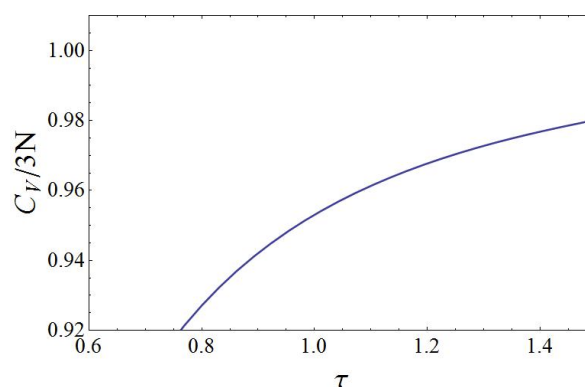
Figure 5. The normalized heat capacity of diamond at a constant volume, calculated from equation (48), ($\Lambda = -0.00817$). The upper temperature limit is constrained by the melting point.

Using the developed approach, one can calculate corrections to the thermodynamic coefficients of crystals under conditions when the phonon gas cannot be considered as weakly interacting. Also, it is possible to obtain the temperature dependences of the longitudinal and transverse Debye energies, if we do not average the speed of phonon. Estimates show that for diamond the difference between the longitudinal and transverse Debye energies can be significant.

ORCID IDs
Valery Khodusov, https://orcid.org/0000-0003-1129-3462, Yurii M. Poluektov, https://orcid.org/0000-0002-3207-3226
Artem S. Naumovets, https://orcid.org/0000-0001-6882-5672

REFERENCES

[1] L.D. Landau, and E.M. Lifshitz, *Statistical physics. Part 1, 3rd ed.,* (Elsevier Science & Technology, 1980).
[2] Yu.M. Poluektov, Low Temperature Physics, **41**, 922 (2015). https://doi.org/10.1063/1.4936228.
[3] Yu.M. Poluektov, East European Journal of Physics, **3**, 35-46 (2016), https://doi.org/10.26565/2312-4334-2016-3-03.
[4] F.I. Fedorov, *Theory of Elastic Waves in Crystals*, (Plenum Press, New York, 1968).
[5] A.I. Akhiezer, V.F. Aleksin, and V.D. Khodusov, Low Temp. Phys. **20**, 939-970 (1994).
[6] P.B. Ghate, Journal of Applied Physics, **35**, 337 (1964), https://doi.org/10.1063/1.1713312.
[7] H. Wang, and M. Li, Phys. Rew. B, **79**, (2009) 224102, https://doi.org/10.1103/PhysRevB.79.224102.
[8] M. Destrade, and R.W. Ogden, The Journal of the Acoustical Society of America, **128** 3334 (2010). https://doi.org/10.1121/1.3505102.
[9] O. Burlayenko, V. Khodusov, and A. Naumovets, East Eur. J. Phys. **5**, 70-73 (2018), https://doi.org/10.26565/2312-4334-2018-1-08.
[10] C. Kittel, *Introduction to Solid State Physics*, 8th ed., (John Wiley and Sons LTD, 2004).
[11] S.Sh. Rekhviashvili, and Kh.L. Kunizhev, High Temperature, **55**, 312–314 (2017). https://doi.org/10.1134/S0018151X17020146.
[12] Yu.M. Poluektov, Russian Physics Journal, **47**, 74-79 (2004), https://doi.org/10.1023/B:RUPJ.0000047847.43927.41.
[13] Yu.M. Poluektov, Russian Physics Journal, **52**, 30-40 (2009), https://doi.org/10.1007/s11182-009-9202-y.
[14] V.Yu. Bodryakov, and A.A. Povzner, Physics of the Solid State, **47**, 1196-1200 (2003).
[15] V.Yu. Bodryakov, Solid Stat. Comm. **83**, 1053-1055 (1994).
[16] V.A. Oskina, A.A. Povzner, A.N. Filanovich, A.G. Volkov, N.A. Zaytseva, T.A. Nogovitsyna, L.R. Kabirova, and K.A. Shumikhina, Fundamental Research, **8**, 73-76 (2013).
[17] A.A. Povzner, A.G. Volkov, and A.N. Filanovich, Physics of the Solid State, **53**, 1673-1678 (2011).
[18] L.D. Landau, L.P. Pitaevskii, A.M. Kosevich, and E.M. Lifshitz, *Theory of Elasticity*, 3rd ed., (Butterworth-Heinemann, 2012).
[19] Yu.M. Poluektov, Ukr. J. Phys., **50**, 1237 (2005), https://arxiv.org/abs/1303.4913.
[20] Yu.M. Poluektov, Low Temperature Physics, **28**, 429-441 (2002), https://doi.org/10.1063/1.1491184.
[21] Yu.M. Poluektov, Ukr. J. Phys., **52**, 579 (2007). https://arxiv.org/abs/1306.2103.
[22] Y.M. Poluektov, Russian physics journal, **47**, 656-663 (2004), https://doi.org/10.1023/B:RUPJ.0000047847.43927.41.
[23] Y.M. Poluektov, Russian physics journal, **52**, 33-45 (2009), https://doi.org/10.1007/s11182-009-9202-y.
[24] J. M. Ziman, *Principles of the Theory of Solids*, 2nd edition, (Cambridge Univ. Press, 1972).
[25] J.A. Reissland, *The Physics of Phonons*. (London, John Wiley and Sons LTD., London; New York; Sydney; Toronto, 1973).
[26] D. Gerlich, Journal of Applied Physics, **77**, 4373-4379 (1995), https://doi.org/10.1063/1.359462.
[27] A.V. Telichko, S.V. Erohin, G.M. Kvashnin, P.B. Sorokin, B.P. Sorokin, and V.D. Blank, J. Mater. Sci. **52**, 3447 (2017). https://doi.org/10.1007/s10853-016-0633-x.
[28] Yu.M. Poluektov, East Eur. J. Phys. **5**, 4-12 (2018)б https://doi.org/10.26565/2312-4334-2018-3-01.
[29] K. Wang, and R.R. Reeber, Phys. Chem. Minerals. **23**, 354-360 (1996), https://doi.org/10.1007/BF00199501.
[30] R.R. Reeber, and K. Wang, Journal of Electronic Materials, **25**, 63-67 (1996), https://doi.org/10.1007/BF02666175.
[31] A.C. Victor, The Journal of Chemical Physics, **36**, 1903 (1962), https://doi.org/10.1063/1.1701288.

НЕЛІНІЙНІ ЕФЕКТИ У ФОНОННІЙ СИСТЕМІ АЛМАЗУ

А. Наумовец[a,b], Ю.М. Полуектов[a,b], В.Д. Ходусов[a]
[a]Харківський національний університет ім. В.Н. Каразіна, пл. Свободи, 4, м Харків, 61022, Україна
[b]Національний науковий центр «Харківський фізико-технічний інститут», вул. Академічна, 1, м Харків, 61108, Україна

На основі методу самоузгодженого опису газу фононів в решітці, узагальнюючого модель Дебая з урахуванням фонон-фононної взаємодії, теоретично досліджені термодинамічні властивості алмазу. Властивості кристалів певної симетрії у багатьох випадках можуть бути добре апроксимовані моделлю ізотропного суцільного середовища, якщо його модулі пружності вибрати оптимальним чином. Їх слід шукати для кристала кожної симетрії з умови їх близькості до точних модулів пружності, які вимірюються експериментально і наведені у відповідних таблицях. В області високих температур нелінійне взаємодії фононів враховує як трьох-, так і чотирьох фононні взаємодії. Це призводить до того, що в моделі наведеного ізотропного кристалу необхідно враховувати не тільки тензори модулів пружності другого порядку, а й модулів пружності третього і четвертого порядків, які характеризуються дев'ятьма незалежними компонентами. Врахування фонон-фононної взаємодії в наближенні самоузгодженого поля призводить до появи залежності швидкості таких фононів і температури Дебая від температури. За відсутності взаємодії та нехтуванні нелінійними ефектами, фонони в даній теорії такі ж, як в теорії Дебая. Їх називаємо «голими» або «дебаєвськими». Фонони, швидкість яких перенормована внаслідок взаємодії, називаємо «самоузгодженими». Показано, що при високих температурах теорія передбачає лінійне за температурою відхилення ізохоричної теплоємності від закону Дюлонга-Пті. На відміну від більшості кристалів, де спостерігається зменшення ізохоричної теплоємності, теорія для алмазу і алмазоподібних кристалів передбача лінійне зростання цієї теплоємності з температурою, що відповідає експерименту. Ізобарична теплоємність алмазу, як і у інших речовин, лінійно зростає з температурою.
КЛЮЧОВІ СЛОВА: фонон, ізохорична теплоємність, ізобарична теплоємність, фонон-фононна взаємодія, енергія Дебая, решітка алмазу, модулі пружності

НЕЛИНЕЙНЫЕ ЭФФЕКТЫ В ФОНОННОЙ СИСТЕМЕ АЛМАЗА

А. Наумовец[a,b], Ю.М. Полуэктов[a,b], В.Д. Ходусов[a]
[a]Харьковский национальный университет им. В.Н. Каразина, пл. Свободы, 4, г. Харьков, 61022, Украина
[b]ННЦ «Харьковский физико-технический институт», ул. Академическая, 1, г. Харьков, 61108, Украина

На основе метода самосогласованного описания газа фононов в решетке, обобщающего модель Дебая с учетом фонон-фононного взаимодействия, теоретически исследованы термодинамические свойства алмаза. Свойства кристаллов определённой симметрии во многих случаях могут быть хорошо аппроксимированы моделью изотропной сплошной среды, если её модули упругости выбрать оптимальным образом. Их следует находить для кристалла каждой симметрии из условия

их близости к точным модулям упругости, которые измеряются экспериментально и приведены в соответствующих таблицах. В области высоких температур нелинейное взаимодействия фононов учитывает как трех-, так и четырех фононные взаимодействия. Это приводит к тому, что в модели приведенного изотропного кристалла необходимо учитывать не только тензоры модулей упругости второго порядка, но и модулей упругости третьего и четвертого порядков, которые характеризуются девятью независимыми компонентами. Учет фонон-фононного взаимодействия в приближении самосогласованного поля приводит к появлению зависимости скорости таких фононов и температуры Дебая от температуры. В отсутствие взаимодействия в пренебрежении нелинейными эффектами, фононы в данной теории такие же, как в теории Дебая. Их называем «голыми» или «дебаевскими». Фононы, скорость которых перенормирована вследствие взаимодействия, называем «самосогласованными». Показано, что при высоких температурах теория предсказывает линейное по температуре отклонение изохорической теплоемкости от закона Дюлонга-Пти. В отличие от большинства кристаллов, где наблюдается уменьшение изохорической теплоемкости, теория для алмаза и алмазоподобных кристаллов предсказывает линейное возрастание этой теплоемкости с температурой, что соответствует эксперименту. Изобарическая теплоёмкость алмаза, как и у других веществ, линейно возрастает с температурой.

КЛЮЧЕВЫЕ СЛОВА: фонон, изохорическая теплоемкость, изобарическая теплоемкость, фонон-фононное взаимодействие, энергия Дебая, решетка алмаза, модули упругости

AN AB INITIO CALCULATIONS OF SINGLE-ELECTRON TRANSISTOR BASED SINGLE WALLED CARBON NANOTUBE OF ULTRA-SMALL DIAMETER

Sraja Chauhan, Ajay Singh Verma*

Department of Physics, Banasthali Vidyapith, Rajasthan, 304022, India
Corresponding author: ajay_phy@rediffmail.com
Received March 2, 2020; accepted March 27, 2020

In this paper, we have investigated the charge stability diagram and conductance dependence on source drain bias and gate voltage of carbon nanotube based single electron transistor (SET) by using first principle calculations. All calculations have been executed by using ATK-VNL simulation package based on density functional theory (DFT). We have applied these calculations for carbon nanotube based SET; the nanotube has been placed just above the dielectric ($\mathcal{E}o = 10$) in between the source and drain electrodes of gold. The single walled carbon nanotube has been used in SET, which have ultra-small diameter and (4,0) configuration. The addition energy of the device has been calculated, which can be defined as the difference between the electron affinity, and ionization energies. The calculated values of energies have been found to be -10.17694 eV and -11.04034 eV for isolated phase and SET environment respectively. In electrostatic environment, the results were showing the regularization of molecular energy levels and therefore the addition energy reduced. The calculations for additional energies, variations of total energies to that of the gate voltages and charge stability diagram (CSD) have also been done in this study.

KEYWORDS: Single walled carbon Nanotube, Single-Electron Transistor (SET), Electron Affinity, Ionization Energy, Addition Energy, Charge stability diagram (CSD)

Carbon nanotubes have been known to show astonishing electrical properties; therefore could be used in electronic industry as a future alternative for Silicon based devices. Over the last few decades, the advancement in the speed, complexity and low power consumption of electronic devices, have been dramatically developed and achieved by decreasing the device dimensions and evolving new device structures. Since the objective of modern technology is to reduce the size of the devices; therefore the researchers as well as the engineers have been inclined towards Nano electronics. In decreasing the size of the transistor, scaling has always played an important character to observe Moore's law [1]; but the decrement in the size of a device leads to the drooping of device. Drain-induced barrier lowering, threshold voltage shift, leakage current, gate-induced drain lowering etc., are the effects, named as short channel effects, which become prominently dominant when device size is decreased [2]. To reduce, these effects and to increase device performance, the researchers have done many research and Single-electron transistors are one of them. A Single-electron transistor [3-6] (SET) is an electronic tool system by which the flow of even a single electron can be governed.

Carbon nanotubes [7-9] are the nanostructures of high aspect ratio; also they used to show excellent electronic, thermal, mechanical, structural properties [10] so could be used in electronic devices. Depending upon the type of rolling, nanotubes may exhibit semiconducting or metallic nature. CNTs have been investigated since a very long time and being used in electronic devices such as in field effect transistors (FETs) [11,12], but in FETs the flow of current occurs due to the tunneling of many electrons through the junctions. While if instead of many electrons, the flow of only single electron may cause the current flow, then the circuit power consumption and probability of high switching can be achieved [13]. Low power consumption and sensitivity of SETs make it a good candidate for VLSI technologies [14]. In spite of being the low temperature phenomenon, the room temperature fabrication of SETs has been executed [15]. In this paper, we have studied the single walled carbon nanotube, of ultra-small diameter and zigzag type, incorporated in the single electron transistor. In this study we had used the zigzag nanotube of ultra-small diameter (4,0) in single electron transistor. The conductance as well as the charge stability diagram (CSD) of the device had been studied.

THEORY, RESULTS AND DISCUSSION

In the present work, theoretical calculations based on Density Functional Theory (DFT) were done to calculate the above said quantities. In order to do the calculations the single electron transistor was modeled by using density functional theory based software Atomistic toolkit (ATK) [16] package by which all the modeling and the analysis of the device had been carried out. Local Density Approximation (LDA) [17] was chosen as the exchange-correlation function. The gate electrode thickness, gate-oxide (dielectric constant of material $\epsilon o = 10$) [18] thickness and the source-drain width are considered to be 1A°, 3.8A° and 4A° in order to design the SET. Source/drain electrodes were taken as metallic electrodes of 5.28 eV work function i.e., gold [19]. Normal components of electric field had been set to be zero using Neumann boundary conditions for device analysis. Also, in the molecular energy spectrum the energy was set to absolute energy. As in the Fig.1 (a) it can be seen that a single-electron transistor was assembled by placing an island in

between the two electrodes named as source (left) and drain (right) respectively. The island is isolated from the third electrode (gate), source and drain electrodes by an ultra-thin dielectric material. The third terminal gate is capacitively coupled to the conducting island. Two junctions source-material and material-drain have been observed which are necessary to be crossed in order to maintain the current flow in the device. The source was kept at higher potential as compared to the drain electrode. An electron will tunnel from the source to the material until or unless its energy becomes equal to the coulomb's energy and till then electron will be trapped onto the barrier [20-23]. This phenomenon of trapping the electron is called as the coulomb blockade by which the flow of electron can be controlled. Gate voltage is the main key controller of SET.
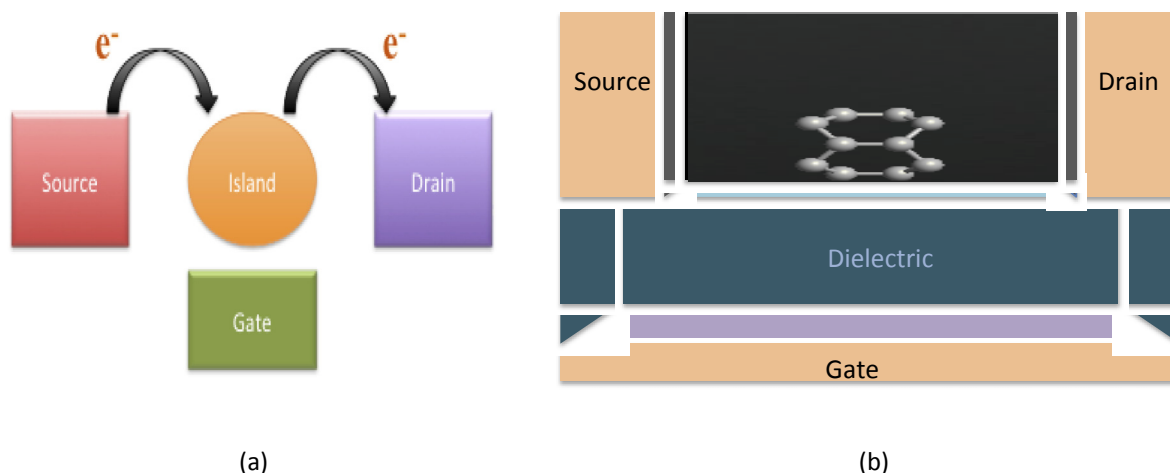

(a)   (b)

Figure 1. (a) Structure of conventional Single Electron Transistor, (b) the modeled structure
of CNT (4,0) based Single Electron Transistor

Using the DFT based ATK-VNL simulation package we have optimized CNT (4,0), which was the basic need in order to design SET. From the optimized structure, CNT was modeled in the SET configuration using the software with local density approximations (LDA). The modeled structure has been shown in Fig.1 (b) in which the nanotube was kept just above the dielectric material, which was connected to gate electrode, and metallic electrodes surround the system.

After the completion of the modeling the structure, the SET configuration was used to calculate charge stability diagram (CSD), also against the gate voltage the variation of total energies have been observed. First, we have calculated the total energies in isolated state and then for SET environment for individual charge states (0, 1, 2,-1,-2) that are required to calculate the charging energies i.e. electron affinity (E_A) and ionization energy (E_I). Both of these can be defined as the amount of energy required adding one electron to the molecule and the amount of energy required to eliminate one electron from the molecule respectively.

In the equation form these can be written as:

$$E_A = E^{-1} - E \quad \text{and} \quad E_I = E^{+1} - E$$

Where E is the energy of the molecule in neutral state, E^{-1} is the energy of the molecule when one electron is added to the molecule, and E^{+1} is the energy of the molecule after the elimination of one electron.

The energies have been calculated in both the configurations and shown in the table 1. It has been found that there is a reduction in electron affinity (E_A) and in ionization energy (E_I) in SET environment, which may due to the stabilization of charges due to electrostatic surrounding. This reduction enhances the switching property of device since as the energies become lower; the switching speed as well as the conductance will be improved. By addition energy the conductance improvement can be further explained since $E_{add} = E_A - E_I$; shown in table 2. It is clear that in SET environment the addition energy is lower; which is indicating the better stability of the system.

Table 1

Calculated values of electron affinity and ionization energies in isolated and in SET configuration

Energy (eV)	Isolated (eV)	SET (eV)
E_I^{+1}	9.86443	8.08661
E_I	6.65266	6.36309
E_A^{-1}	-0.45897	-2.92933
E_A	-3.52428	-4.67725

For distinct charge states the variation of total energies with respect to gate voltage has shown in Fig. 2(a); in which different color map shows different charge states i.e. blue (-2), green (-1), red (0), turquoise (1), and violet (2). Figure 2(a) shows that the system has minimum energy in its neutral state i.e. in 0 charge state. Since minimum energy

expresses the stability of the system so the system is stable in its neutral state. Also it can be seen from the figure that when the negative bias is applied then positive states are getting stable and when the positive bias is applied then the negative charge states are getting stable. This indicates that whenever the gate is positively biased then an electron is attracted towards CNT and making it negatively charged as a result the LUMO level of CNT appears to be lower than that of electrode's Fermi level. While on the other hand, when the gate is negatively biased then an electron is eliminated from the CNT and making it positively charged and HOMO level of CNT appears to be above the electrode's Fermi level.

Table 2

Calculated values of addition energies in both the environments

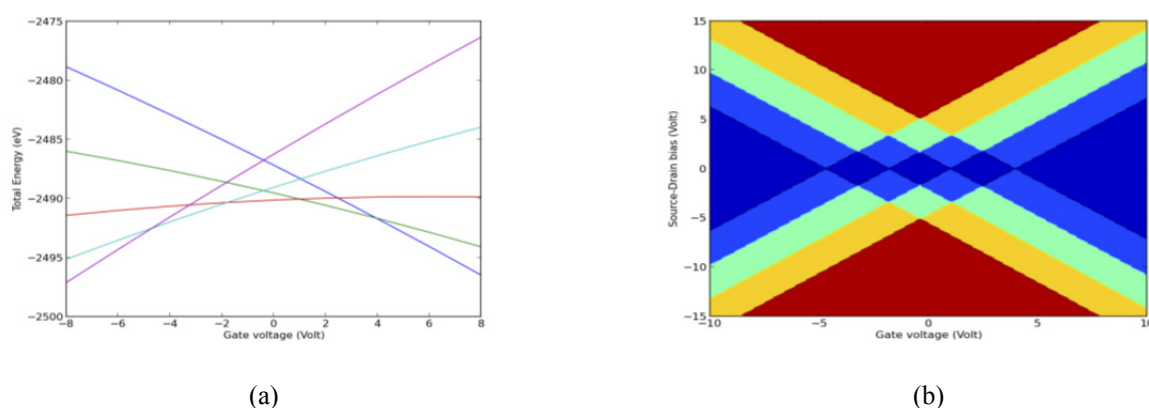| Energy (eV)	Isolated (eV)	SET (eV)
E_{add}	-10.17694	-11.01594
E^1_{add}	-10.3234	-11.01594

(a)	(b)

Figure 2. (a) Variation of total energies with gate voltage for different charge states [blue (-2), green (-1), red (0), turquoise (1), and violet (2)] for a CNT_SET. (b) Charge Stability Diagram (CSD) for CNT_SET. CSD shows different number of charge states for different bias with blue (0), light blue (1), green (2), orange (3) and red (4).

Charge stability diagram (CSD) has been plotted for the investigation of conductance and shown in fig. 2(b). CSD explains the dependence of conductance on the source drain and gate voltage. In this diagram the charging energy of CNT in SET surroundings is plotted for different gate voltages. A particular number of energy levels i.e. charge states are present there for a fixed value of source-drain and gate voltage. Different energy levels are represented by a coding of different colors i.e. blue (0), light blue (1), green (2), orange (3) and red (4) in CSD and conductance depends upon the number of charge states in bias window. As much as the width of the central dark region decreases, less the charging energy will be needed to bring SET into conduction state. From the figure, it is clear that the central dark blue region is not much broad therefore the device will be needed less energy to bring SET in conduction state and the device can act as a fast switching device.

CONCLUSIONS

The present work validates the application of Density Functional Theory (DFT) to calculate the properties of carbon nanotube (CNT) based single electron transistor (SET) in Coulomb blockade regime. Single-electron transistor with island CNT of (4,0) configuration had been modeled and simulated. It shows better stability and higher conductance. With the help of Charge stability diagram (CSD) and variation of total energies with respect of gate voltages at different charge states the system shows high conductance.

ORCID IDs
Sraja Chauhan, https://orcid.org/0000-0002-7055-8574; **Ajay Singh Verma,** https://orcid.org/0000-0001-8223-7658

REFERENCES
[1] G.E. Moore, *Progress in digital integrated electronics. Electron Devices Meeting*, 11–13 (1975).
[2] S.I. Garduño, A. Cerdeira, M. Estrada, J. Alvarado, V. Kilchystka, and D. Flandre, J. Applied Physics, **109**(8), 084524 (2011), https://doi.org/10.1063/1.3575324.
[3] K.K. Likharev, Proceedings of the IEEE, **87**, 606-632 (1999), https://doi.org/10.1109/5.752518.
[4] M.A. Kastner, Rev. Mod. Phys. **64**, 849-858 (1992), https://doi.org/10.1103/RevModPhys.64.849.

[5]   Y. Takahashi, Y. Ono, A. Fujiwara, and H. Inokawa, J. Physics: Condensed Matter, **14**, 995-1033 (2002), https://doi.org/10.1088/0953-8984/14/39/201.

[6]   T.A. Fulton, and G.J. Dolan, Physics Review Letters, **59**, 109 (1987), https://doi.org/10.1103/PhysRevLett.59.109.

[7]   A. K. Geim, and K.S. Novoselov, Nature Materials, **6**, 183–191 (2007), https://doi.org/10.1142/9789814287005_0002.

[8]   S. Iijima, Nature, **354**, 56-58 (1991), https://doi.org/10.1038/354056a0.

[9]   V.N. Popov, Materials Science and Engineering, **43,** 61–102 (2004), https://doi.org/10.1016/j.mser.2003.10.001.

[10] M.S. Dresselhaus, G. Dresselhaus, Ph. Avouris (Eds.), *Carbon nanotubes: Synthesis, Structure, Properties, and Applications*, (Springer, 2001), pp. 287-292.

[11] A. Javey, J. Guo, Q. Wang, M. Lundstrom, and H. Dai, Nature, **424**, 654–657 (2003), https://doi.org/10.1038/nature01797.

[12] A. Naderi, and S.A. Ahmadmiri, ECS Journal of Solid State Science and Technology, **5**, 63-68 (2016), https://doi.org/10.1149/2.0061607jss.

[13] V.K. Hosseini, D. Dideban, Md. T. Ahmadi, and R. Ismail, Int. J. Electronics and Communications, **90**, 97-102 (2018), https://doi.org/10.1016/j.aeue.2018.04.015.

[14] C. Wasshuber, in: *Proceedings of 40th Design Automation Conference*, pp. 274-275, (2003), https://doi.org/10.1145/775832.775901.

[15] S.J. Tans, A.R.M. Verschueren, and C. Dekker, Nature, **393**, 49–52 (1998), https://doi.org/10.1038/29954.

[16] Atomistic Toolkit-Virtual Nanolab. Quantumwise A/S, http://quantumwise.com/. Accessed 8th September 2017.

[17] M. Brandbyge, J.-L. Mozos, P. Ordejón, J. Taylor, and K. Stokbro, Phys. Rev. B, **65**, 165401 (2002), https://doi.org/10.1103/PhysRevB.65.165401.

[18] J. Robertson, Eur. Phys. J. Appl. Phys., **28**, 265–291 (2004), https://doi.org/10.1051/epjap:2004206.

[19] http://docs.quantumwise.com/tutorials/work_function_ag_100/work_function_ag_100.html, 12th September 2017.

[20] Z.A.K. Durrani, *Single-electron devices and circuits in silicon*, (World Scientific, 2010).

[21] M. Devoret, and H. Grabert, in: *Single Charge Tunneling*, (Plenum Publishing Corporation, 1992), pp. 1–19.

[22] H. Grabert, G.-L. Ingold, M.H. Devoret, D. Est`eve, H. Pothier, and C. Urbina, Zeitschrift für Physik B Condensed Matter, **84**, 143–155 (1991), https://doi.org/10.1007/BF01453767.

[23] L. Kouwenhoven, N.C. van der Vaart, A. Johnson, W. Kool, C. Harmans, J. Williamson, A. Staring, and C. Foxon, Zeitschrift für Physik B Condensed Matter, **85**, 367–373, (1991), https://doi.org/10.1007/BF01307632.

ПОЧАТКОВІ РОЗРАХУНКИ ОДНОЕЛЕКТРОННОГО ТРАНЗИСТОРА НА ОСНОВІ ОДНОСТІННОЇ ВУГЛЕЦЕВОЇ НАНОТРУБКИ УЛЬТРАМАЛОГО ДІАМЕТРУ

Сраджа Чаухан, Аджай Сінг Верма

Фізичний факультет, Банастхалі Відьяпіт, Раджастхан, 304022, Індія

У цій статті ми досліджували діаграму стабільності заряду і залежність провідності від зсуву витоку і напруги на затворі одноелектронного транзистора (SET) на основі вуглецевих нанотрубок, використовуючи первопрінціпние обчислення. Всі розрахунки виконані з використанням пакета моделювання ATK-VNL, заснованого на теорії функціонала щільності (DFT). Ми застосували ці розрахунки для SET на основі вуглецевих нанотрубок. Нанотрубка була поміщена трохи вище діелектрика (Eo = 10) між золотих електродів витоку і стоку. У SET використовувалася одностінна вуглецева нанотрубка, яка має надмалих діаметр і (4,0) конфігурацію. Була розрахована додаткова енергія пристрою, яка може бути визначена як різниця між спорідненістю до електрону і енергією іонізації. Встановлено, що розраховані значення енергій складають - 10,17694 еВ і -11,04034 еВ для ізольованою фази і SET-середовища відповідно. У електростатичного середовищі результати показали регуляризацію рівнів молекулярної енергії і, отже, додаткова енергія зменшувалася. Розрахунки для додаткових енергій, варіацій повних енергій до напруг затвора і діаграми стабільності заряду (CSD) також були виконані.

КЛЮЧОВІ СЛОВА: одностінна вуглецева нанотрубка, одноелектронний транзистор (SET), спорідненість до електрону, енергія іонізації, додаткова енергія, діаграма стабільності заряду (CSD).

НАЧАЛЬНЫЕ РАСЧЕТЫ ОДНОЭЛЕКТРОННОГО ТРАНЗИСТОРА НА ОСНОВЕ ОДНОСТЕННОЙ УГЛЕРОДНОЙ НАНОТРУБКИ УЛЬТРАМАЛОГО ДИАМЕТРА

Сраджа Чаухан, Аджай Сингх Верма

Физический факультет, Банастхали Видьяпит, Раджастхан, 304022, Индия

В этой статье мы исследовали диаграмму стабильности заряда и зависимость проводимости от смещения истока и напряжения на затворе одноэлектронного транзистора (SET) на основе углеродных нанотрубок, используя первопринципные вычисления. Все расчеты выполнены с использованием пакета моделирования ATK-VNL, основанного на теории функционала плотности (DFT). Мы применили эти расчеты для SET на основе углеродных нанотрубок. Нанотрубка была помещена чуть выше диэлектрика ($\mathcal{E}o = 10$) между золотых электродов истока и стока. В SET использовалась одностенная углеродная нанотрубка, которая имеет сверхмалый диаметр и (4,0) конфигурацию. Была рассчитана добавочная энергия устройства, которая может быть определена как разница между сродством к электрону и энергией ионизации. Установлено, что рассчитанные значения энергий составляют -10,17694 эВ и -11,04034 эВ для изолированной фазы и SET-среды соответственно. В электростатической среде результаты показали регуляризацию уровней молекулярной энергии и, следовательно, добавочная энергия уменьшалась. Расчеты для добавочных энергий, вариаций полных энергий к напряжениям затвора и диаграммы стабильности заряда (CSD) также были выполнены.

КЛЮЧЕВЫЕ СЛОВА: одностенная углеродная нанотрубка, одноэлектронный транзистор (SET), сродство к электрону, энергия ионизации, добавочная энергия, диаграмма стабильности заряда (CSD).

Алла Таньшина*

Посвящается доброй памяти фундаторов УФТИ
К 90-годовщине криогенной лаборатории Украинского (Харьковского) физико-технического института

Основное, что характеризует ХФТИ и относится к его бесспорным достоинствам,
это его колоссальное оборудование и огромный технический опыт.
По своему техническому оснащению ХФТИ
является первым физическим институтом в СССР.
Из резолюции проверочной комиссии ОФМН АН СССР от 12-18 мая 1939 г.

«НАДО ПОМНИТЬ, ЧТО ДО ПОЯВЛЕНИЯ ПЕТРА КАПИЦЫ МЫ БЫЛИ ПЕРВОЙ И ЕДИНСТВЕННОЙ ЛАБОРАТОРИЕЙ В СССР…»

Если бы меня попросили назвать всего двух физиков,
в максимальной мере прославивших украинскую науку,
то я бы назвал теоретика Л.Д. Ландау
и экспериментатора Л.В. Шубникова.
*Академик А.И. Ахиезер***

Именно Лев Васильевич Шубников возглавил – в Украинском (Харьковском) физико-техническом институте – первую и единственную в СССР криогенную лабораторию (1930 г. – дата основания). В 1937 году Лев Васильевич был необоснованно арестован и расстрелян.

Лев Васильевич Шубников
Alma mater

Лев Васильевич Шубников родился 1901 года в Санкт-Петербурге. Его отец, Василий Васильевич, работал бухгалтером, а мама – Любовь Сергеевна – вела домашнее хозяйство.

В 1911 году Лев Шубников был зачислен в одно из лучших санкт-петербургских средних учебных заведений – гимназию Марии Андреевны Лентовской. Учился, как свидетельствуют архивные документы гимназии, прилежно. В табеле за выпускной, 8 класс, в графе «физика» записано – «интерес к предмету большой».

В 1918 году Шубников поступает в Петроградский университет на физико-математический факультет (специальность «физика»). Но он был единственным студентом-физиком набора этого года, и ему пришлось слушать лекции сначала с теми, кто был на курс старше, затем – на курс младше.

Иллюстрация студенческой жизни тех лет – мемуарные воспоминания его сокурсницы Ольги Николаевны Трапезниковой, доктора физико-математических наук: *«В 1919 году я поступила на физическое отделение Петроградского университета. В университете встретилась со Львом Васильевичем…*

Жизнь была трудная. После лекций Лев Васильевич составлял список присутствующих, лектор подписывал, и всем нам выдавалось по тоненькому кусочку хлеба с повидлом – мы называли это чайным довольствием…

В 1919 году уже существовал Оптический институт, и Д.С. Рождественский устроил всех старших студентов… туда лаборантами. Отдельного здания ГОИ [Государственный оптический институт. – Прим. А.Т.] *тогда ещё не имел и размещался в Физическом институте при университете. Все лаборанты получали так называемый атомный паёк, и это их очень поддерживало. Такой же паёк получали и преподаватели».* Заслуживают упоминания и следующие исторические факты: первая мировая война, революция, гражданская война и интервенция породили в стране разруху, голод, холод.

Приведенные ниже извлечения из правительственных документов того времени позволяют наглядно обрисовать тогдашние реалии.

*Проект декрета СНК**** об улучшении положения научных специалистов*
23 декабря 1919 г.

В целях сохранения научных сил, необходимых для социалистического строительства, для поднятия производительности народного хозяйства и культуры, а также наиболее целесообразного обеспечения нужд рабоче-крестьянской обороны Совет Народных Комиссаров постановляет:

---

*Юбилейный очерк подготовлен по диссертационным материалам (научный руководитель – академик НАН Украины Виктор Григорьевич Барьяхтар).

**Ахиезер Александр Ильич (1911-2000) – физик-теоретик, академик АН УССР (1964).
Родился 31 октября 1911 г. в г. Черикове (Белоруссия). В 1938-1988 гг. – заведующий отделом теоретической физики Украинского (Харьковского) физико-технического института.

***Совет Народных Комиссаров (СНК) – в 1917-1946 гг. название высших исполнительных и распорядительных органов государственной власти. Народный комиссариат (наркомат) – центральный орган управления отдельной сферой деятельности или отдельной отраслью народного хозяйства. Возглавлялся народным комиссаром (наркомом). Впервые наркоматы были созданы в октябре 1917 года, в 1946-м преобразованы в министерства.

1. Предоставить усиленное довольствие наиболее выдающимся специалистам тех отраслей, которые являются существенными для разрешения указанных выше задач.

2. Освободить этих специалистов от всякого рода повинностей (трудовой, военной и т. д.), не имеющих отношения к их научным занятиям.

3. Создать для научной работы этих специалистов жилищные условия, обеспечивающие их минимальными, безусловно для такой работы необходимыми удобствами...

Постановление Центральной комиссии по улучшению быта
научных специалистов при Совнаркоме
об увеличении количества пайков научным специалистам Петрограда и Москвы
и о выдаче им обуви и одежды

17 мая 1920 года

…3. Выдавать научным специалистам как Москвы, так и Петрограда, кроме продовольственных пайков, по одной паре обуви, одному костюму (или материи на костюм), три пары белья (или материи на белье) и шести пар носков (или чулок) в год. Что касается теплого платья, то таковое выдавать отдельным лицам лишь в зависимости от степени нуждаемости в нем…

Также не случайно в числе прочих тогдашних лозунгов был и следующий: *«Научиться ценить науку, отвергать "коммунистическое" чванство дилетантов и бюрократов».*

Play off

У студента Льва Шубникова было хобби – парусный спорт, сыгравшее роковую роль в его судьбе. Далее со слов его жены Ольги Трапезниковой, *«самым главным развлечением для нас была яхта, которую Физический институт арендовал в бывшем императорском яхт-клубе. Всем хозяйством яхт-клуба ведал некто Рябов. Однажды университетская компания химиков обратилась к нему с просьбой подобрать матросов для похода по Финскому заливу (яхта у них была довольно большая). Рябов предложил Льву Васильевичу пойти в этот поход в качестве матроса, и Лев Васильевич с удовольствием согласился. Время шло, но он не возвращался. Рябов высказал предположение о крушении.*

В действительности эта компания похитила в университете приборную платину и решила сбежать за границу. Их прибило к Финляндии, где их всех за незаконный переход границы посадили в тюрьму. Им было предложено покинуть Финляндию. Но возвращаться назад никто, кроме Льва Васильевича, не хотел. Тогда их выслали в Германию…

Он работал фотографом, затем на кварцевом заводе. В конце концов он обратился в наше консульство с просьбой о возвращении. В это время в Германии по служебным делам находился преподаватель М.М. Глаголев, прибывший в командировку для покупки трансформаторов. Он подсказал Льву Васильевичу, к кому обратиться, и разрешение вернуться было получено».

Более года провёл Шубников за границей. Вернувшись, в 1922 году, он не стал восстанавливаться в университете, а перевелся на 3-й курс физико-механического факультета Политехнического института.

Льву Шубникову удавалось сочетать учебу с подработкой в Ленинградском физико-техническом институте (далее – ЛФТИ), в лаборатории Ивана Васильевича Обреимова. И по окончании Политехнического института он имел две опубликованные научные работы: одна из них – о способе выращивания крупных совершенных металлических монокристаллов заданной формы (метод Обреимова-Шубникова), другая – об оптическом методе наблюдения деформаций в каменной соли.

Лейденский университет

Осенью 1926 года Лев Шубников уезжает – по протекции Пауля Эренфеста[****] и директора ЛФТИ Абрама Иоффе[*****] – на стажировку в Лейденский университет. И выбор для научной стажировки именно Лейденского университета был тогда не случайным, ибо еще в 1894 году при этом университете была организована первая в

[****]Эренфест (Ehrenfest) Пауль (Павел Сигизмундович) (1880-1933) – физик-теоретик, иностранный член-корреспондент РАН (1924).
Родился в Вене. Окончил Венский университет (1904). В 1907-1912 гг. работал в Петербурге.
С 1912 г. – зав. кафедрой теоретической физики Лейденского университета.
В 1929-1933 гг. – научный консультант Украинского физико-технического института. В числе его самых близких друзей были А. Эйнштейн, Н. Бор и А. Иоффе.
[*****]Иоффе Абрам Фёдорович (1880-1960) – физик-экспериментатор, академик (1920), фундатор Украинского физико-технического института.
Родился 29 октября 1880 года в г. Ромны Полтавской области. В 1927-1929 гг. и 1942-1945 гг. – вице-президент Академии наук СССР. С 1918-го по 1950 г. – директор Ленинградского физико-технического института. В 1952-1955 гг. – директор Лаборатории полупроводников АН СССР.

мире криогенная лаборатория, которая впоследствии стала одним из самых авторитетных мировых центров физики низких температур.

ИСТОРИЧЕСКАЯ СПРАВКА

Лейденский университет основан в 1575 году принцем Вильгельмом I Оранским в ознаменование героической обороны города от испанских войск.

В 1894 году Гейке Камерлинг-Оннес (*Heike Kamerlingh Onnes,* 1853-1926) организовал в университете первую в мире криогенную лабораторию. Именно он впервые достиг температур, близких к абсолютному нулю; в 1908 году он первый в мире получил жидкий гелий, а в 1911-м открыл явление сверхпроводимости. После его ухода с поста директора руководителями (содиректорами) криогенной лаборатории стали его ученики Вандер Иоханес де Гааз (*Wander Johanes de Haas,* 1878-1960) и Виллем Гендрик Кеезом *(Willem Hendrik Keesom,* 1876-1956).

Основополагающий девиз лаборатории: *«Door meten – tot weten»* (*«Через измерение – к знанию»*).

Немаловажен и следующий факт: именно Пауль Эренфест содействовал научной стажировке наиболее перспективных сотрудников ЛФТИ (впервые в СССР!) в ведущих физических центрах мира.

В частности, именно благодаря его хлопотам Иван Васильевич Обреимов получил возможность в 1927-1928 гг. проводить научные исследования по спектроскопии кристаллов при низких температурах в Лейденской криогенной лаборатории.

По этому поводу примечательна выдержка из лейденского письма П. С. Эренфеста, адресованного А.Ф. Иоффе: *«Криогенная лаборатория только что получила 100 000 долларов из фонда Рокфеллера*[******] *на проведение работ при низких температурах. В соответствии с этим (это сообщение только для А. Ф.!) здесь очень заинтересованы в таких криогенных работах, которые должны быть проведены в наступающем году и которые бы продемонстрировали, что если только Лейден берет на себя «холод», то наиболее высококвалифицированные специалисты со всех частей света проводят свои специальные низкотемпературные исследования только в Лейдене, где они могут располагать наиболее совершенной техникой.*

Я прошу А. Ф. продумать какую-либо красивую работу, которую можно было бы (после подготовки при комнатной температуре и в жидком воздухе) в течение двух месяцев полностью проделать в (жидком) водороде или гелии. Может быть, что-либо, касающееся свойства деформации сверхпроводящих монокристаллов в точке перехода».

Ольга Трапезникова также была направлена на стажировку в криогенную лабораторию Лейденского университета. Явно непредвзяты и следующие её мемуарные заметки: *«Криогенная лаборатория, или, как она официально называлась, "Физическая лаборатория Лейденского университета, основанная Камерлинг-Оннесом", произвела на меня большое впечатление.*

В Лейдене была специальная комната для измерений («Meet Kamer»). Многочисленные мальчики-помощники, работники мастерских делали все для научных сотрудников. Была такая атмосфера, в которой научные сотрудники высоко ценились,

было уважение к научной работе. Стиль лаборатории заключался в том, что измерения должны быть очень точными, мерить нужно на чистых образцах. Там был совсем другой дух, отличный от нашего. В Ленинградском университете, да и в Физтехе количественным измерениям такой точности не придавалось значения. Кроме того, у нас не было таких приборов. Я впервые увидела, как нужно мерить».

В Лейденской лаборатории Лев Шубников изучал свойства висмута в магнитном поле при низких температурах. Следует заметить, что, несмотря на интенсивные исследования ученых того времени, поведение висмута оставалось неразгаданным – не удавалось объяснить существенные расхождения в экспериментальных результатах.

В. де Гааз и Л. Шубников предположили, что проблема заключается в самих монокристаллических образцах висмута: в наличии дефектов и содержании примесей. Следовательно, первостепенной задачей в исследовании висмута было получение достаточно чистых образцов.

В течение первого года пребывания в Лейдене Шубников был занят химической очисткой и перекристаллизацией висмута. Получив кристаллы висмута исключительно высокого качества с малым содержанием примесей и дефектов, он начал исследования поведения этих образцов в магнитном поле при азотных и водородных температурах. Полный цикл экспериментов занял четыре года.

[******]Рокфеллеровский фонд был создан в мае 1913 г. с целью *«содействия процветания человечества во всем мире»*. Основатель фонда – Дж. Д. Рокфеллер (Rockefeller)-старший (1839-1937), родоначальник американской династии промышленников и финансистов.

Фонд субсидировал научные стажировки молодых перспективных ученых (как правило, одногодичные), оказывал финансовую поддержку научным институтам (например, *Институту теоретической физики* Н. Бора в Копенгагене, *Лаборатории низких температур* Г. Камерлинг-Оннеса в Лейдене), оплачивал научные командировки ведущих ученых мира (в частности, их лекционную работу).

Главным результатом этих исследований было открытие нового явления – низкотемпературных осцилляций сопротивления при изменении магнитного поля. Это открытие получило название – эффект Шубникова-де Гааза.

Примечательно, что во всех научных статьях, посвященных открытию этого эффекта, В. Де Гааз принципиально ставил фамилию Шубникова впереди своей – в нарушение алфавитного порядка, желая подчеркнуть решающую роль Льва Васильевича в данном открытии.

Л.В. Шубников проработал в Лейденской лаборатории полных четыре года – с 1926 по 1930. Здесь он познакомился со многими выдающимися учёными того времени. По свидетельству Трапезниковой, *«в научной жизни Лейдена П.С. Эренфест играл огромную роль. Он был дружен с В. де Гаазом и, хотя редко посещал лабораторию, был в курсе всех полученных результатов.*

А самое главное – П.С. Эренфест проводил знаменитые теоретические семинары, на которые съезжались учёные всего мира. Заседания семинара проходили в аудитории теоретического корпуса. Сначала был доклад одной из приезжих знаменитостей, затем чаепитие и дискуссии без ограничения времени. Лев Васильевич, Э. Вирсма и я посещали все семинары П.С. Эренфеста».

«ХАРЬКОВСКИЙ ФИЗИКО-ТЕХНИЧЕСКИЙ ИНСТИТУТ БУДЕТ ЦЕНТРАЛЬНЫМ ДЛЯ СССР… ИНСТИТУТОМ НИЗКИХ ТЕМПЕРАТУР И НАУЧНО-ТЕХНИЧЕСКОЙ БАЗОЙ ПРОМЫШЛЕННОСТИ»

> Надо помнить, что до появления Петра Капицы
> мы были первой и единственной лабораторией в СССР
> и четвертой в мире, где был жидкий водород,
> а с 1933 г. и жидкий гелий.
> *Академик И.В. Обреимов,*
> *директор-организатор УФТИ*

В 1930 году Лев Васильевич Шубников получил предложение продолжить научную деятельность в Украинском (Харьковском) физико-техническом институте (далее – УФТИ). Как уточняет Ольга Николаевна, *«еще в нашу бытность в Лейдене И.В. Обреимов предложил Льву Васильевичу переехать в Харьков, во вновь созданный УФТИ, директором которого он стал».*

Приведенные ниже выдержки из официальной и личной корреспонденции позволяют правдиво осветить и другие тогдашние замыслы.

И.В. Обреимов – П.Л. Капице

Лейден,12 июня 1928 г.

… В наш ГФТИ поступило разом два предложения организовать 2 физических института, один в Томске, другой у **Харкові** [так выделено в первоисточнике. – *Прим. А.Т.*].

С Томском дело сделано… С Харьковом дело не только не кончено, но даже и не начато. В жертву Харькову обречен Ваш покорный слуга. **В Харькове предполагается дело очень интересное – большая криогенная лаборатория с водородом и гелием. Отчасти по моей инициативе...**

Должен Вам сказать, что к институтам сверхдредноутам у меня влечения нет, т. ч. я мыслю себе – это очень скромный институт. Но вот когда я думаю о Вас, то мне кажется, что если бы Вы там были, то это был бы допинг для нашей физики, и для физики вообще.

Вы подумайте, что можно сделать в таком институте. А для отечества – это ведь тоже будет институт, который будет конкурировать по своему значению с Питером и будет Питер подтягивать...

Л.В. Каменев – П.Л. Капице

Москва, 23 января 1929 г.

Уважаемый Петр Леонидович. Сейчас мы организуем в Харькове Физико-технический институт по типу Ленинградской [физико-технической] лаборатории академика А.Ф. Иоффе. Придавая этому делу исключительное значение, я решил просить Вас принять участие в организации этого института в качестве консультанта. Если Вы соглашаетесь на мое предложение, то на Вашей обязанности будет лежать ежегодный приезд в СССР на 2-3 месяца. Вопрос о визах (въездных и проездных) для Вас и Вашей семьи не будет связан для Вас ни с какими затруднениями и может быть при Вашем первом приезде сюда урегулирован так, как это Вам будет удобно. За Вашу работу здесь Вы будете получать ежегодно 2 000 рублей, причем в эту же сумму будут входить и Ваши расходы по поездкам сюда.

Зная о ваших научных успехах, я полагаю, что Ваши приезды сюда окажут вообще существенное значение не только для Харьковского института, но и вообще для дела научно-технического развития СССР. Ознакомившись с Вашим вопросом, я вообще был удивлен, что до сего времени не велось официальных переговоров с Вами о перенесении Ваших работ, как советского ученого, в СССР. Те средства, которыми располагает НТУ, вполне позволят создать для Вас в СССР – Ленинграде, Москве или Харькове – те условия,

которые необходимы для успешного развития Вашей работы. Я полагаю, что при приезде сюда мы побеседуем с Вами об этих возможностях. Я вполне гарантирую вам, однако, что никакие давления в смысле немедленного переезда сюда на Вас не будут оказаны и весь вопрос будут решен в смысле наиболее успешного и бесперебойного хода Вашей работы.

Уважающий Вас,

Л. Каменев.

И.В. Обреимов – П.Л. Капице

Кембридж, 17 ноября 1929 г.

Дорогой Петр Леонидович. Нас всех крайне порадовало твое согласие быть консультантом у нас в Институте, и я надеюсь, что это лишь первый шаг к твоему постоянному переезду в СССР для постоянной научной работы. Ты прекрасно знаешь, как быстро научная работа развивается у нас в стране, и какое громадное значение придается ей у нас.

Я тебя могу уверить, что всё необходимое, чтобы облегчить твой переезд, будет предпринято и частично уже предпринято с нашей стороны.

1. Принимая во внимание твои моральные обязательства по отношению к Кавендишской лаборатории, мы включили в пятилетний план УФТИ на 1929/30 г. сумму в 250 тысяч рублей валютой на выкуп твоей лаборатории. Этот 5-летний план утвержден Президиумом ВСНХ УССР...

3. В пятилетний план на 1929/30 год включена сумма в 300 тысяч рублей на постройку твоей Магнитной Лаборатории на участке нашего института.

4. Что касается твоего положения, то оно будет таким, каким ты пожелаешь, т. е. либо директором УФТИ, либо независимым Старшим Физиком, либо можешь иметь совершенно независимую лабораторию...

Стоит также напомнить и другие подзабытые факты (из письма А.Ф. Иоффе председателю СНК УССР В.Я. Чубарю): *«...мы столкнулись с необходимостью работать при низких температурах, и такую лабораторию мы устроим во что бы то ни стало. Харьковский физико-технический институт будет центральным для СССР (и, вероятно, для окрестных государств – Эстонии, Латвии, Польши и т. д.) институтом низких температур и научно-технической базой промышленности».*

В становлении лаборатории весьма серьёзную помощь оказала Лейденская лаборатория, в частности один из ведущих сотрудников В. де Гааза Э. Вирсма.

Ольга Николаевна Трапезникова с особой признательностью подчёркивает, что *«очень большую помощь оказывал Э. Вирсма. Он каждый год, вплоть до 1935, приезжал в Харьков и привозил массу всяких вещей, без которых мы не могли работать. Будучи в Лейдене, он узнал о новой гелиевой машине, сконструированной Ф. Саймоном. Он немедленно выслал нам эскизы машины, опередив П. Эренфеста, который хотел сделать то же самое.*

Нам нечем было измерять низкие температуры, для этого требовались специальные платиновые термометры. Чтобы их изготовить, следовало намотать платиновую проволоку на фарфоровый цилиндр, отжечь всё это при высоких температурах и откалибровать. У нас не было платины нужной степени чистоты, был грязный фарфор, из которого при обжиге испарялись различные примеси, загрязнявшие платину. Правда, для калибровки был у нас платиновый термометр Pt-38, подаренный нам В. Кеезомом. Э. Вирсма привозил нам из Лейдена чистую платиновую проволоку и специальные фарфоровые цилиндры, чтобы мы могли сами сделать термометры.

Для хранения жидкостей нужны были дьюары. Металлические дьюары паяли оловом. При низких температурах наше олово трескалось, и дьюары выходили из строя. Э. Вирсма привозил в большом количестве специальный припой, который не трескался при низких температурах.

Он привозил все, что мы в Союзе не могли достать...

Лейкопластыря не было – он и лейкопластырь привёз... Разумеется, всё это Э. Вирсма делал с одобрения В. де Гааза...

Э. Вирсма очень помог криогенной лаборатории, хотя об этом мало кто знает».

Вирсма также хотел переехать на постоянное место жительства в Харьков – даже продал всё своё имущество, но визу так и не получил.

Много лет спустя Борис Георгиевич Лазарев – преемник Льва Васильевича Шубникова – на страницах своих мемуарных заметок не без заслуженной гордости перечислил достижения лаборатории тех лет: *«Безусловно, криогенная лаборатория в этот период играла роль центральной криогенной организации и в развитии новых технических решений, внедрённых в народное хозяйство:*

•к 1936 г. были полностью разработаны конструкции металлических дьюаров емкостью до 50 л. Вначале дьюары изготовлялись в институте порядочными партиями для внешнего потребления, а в 1936 г. вся документация вместе с большим опытом была передана Московскому автогенному заводу, выпускающему дьюары в промышленных масштабах;

•в 1936 г. успешно было испытано применение жидкого метана как горючего – сравнены показатели работы 1,5-тонной грузовой машины на проселочных дорогах протяженностью 300 км на бензине и метане с хорошими показателями в пользу последнего…

•в 1937 г. успешно были испытаны криогенные устройства с жидким кислородом, с одной стороны – для резки, сварки, с другой – для жизнеобеспечения экипажей высотных полетов…

С применением аппаратуры были выполнены в 1937 г. рекордные полеты экипажа М. Громова (Москва – Северный полюс – Сан-Джасинто (США)) и экипажа В. Гризодубовой, а также другие полеты в военные годы…

Перечисляя результаты, полученные Л.В. Шубниковым и его сотрудниками в такой короткий срок и оценивая их влияние на формирование новых представлений и направлений в физике и новых технических решений, поражаешься, как быстро делается наука, когда она становится государственным делом».

Также и Александр Ильич Ахиезер – тогдашний сотрудник теоротдела УФТИ, возглавляемого в 1932-1937 гг. Львом Давидовичем Ландау – на страницах своих мемуаров акцентирует внимание на явно принципиальных фактах: *«С большой охотой он [Л.Д. Ландау. – Прим. А.Т.] обсуждал результаты экспериментальных исследований, проводившихся в УФТИ. Часто далеко за полночь он просиживал в криогенной лаборатории Л.В. Шубникова, обсуждая с ним результаты его опытов, которые привели к важным открытиям.*

К числу их относится в первую очередь доказательство невозможности проникновения магнитного поля в сверхпроводник. Это явление получило название эффекта Мейснера, хотя оно независимо было открыто Шубниковым, впервые показавшим, что магнитная индукция в сверхпроводнике точно равна нулю. Шубникову принадлежит также открытие промежуточного состояния сверхпроводников, теория которого была создана Ландау.

До сих пор старожилы вспоминают, как поздно вечером жена Л.В. Шубникова О.Н. Трапезникова приносила в лабораторию мужа ужин для двух Львов».

Представляется весьма принципиальным и следующий исторический нюанс. В резолюции первого выездного заседания Физической группы Академии наук СССР, которое состоялось в Харькове (23-24 января 1937 года), в числе прочих успехов было отмечено, что *«УФТИ за шесть лет своего существования превратился в один из ведущих физических институтов Советского Союза. **Сессия отметила огромное научное и техническое значение создания в УФТИ криогенной лаборатории, стоящей на уровне лучших мировых лабораторий низких температур».***

Также феномен УФТИ был довольно подробно освещён и на XVII съезде ВКП(б)**:**

«Исследовательская работа по физике в сколько-нибудь широком масштабе велась в СССР до последнего времени только в Ленинграде и Москве. Рост промышленности Союза поставил задачу создания крупных научных учреждений, работающих в области физики, и в других важнейших промышленных центрах.

По инициативе Украинского правительства в план первой пятилетки ВСНХ СССР была внесена организация научно-исследовательского Физико-технического института в Харькове (УФТИ).

Организация нового института была поручена Ленинградскому физико-техническому институту, который выделил для него большую группу (около 20 чел.) научных работников. Эта группа вместе с частью харьковских физиков и составила основное ядро института...

Развитию работ по теоретической физике институт всё время уделяет особое внимание, так как эти работы, кроме их непосредственного значения, в сильной степени способствуют общему высокому уровню работ института.

Тесное взаимодействие теоретических и экспериментальных работ составляет одну из самых существенных черт научного лица института...

Большой успех работы теоретиков вызвал приток ученых из других институтов Союза и из-за границы для временной работы в институте...

За истекшие три года своей работы Украинский физико-технический институт стал одним из крупнейших научных центров Союза в области физики и пользуется большим авторитетом за границей».

Научному престижу УФТИ способствовал и тот нюанс, что почетным членом тогдашнего Ученого совета был избран лауреат Нобелевской премии П. А. М. Дирак, а научными консультантами института согласились стать П. С. Эренфест, П. Л. Капица и Г. А. Гамов.

К тому же зачастую упускается из виду и тот исторический факт, что именно в Харькове, на базе УФТИ, впервые в СССР начал издаваться (в 1932-1937 гг.) физический журнал на иностранных языках – *«Physikalische Zeitschrift der Sowjet Union».*

Но… вскоре настали смутные времена – необоснованные репрессии. Отчасти показательны воспоминания иностранного сотрудника УФТИ А. Вайсберга: *«Наш институт – один из самых значительных в Европе. Возможно даже, что в Европе нет института, столь же хорошо оснащенного и имеющего так много различных лабораторий, как наш. Правительство не пожалело денег. Ведущие ученые частично получили образование за границей. Долгое время их посылали за государственный счет к знаменитейшим физикам мира для продолжения образования.*

В нашем институте 8 отделов, во главе их стояли 8 научных руководителей. Как все это выглядит теперь?

Лаборатория кристаллов... Руководитель Обреимов – арестован.

1-я криогенная лаборатория... Руководитель Шубников – арестован.

2-я криогенная лаборатория... Руководитель Руэманн – выдворен из страны.

ядерная лаборатория... Руководитель Лейпунский – арестован.

Рентгеновский отдел ... Руководитель Горский – арестован.

Отдел теоретической физики... Руководитель Ландау – арестован.

Опытная станция глубокого охлаждения... Руководитель Вайсберг – арестован.

Лаборатория ультракоротких волн... Руководитель Слуцкин пока работает»…

Согласно архивно-следственным документам 10 ноября 1937 года Лев Васильевич Шубников был расстрелян.

Репрессии в УФТИ спровоцировали огромный международный резонанс. Буквально не весь мировой олимп физической науки XX века поднял свои голоса в защиту несправедливо осужденных уфтинцев.

В частности, лауреат Нобелевской премии А. Эйнштейн в официальном порядке обращался к И. Сталину, поскольку искренне был убеждён в лояльности репрессированных учёных.

Господину Иосифу Сталину,
Москва, СССР.
Пасадена, 16 мая 1938 года

Глубокоуважаемый господин Сталин!

В последнее время мне стали известны много случаев, когда видные ученые в России обвиняются в тяжких преступлениях, как люди, сохраняющие полное доверие в своих человеческих отношениях с зарубежными коллегами. Я понимаю, и Вам это известно, что во времена кризисов и волнений случается, что подозрение падает на невиновных и достойных людей. Но я также убеждён в том, что как с общечеловеческой точки зрения, так и в интересах успешного развития русского созидания исключительно важным является крайне осторожное обращение с людьми больших творческих сил и редких способностей.

В этой связи я очень просил бы Вас обратить внимание на дело Александра Вайсберга, г. Харьков. Господин Вайсберг, австрийский гражданин, инженер-физик, работал в Украинском физико-техническом институте в Харькове. В особенности я хотел бы попросить о том, чтобы было принято во внимание заключение о деятельности доктора Вайсберга, которое профессор Мартин Руэманн (руководитель опытного участка низких температур) направил весной 1937 года в Народный комиссариат тяжёлой промышленности.

С уважением, профессор Альберт Эйнштейн

Сколь веским был международный резонанс, освещает и следующее ходатайство за подписью трёх лауреатов Нобелевской премии:

Господину Генеральному прокурору СССР.
Париж, 15 июня 1938 г.

Глубокоуважаемый господин Генеральный прокурор!

Мы, нижеподписавшиеся, друзья Советского Союза, считаем своим долгом поставить Вас в известность о следующем.

Содержание под стражей двух выдающихся иностранных физиков, доктора Фридриха Хоутерманса, арестованного 1 декабря 1937 г. в Москве, и господина Александра Вайсберга, арестованного 1 марта этого же года в г. Харькове, воспринято в научных кругах Европы и США с большим недоумением.

Так как господа Хоутерманс и Вайсберг пользуются в этих кругах авторитетом, следует опасаться, что их продолжительное содержание под стражей станет ещё одним толчком в той кампании, которая в настоящее время приносит значительный ущерб авторитету страны социализма и сотрудничеству СССР с западными странами.

Это усложняется ещё тем обстоятельством, что учёные, считающие себя друзьями и постоянными защитниками СССР от нападок противников, не получают никакой информации от советских властей о положении Хоутерманса и Вайсберга, несмотря на их длительное заключение, и они с большим недоумением воспринимают происходящее.

Хоутерманс и Вайсберг имеют среди всемирно известных ученых многочисленных друзей, например, профессора Эйнштейна в Пасадене, профессора Блэкетта в Манчестере, профессора Нильса Бора в Копенгагене, которые сочувствуют им и будут участвовать в судьбе обоих ученых.

Господин Вайсберг, являющийся одним из основателей и редактором журнала *«Zeitschrift fur Physik»* в СССР, получил приглашение профессора Эйнштейна в университет в г. Пасадена. Из-за своего ареста он не имеет возможности воспользоваться этим приглашением.

По этой же причине и доктор Хоутерманс, получивший приглашение в институт в Лондоне для проведения научных исследований, не смог им воспользоваться – в момент ареста он находился уже в таможенном зале московского вокзала...

Ответственные лица в СССР в последнее время сделали несколько официальных заявлений о том, что во время чистки, которая была необходима из-за угрозы стране со стороны внутренних и внешних врагов, исполнительными органами были допущены ошибки, неизбежные в подобное критическое время; официальные лица считали крайне важным подчеркнуть необходимость устранения таких ошибок и злоупотреблений.

Мы, нижеподписавшиеся и все друзья обоих обвиняемых, убеждены в том, что в данном случае это и есть подобное недоразумение.

Поэтому они обращаются к Генеральному прокурору СССР с тем, чтобы обратить его внимание на дела Хоутерманса и Вайсберга и просят его ради авторитета СССР в зарубежных научных кругах предпринять срочные меры к немедленному освобождению обоих.

Важнейшее политическое значение этого обстоятельства даёт нам право переслать копию этого письма через посольство СССР в Париже господину Сталину...

<div align="right">

Ирен Жолио-Кюри, лауреат Нобелевской премии.

Жан Перрен, лауреат Нобелевской премии.

Фредерик Жолио-Кюри, лауреат Нобелевской премии
</div>

Также и цитируемая ниже корреспонденция – яркое свидетельство тому, что именно в лихолетье проявляется истинная суть человека.

Белый Дом Вашингтон
21 октября 1940
Моя дорогая Миссис Хоутерманс:

Очень Вам благодарна за Ваше письмо.
Я рада узнать, что Ваш муж освобожден и что он на свободе и чувствует себя хорошо. Не попытается ли он позднее приехать в нашу страну?
Искренне Ваша
Элеонора Рузвельт

Белый Дом Вашингтон
29 ноября 1940
Моя дорогая Миссис Хоутерманс:

Миссис Рузвельт просила меня поблагодарить Вас за Ваше письмо.
Она очень рада, что Ваш муж спасен, и надеется, что все будет хорошо.
Искренне Ваша
Мальвина К. Томпсон
Секретарь Миссис Рузвельт

<div align="center">

Продолжение следует
</div>

REFERENCES
[1]   A. Tan'shyna, East European Journal of Physics, **5**(3), 82-88 (2018), https://doi.org/10.26565/2312-4334-2018-3-10.
[2]   A. Tan'shyna, East European Journal of Physics, **4**, 111-118 (2018), https://doi.org/10.26565/2312-4334-2018-4-15.
[3]   A. Tan'shyna, East European Journal of Physics, **1**, 86-91 (2019), https://doi.org/10.26565/2312-4334-2019-1-08.
[4]   A. Tan'shyna, East European Journal of Physics, **2**, 113-116 (2019), https://doi.org/10.26565/2312-4334-2019-2-13.
[5]   A. Tan'shyna, East European Journal of Physics, **4**, 95-100 (2019), https://doi.org/10.26565/2312-4334-2019-4-11

<div align="center">

"ТРЕБА ПАМ'ЯТАТИ, ЩО ДО ПОЯВИ ПЕТРА КАПІЦИ МИ БУЛИ ПЕРШОЮ І ЄДИНОЮ ЛАБОРАТОРІЄЮ В СРСР ..."
</div>

<div align="center">

А. Таньшина

Національний науковий центр «Харківський фізико-технічний інститут»
м. Харків, Україна
</div>

Лев Васильович Шубніков народився 1901 року в Санкт-Петербурзі. Його батько, Василь Васильович, працював бухгалтером, а мама - Любов Сергіївна - вела домашнє господарство. У 1911 році Лев Шубніков був зарахований до одного з кращих Санкт-петербурзьких середніх навчальних закладів - гімназії Марії Андріївни Лентовського. Навчався, як свідчать архівні документи гімназії, старанно. У табелі за випускний, 8 клас, в графі «фізика» записано - «інтерес до предмету великий». У 1918 році Шубніков надходить в Петроградський університет на фізико-математичний факультет (спеціальність «фізика»). Але він був єдиним студентом-фізиком набору цього року, і йому довелося слухати лекції спочатку з тими, хто був на курс старше, потім - на курс молодше. Ілюстрація студентського життя тих років - мемуарні спогади його однокурсниці Ольги Миколаївни Трапезнікової, доктора фізико-математичних наук: «У 1919 році я поступила на фізичне відділення Петроградського університету. В університеті зустрілася зі Львом Васильовичем ... Життя було важким. Після лекцій Лев Васильович становив список присутніх, лектор підписував, і всім нам видавали по тоненькому шматочку хліба з повидлом - ми називали це чайним постачанням ... У 1919 році вже існував Оптичний інститут, і Д.С. Різдвяний влаштував усіх старших студентів ... туди лаборантами. Окремої будівлі ГОІ [Державний оптичний інститут. - Прим. А.Т.] тоді ще не мав і розміщувався в Фізичному інституті при університеті. Все лаборанти отримували так званий атомний пайок, і це їх дуже підтримувало. Такий же пайок отримували і викладачі ». Заслуговують на увагу і

такі історичні факти: перша світова війна, революція, громадянська війна і інтервенція породили в країні розруху, голод, холод. Наведені нижче витяги з урядових документів того часу дозволяють наочно змалювати тодішні реалії.
КЛЮЧОВІ СЛОВА: Лев Шубніков, кріогенна лабораторія, Харків

"WE MUST REMEMBER THAT BEFORE ARRIVAL OF PETER KAPITSA, WE WERE THE FIRST AND EXCLUSIVE LABORATORY IN THE USSR …"

A. Tan'shyna
National Science Center "Kharkov Institute of Physics and Technology"
Kharkiv, Ukraine

Lev Vasilievich Shubnikov was born in 1901 in St. Petersburg. His father, Vasily Vasilievich, worked as an accountant, and his mother, Lyubov Sergeyevna, ran a household. In 1911, Lev Shubnikov was enrolled in one of the best St. Petersburg secondary schools - the Maria Andreevna Lentovskaya gymnasium. He studied diligently, as evidenced by the archival documents of the gymnasium. In the report card for graduation, grade 8, in the column "physics" it says "there is a great interest in the subject". In 1918, Shubnikov entered the Petrograd University at the Faculty of Physics and Mathematics (specialty "Physics"). But he was the only recruiting physics student of this year, and he had to listen to lectures first with those who were a year older, then - a younger course. An illustration of the student life of those years is the memoirs of his classmate Olga Nikolaevna Trapeznikova, doctor of physical and mathematical sciences: "In 1919 I entered the physical department of Petrograd University. I met Lev Vasilievich at the university … Life was difficult. After the lectures, Lev Vasilievich compiled a list of those present, the lecturer signed, and we all were given a thin piece of bread with jam - we called it tea allowance … In 1919, the Optical Institute already existed, and D.S. Rozhdestvensky arranged for all senior students … laboratory assistants. Separate building GOI [State Optical Institute. - Note A.T.] then did not yet have and was housed at the University's Physics Institute. All laboratory assistants received the so-called rations, and this supported them very much. Teachers received the same ration. " The following historical facts deserve mention: the First World War, revolution, civil war and intervention gave rise to devastation, famine, cold in the country. The following extracts from government documents of that time allow you to clearly describe the then realities.
KEYWORDS: Lev Shubnikov, Cryogenic Laboratory, Kharkiv

INSTRUCTIONS FOR PREPARING MANUSCRIPT IN EAST EUROPEAN JOURNAL OF PHYSICS

[1]N.N. Author*, [2]N.N. Co-author(s)
[1]Affiliation of first author
[2]Affiliation of second author (if different from first Authors)
*E-mail: corresponding_authors@mail.com, [1]ORCID ID
E-mail: co_authors@mail.com, [2]ORCID ID
Received October 25, 2019; revised November 25, 2019 accepted December 5, 2019

Each paper must begin with an abstract. The abstract should be typed in the same manner as the body text (see below). Please note that these Instructions are typed just like the manuscripts should be. The abstract must have at least 1800 phonetic symbols, supplying general information about the achievements, and objectives of the paper, experimental technique, methods applied, significant results and conclusions. Page layout: the text should be printed on the paper A4 format, at least 5 pages, with margins of: Top - 3, Bottom, Left and Right - 2 cm. The abstract should be presented in English (only for foreign authors), Ukraine and Russian.
KEYWORDS: there, must, be, at least, 5 keywords

This is introduction section. This paper contains instructions for preparing the manuscripts. The text should be prepared in .doc format (using MS Word).

INSTRUCTIONS

The text should be typed as follows:
• **title**: Times New Roman, 12 pt, ALL CAPS, bold, 1 spacing, centred;
• **authors**: name, initials and family names; Times New Roman, 12 pt, bold, 1 spacing, centred;
• **affiliation(s)**: Times New Roman, 9 pt, italic, 1 spacing, centred;
• **abstract**: Times New Roman, 9 pt, 1 spacing, justified;
• **body text**: Times New Roman, 10 pt, 1 spacing, justified; paragraphs in sections should be indented right (tabulated) for 0.75 cm;
• **section titles**: Times New Roman, 10 pt, bold, 1 spacing, centred, without numbering, one line should be left, blank above section title;
• **subsection titles**: Times New Roman, 10 pt, bold, 1 spacing, centred, without numbering in accordance to the section (see below), one line should be left blank above subsection title;
• **figure captions**: width of the figure should be 85 or 170 mm, figures should be numbered (Fig. 1) and titled below figures using sentence format, Times New Roman, 9 pt, 1 spacing, centred (if one line) or justified (if more than one line); one line should be left blank below figure captions;
• **table captions**: width of the table should be 85 or 170 mm, tables should be numbered (Table 1.) and titled above tables using sentence format, Times New Roman, 10 pt, 1 spacing, centred (if one line) or justified (if more than one line), tables should be formatted with a single-line box around the outside border and single ruling lines between rows and columns; one line should be left blank below tables;
• **equations**: place equations centred, numbered in Arabic (1), flush right, equations should be specially prepared in MathType; one line should be left blank below and above equation.

Additional instructions

Numerated figures and tables should be embedded in your text and placed after they are cited. Only black and white drawings and sharp photographs are acceptable. Letters in the figures should be 3 mm high. The figures should be presented in one of the following graphic formats: jpg, gif, pcx, bmp, tif.

REFERENCES

Cite references in AIP style (https://guides.lib.monash.edu/citing-referencing/aip). Numbering in the order of referring in the text, e.g. [1], [2-5], etc. References should be listed in numerical order of citation in the text at the end of the paper (justified), Times New Roman, 9 pt, 1 spacing.

Journal Articles
[1] T. Mikolajick, C. Dehm, W. Hartner, I. Kasko, M. J. Kastner, N. Nagel, M. Moert and C. Mazure, Microelectron. Reliab. **41**, 947 (2001).
[2] S. Bushkova, B.K. Ostafiychuk and O.V. Copaiev, Physics and Chemistry of Solid State. **15**(1), 182-185 (2014), http://page.if.ua/uploads/pcss/vol15/!1501-27.pdf. (in Ukrainian)
[3] M. Yoshimura, E. Nakai, K. Tomioka and T. Fukui, Appl. Phys. Lett. **103**, 243111 (2013), http://dx.doi.org/10.7567/APEX.6.052301.

E-print resourses with collaboration research
[4] M. Aaboud et al. (ATLAS Collaboration), Eur. Phys. J. C, **77**, 531 (2017), http://dx.doi.org/10.1140/epjc/s10052-017-5061-9
[5] Sjöstrand et al., *Comput. Phys. Commun.* **191,** 159-177 (2015), http://arxiv.org/abs/1410.3012.
[6] Boudreau, C. Escobar, J. Mueller, K. Sapp, and J. Su, (2013), http://arxiv.org/abs/1304.5639.

Books
[7] S. Inoue and K.R. Spring, *Video Microscopy*: *The fundamentals*, 2nd ed. (Plenum, New York, 1997), pp. 19-24.
[8] I. Gonsky, T.P. Maksymchuk and M.I. Kalinsky, *Біохімія Людини [Biochemistry of Man],* (Ukrmedknyga, Ternopil, 2002), p. 16. (in Ukrainian)
[9] V.V. Mal'tsev, *Металлография промышленных цветных металлов и сплавов [Metallography of industrial nonferrous metals and alloys],* (Moscow, Metallurgiya, 1970), p. 364. (in Russian)
[10] M. Garkusha, *Основи Фізики Напівпровідників [Fundamentals of Semiconductor Physics]* (Vysshaja shkola, Moscow, 1982), retrieved from http://gagago.ru/g20-osnovi-fiziki-napivprovidnikiv-pidruchnik-dlya-tehniku.html.

Book Chapters
[11] M. Gonzalez-Leal, P. Krecmer, J. Prokop and S.R. Elliot, in: *Photo-Induced Metastability in Amorphous Semiconductors*, edited by A.V. Kolobov (Wiley-VCH, Weinheim, 2003), pp. 338-340.
[12] A. Kochelap and S.I. Pekar, in: *Теория спонтанной и стимулированной хемилюминесценции газов [Theory of Spontaneous and Stimulated Gas Chemiluminescence]* (Naukova dumka, Kyiv, 1986), pp. 16-29. (in Russian)

Conference or symposium proceedings
[13] C. Yaakov and R.Huque, in: *Second International Telecommunications Energy Symposium Proceedings*, edited by E. Yow (IEEE, New York, 1996), pp. 17-27.
[14] V. Nikolsky, A.K. Sandler and M.S. Stetsenko, in: *Автоматика-2004: Матеріали 11 Міжнародної Конференції по Автоматичному Управлінню [Automation-2004: Materials of the 11th International Conference on Automated Management]* (NUHT, Kyiv, 2004), pp. 46-48. (in Ukrainian)

Patent
[15] I.M. Vikulin, V.I. Irha and M.I. Panfilov, Patent Ukraine No. 26020 (27 August 2007). (in Ukrainian)

Special Notes
1. Use International System of Units (SI system). 2. It is undesirable to use acronyms in the titles. Please define the acronym on its first use in the paper. 3. Refer to isotopes as ^{14}C, ^{3}H, ^{60}Co, etc.